Dissertation
submitted to the
Combined Faculties for the Natural Sciences and Mathematics
of the Ruperto-Carola-University of Heidelberg, Germany
for the degree of
Doctor of Natural Sciences

presented by
Christian-Eric Roux
born in Mühlacker, Germany

Date of oral examination: November 05, 2012

High-Resolution Mass Spectrometry:
The Trap Design and Detection System of Pentatrap
and New Q-Values for Neutrino Studies

Referees: Prof. Dr. Klaus Blaum

Priv.-Doz. Dr. Wolfgang Quint

Abstract

The novel Penning-trap mass spectrometer PENTATRAP aims for mass-ratio measurements of highly-charged ions with a relative precision of a few parts in 10^{12}. As the key part, an innovative trap assembly was designed. It consists of five cylindrical traps allowing for simultaneous measurements of two ion species and for continuous monitoring of the trapping conditions. This promises a substantial reduction of systematic errors. Moreover, in the course of this thesis a detection system was developed and characterized, which will enable fast and accurate measurements through its single-ion sensitivity and high signal-to-noise ratio.
In neutrino physics, the detection of neutrinoless double-electron capture would unambiguously prove the Majorana nature of neutrinos. In search for a suitable nuclide for the observation of this process, precise information about the total decay energy (Q-value) is needed in order to find a transition with a resonant enhancement of the decay rate. The mass ratios of ^{152}Sm/^{152}Gd and ^{164}Dy/^{164}Er were measured to a relative uncertainty of $\sim 10^{-9}$ at SHIPTRAP. This presents the first directly determined Q-values for the corresponding transitions.

Zusammenfassung

Das neuartige Penningfallen-Massenspektrometer PENTATRAP ist für Messungen von Massenverhältnissen hochgeladener Ionen konzipiert, bei denen eine relative Genauigkeit von einigen Teilen pro 10^{12} angestrebt wird. Als zentraler Bestandteil wurde eine innovative Fallenanordnung, bestehend aus fünf zylindrischen Fallen, konzipiert. Dies ermöglicht eine simultane Messung zweier Ionen und eine kontinuierliche Überwachung der Speicherbedingungen, was eine deutliche Reduzierung von systematischen Fehlern verspricht. Darüber hinaus wurde im Rahmen dieser Arbeit ein Detektionssystem entwickelt und charakterisiert, dessen Einzelionensensitivität und hohes Signal-zu-Rauschverhältnis schnelle und genaue Messungen erlauben wird.
Für die Neutrinophysik würde der Nachweis des neutrinolosen doppelten Elektroneinfangs den Majoranacharakter des Neutrinos beweisen. Bei der Suche nach einem aussichtsreichen Nuklid werden präzise Informationen über die Zerfallsenergie (Q-Wert) benötigt, um einen Übergang mit einer resonanten Überhöhung der Zerfallsrate zu finden. Dazu wurden die Massenverhältnisse von ^{152}Sm/^{152}Gd und ^{164}Dy/^{164}Er mit einer relativen Genauigkeit von etwa 10^{-9} an SHIPTRAP gemessen, was die erste direkte Bestimmung des Q-Wertes der zugehörigen Übergänge darstellt.

Table of Contents

List of Figures

List of Tables

1 Introduction

In modern science, the term "*mass spectrometry*" covers a wide field with a variety of different techniques and applications. Therein, the major activity is concerned with the determination of the abundance of particles, which range from simple atoms over molecules up to proteins. Applications arise in chemistry, biology or archeology and can be found even beyond science, such as in pharmaceutical industry, forensics or biomedicine [1–3].
In this thesis, the focus is on the branch of high-accuracy mass spectrometry on individual atoms. Here, nuclear and atomic interactions can be probed due to the relation of the binding energies to the mass of a bound system, provided by, probably, the most famous relation in science $E = mc^2$ derived by Einstein [4]. In order to reveal the importance of this beautiful topic for many branches of modern physics, the most important steps in the history of high-accuracy mass spectrometry are reviewed below, following very closely the guidelines given in [5, 6].

Brief History of Mass Measurements

The beginning of mass spectrometry might be defined by the discovery of the electron and the measurement of its charge-to-mass ratio in a combination of electric and magnetic fields in 1897 by Thomson [7]. Nowadays, the charge and mass dependent response on electromagnetic fields are still the basis of every mass spectrometer. In progress of his work, Thompson developed the first mass spectrograph in which an ion beam passes crossed electric and magnetic fields. Ions of the same charge-to-mass ratio were focussed along parabolas on a photographic plate. In 1912, he discovered the existence of isotopes of Ne with $A = 20$ and $A = 22$ with this instrument [8]. A student of Thompson, Aston, continued the work leading to the discovery and classification of a large number of isotopes [9], which was awarded with the Nobel Prize in chemistry "*for his discovery, by means of his mass spectrograph, of isotopes, in a large number of non-radioactive elements, and for his enunciation of the whole-number rule*" in 1922. Scientifically, an even more remarkable step resulted from the refinement of the spectrograph, which enabled a focusing independent of the ion velocity (energy focussing) with an increased relative precision of 10^{-4} in the mass measurement. From the investigation of a large number of stable isotopes, Aston observed that the actual masses do not only differ by multiples of the neutron mass [10]. This "*mass defect*" is the consequence of the nuclear binding energy, which lowers the mass of the bound nucleus due to $E = mc^2$. He was able to extract the value of the binding energy to ~ 8 MeV per nucleon for most stable isotopes. Furthermore, the mass values even gave hints to closed shells in nuclei, which was realized by Elsasser [11]. However, at that

time physicists were satisfied with the "*liquid drop model*" of the nucleus developed by Gamow, von Weizsäcker, Bethe and Bacher. Further improvement of the mass spectrographs by, e.g., double focusing techniques of direction and velocity led to an increased precision of 10^{-7} till 1950, where many contributors were involved, such as Dempster, Matthauch and Herzog or Barber and Duckworth (see references in [5]). Based on those improved mass measurements, the nuclear shell model was finally established in 1948 by Goeppert-Mayer [12], Haxel and Jensen [13].
Parallel to the ongoing improvement of beam spectrometers, the development of storage devices of charged particles started around 1950 with the leading actors Paul and Dehmelt. The Paul trap is based on electric radiofrequency (RF) fields of quadrupolar shape [14], which enables a confinement of the charged particles. A linear version, the so-called RF quadrupole mass filter is nowadays widely used for rest gas analysis, gas chromatography or molecular studies. However, the accuracy in mass determination with Paul traps is severely limited by the stability of the RF fields.
By far superior mass resolution can be achieved by Penning traps, which were developed by Dehmelt for outstanding experiments on single electrons [15]. This type of trap consists of a strong homogeneous magnetic field and a weak quadrupolar electrostatic field (see Chap. 3). The mass measurement is converted into the measurement of the cyclotron frequency $\omega_c = (q/m)B$ of a particle with charge q and mass m in a magnetic field B. The reduction to a frequency measurement is one of the keystones of high-precision mass measurements in a Penning trap, frequencies are the physical quantities which can be measured with highest intrinsic accuracy[1].
The very first high-accuracy Penning-trap mass measurements were performed in 1980 on the proton-to-electron mass ratio by Gräff [17]. Almost at the same time, a student of Dehmelt, Van Dyck, started with mass measurements on the electron-to-positron mass ratio [18]. In the following, more groups joined around 1990 such as SMILETRAP [19] or the group of Pritchard [20], and the branch of Penning-trap mass spectrometry expanded for the first time to measurements on short-lived nuclides at radioactive beam facilities with ISOLTRAP [21].

Modern Penning-Trap Mass Spectrometry and PENTATRAP

Currently, around 20 high-precision Penning-trap mass spectrometers are in operation or under construction world wide and impressive results were achieved. With a destructive time-of-flight detection technique, most accurate mass ratios are measured well below 10^{-9} (see, e.g. references in [5]). Even for extremely short-lived nuclides with half-lives down to $t_{1/2} = 8.8$ ms, measurements with relative accuracies were demonstrated in the order of 5×10^{-8} [22]. For stable and light nuclides and with a non-destructive image current detection technique, mass ratios are reported below the barrier of 10^{-11}, see e.g. [23].

[1] The principle of a frequency measurement for mass determination is also used in storage rings such as the ESR at GSI Darmstadt [16]. There, many different masses can be measured simultaneously by their revolution frequency in the ring. However, the mass resolution is limited due to, e.g., the stability of the many magnets involved and cannot reach the precision of Penning traps.

The keystones of this tremendous success are the development of detection techniques with a sensitivity down to a single stored ion and efficient and fast cooling techniques. Furthermore, technical developments of the trapping setups have reached extremely high levels, such as the stabilization of the magnet system in [24]. Experimental strategies were refined, e.g., to the measurement on highly-charged ions [25] or the remarkable method of the simultaneous measurement of two ion species in the same trap [23].
The output of Penning-trap mass spectrometry has contributed immensely to many branches of fundamental physics. A review and future suggestions can be found in [26], and a prominent, but not complete, list of examples is pointed out in the following. In astrophysics, a large number of nuclear masses of unstable nuclides are related to the question of element formation in the universe [27]. The comparison of the charge-to-mass ratio of the proton and antiproton serves as the most stringent CPT test in the baryon sector on the level of 9×10^{-11} [28]. Fundamental constants such as the electron-to-proton mass ratio have deep impact in calculations in many fields of physics and a direct measurement[2] was performed on the level of 4×10^{-9} [31].

Highest accuracies in mass-ratio measurements have, so far, only been achieved for light up to medium-heavy nuclides. However, as shown in Chap. 2, numerous examples for fundamental-physics applications arise for the medium-heavy and heavy mass range, too, where relative accuracies of mass-ratio measurements in the order of 10^{-11} and below are needed. Such measurements are the main motivation and aim of the novel Pentatrap mass spectrometer [32], which is currently under development at the Max-Planck-Institut für Kernphysik, Heidelberg, and is the focus of Part I within this thesis.
In order to make those ultra-high accuracy feasible, Pentatrap is characterized by several advanced aspects. First of all, the open access to two electron beam ion traps (EBIT) enables measurements on highly-charged ions. Since the cyclotron frequencies ω_c of the ions scale with the charge-to-mass ratio q/m, high charge states are a prerequisite for high absolute frequencies and, thus, low relative accuracies in the heavy mass range. In a future prospect, Pentatrap might even move to the Hitrap facility [33] at GSI, Darmstadt, for measurements on heaviest highly-charged ions up to bare uranium.
Pentatrap will be the first mass spectrometer which utilizes a stack of five Penning traps. The great benefit of such a structure is the possibility of the simultaneous measurement of two ion species in adjacent traps. This largely eliminates the effect of magnetic-field fluctuations on the frequency-ratio determination and, at the same time, ion-ion interaction of the highly-charged ions are negligible. The cylindrical geometry of the traps enables easy and fast switching of the ions between the trap used for the ratio measurement and traps dedicated for parking the ions during these measurements. In the remaining traps, high-accuracy monitoring of the magnetic field is possible or,

[2] The electron-proton mass ratio and the electron mass can even be determined indirectly with higher accuracy from measurements of the electron's magnetic moment in a Penning trap, see [29] and recent measurements in [30].

alternatively, these traps might serve as references for the voltage source providing the ultrastable trapping voltages for the measurement traps.
The detection and cooling of the ion's motions will be performed with a non-destructive image-charge detection system, where the single-ion sensitivity and elaborate detection schemes allow for the highly-accurate determination of the ion's motional frequencies. Moreover, enormous effort is spent to keep the overall fluctuations of the magnetic field as low as possible. External fluctuations are shielded by a combination of a flux-gate magnetometer and a pair of Helmholtz coils and variations in the field of the superconducting magnet are stabilized by a pressure- and temperature-regulation system.
A selection of physics cases motivating measurements at PENTATRAP is given in Chap. 2 and the basic principles of Penning-trap mass spectrometry are discussed in Chap. 3. The PENTATRAP facility is described in Part I, where an overview over the setup is given in Chap. 4. The design of the core piece at PENTATRAP, the trap tower, is elaborated in Chap. 5. The basic principles of non-destructive image-charge detection and the development of the detection system at PENTATRAP are discussed in Chap. 6.

Mass-Ratio Measurements Related to Neutrino Physics at SHIPTRAP

In the second part of this thesis work, mass-ratio measurements related to neutrino physics, in particular to the neutrinoless double-electron capture [34] (see Sec. 2.1.4), are discussed. A detection of this process would mark physics beyond the Standard Model of elementary particles by the unambiguous proof that the neutrino is a Majorana rather than a Dirac particle (the neutrino being its own anti-particle). This decision is a long-standing open question in neutrino physics and of basic interest for the construction of theories superior to the Standard Model. Moreover, the measurement of the decay rate of this process would give access to the effective Majorana mass of the neutrino. Unfortunately, for most nuclides life-times are expected to be far beyond the scope of an experimental realization of the measurement. However, if a mother and excited daughter nuclide are degenerate in energy, the decay rate is resonantly enhanced [35], possibly leading to the feasibility of the detection of this process in advanced micro-calorimetric experiments.
Penning-trap mass spectrometry offers the possibility of a precise determination of the total decay energy (Q-value) of this process by measuring the cyclotron-frequency ratio of ions of the mother and daughter nuclides in their energetic ground states. Together with calculations of the binding energy of the holes of the captured electrons and their decay rate, this allows for an accurate determination of the resonance condition. With theoretical calculations of the nuclear matrix elements, predictions on the range of the life-time of this process are possible, providing the basis for the search of the most suitable nuclide for the detection of this process.

In Part II, measurements on the Q-value of double-electron capture in the nuclides ^{152}Gd and ^{164}Er are presented. The estimates leading to the selection of ^{152}Gd and ^{164}Er as promising candidates for the detection of neutrinoless double-electron capture are considered in Chap. 7, where also the principles of a Q-value determination by

Penning-trap mass spectrometry are discussed. The measurements were performed with the Penning-trap mass spectrometer SHIPTRAP [36] at GSI, Darmstadt. An overview of the experimental setup and the basic principles of the time-of-flight detection method is given in Chap. 8. The measurements are presented in Chap. 9, together with a detailed description of the data-analysis procedure and, finally, a discussion of the results in the context of the search for neutrinoless double-electron capture.

2 Applications of High-Precision Mass Data

The list of applications of highly accurate mass and mass-ratio data is manifold and impressive results have been achieved, where a comprehensive review is given in [5]. In this chapter, the main motivations for highly accurate mass-ratio measurements with the novel Penning-trap mass spectrometer PENTATRAP (see Part I), and for the mass-ratio determinations at SHIPTRAP (see Part II), are given. Most suggestions can also be found in [26].

2.1 Neutrino Physics and Mass Measurements

In the following section, a brief introduction into neutrino physics and the relation to Penning-trap mass-ratio measurements is given. After short notes on the general neutrino properties in Sec. 2.1.1, the focus is turned to the neutrino-mass determination. The probably most natural way for the direct determination of the neutrino mass are ordinary β-transitions, which are discussed in Sec. 2.1.2. Another possibility for neutrino-mass determination are the second-order neutrinoless double-β transitions where, additionally, the mere detection of such transitions would immediately proof the Majorana nature of the neutrino. The general issues of double-β transitions are discussed in Sec. 2.1.3, together with a short review on neutrinoless double-β decay experiments. In Sec. 2.1.4, the focus is on the neutrinoless double-electron capture process, which is the main topic of Part II within this thesis. More details about neutrino physics are available in numerous review articles, from which most information here is taken, see e.g. [37, 38].

2.1.1 The Neutrino

The neutrino is one of the fundamental particles in the Standard Model of elementary particles (SM). The deep interest in its basic properties is closely related to our understanding of weak interactions within the SM. However, due to very low interaction rates with other particles or matter, a lot of fundamental questions about the neutrino are still hidden to our understanding, making the neutrino one of the most unknown and mysterious particle in modern physics. Prior to turning to neutrino-related mass measurements in the next section, the very basic properties of the neutrino are reviewed below.

Discovery of Neutrinos and the Standard Model of Elementary Particles

The existence of the neutrino was postulated in 1930 by Pauli in an open letter to explain the continuous shape of the spectrum of nuclear β-decay

$$n \rightarrow p + e^- + \overline{\nu}_e, \tag{2.1}$$

where a neutron n decays spontaneously into a proton p, an electron e^- and a neutrino[1] $\overline{\nu}_e$. The first theoretical description of the β-decay including neutrinos was given by Fermi in 1934 [39]. It then took about 20 years until the first observation of the anti-neutrino in 1956 by the detection of the inverse β-decay

$$p + \overline{\nu}_e \rightarrow n + e^+ \tag{2.2}$$

by Cowan and Reines [40]. As a further important step, it was shown in 1962 that there must exist different types of neutrinos [41], which is nowadays constrained to three flavors.
The Neutrinos are implemented in the minimal content of the Standard Model as leptonic fermions with spin 1/2. They are electrically neutral and only interacting by the weak interaction (by exchange of W or Z bosons). Neutrinos are assigned to every generation of leptons (e^-, μ^- and τ^-), resulting in the neutrino flavors ν_e, ν_μ and ν_τ, as well as the corresponding anti-neutrinos $\overline{\nu}_e$, $\overline{\nu}_\mu$ and $\overline{\nu}_\tau$. Up to now, only left-handed neutrinos (with helicity -1) and right-handed anti-neutrinos were detected in weak interactions. According to the SM, the lepton number is conserved for each flavor family of leptons in every weak interaction with neutrinos involved.
Furthermore, due to the lack of experimental evidence for any mass in early days of neutrino physics, neutrinos were implemented in the minimal content of the SM as massless particles [42]. However, already in 1957 first predictions were made that neutrinos can have a finite mass and the idea of lepton-number violating oscillations was introduced for transitions between neutrino and anti-neutrino [43]. The principle of such oscillations was then picked up again with respect to transitions between the neutrino flavors in 1962, e.g. in [44].

Proof of Massive Neutrinos: Flavor Oscillations

If massive neutrinos are assumed, the general concept of neutrino oscillations is based on the fact that for the weak interaction the flavor eigenstates $\nu_{e,\mu,\tau}$ are non-trivial superpositions of the mass eigenstates $\nu_{1,2,3}$

$$\nu_\alpha = \sum_{j=1}^{3} U_{\alpha,j}\nu_j, \quad \text{with} \;\; \alpha = (e, \mu, \tau), \tag{2.3}$$

[1] After the discovery of different neutrino flavors and for reasons of lepton-number conservation, the neutrino involved in this process was later called electron anti-neutrino.

where the mass eigenstates in Eq. (2.3) are assigned to an energy E_j and a momenta p_j. The unitary matrix U is called Pontecorvo-Maki-Nakagawa-Sakata (PMNS) matrix in literature. It depends on three mixing angles $\theta_{12}, \theta_{13}, \theta_{23}$ and on a CP-violating phase δ in case of Dirac neutrinos, while for Majorana neutrinos three CP-violating phases $\delta_{12}, \delta_{13}, \delta_{23}$ occur. By calculating the quantum-mechanical transition probability between two flavor eigenstates α and β at the distance L from a neutrino source, the famous oscillation formula writes to (see, e.g. [45])

$$P_{\alpha\beta}(L) = \sin^2(2\theta)\sin^2\left(\frac{\pi L}{L_{jk}^{\text{osc}}}\right), \quad \text{with} \quad L_{jk}^{\text{osc}} = \frac{4\pi E}{\Delta m_{jk}^2}. \tag{2.4}$$

Here, only two neutrinos with one mixing angle θ are considered and the neutrino mass eigenstates are assumed to be emitted at the same energy E, for simplicity. In Eq. (2.4), $\Delta m_{jk}^2 \equiv m_j^2 - m_k^2$ is the difference of the squared masses of the mass eigenstates. Hence, the detection of neutrino-flavor oscillations in Eq. (2.4) would prove that the mass difference between two neutrino-mass eigenstates is non-zero, implying at least one non-zero neutrino mass.
First indications that the SM description of the neutrino might be incomplete appeared in 1968, when the Homestake experiment discovered a deficit in the flux of solar neutrinos compared to astrophysical sun models [46]. Confirmation of this "*solar neutrino problem*" was done by, e.g. Kamiokande [47], and similar anomalies have been detected for atmospheric neutrinos by several other experiments (see, e.g. [48]).
In 1998, strong evidence for atmospheric neutrino oscillations was presented by the Super-Kamiokande experiment [49], and in 2002 oscillations of solar neutrinos have been detected by the SNO collaboration [50]. At SNO, all three neutrino flavors were detected at the same time being consistent with latest solar models. Later, neutrino oscillations were confirmed by several other experiments, e.g., with neutrinos from accelerators or reactors (see, e.g. [51]).
From oscillation experiments it is possible to determine the mixing angles and phases of the PMNS matrix in Eq. (2.3), where the mixing is much more pronounced than for the quark or hadronic sector. For a recent overview of experimental results see [52]. The resulting mass differences are given in [53] to

$$\begin{aligned} |\Delta m_{12}^2| &= (7.59 \pm 0.20) \cdot 10^{-5} \left(\text{eV/c}^2\right)^2, \\ |\Delta m_{23}^2| &= (2.43 \pm 0.13) \cdot 10^{-3} \left(\text{eV/c}^2\right)^2. \end{aligned} \tag{2.5}$$

With the evidence for massive neutrinos, neutrino oscillations marked physics beyond the SM for the first time. It is also clear from these oscillations that the concept of lepton-number conservation has to be given up in superior theories. However, neutrino-oscillation experiments can only give access to differences in neutrino masses but not to the absolute value, see Eq. (2.4). Furthermore, depending on the absolute value of the masses, there are still different ordering scenarios possible for the individual neutrino masses within the constraints of the mass differences in Eq. (2.5).

2.1.2 Direct Neutrino Mass Measurements by Ordinary β-Transitions

As discussed in the previous section, the absolute neutrino mass is of fundamental importance for modern physics. The currently most strict bound is derived from cosmology, where neutrinos act as mass and energy carriers. Mapping the microwave background, latest cosmological models, and a survey of the large scale structure of the universe leads to $\sum m_\nu \leq 0.5$ eV/c^2 [54]. However, interpretations of cosmological data are highly model-dependent and small deviations in the multiple parameters can lead to significant shifts in the indirectly deduced neutrino mass. Therefore, direct measurements of the neutrino mass are of high interest and enormous experimental effort is invested. In focus are ordinary β-transitions of the weak interaction, where part of the decay energy is invested in the neutrino mass.
Future spectrometers or calorimeters will be capable of a precise determination of the decay energy reduced by the neutrino energy. Penning-trap mass spectrometry can contribute by precise determinations of the total decay energy by measurement of the ground-state mass differences. The difference between both is the neutrino energy.
In the following section, a brief review on the main approaches for the determination of the neutrino mass by ordinary β-transitions is given. More details can be found, e.g. in [55]. For our main interest, the role of Penning-trap mass spectrometry as a contributor to neutrino physics, a broad review can be found in [26].

β-Decay Spectrum

The probably most natural way to search for the mass of the electron anti-neutrino $\overline{\nu}_e$ is the investigation of the electron spectrum in the nuclear β-decay. This technique was already proposed by Fermi within the framework of the first theoretical description of nuclear β-decay [39]. The spectrum of the β-decay derived from Fermi's Golden Rule is given by [56]

$$\begin{aligned} \frac{d\Gamma}{dE} \propto C \cdot \left|M_{\mathrm{fi}}\right|^2 \cdot F(E, Z+1) \cdot (E+m_e)p_e \qquad &\simeq \; E_0 \\ \times \sum_j P_j \sqrt{\left(E_0 - E_j - E\right)^2 - m_\nu^2} \cdot (E_0 - E_j - E) \qquad &\widehat{=} \; p_\nu \cdot E_\nu. \end{aligned} \tag{2.6}$$

The first factor is close to the endpoint energy of the spectrum E_0 with contributions from the weak coupling constant (in C), the nuclear matrix element M_{fi} of the transition from the initial state (i) to the final state (f), the Fermi function F and the phase space factor $(E + m_e)p_e$ of the electron. The second and third factors together are the neutrino phase space, consisting of the neutrino momentum p_ν and its relativistic energy E_ν. It is summed up over the final states E_j of the daughter nucleus, populated with probability P_j.
Especially close to the endpoint of the spectrum at E_0, the contribution from the neutrino phase space shapes the spectrum, in which the flavor mass $m(\overline{\nu}_e)$ of the electron anti-neutrino enters by its square. For the tritium β-decay, a detailed discussion of the

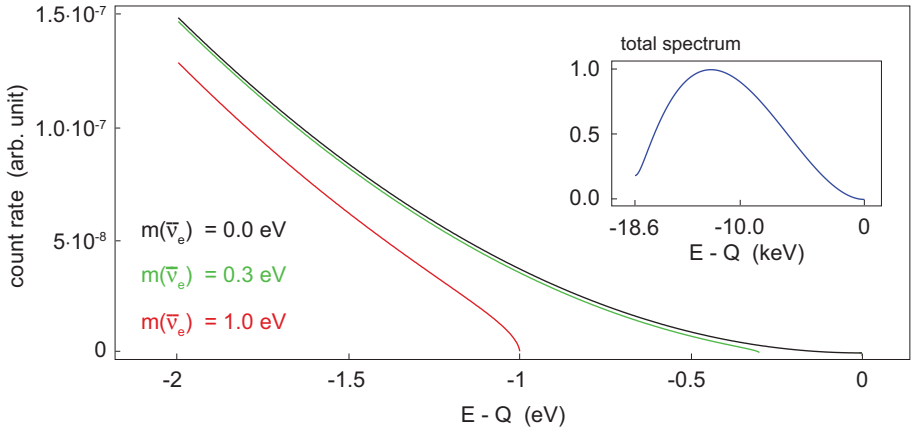

Figure 2.1: Electron spectrum of the tritium β-decay. The total decay energy is $Q \approx 18.6$ keV and the spectrum is truncated at $Q - m(\overline{\nu}_e)$.

spectra can be found in [55] and theoretical curves are shown in Fig. 2.1, depending on the actual mass of the neutrino.
In principle, every nucleus undergoing β-decay can be used for the search of the electron anti-neutrino mass. However, the number of electrons of the spectrum in an energy interval ΔE close to the endpoint E_0 scales with [57]

$$n(Q, \Delta E) \propto \left(\frac{\Delta E}{Q}\right)^3, \tag{2.7}$$

which clearly favors nuclides with low total decay energy Q and, thus, an increased relative effect of the neutrino mass.

Tritium β-Decay

Up to now almost all experimental effort has been invested in the decay of tritium to helium

$$^3\mathrm{H} \rightarrow {}^3\mathrm{He}^+ + e^- + \overline{\nu}_e, \tag{2.8}$$

which has a Q-value of 18.5898(12) keV [58] being one of the lowest of all β-emitters. There are several more reasons making tritium the preferred candidate for direct neutrino mass measurements [55], such as a low half-life of 12.3 years, high reachable accuracy in the calculation of the matrix element of the final state in the daughter nucleus and high availability, since tritium is a side-product of heavy-water nuclear reactors. Nevertheless, even in this case only a small fraction of all electrons are emitted in the energy region close to the endpoint ($\sim 10^{-10}$ in the last 10 eV), setting a severe experimental challenge.
Numerous experiments have been performed so far with different tritium sources and spectrometer designs. For an overview, see e.g. [55]. The most recent experiments at

Troitsk [59] and Mainz [60] reached a similar sensitivity with the best combined upper limit of the direct measurement of the electron anti-neutrino mass [55]

$$m(\overline{\nu}_e) < 2 \text{ eV/c}^2 \quad \text{at} \quad 95\ \% \text{ C.L.}. \tag{2.9}$$

As a successor of these experiments, both groups collaborate in the KArlsruhe TRItium Neutrino (KATRIN) experiment [61]. There, the sensitivity to the neutrino mass will be improved to, at least, 0.2 eV/c^2 by scaling up the heart of the experiment, a MAC-E filter (Magnetic Adiabatic Collimation applied to an Electrostatic Filter), to a factor of 10 compared to its predecessors.
The contribution of Penning-trap mass spectrometry for β-decay experiments can be seen as a necessary calibration of the spectral data [26]. For a daughter in the ground state, the endpoint energy E_0 as the main observable of these experiments is given by

$$E_0 = Q - E_{\text{recoil}} = E_e + E_\nu, \tag{2.10}$$

where Q is the total energy release in the nuclear decay and E_{recoil} is the recoil energy of the daughter nucleus. E_e and E_ν are the total energies of the electron and the electron anti-neutrino, respectively. If, for simplicity, dissociation energies of the tritium and helium molecules used at the KATRIN source are neglected, the Q-value is accessible by Penning-trap mass spectrometry via (see also Sec. 7.2)

$$Q = \Delta m(^3\text{H}, ^3\text{He}) \cdot c^2 = \Delta m(^3\text{H}^+, ^3\text{He}^+) \cdot c^2 - \Delta B_{\text{ion}}(^3\text{H}, ^3\text{He}), \tag{2.11}$$

where $\Delta m(^3\text{H}^+, ^3\text{He}^+)$ is the mass difference between the ions of ^{3}H and ^{3}He and ΔB_{ion} the difference between their ionization energies. The profit of independent Q-value measurements for experiments like KATRIN is discussed in detail in [62], giving primarily an important check of the systematics in the measured spectra.
The most precise value is $Q = 18.5898(12)$ keV, measured at SMILETRAP [58]. However, in order to give useful contributions for the internal fitting procedure at KATRIN, an uncertainty of ~ 5 meV is needed for the external determination of Q. To this end, a high-precision Penning-trap mass spectrometer called THE-TRAP (Tritium-Helium-Trap) is currently in development at the Max-Planck-Institut für Kernphysik[2], Heidelberg, aiming for mass-ratio measurements of ^{3}H/ ^{3}He in the order of a few parts in 10^{12} [63], where the resulting Q-value should at least be capable for identification of systematics in the KATRIN spectra.
As a further indirect contribution to KATRIN, Penning traps will be employed in the transport section between the tritium source and the spectrometer in order to monitor contaminations from the source [64].

[2]This Penning trap was originally designed at the University of Washington, Seattle, and was transferred to Heidelberg in 2008. In Seattle it was called UW-PTMS (University of Washington-Penning Trap Mass Spectrometer).

β-Decay of ^{187}Re

An alternative candidate for direct neutrino-mass determination in terms of β-decay is

$$^{187}\mathrm{Re} \rightarrow {}^{187}\mathrm{Os} + e^- + \overline{\nu}_e, \tag{2.12}$$

which has the second lowest[3] known β-transition energy of $Q \approx 2.5$ keV [67]. Hence, according to Eq. (2.7), high fractional statistic is expected close to the endpoint of the spectrum. However, the very low decay rate with a half-life of 43.2×10^9 years implies massive and thick source material, which requires a measurement in, e.g., a calorimetric way. In such a technique, the β-source is embedded in the detector and the temperature rise at thermal equilibrium is measured by a suitable thermometer. To this end, the totally released decay energy reduced by the neutrino energy is measured in the source. Hence, systematic effects at KATRIN by, e.g., energy loss during the transition from source to spectrometer as well as final state effects or molecular binding energies are negligible in this technique.
Up to now, two experiments have measured the ^{187}Re β-spectrum with thermal detectors, which are Mi-BETA [68] and MANU [69]. Both experiments used statistics of about 10^7 β-decays in a metallic Re single crystal (MANU) or an array of $AgReO_4$ crystals (Mi-BETA). The limits on $m(\overline{\nu})$ resulted to about 26 eV (95 % C.L.) and 15 eV (90 % C.L.) for MANU and Mi-BETA, respectively, both limited by statistics. In order to be competitive with current tritium experiments, a new ^{187}Re experiment called MARE (Microcalorimeter Array for a Rhenium Experiment) [70, 71] is planned, based on the experience from MANU and Mi-BETA. With detectors improved in resolution and rise time, MARE plans to collect statistics of up to 10^{14} β-decays from a large array of metallic superconducting Re absorbers in a second stage. The corresponding sensitivity to the electron anti-neutrino mass is then given by $m(\overline{\nu}_e) \leq 0.2$ eV, being competitive with KATRIN.
In analogy to tritium, a precise mass-ratio measurement of ^{187}Re/ ^{187}Os and, hence, the total decay energy Q by Penning-trap mass spectrometry can contribute to fix the endpoint of the spectrum and for identification of systematics in the MARE spectrum. To this means, the Q-value has to be determined with an uncertainty below 1 eV, which corresponds to a relative uncertainty of the mass ratio measurement of $\Delta R/R \sim 6 \times 10^{-12}$ (see Sec. 7.2). With the novel Penning-trap mass spectrometer Pentatrap (see Part I), this accuracy seems to be reachable, which is, therefore, one of the first physics goals for this trap.

Electron Capture in ^{163}Ho

Complementary to β-decay is the electron-capture (EC) process, where a nucleus absorbs an electron from an inner shell of the atom and a proton decays into a neutron with the emission of an electron neutrino ν_e. Subsequently, the daughter atom relaxes

[3] The lowest Q-value is known for the transition to an excited state in the reaction $^{115}\mathrm{In} \rightarrow {}^{115}\mathrm{Sn}^* + e^- + \overline{\nu}_e$, with $Q = 155(24)$ eV [65, 66].

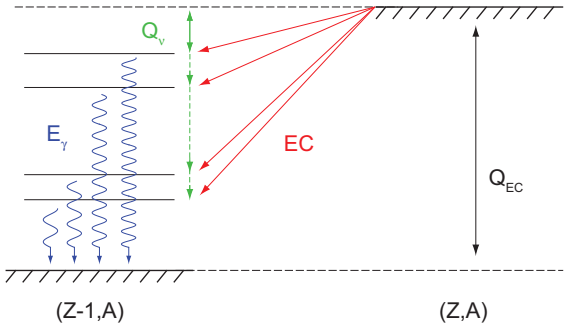

Figure 2.2: Simplified level scheme of the electron-capture process. The total decay energy Q_{EC} is the difference between the mother and daughter ground states. The energy taken away by the neutrino is given by $Q_\nu = E_\nu + m(\nu_e) \cdot c^2 = Q_{\mathrm{EC}} - B_e$, where E_ν is the kinetic energy of the neutrino and $m(\nu)$ its rest mass. $B_e = E_\gamma$ is the binding energy of the captured electron.

into its energetic ground state by photon emission. The process can be written as

$$Z + e^- \rightarrow (Z-1) + \nu_e + \gamma, \tag{2.13}$$

which is sometimes called "*inverse β-decay*". EC was first detected in ^{49}V in 1937 [72] and is the predominant decay mode for proton-rich nuclides, if β^+-decay is energetically forbidden[4].
The EC process (in analogy to β-decay), may allow for a complementary determination of the electron-neutrino mass $m(\nu_e)$, while the CPT-theorem ensures the equivalence of neutrino and anti-neutrino mass $m(\overline{\nu}_e) = m(\nu_e)$. In Fig. 2.2, a simplified level scheme of the EC process is shown. The total decay energy Q_{EC} is given by the difference of the ground states of the corresponding isobars. The energy Q_ν taken away by the neutrino is the total decay energy reduced by the binding energy B_e ($\widehat{=}$ E_γ) of the captured electron

$$Q_\nu = E_\nu + m(\nu_e) \cdot c^2 = Q_{\mathrm{EC}} - B_e, \tag{2.14}$$

where E_ν is the kinetic energy of the neutrino. In Eq. (2.14), the recoil energy has been neglected since it is typically small for heavy atoms. The best candidates for the search for the neutrino mass are nuclides with Q_{EC} close to an atomic level. In this case, the neutrinos are emitted at low energy with a high relative contribution of the rest mass. The currently most promising nuclide for neutrino mass determination via EC is ^{163}Ho, with the EC decay

$$^{163}\mathrm{Ho} \rightarrow {}^{163}\mathrm{Dy} + \nu_e + \gamma, \tag{2.15}$$

[4]For β^+-decay with positron emission, a transition energy of at least $Q = 2m_e c^2 = 1022$ keV is needed for the creation of the positron.

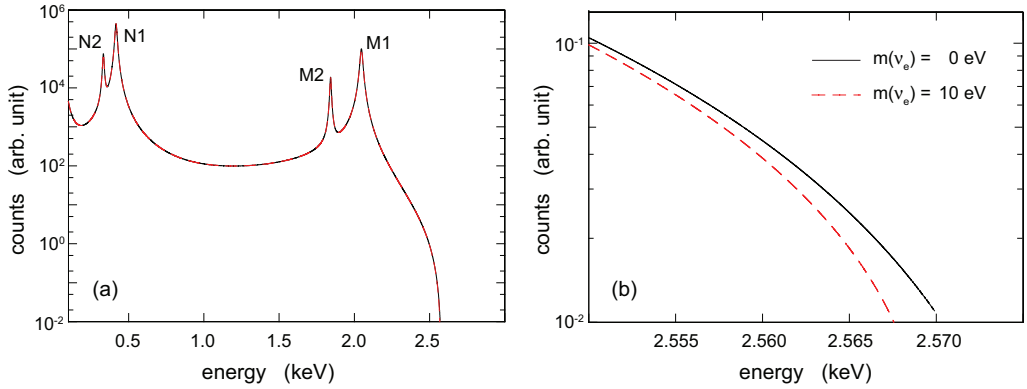

Figure 2.3: (a) Total electron-capture absorption spectrum of ^{163}Ho. The position and width of the peaks correspond to the atomic levels from which the electron is captured. (b) Zoom close to the endpoint $E_0 = Q_{\mathrm{EC}} - m(\nu_e)$ of the absorption spectrum. Courtesy of L. Gastaldo.

which is in focus of experimental investigation since the eighties. With the very low $Q_{\mathrm{EC}} = 2.56(2)$ keV at a half life of about 4570 years [67], it offers a pure EC decay, where the capture is only allowed from the M shell or higher.

There are several methods proposed for neutrino mass determination via EC (see, e.g. [73, 74]), where the investigation of the endpoint of inner Bremsstrahlung during the EC process has led to a limit of $m(\nu_e) < 225$ eV (95 % C.L.) [75]. More promising is the calorimetric measurement at the endpoint E_0 of the total absorption spectrum, which was already proposed in 1982 by De Rújula and Lusignoli [76]. A simulation of the total absorption spectrum is shown in Fig. 2.3a. The position and width of the peaks correspond to the atomic levels from which the electron is captured, while the relative intensities are due to the capture probability. Again, the endpoint of the spectrum in Fig. 2.3b is given by $E_0 = Q_{\mathrm{EC}} - m(\nu_e)$, where the emitted neutrino is at rest. To be competitive with the tritium β-decay in future neutrino mass determination, both the measurement of E_0 by, e.g., MARE, and the determination of the total decay energy Q_{EC} has to be done below an uncertainty of 1 eV. Again, Penning-trap mass spectrometry is the ideal tool for the determination of Q_{EC}, by a measurement of the mass difference of the two ground-state atoms

$$Q_{\mathrm{EC}} = \left[M\left(^{163}\mathrm{Ho}\right) - M\left(^{163}\mathrm{Dy}\right)\right] \cdot c^2. \tag{2.16}$$

Here, the uncertainty aimed for corresponds to about 7×10^{-12} in the relative uncertainty of the mass ratio.
Micro-calorimeters have currently reached a resolution of 1 eV [77]. Nevertheless, precise measurements of spectra with this technique are technically still very challenging due to, e.g., background from contamination. Furthermore, the spectra are strongly varying on details of atomic parameters (e.g. natural widths and capture probabili-

ties). In particular, the proximity of Q_{EC} to atomic levels changes the steepness close to the endpoint and therefore the sensitivity to $m(\nu_e)$ [71]. To decide on the real feasibility of calorimetric spectra, it is mandatory to precisely measure atomic parameters and especially Q_{EC}, where current determinations span from 2.2 to 2.8 eV in case of ^{163}Ho [78]. In that sense, precise Q_{EC} determinations are previously needed to decide on experimental strategies in calorimetric measurements.
Furthermore, as pointed out in [79] there are about half a dozen more relevant nuclides (e.g.^{157}Tb, ^{193}Pt), where the emission of low-energy neutrinos by EC is within the scope of present data. But, the data are currently not accurate enough to decide on their real usefulness with respect to calorimetric neutrino mass determination. Penning-trap facilities like PENTATRAP are capable of improving data of the total decay energy in EC and can help in the search for the best candidates. As an example (though with negative answer), K-capture in ^{194}Hg with expected very low neutrino energy was excluded by a new measurement of Q_{EC} presented in [79].

2.1.3 Double-β Transitions: General Issues and $0\nu\beta\beta$

Besides the ordinary β-transitions discussed in the previous section, double-β transitions are in the focus of modern neutrino physics, both on the experimental and the theoretical side. After indicating the reason for the high interest into double-β transitions in general, the most prominent example of double-β transitions, the double-β decay, is discussed below, where Penning-trap mass spectrometry can strongly contribute to the detection of this process.

Basic Interest

All double-β transitions can appear with the emission of two neutrinos, or neutrinoless. In the neutrinoless modes, such second-order weak interaction processes offer the possibility for the determination of the absolute scale of the neutrino mass from their transition rates (see Eq. (2.19) for the double-β decay). If the sensitivity of ordinary β-decay experiments is not sufficiently high for small neutrino masses, those processes might be the only way for the direct determination of the neutrino mass.
Furthermore, another basic question about the nature of the neutrino is the Dirac or Majorana character. For Dirac-type neutrinos, the neutrino and anti-neutrino are fundamentally different. However, since the neutrino is neutral, it is also possible that the neutrino is its own anti-particle, which is then called Majorana-type neutrino. Details of the theoretical description and the consequences can be found in, e.g. [37, 38, 80]. The neutrinoless double-β transitions are only possible for massive Majorana neutrinos. Hence, a detection of those processes would unambiguously establish the massive Majorana nature (see, e.g. [81]), which is not included in the Standard Model of the electroweak interaction (SM). Additionally, the basic concept of Lepton number conservation in the SM is not fulfilled within those processes and, consequently, would have to be given up. An answer to this question is of fundamental interest.
However, the proof for massive neutrinos already showed that the SM is incomplete and

pointed to superior theories. Hence, physics beyond the SM is currently investigated on many fronts and further constriction of fundamental neutrino properties as, e.g., the Majorana character can help to find the proper extension to the SM.

Neutrinoless Double-Beta Decay ($0\nu\beta\beta$)

Already one year after Fermi's theory of the β-decay in 1934 [39], Goeppert-Mayer investigated atoms decaying by double-β emission in the process [82]

$$(A, Z) \rightarrow (A, Z+2) + 2e^- + 2\overline{\nu}, \tag{2.17}$$

which is a second order weak decay with very long lifetimes in the order of 10^{20} years and above. It is the dominant decay channel, if ordinary β-decay is energetically forbidden [83][5]. In nature, 35 nuclides are known with ground state configuration sufficient for double-β decay and the process has already been detected in 10 of them (^{48}Ca, ^{76}Ge, ^{82}Se, ^{96}Zr, ^{100}Mo, ^{116}Cd, ^{128}Te, ^{130}Te, ^{150}Nd, ^{238}U) [84].
However, already in 1939 Furry realized the alternative possibility that the two decaying neutrons can rather exchange than emit the two neutrinos in the process [85]

$$(A, Z) \rightarrow (A, Z+2) + 2e^-, \tag{2.18}$$

which is termed the neutrinoless double-β decay ($0\nu\beta\beta$). The virtual exchange of the neutrinos can only happen if neutrinos are their own anti-particle. In addition, for reasons of helicity matching of the two virtual neutrinos it is only possible if the neutrino has right- and left-handed components, which is the case for massive neutrinos. Over the years, tremendous theoretical and experimental effort has been invested in the search for this process. For numerous reviews see, e.g. [83, 86, 87]. The transition rate of the neutrinoless mode is given by [87]

$$\Gamma^{0\nu\beta\beta} = \frac{1}{T^{0\nu\beta\beta}_{1/2}} = \left|m_{\beta\beta}\right|^2 \left|M^{0\nu\beta\beta}\right|^2 G^{0\nu\beta\beta}(Q_{\beta\beta}, Z), \tag{2.19}$$

where $G^{0\nu\beta\beta}(Q_{\beta\beta}, Z)$ is the three-body phace-space factor, $M^{0\nu\beta\beta}$ the nuclear matrix element and $m_{\beta\beta}$ the effective neutrino mass. This neutrino flavor mass is given as a coherent sum of the mass eigenstates $m_{\beta\beta} = \sum_j U_{e,j} m_j$, see Eq. (2.3).
In general, the scaling of the well known phase-space factor with $Q^5_{\beta\beta}$ guides the attention to 11 nuclides with $Q_{\beta\beta} > 2$ MeV [83]. The experimental signal for $0\nu\beta\beta$-decay are the two emitted electrons, whose energy add up to a peak at the total decay energy $Q_{\beta\beta}$, while for the two-neutrino process the electron energies are continuously distributed in the spectrum (similar to the ordinary β-decay).
Up to now, in several experiments it was not possible to detect the $0\nu\beta\beta$ peak and only

[5] A necessary requirement for double-β decay to occur is $m(Z, A) > m(Z+2, A)$. Since it competes with the ordinary β-decay along isobaric chains, the latter has to be forbidden by $m(Z, A) < m(Z+1, A)$. This situation is only given for nuclides with even number of protons and neutrons and, thus, even A. For details see, e.g. [83].

limits on the transition rates and the neutrino mass can be given [86]. There is one exception, where a subgroup of the Heidelberg-Moscow experiment on ^{76}Ge claimed the detection of the $0\nu\beta\beta$-decay with a half-life of $T^{0\nu}_{1/2} \approx 2.23 \times 10^{25}$ years [88, 89]. This would imply a Majorana neutrino mass of $|m_{\beta\beta}| \simeq 0.18 - 0.30$ eV with use of the nuclear matrix elements given in [90]. However, this claim is heavily disputed and several upcoming experiments will put it under test by improving the sensitivity limits by more than one order of magnitude. The most promising collaborations are currently GERDA [91] and MAJORANA [92], the former with strong contributions from the Max-Planck-Institut für Kernphysik, Heidelberg.

Penning-trap mass spectrometry can provide precise $Q_{\beta\beta}$-values by determination of the ground state mass differences. In the search of $0\nu\beta\beta$-decay the implications are manifold. First of all, for the mere detection a precise knowledge of the total decay energy $Q_{\beta\beta}$ for identification of the peak in presence of background is needed. Furthermore, precise knowledge of $Q_{\beta\beta}$ enters in the calculation of the phase-space factor $G^{0\nu\beta\beta}(Q_{\beta\beta}, Z)$, and in the nuclear matrix elements[6] $M^{0\nu\beta\beta}$, which is, thus, important for the calculation of life-times or, ultimately, the extraction of the neutrino mass. Hence, new precise measurements on $Q_{\beta\beta}$-values were performed recently by several Penning-trap facilities, see e.g. [94–98].

2.1.4 Neutrinoless Double-Electron Capture

Besides the double-β decay, there is another second-order weak-interaction process, where recently increased interest was inspired both on the theoretical and the experimental side. This process is the main subject for the mass-ratio measurements at SHIPTRAP presented in Part II within this thesis. The main properties are given below.

Double-Electron Capture

The second-order weak-interaction process of double-electron capture ($\epsilon\epsilon$) can be described by the transition formula

$$\begin{aligned} 2e^- + (A, Z) \rightarrow (A, Z-2)^{**} \quad (+2\nu_e) \\ \rightsquigarrow (A, Z-2) + 2X \quad (+\gamma). \end{aligned} \tag{2.20}$$

In this process, two bound electrons from the atomic shell are captured by two protons in the nucleus, which decay into two neutrons. Hence, the nuclear charge is lowered by two units. A simplified level scheme is shown in Fig. 2.4. The daughter atom is left in an excited state $(A, Z-2)^{**}$ due to the holes in the atomic shell with binding energy $B_{2\mathrm{h}}$ and, probably, nuclear excitations E_γ. It de-excites by emission of X-rays from the atomic shell relaxation and a γ-ray in case of a nuclear excitation.
The decay can, again, happen with emission of two electron neutrinos ($2\nu\epsilon\epsilon$) or neutri-

[6] The calculation of nuclear matrix elements to high precision is still very challenging due to higher-order weak contributions. A preferred method is the QRPA approach, see, e.g. [90, 93].

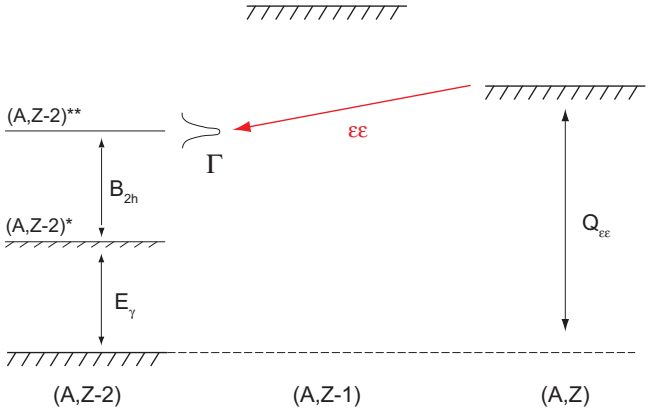

Figure 2.4: Level scheme of the double-electron capture process.

noless ($0\nu\epsilon\epsilon$). The latter one is only possible for massive Majorana neutrinos and the total lepton number is violated, which is common to all neutrinoless double-β transitions.
The double-electron capture was considered by Winter in 1955 [34], both with and without emission of neutrinos. In the two neutrino case $2\nu\epsilon\epsilon$, the decay-energy excess (also called degeneracy parameter), defined by

$$\Delta = Q_{\epsilon\epsilon} - (B_{2\mathrm{h}} + E_{\gamma})\,, \tag{2.21}$$

can be taken away by the neutrinos, while in the neutrinoless case Δ must be balanced by an extra photon with $E_{h\nu} = \Delta$. Unfortunately, the coupling to this additional photon leads to half-lives significantly longer than for, e.g., the neutrinoless double-β decay. This is the reason why this process has not been considered for experimental research for a long time.

Resonant Enhancement of $0\nu\epsilon\epsilon$

It was already pointed out by Winter that for decay energies Δ close to zero, a resonance condition might exist. The same idea was proposed in [99] for transitions to the ground state of the daughter. In 1983, Bernabéu, De Rújula and Jarlskog again investigated the resonance condition [35]. They identified a best candidate ^{112}Sn, where their estimation of the life-time for a $m(\nu_e) = 30$ eV neutrino mass led to 10^{22} to 10^{27} years, limited by the insufficiently well determined distance to resonance at that time[7]. In 2004, neutrinoless double-electron capture was discussed in more detail with a perturbative approach [100], with the conclusion that a energy degeneracy could make $0\nu\epsilon\epsilon$ competitive to the neutrinoless double-β decay.
In the following, a recent approach in [101] will be reviewed, in which the resonant enhancement of $0\nu\epsilon\epsilon$ is treated in the context of oscillations between two atoms with

[7] Recently, the resonance case for this nuclide was excluded by a mass measurement at Jyväskylä [97].

different total lepton number[8]. The mass degeneracy is realized by excitation of one of the atoms. Lepton number violating transitions $(A, Z) \to (A, Z \pm 2)^{**}$ can be described phenomenologically by the Hamiltonian

$$H_{\text{eff}} = M_+ + V_{\epsilon\epsilon}\sigma_1 + M_-\sigma_3, \qquad \text{with} \qquad M_\pm = \frac{M_\text{i}c^2 \pm M_\text{f}c^2}{2} \mp \frac{\text{i}}{4}\Gamma, \tag{2.22}$$

which is the same for neutron-antineutron oscillations in matter and similar to the Hamiltonian responsible for oscillations of neutral kaons. Here, σ_i are Pauli matrices, M_i is the mass of the initial atom, while M_f and Γ are the mass and total decay-width of the excited final atom, respectively. Responsible for the lepton-number violating transition is the potential $V_{\epsilon\epsilon}$. For stable atoms, the transition probability $\left|\langle \text{f}\,|\, e^{-\text{i}H_{\text{eff}}t}\,|\,\text{i}\rangle\right|^2$ is excessively low even for hypothetical near-degenerate ground-state masses. On the other hand, for transitions from ground state atoms to excited atomic states, the decay rate of the initial atom in lowest order approximation[9] can be written as

$$\lambda_{\epsilon\epsilon} = |V_{\epsilon\epsilon}|^2 \frac{\Gamma}{\Delta^2 + (\Gamma/2)^2} = |V_{\epsilon\epsilon}|^2 \cdot r_{\epsilon\epsilon}, \tag{2.23}$$

where $r_{\epsilon\epsilon}$ is called resonance-enhancement factor. In this context, the full resonant enhancement of the decay rate is given for a complete degeneracy of the masses of initial and exited final state ($\Delta = 0$), leading to $\lambda_{\epsilon\epsilon} = 4 \cdot |V_{\epsilon\epsilon}|^2/\Gamma$.

Lepton-Number Violating Potential $V_{\epsilon\epsilon}$

Most favorable for the $\epsilon\epsilon$-decay process are transitions of even-even nuclei (see arguments in [83]). Hence, the initial nucleus has angular momentum and parity $J_\text{i}^\pi = 0^+$ and, consequently, the angular momentum of the final nucleus must be balanced by the capture of the electrons and the angular momentum the atomic state. In that case, the lepton number violating potential in Eq. (2.23) can be written as [101]

$$V_{\epsilon\epsilon} = \frac{1}{4\pi} G_\beta^2 m_{\beta\beta} \frac{g_\text{A}^2}{R_\text{nucl}} \sqrt{2J_\text{f} + 1} \cdot \mathcal{M}_{\alpha\beta}(J_\text{f}^\pi). \tag{2.24}$$

Here, $G_\beta = G_\text{F} \cos(\Theta_\text{c})$ is the Fermi constant G_F times the cosine of the Cabibbo angle Θ_c, g_A is the axial-vector coupling constant, R_nucl is the nuclear radius and $m_{\beta\beta}$ the effective Majorana neutrino mass discussed above. $\mathcal{M}_{\alpha\beta}(J_\text{f}^\pi)$ is the total matrix element of the transition for the capture of two electrons with J^π. For further analysis it can be factorized into the contribution from the atomic shell structure and the nuclear transition. The total matrix element can then be written as

$$\mathcal{M}_{\alpha\beta}(J_\text{f}^\pi) \approx \mathcal{A}_{\alpha\beta} M^{0\nu}(J_\text{f}^\pi), \tag{2.25}$$

[8] For the degeneracy case, this approach is consistent with the earlier approaches in [35, 100].
[9] The arguments for the approximation can be found in [102].

where $M^{0\nu}$ is the nuclear matrix element. $\mathcal{A}_{\alpha\beta}$ is the so-called electron factor, which is a combination of the upper and lower bi-spinor components of the electron wave functions, averaged over the nuclear volume. Here, α and β denote the principal quantum numbers of the captured electrons.
The calculation of nuclear matrix elements $M^{0\nu}$ is still very challenging due to the complicated structure of the nuclear state. A broad analysis throughout the periodic table has not been performed yet. The most compromising theoretical approach is the Quasiparticle Random Phase Approximation (QRPA), as done for the $0\nu\beta\beta$ matrix elements (see, e.g. [90]). Nevertheless, the general treatment of the electron wave functions entering $\mathcal{A}_{\alpha\beta}$, and of the nuclear matrix elements $M^{0\nu}(J^{\pi}_{\mathrm{f}})$ in [103] gives important hints for the search of neutrinoless double-electron capture candidates.
In the relativistic description, parity-violating transitions become possible, enabling the capture of a $s_{1/2}$ and a $p_{1/2}$ electron associated with a $0^+ \rightarrow 0^+$ transition of the nucleus. On the atomic shell side, the capture of electrons from the K shell is most likely due to the large overlap of the wave function with the nucleus. On the other hand, due to the similar asymptotes of $s_{1/2}$ and $p_{1/2}$ wave functions at small distances, the capture of two L electrons is comparable to the capture probability of one K and one L electron. The capture from higher shells is suppressed due to the little overlap with the nucleus (reducing $\mathcal{A}_{\alpha\beta}$), but this can be partly balanced due to the higher decay rates entering $r_{\epsilon\epsilon}$.
From the nuclear point of view, the nuclear matrix elements are lowered for transitions to excited nuclear states due to the dissimilarity of the involved nuclear wave functions (see, e.g. [104]), which clearly favors transitions from nuclear ground state to ground state. Furthermore, it is shown that the nuclear matrix elements are strongly suppressed in case of the change of the nuclear spin with $\Delta J \geq 2$.

Binding Energy of the Hole States and Total Decay Width

As discussed above, electrons are most likely captured by the inner shells, where their binding energy varies from 10 eV in light nuclei to 10^5 eV in heavy atoms. Those binding energies are known to accuracies of $\sim 1 - 10$ eV for light and heavy atoms, respectively (see, e.g. [105]). In the $0\nu\epsilon\epsilon$-process, however, the binding energy of the two hole states $B_{2\mathrm{h}}$ are of interest, where noticeable corrections arise from the Coulomb interaction. This interaction can reach a few keV [101], which is not negligible in accurate calculations.
In, e.g. [106, 107], the energy of single electron holes E_a and E_{b} are taken from [105] and the Coulomb interaction E_{C} of the two holes is calculated with the Dirac-Fock method, including electron-correlation and QED corrections and nuclear charge effects within the Fermi model. Furthermore, an approximation is used where the energy is averaged over all involved atomic terms of the valence configuration. The final uncertainty is on the order of 10 eV, limited by QED screening effects of the nuclear charge.

The total decay width Γ of the excited final atoms is sum of the width of the atomic and nuclear state. The nuclear width is in most cases smaller than the atomic width

by at least one order of magnitude and can safely be neglected. The decay width of the atomic shell is determined by dipole-transition rates. For K-shell holes, X-ray emission is dominant for $Z > 35$ with $\Gamma = 4 \times 10^{-7} Z^4$ eV, whereas the width decreases with $\Gamma \sim 1/n^5$ for transitions from higher orbits. For lower Z, the alternative de-excitation process of Auger-electron emission becomes more important. Both mechanisms are well understood theoretically.
For the $0\nu\epsilon\epsilon$-process, the radiative width of the atomic shell with two holes can be estimated as the sum of the radiative widths of two single vacancies $\Gamma_{ab} = \Gamma_a + \Gamma_b$, where numerical values can be taken from [108].

Experimental Signature

As discussed in Sec. 2.1.3, all double-β experiments have to deal with excessively long interaction times, especially in the neutrinoless modes. Currently, the experimental effort is predominantly focussed on the $0\nu\beta\beta$-decay and several experiments are already running or in the commissioning phase. Those experiments are characterized by the need for an enormous effort in background reduction and, typically, tens or hundreds of kilograms of active material have to be used (e.g. $\sim$ 50 kg of enriched Ge oxide in phase II of the GERDA experiment [91]).
As discussed above, due to the possibility of resonant enhancement, the $0\nu\epsilon\epsilon$-process can reach life-times competitive to $0\nu\beta\beta$-decay. This is, however, only expected if full mass degeneracy is provided. On the other hand, in the resonance case several advantageous occur compared to $0\nu\beta\beta$. First, the experimental signature is given by the narrow de-excitation of the atomic-shell holes, typically in the X-ray regime or by Auger electron emission as discussed in Sec. 2.1.4. In case of nuclear excitations, there will be a coincidence with the γ-rays de-exciting the nuclear state. Coincidence setups could therefore eliminate random external background (e.g. by cosmic radiation) from the beginning. Additionally, nuclear de-excitation typically proceeds through unique and easy to detect cascades. Furthermore, in the $0\nu\beta\beta$-decay the continuous electron spectrum of the competing two-neutrino mode extends to the mono-energetic peak of the neutrinoless mode at the endpoint, serving as internal background. In case of double-electron capture, the two-neutrino mode is strongly suppressed due to the phase-space dependence of Q^5 [109]. For a Q-value in the MeV region, a $2\nu\epsilon\epsilon$ half-life is expected to be on the order of 10^{22} y [101]. Resonance might occur due to the capture from inner shells at Q-values in the range of some tens of keV. Consequently, the two-neutrino mode is already suppressed by another ten orders of magnitude, being negligible in terms of background for the neutrinoless mode.
If suitable nuclides for the $0\nu\epsilon\epsilon$-process are found, experimental detection might be realized in calorimetric setups, as discussed for the ordinary electron-capture process in Sec. 2.1.2. Another approach is currently running with crystal scintillators, looking for the characteristic X-rays of the hole-relaxation in the daughter of the transition $^{106}\mathrm{Cd} \rightarrow {}^{106}\mathrm{Pd}$ [110]. A quite impressive level of sensitivity has been already reached with the limit $T_{1/2}(0\nu\epsilon\epsilon) > 3.6 \times 10^{20}$ y. This is, however, still very far away from expected life-times of this nuclide in the order of 10^{30} y [101].

2.2 Further Examples

Besides the need for mass-ratio measurements related to neutrino physics presented in the previous section, the list of motivations for highly-accurate measurements at PENTATRAP can be further extended. Some prominent examples are given below, ranging from contributions to the determination of fundamental constants up to stringent test of quantum electrodynamics (QED) predictions and fundamental symmetries.

2.2.1 g-Factor of the Electron

Free Electron and the Fine Structure Constant

The g-factor of the electron relates its magnetic moment $\vec{\mu}$ with the spin $\vec{s}$. Usually, this relation is expressed in units of the Bohr magneton μ_B and is given by

$$\vec{\mu} = g\frac{\mu_\mathrm{B}}{\hbar} \cdot \vec{s}. \tag{2.26}$$

In a magnetic field B, the magnetic moment processes with the Larmor frequency $\omega_\mathrm{L} = g(e/2m_e)B$. The simultaneous measurement of ω_L and the electron's cyclotron frequency $\omega_\mathrm{c} = (e/m_e)B$ in a Penning trap has led to the presently most precise value of $g = 2.00231930436146(56)$ for the free electron by Hanneke *et al.* [111]. The Standard Model of elementary particles relates g with the fine structure constant α by the power series [112]

$$\begin{aligned}\frac{g}{2} = 1 &+ C_2\left(\frac{\alpha}{\pi}\right) + C_4\left(\frac{\alpha}{\pi}\right)^2 + C_6\left(\frac{\alpha}{\pi}\right)^3 + C_8\left(\frac{\alpha}{\pi}\right)^4 + \dots \\ &+ a_{\mu\tau} + a_\mathrm{hadronic} + a_\mathrm{weak},\end{aligned} \tag{2.27}$$

with contributions from the muon, tau, hadrons and the weak interaction. The fine structure constant α gives the strength of the electromagnetic interaction and is integrated deeply in the system of fundamental constants [113]. The measurement of g, together with the quantum electrodynamic (QED) calculations in [112] can be used for the currently most precise determination of the fine structure constant $\alpha^{-1} = 137.035999084(51)$ [111].
From the opposite point of view, an independent determination of α together with the measured g-factor opens the way to put the QED calculations under test. The currently most accurate independent determination of α is reported from photon recoil measurements, with $\alpha^{-1} = 137.035999037(91)$ [114]. Consequently, the calculations in [112] can be compared to the experimental values, with perfect agreement on the level of 10^{-9}. This marks the presently most stringent test of QED, where the contributions of the muon and hadrons are visible for the first time.
The relation of mass measurements to the recoil measurements of atoms is discussed in [115]. In such atom-interferometric experiments, the ratio h/m_atom of the atomic mass m_atom is measured. It is extracted from the recoil velocity $v_r = \hbar k/m_\mathrm{atom}$ due

to absorption of a photon with momentum $\hbar k$. The fine structure constant is obtained from

$$\alpha^2 = \frac{2R_\infty}{c} \cdot \frac{h}{m_e} = \frac{2R_\infty}{c} \cdot \frac{m_{\mathrm{atom}}}{m_e} \frac{h}{m_{\mathrm{atom}}}, \tag{2.28}$$

where the Rydberg constant R_∞ is known to the level of 7×10^{-12} [116]. Obviously, for the determination of α, independent values of m_{atom} and the electron mass m_e are needed. The electron mass[10] is known to 4.2×10^{-10} [113]. In recoil measurements, alkali atoms are favored due to the possibility of cooling them with visible or near-infrared lasers. For the measurement on ^{87}Rb in [114], the mass value is taken from Mount *et al.* [118], who has determined the atomic masses of the alkalis ^{6}Li, ^{23}Na, ^{39,41}K, ^{85,87}Rb and ^{133}Cs on the level of $\sim 1 \times 10^{-10}$ or even below.
Besides ^{87}Rb, several classical recoil experiments are currently running (e.g. with ^{133}Cs in [119]). Furthermore, attempts on recoil measurements with non-alkalis are considered in Bose-Einstein-Condensates for Yb isotopes in [120]. With an increase in precision in the recoil measurements, the atomic masses will have to be determined to an even lower level of uncertainty, which provides a further motivation for measurements at Pentatrap.

g-Factor of the Bound Electron

For the electron bound to a nucleus in hydrogenlike ions, corrections of g arise from very strong binding fields, bound-state quantum electrodynamics (BS-QED) contributions, and nuclear structure effects [121]. Again, the g-factor can be measured in a Penning trap by the simultaneous determination of ω_{L} of the electron's magnetic moment and the cyclotron frequency of the ion $\omega_{\mathrm{c}} = (q_{\mathrm{ion}}/m_{\mathrm{ion}})B$, resulting in

$$g = 2\frac{\omega_{\mathrm{L}}}{\omega_c} \frac{m_e}{m_{\mathrm{ion}}} \frac{q_{\mathrm{ion}}}{e}. \tag{2.29}$$

Measurements were performed on $^{12}C^{5+}$ [122] and $^{18}O^{7+}$ [123]. Recently, tremendous progress in the determination of $\omega_{\mathrm{L}}/\omega_{\mathrm{c}}$ has been achieved by S. Sturm *et al.* in case of $^{28}Si^{13+}$, where the ratio was determined with a relative accuracy of 2.6×10^{-10} [30, 124]. The mass of the Si ion was extracted from the mass of the Si atom, which was determined with a relative uncertainty of 2.1×10^{-11} in [125]. The final determination of the g-factor marks the most stringent test of BS-QED, which is limited by the uncertainty of the electron mass taken from [126]. For the first time, the experiment has become sensitive to two-loop corrections of the order $(Z\alpha)^2$ and $(Z\alpha)^4$ in the theoretical calculations. In a second measurement series, the relative uncertainty of $\omega_{\mathrm{L}}/\omega_{\mathrm{c}}$ was even improved to an impressive level of 4×10^{-11} [127].
Future progress can be achieved with heavier systems due to the approximate scaling of BS-QED contributions with Z^2 [121]. In view of the recent and ongoing progress in the determination of $\omega_{\mathrm{L}}/\omega_{\mathrm{c}}$, highly precise mass values of the ions on the level of 10^{-11} or

[10] Actually, the electron mass itself is extracted from precise g-factor measurement, see [117].

below are needed for future candidates in order not to limit the g-factor determination. Of special interest are nuclides with double-magic proton and neutron numbers, where calculations of nuclear structure effects are most reliable in order to extract the BS-QED effects. Consequently, in the Mainz g-factor trap, one of the next candidates will be hydrogenlike $^{40}Ca^{19+}$ and $^{48}Ca^{19+}$. With this double-magic isotope pair, a possible isotope effect of the g-factor can be studied, too. This effect might arise from a slightly closer distance of the electron wave function to the nucleus in the heavier isotope, resulting in a stronger Coulomb field felt by the electron (see proposal for ^{24}Mg and ^{26}Mg in [128]). In this context, the isotope $^{30}Si^{13+}$ is of interest, too, where precise mass values are currently missing.
Besides the Mainz experiments, measurements of g-factors are planned at the HITRAP facility [33] at GSI, Darmstadt. There, a new laser-microwave double-resonance technique in a Penning trap will be utilized for the determination of the g-factors. On the candidate list are nuclides with even higher Z and extremely high charge states, such as the double-magic $^{208}Pb^{81+}$, or even $^{235}Pb^{91+}$ [129–131].

2.2.2 Atomic Binding Energy

In the last decades, highly charged ions (HCI) have become an attractive system to probe relativistic and quantum electrodynamic (QED) theories of atomic structure. Effects of relativistic corrections of electron-electron correlation, higher orders of the pertubative treatment of self-energy or vacuum polarization and nuclear size effects increase with high powers of the nuclear charge Z, corresponding to an extremely high strength of the confining electromagnetic field (up to 10^{16} V/cm and 10^8 T close to the nucleus).
Theoretical approaches were refined over years and utilize, nowadays, e.g. the Dirac-Fock method (a relativistic equivalent to the Hartree-Fock method) or QED many-body theories (see, e.g. [132, 133]). Of special interest are few-electron systems, where QED effects reach magnitudes on the order of few 10^2 eV for high-Z atoms. At the same time, correlation effects are still well defined by the small number of electrons, though reaching also significant relativistic and non-relativistic contributions, already for He-like atoms. On the experimental side, measurements of transition energies and probabilities or ionization cross sections have significantly contributed to the modern understanding and refinement of theory (see, e.g. [134] for measurements of the Lamb shift in hydrogen-like uranium and tests of few-electron correlations in mercury [133, 135]).
However, due to the cancellation of specific error sources in the difference between two energy levels, transition energies are much easier to reproduce for theoretical models than the absolute scale of an energy level [136]. Furthermore, with an increasing number of electrons, correlation terms get more and more important. As an example, the Breit contribution (taking magnetic interaction and retardation effects into account) exceeds the Coulomb interaction in high-Z atoms. Hence, a Coulomb-Breit-correlation energy has to be added on the order of 1 eV/electron [137], with challenging demands on many-body theories.

Penning-trap mass spectrometry can put such calculations under test, where the absolute binding energy $B_e^{(k)}$ of the k-th electron can be measured by

$$B_e^{(k)}/c^2 = m(\mathrm{X}^{k+}) - m(\mathrm{X}^{(k-1)+}) + m_e, \tag{2.30}$$

in a series of measurements of the two charge states $k-1$ and k. As an example, in ^{208}Pb a determination of the masses of ions with consecutive charge state to a relative uncertainty of 5×10^{-12} corresponds to an energy resolution of ~ 1 eV, where the correlation terms of the Breit interaction are visible at medium charge states and uncertainties from QED and nuclear size errors can be inspected in few-electron configuration.

2.2.3 Direct Test of $E = mc^2$

In the previous section, the relation $E = mc^2$ is implicitly used to relate the mass difference measured in a Penning trap to the determination of the binding energy E_b. From the opposite point of view, a determination of the mass difference together with an independent determination of the binding energy E_b can be used for a direct test of $E = mc^2$.
In [138], Rainville *et al.* presented the currently most precise direct test based on the nuclear reaction of neutron capture

$$^{A}\mathrm{X} + n \rightarrow {}^{A+1}\mathrm{X} + \gamma, \tag{2.31}$$

in the two candidates $^{A}\mathrm{X} = {}^{32}\mathrm{S}$ and $^{A}\mathrm{X} = {}^{28}\mathrm{Si}$. From $E = mc^2$ and energy conservation, it follows that the mass difference of the initial and final state $\Delta m = m(^{A}\mathrm{X}) + m(n) - m(^{A+1}\mathrm{X})$ has to compensate the energy $E_\gamma = h\nu$ of the emitted photon:

$$\Delta m c^2 = h\nu. \tag{2.32}$$

The mass differences Δm were measured in a Penning trap and the gamma energy E_γ was measured independently by Bragg diffraction from sources near the high-flux reactor core at the Laue-Langevin Institute (ILL) in Grenoble [139]. The comparison of the right- and left-hand side in Eq. (2.32) shows a fractional difference of $-1.4(4.4) \times 10^{-7}$, combined from both measurements on S and Si and limited by the determination of E_γ.
Tests of special relativity were performed by different type of experiments down to the level of 1×10^{-23} (see, e.g. [140–142]). However, the direct way presented above offers an additional aspect. In special relativity, two distinct quantities can be considered in the context of the speed of light. First, the velocity of an electromagnetic wave in vacuum denoted by c_{em} and, second, the limiting velocity of a massive particle c_m. The fundamental assumption of special relativity is $c_m = c_{em} = c$ (see discussion in [143]). In Eq. (2.32), the left side denotes the energy content of a massive particle, whereas on the right side the energy of a electromagnetic wave is depicted. Hence, the relation

translates to $\Delta m c_m^2 = h c_{em}/\lambda$. Consequently, the experiment described in [138] can be understood as a test of $c_m = c_{em}$ giving, currently, the most stringent bounds.
For the future, a similar test might be performed on, e.g., the mass difference of ^{35}Cl and ^{36}Cl, where it was already shown in [144] that a relative uncertainty of 5×10^{-8} for the E_γ measurements is possible, if enough statistics is accumulated. Moreover, a new spectrometer called GAMS-6 is under construction at ILL, which promises further improvements on such measurements [145, 146].
The masses of both isotopes are known to a relative uncertainty of $\sim 10^{-9}$ [147]. However, at a mass difference of ~ 1 u, the relative uncertainty of the mass difference is about $\sim 10^{-7}$, being approximately two orders of magnitude worse than the relative uncertainty of the masses (see Sec. 7.2). Thus, in order to be competitive with the E_γ measurements, the absolute masses have to be measured more precisely, e.g., to a relative uncertainty of 10^{-11} for E_γ in the order of 10^{-9}.

3 Basics of Penning-Trap Physics

As already pointed out by Earnshaw in 1842 [148], three-dimensional confinement of charged particles by purely electrostatic or, respectively, static magnetic fields is impossible to achieve. Considering the Maxwell equations [149], this theorem is understood as the lack of a three-dimensional potential extremum in a divergence-free space, where, at most, only saddle points can exist.
However, by a superposition of a homogeneous magnetic field and a quadrupolar electrostatic potential, three-dimensional confinement of a charged particles is possible. The first description of such devices by Pierce dates back to 1949, who called them magnetron traps [150]. In 1989, Dehmelt was honored with the Nobel Prize[1] for the first experimental realization in 1959, the introduction of such traps to atomic precision spectroscopy [15] and, especially, for the high-precision measurement of the g-factor of the free electron [152, 153]. He also coined the name Penning trap, in recognition of F. M. Penning for the idea of the radial confinement of particles in an axial magnetic field in the context of vacuum gauges, though without electrostatic trapping fields [154]. Nowadays, Penning traps are commonly used for high-precision measurements of ground-state properties of fundamental particles or atoms, in particular for mass measurements and measurements of magnetic moments. Comprehensive reviews and physics applications are given in [5, 26, 117].

3.1 The Ideal Penning Trap

In this section, the basic field configuration of an ideal Penning trap is defined, from which the charged-particle trajectories, a superposition of three independent harmonic motions, result. Information beyond this brief introduction can be found in a comprehensive review on Penning-trap physics, given in [155].

Particle Motion and Frequencies

In a homogeneous magnetic field $\vec{B} = B_0\hat{z}$ in z-direction, a particle with charge[2] q and velocity $\vec{v}$ is constrained to a circular orbit perpendicular to the magnetic-field axis due

[1] This Nobel Prize for the development of "*the ion trap technique*" was shared with Paul. He developed an alternative trapping approach, in which the charged particle are stored by quadrupolar time-dependent electrical fields [151].

[2] The total charge q of a particle is a multiple of the elementary charge $e = 1.602176487(40) \times 10^{-19}$ C [126]. Occasionally, q is also referred to the *charge state* of the ions, which denotes the total charge in units of e.

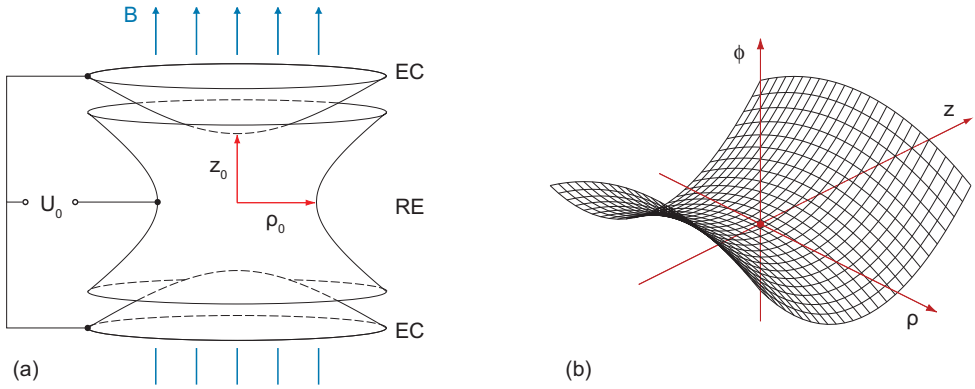

Figure 3.1: (a) Hyperbolical trap-electrode structure. The inner radius of the ring electrode (RE) is given by ρ_0 and the distance from the center of the trap to the endcaps (ECs) is z_0. The trapping voltage U_0 is applied between the endcaps and the ring electrode, while the homogeneous magnetic field $\vec{B}$ points in the axial direction. (b) Resulting quadrupolar electrostatic potential ϕ.

to the Lorentz force $\vec{F} = q(\vec{v} \times \vec{B})$. The angular frequency of this periodic motion for a particle with mass m is given by the "*free cyclotron frequency*"

$$\omega_c = \frac{q}{m} \cdot B. \tag{3.1}$$

In order to attain a harmonic confinement in z-direction ("*axial direction*"), an electrostatic quadrupolar potential of the form

$$\phi(\rho, z) = c_2 U_0 \left(z^2 - \frac{x^2 + y^2}{2} \right) = c_2 U_0 \left(z^2 - \frac{\rho^2}{2} \right) \tag{3.2}$$

is superimposed, where U_0 is the voltage difference applied to a suitable electrode structure and $[\rho, z]$ are cylindrical coordinates with $\rho = \sqrt{x^2 + y^2}$. The coefficient c_2 reflects the strength of this potential determined by the geometry of the electrode structure. Most simply, a quadrupolar field can be realized by a hyperbolical electrode structure[3], which resembles the equipotential surfaces of Eq. (3.2). In Fig. 3.1, such a configuration is shown together with the resulting potential.
In the presence of both the quadrupolar electrostatic field and the homogeneous magnetic field, the equation of motion is determined by the total Lorentz force

$$\vec{F} = q\left(\vec{E} + \vec{v} \times \vec{B}\right) = q\left(-\vec{\nabla}\phi + \vec{v} \times \vec{B}\right) = m\ddot{\vec{r}}. \tag{3.3}$$

The solutions are three independent harmonic motions, which are derived in detail in Chap. A and an illustration of the particle trajectories is shown in Fig. 3.2. The axial oscillation of the charged particle between the trap endcaps is only determined

[3] For a hyperbolical trap, c_2 is given by $1/(2d^2)$, where d is the characteristic trap length defined by $d^2 = 1/2\left(z_0^2 + \rho_0^2/2\right)$. The definitions of z_0 and ρ_0 are depicted in Fig. 3.1.

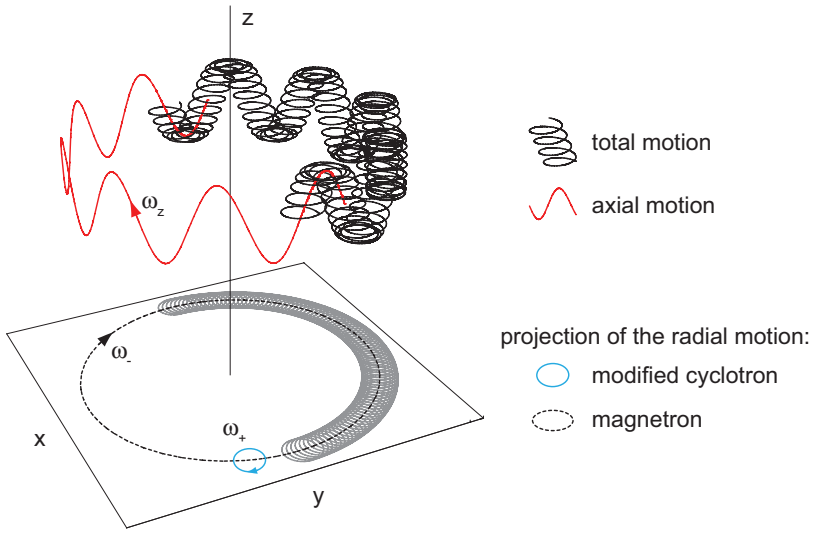

Figure 3.2: Illustration of the trajectory of a charged particle in an ideal Penning trap, consisting of three independent motions. In the axial direction, the particle oscillates between the endcaps with the axial frequency ω_z. In the radial direction two circular motions appear, the fast cyclotron motion with the frequency ω_+ and the slow magnetron drift with ω_-. The superposition of all three eigenmotions leads to a complicated total trajectory, indicated by the black line.

by the z-component of Eq. (3.2). In the radial direction, the free cyclotron frequency is modified by the repulsive character of Eq. (3.2), resulting in the so-called *modified cyclotron motion*. In addition, a third motion results from an $\vec{E}\times\vec{B}$-drift[4] in the radial plane, which is called *magnetron motion*. The eigenfrequencies of all motions are given by

$$\omega_z = \sqrt{\frac{q}{m}\cdot 2c_2U_0}, \qquad \text{the axial frequency,} \tag{3.4a}$$

$$\omega_+ = \frac{1}{2}\left(\omega_\mathrm{c} + \sqrt{\omega_\mathrm{c}^2 - 2\omega_z^2}\right), \qquad \text{the modified cyclotron frequency,} \tag{3.4b}$$

$$\omega_- = \frac{1}{2}\left(\omega_\mathrm{c} - \sqrt{\omega_\mathrm{c}^2 - 2\omega_z^2}\right), \qquad \text{the magnetron frequency.} \tag{3.4c}$$

In the PENTATRAP experiment, discussed in Part I within this thesis, the axial frequency will be fixed to the resonance frequency of a narrow-band detection system by the choice of a suitable trap voltage U_0 determined from $\omega_z(U_0) \sim 2\pi\cdot 600$ kHz (see Sec. 6.3). The resulting radial frequencies for a few different isotopes in the 7-T magnetic field are shown in Fig. 3.3 for illustration[5].
From the ideal eigenfrequencies given in Eq. (3.4), it can be seen that the periodic so-

[4] This drift is the basic principle of a Wien filter.

[5] Here and in following illustrations, the frequencies $\nu_i = \omega_i/(2\pi)$ are shown, which are the quantities in an experimental measurement. In theoretical calculations, the angular frequencies ω_i are used for simplicity.

lutions to the equations of motion require real roots, which results in the conditions

$$qc_2U_0 > 0, \tag{3.5a}$$

$$\omega_\mathrm{c} > \sqrt{2}\cdot\omega_z \quad \leftrightarrow \quad \sqrt{\frac{q}{m}} > 2\sqrt{\frac{c_2U_0}{B^2}}. \tag{3.5b}$$

These relations are the stability criteria for the trapping of a charged particle in a Penning trap. The first condition simply reflects that a negatively charged particle can only be trapped in an electrostatic potential minimum in the axial direction, or vice versa. The second condition states that in the radial direction the force due to the repulsive part of the electrostatic potential, in Eq. (3.2), must not exceed the force resulting from the magnetic field, which holds the particle on the circular orbit. Typically, Penning traps make use of strong homogeneous magnetic fields and weak electrostatic fields, from which the hierarchy $\omega_+ \gg \omega_z \gg \omega_-$ results, see Fig. 3.3.
For the ideal trap, the following useful relations between the eigenfrequencies can be derived from equations (3.1) and (3.4):

$$\omega_\mathrm{c} = \omega_+ + \omega_-, \tag{3.6}$$

$$\omega_\mathrm{c}^2 = \omega_+^2 + \omega_z^2 + \omega_-^2, \tag{3.7}$$

$$\omega_z^2 = 2\omega_+\omega_-. \tag{3.8}$$

Thus, the free cyclotron frequency ω_c can be determined by measurements of the trap eigenfrequencies, either following Eq. (3.6) or (3.7). Whereas the first relation only holds exactly for the ideal trap, the latter one is more robust with respect to some imperfections of a real trap [155] (see also Sec. 3.3.2).
Furthermore, another important characteristic for mass spectrometry is the independence of the magnetron frequency of the particle properties to first order, seen by a series expansion of Eq. (3.4c):

$$\omega_- \approx \frac{c_2U_0}{B}. \tag{3.9}$$

The magnetron frequency is a pure function of the electrostatic and magnetic field, while the other mode frequencies change, in addition, with the charge q and mass m of the particle.

Energy of the Charged Particle

The total energy of a spinless charged particle in a Penning trap is the sum of the total energies in each mode. It is given by [156, 157]

$$E_\mathrm{total} = \underbrace{\frac{m}{2}\rho_+^2\left(\omega_+^2 - \omega_+\omega_-\right)}_{=E_+} + \underbrace{\frac{m}{2}z_0^2\omega_z^2}_{=E_z} + \underbrace{\frac{m}{2}\rho_-^2\left(\omega_-^2 - \omega_+\omega_-\right)}_{=E_-}, \tag{3.10}$$

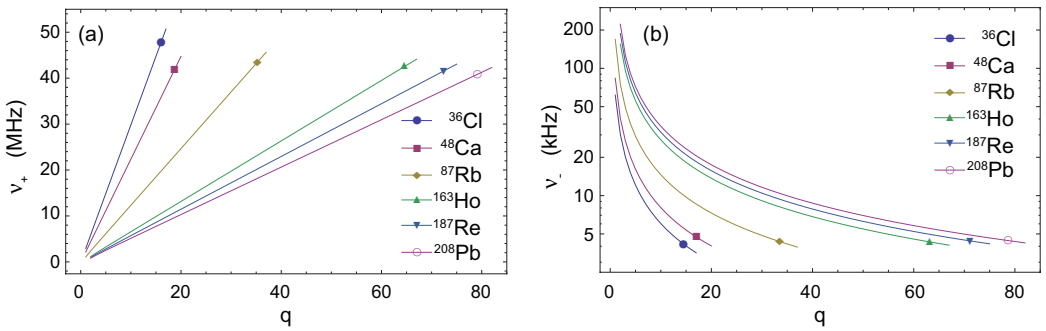

Figure 3.3: (a) Reduced cyclotron frequencies ν_+ as a function of the charge state q for possible measurement candidates of PENTATRAP. (b) Corresponding magnetron frequencies ν_-. The trap voltage U_0 is adjusted for each charge state, such that an axial frequency of $\nu_z = 600$ kHz results.

where ρ_+, z_0 and ρ_- are the amplitudes of the eigenmodes (see Chap. A). The axial energy E_z results from the simple harmonic oscillator. In the radial plane, the mean kinetic energy is given by $\overline{E}_{\mathrm{kin},\pm} = m\rho_\pm^2\omega_\pm^2/2$, while the electrostatic potential $\phi_\rho = U_0 c_2 \rho_\pm^2/2$ (see Eq. (3.2)) leads to a negative contribution of the mean potential energy

$$\overline{E}_{\mathrm{pot},\pm} = -q\phi_\rho = -\frac{m}{4}\rho_\pm^2\omega_z^2 = -\frac{m}{2}\rho_\pm^2\omega_+\omega_-. \tag{3.11}$$

With the typical hierarchy $\omega_-^2 \ll \omega_+\omega_- = \omega_z^2/2 \ll \omega_+^2$, the total energy of the modified cyclotron motion is almost purely kinetic energy, while the magnetron mode is dominated by its potential energy. Furthermore, the sign of the total magnetron energy is negative and, hence, this motion is "metastable". A decrease of energy leads to larger orbits and, consequently, to a loss of the particle at too large radii (limited by the electrode surfaces).
Besides the classical description given above, also a quantum-mechanical treatment is possible [155] where the eigenmodes are described as independent harmonic oscillators with the total energy (in the spinless case)

$$E_{\mathrm{total}} = \hbar\omega_+\left(n_+ + \frac{1}{2}\right) + \hbar\omega_z\left(n_z + \frac{1}{2}\right) - \hbar\omega_-\left(n_- + \frac{1}{2}\right). \tag{3.12}$$

Here, n_i (for $i = +, z, -$) are the occupation numbers of the corresponding mode. In Fig. 3.4, a level scheme is shown, where the energy is lowered by the increase of the quantum number of the magnetron mode due to its metastability. As an example, in the 7-T magnetic field of PENTATRAP and with the axial frequency fixed to $\omega_z = 2\pi \cdot 600$ kHz, the energy gaps are given for $^{187}\mathrm{Re}^{35+}$ to $\hbar\omega_+ = 83$ neV, $\hbar\omega_z = 2$ neV and $\hbar\omega_- = 37$ peV.
Even if the eigenmodes are in thermal equilibrium with a cryogenic environment, at ~ 4 K and a corresponding energy of $E \sim 345$ μeV, the quantum numbers for heavy ions are larger than a few thousand, which justifies the classical treatment given above.

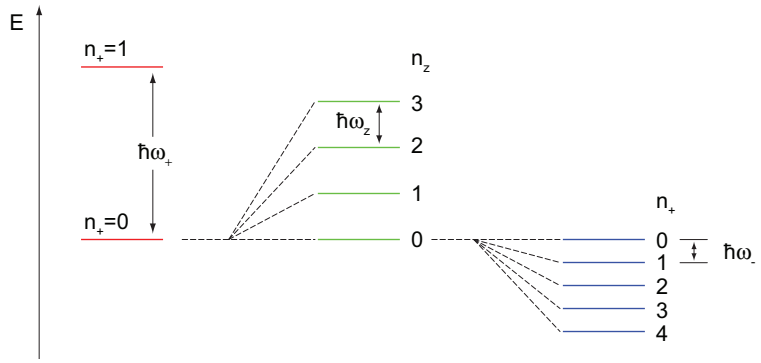

Figure 3.4: Energy levels of the three eigenmotions within an ideal Penning trap, where n_i (for $i = +, z, -$) are the quantum numbers of the individual eigenmodes. The equidistant energy gaps $\hbar\omega$ are not to scale between the different eigenmodes. The decrease of the energy by an increase of the quantum number n_- for the magnetron mode reflects the metastability of this mode.

3.2 Mass-Ratio Determination

As discussed in the previous section, the motion of a charged particle in a Penning trap depends on the particle properties, in particular of its mass m. This opens the way for precise measurements of mass ratios, where the basic principle is pointed out in the following.

Mass Ratios in Penning Traps

In principle, the mass m of an ion is linked to all eigenfrequencies of the ideal Penning trap given in Eq. (3.4), and, consequently, all of them could be used for a mass determination. Nevertheless, the superior stability of the magnetic field produced by superconducting magnets compared to state-of-the-art voltage supplies favors a mass determination via the measurement of the free cyclotron frequency

$$\omega_\mathrm{c} = \frac{q}{m} B. \tag{3.13}$$

However, the charge q and magnetic field B are not known to the precision to which the free cyclotron frequency can be determined. For the current charge uncertainty see [126]. Mass ratios

$$\frac{m_1}{m_2} = \frac{q_1}{q_2} \cdot \frac{B(t_1)}{B(t_2)} \cdot \frac{\omega_{\mathrm{c},2}(t_2)}{\omega_{\mathrm{c},1}(t_1)} \tag{3.14}$$

can be determined to much higher precision, where t_1 and t_2 are the time at which the cyclotron frequencies are measured. The ratio q_1/q_2 is a rational number due to the quantization of charge. Furthermore, if the two cyclotron frequencies are measured at

the same time $t_1 = t_2$, the magnetic-field ratio cancels and the relation reduces to

$$\frac{m_1}{m_2} = \frac{\omega_{c,2}}{\omega_{c,1}} \cdot \frac{q_1}{q_2}. \tag{3.15}$$

For many fundamental physics applications, the mass ratios are of main interest (e.g. in Q-value determinations in Part II) and no absolute mass values are needed. On the other hand, if absolute values are of interest, the use of frequency ratios can be understood as a calibration of the magnetic field by means of a reference ion with known mass. In such cases, typically ^{12}C or clusters of that nuclide are used as a reference, due to the connection to the definition of the atomic mass unit u [158]. However, only the mass ratio m_1/m_2 of two ions can be determined directly in Penning traps from the frequency ratio given in Eq. (3.15). For mass ratios of neutral atoms see the discussion in Sec. 7.2. The binding energies and the mass of the missing electrons have to be taken into account as well, and might introduce additional uncertainties.

Determination of the Free Cyclotron Frequency

For the frequency-ratio determination, the individual free cyclotron frequencies $\omega_{c,1}$ and $\omega_{c,2}$ can be traced from the trap frequencies, see equations (3.6) or (3.7). Equation (3.7) is utilized in the so-called time-of-flight detection technique [17] for the direct measurement of the sideband frequency $\omega_+ + \omega_-$ (see Sec. 8.2.2). Measurements via the time-of-flight method at SHIPTRAP are discussed in Part II.
At PENTATRAP, a much faster and more accurate image-charge detection technique will be deployed (see Chap. 6). In this method, all eigenfrequencies of the trap can be determined, and the free cyclotron frequency can be derived via Eq. (3.7). The relative precision of the free cyclotron frequency is given by

$$\frac{\delta\omega_c}{\omega_c} = \left(\frac{\omega_+}{\omega_c}\right)^2 \frac{\delta\omega_+}{\omega_+} + \left(\frac{\omega_z}{\omega_c}\right)^2 \frac{\delta\omega_z}{\omega_z} + \left(\frac{\omega_-}{\omega_c}\right)^2 \frac{\delta\omega_-}{\omega_-}. \tag{3.16}$$

Hence, if a mass-ratio is to be determined to a precision of 10^{-11}, only the modified cyclotron frequency ω_+ has to be determined to same level of uncertainty, since $(\omega_+/\omega_c)^2 \approx 1$. The relative contributions of the other two frequencies, in Eq. (3.16), are strongly suppressed by the square of the relevant frequency ratios. The suppression factors are plotted as a function of the ionization states in Fig. 3.5 for a few different isotopes. In accordance with Fig. 3.3, the factors are calculated for an axial frequency of $\omega_z = 2\pi \cdot 600$ kHz due to reasons of the narrow-band detection system at PENTATRAP.

3.3 Systematics of the Real Trap

In modern high-precision experiments, enormous technical effort is invested in order to match the conditions of an ideal Penning trap as close as possible. However, remaining or intrinsic systematics will limit the final measurement uncertainties, where

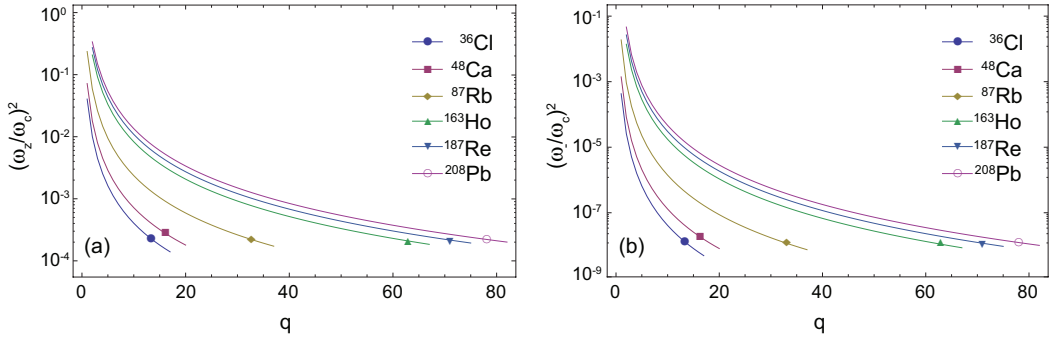

Figure 3.5: Suppression of the relative contribution to the determination of ω_c, shown for the axial frequency ω_z in (a) and the magnetron frequency ω_- in (b). The factors are calculated for an axial frequency of $\omega_z = 2\pi \cdot 600$ kHz.

in the following sections the effects of leading order are reviewed to develop a deeper understanding.

3.3.1 Magnetic-Field Fluctuations

As discussed in the previous section, the magnetic-field ratio in Eq. (3.14) only cancels if the two cyclotron frequencies are measured at the same time $t_1 = t_2 = t$. On the other hand, the measurement of two cyclotron frequencies at the same time, and, in the same trap causes systematic effects, in particular, shifts of the eigenfrequencies by ion-ion interaction. Currently, only one Penning-trap mass spectrometer is capable of measuring two ions at the same time in one trap, where enormous technical effort and systematic studies are invested [23]. The new PENTATRAP experiment will utilize an alternative method, where the two cyclotron frequencies are also measured simultaneously, but in two adjacent traps. In that case, ion-ion interactions are negligible at the relevant length scales and charge states. The temporal magnetic-field fluctuations are expected to be global over the distance of both traps, leading again to a cancellation of the magnetic field in Eq. (3.14) except for small and constant offsets. For details of this method see Sec. 5.1.

In Penning traps without the possibility of simultaneous measurements, the magnetic-field ratio does not cancel and, in case of a drift $\Delta B = B(t_1) - B(t_2) \neq 0$, this leads to a shift in the inferred mass ratio of

$$\begin{aligned}\Delta\left(\frac{m_1}{m_2}\right) &= \left.\frac{m_1}{m_2}\right|_{\Delta B} - \left.\frac{m_1}{m_2}\right|_{B_0} = \left(\frac{B(t_1)}{B(t_2)} - 1\right) \cdot \frac{q_1}{q_2} \cdot \frac{\omega_{c,2}}{\omega_{c,1}} \\ &= \left(\frac{\overline{B} + \Delta B/2}{\overline{B} - \Delta B/2} - 1\right) \cdot \frac{q_1}{q_2} \cdot \frac{\omega_{c,2}}{\omega_{c,1}} = \frac{\Delta B}{\overline{B} - \Delta B/2} \cdot \frac{q_1}{q_2} \cdot \frac{\omega_{c,2}}{\omega_{c,1}} \\ &\approx \frac{\Delta B}{\overline{B}} \cdot \frac{q_1}{q_2} \cdot \frac{\omega_{c,2}}{\omega_{c,1}},\end{aligned} \tag{3.17}$$

where $\overline{B} = (B(t_1) + B(t_2))/2$ is the mean magnetic field. Such shifts are typically the dominant limitation of mass measurements. The resulting uncertainty strongly depends on the actual temporal fluctuations of the magnetic field and the effect can be minimized by measuring in as short intervals as possible and alternating between the ion species, see the experiments at SHIPTRAP in Chap. 9.

3.3.2 The Invariance Theorem

In a real Penning trap it is technically challenging to perfectly align the electrostatic axis, defined by the trap electrodes, with the direction of the magnetic field given by the superconducting magnet. Furthermore, slight elliptic corrections to the rotational symmetry in the electrostatic potential will occur due to machining imperfections, misalignment of the trap electrodes or electrostatic potential offsets.
In the presence of such imperfections, characterized by the tilt angles θ and φ and the ellipticity parameter ϵ, the harmonic eigenmotions are no longer independent and inter-mode coupling results. The measurable eigenfrequencies $\tilde{\omega}_+(\theta, \varphi, \epsilon)$, $\tilde{\omega}_z(\theta, \varphi, \epsilon)$ and $\tilde{\omega}_-(\theta, \varphi, \epsilon)$ become a function of the tilt angles and the ellipticities. However, it is shown in [159] that the determination of the free cyclotron frequency ω_c by Eq. (3.7) is completely independent of such alignment errors and ellipticity. This is expressed by

$$\omega_c^2 = \tilde{\omega}_+^2(\theta, \varphi, \epsilon) + \tilde{\omega}_z^2(\theta, \varphi, \epsilon) + \tilde{\omega}_-^2(\theta, \varphi, \epsilon) = \omega_+^2 + \omega_z^2 + \omega_-^2, \tag{3.18}$$

which is referred to as the "*Brown-Gabrielse Invariance Theorem*". The frequencies on the right hand side are the eigenfrequencies of the ideal trap defined in Eq. (3.4).

In case of the determination of the free cyclotron frequency from Eq. (3.6), there is no complete suppression of those effects and the resulting corrections are discussed in detail in Sec. 9.1.2.

3.3.3 Electrostatic Anharmonicities

The ideal electrostatic trapping potential is defined in Eq. (3.2), and the ideal trap geometry is provided by infinite hyperbolical trap electrodes [160]. However, the sources of imperfections are manifold and examples are simply machining imperfections, the finite length of real trap electrodes, holes in the trap structure for injection or ejection of the ions or segmentation of the electrodes for detection. Furthermore, in cylindrical Penning traps the ideal potential can only be approximated in a limited volume in the center of the trap and higher order contributions are inherently caused by this electrode structure (see Sec. 5.2). Predictions of anharmonic effects on the ion's motion are necessary to develop a suitable field configuration.

Taylor Expansion of the Real Potential

The potential within a real trap is given by the solution of the Laplace equation $\nabla^2\phi(\rho, z) = 0$, where the trap electrodes and applied voltages define the boundary

conditions and, hence, the actual shape and strength of the potential. In order to analyze anharmonic contributions in the trap, the real trap potential can be written as a Taylor expansion in cylindrical coordinates $[\rho, \varphi, z]$ as proposed in [161]. Due to rotational symmetry, the potential has to be independent on φ. At the center of the trap it is given by

$$\begin{aligned}\phi(\rho, z) &= \sum_{j=0}^{\infty}\sum_{i=0}^{j} \frac{1}{i!(j-i)!} \cdot \left.\frac{\partial^j \phi}{\partial \rho^i \partial z^{j-i}}\right|_{(0,0)} \cdot \rho^i z^{j-i} \\ &\equiv U_0 \sum_{j=0}^{\infty}\sum_{i=0}^{j} c_{i,j-i} \cdot \rho^i z^{j-i},\end{aligned} \tag{3.19}$$

where the Taylor coefficients $c_{i,j-i} = \frac{1}{U_0}\frac{1}{i!(j-i)!}\left.\frac{\partial^j \phi}{\partial \rho^i \partial z^{j-i}}\right|_{(0,0)}$ are normalized to the trap voltage U_0 for convenience. To solve the Laplace equation, all coefficients within an order j have to be related to each other by

$$c_{i,j-i} = (-1)^{i/2} \frac{j!}{(j-i)!\left(\frac{i}{2}!\right)^2 2^i} \cdot c_j, \tag{3.20}$$

where the pure axial coefficients are defined by

$$c_j \equiv c_{0,j} = \frac{1}{U_0}\frac{1}{j!}\left.\frac{\partial^j \phi(\rho, z)}{\partial z^j}\right|_{(0,0)}. \tag{3.21}$$

In other words, the coefficients c_j on the trap axis also determine the radial behavior. Furthermore, in a real trap the electrode structure is chosen with mirror symmetry in z. Consequently, all odd orders have to vanish in order to fulfill the boundary conditions and both i and j have to be even numbers. Hence, by inserting Eq. (3.20) in Eq. (3.19), the real trap potential can be expressed as

$$\begin{aligned}\phi(\rho, z)/U_0 = \; & c_0 \\ & + c_2\left(z^2 - \frac{1}{2}\rho^2\right) \\ & + c_4\left(z^4 - 3\rho^2 z^2 + \frac{3}{8}\rho^4\right) \\ & + c_6\left(z^6 - \frac{15}{2}\rho^2 z^4 + \frac{45}{8}\rho^4 z^2 - \frac{5}{16}\rho^6\right) \\ & + \ldots .\end{aligned} \tag{3.22}$$

The coefficients c_j are pure functions of the electrode geometry and the applied voltages, which directly classify the anharmonicities within a real trap (see Sec. 5.2.1 and Sec. 5.3 for the trap tower of PENTATRAP).

Effects on the Eigenfrequencies

To estimate the influence of higher-order electrostatic contributions on the ion's motion, the equation of motion has to be solved in presence of anharmonicities. Inserting Eq. (3.22) in Eq. (3.3) leads to nonlinear differential equations of *Duffing* type (see discussion in, e.g. [162]). In addition to this analytical approach, perturbation theory is used for extensive studies of hyperbolical traps [155, 160][6]. In [163], the results are transferred to cylindrical trap geometries, which are exclusively used here.
Certainly, the lowest order coefficients are most important for the influence on the axial frequency, since typical amplitudes are much smaller than the trap dimensions. The constant contribution c_0 is not observable. The harmonic coefficient c_2 determines the strength of the ideal trap potential discussed in Sec. 3.1, which leads, in combination with the ideal magnetic field, to the unperturbed eigenfrequencies given in Eq. (3.4). The anharmonic coefficients with $j \geq 4$ relate into a shift of the ideal axial frequency, depending on the axial amplitude z_0 or, equivalently, on the axial energy E_z defined in Eq. (3.10). For the leading anharmonic coefficients c_4 and c_6, the relative axial frequency shift is given by

$$\frac{\Delta\omega_z}{\omega_z} = \frac{3}{4}\left(\frac{c_4}{c_2^2} + \frac{5}{4}\frac{c_6}{c_2^3}\frac{E_z}{qU_0}\right)\frac{E_z}{qU_0}. \tag{3.23}$$

The approach based on perturbation theory in [155, 164] leads to a more comprehensive correction matrix, with all eigenfrequencies and mode energies involved. For the leading anharmonic coefficient c_4, it reads to

$$\begin{pmatrix}\Delta\omega_+/\omega_+\\ \Delta\omega_z/\omega_z\\ \Delta\omega_-/\omega_-\end{pmatrix} = \frac{3}{qU_0}\frac{c_4}{c_2^2}\begin{pmatrix}\frac{1}{4}\left(\omega_z/\omega_+\right)^4 & -\frac{1}{2}\left(\omega_z/\omega_+\right)^2 & -\left(\omega_z/\omega_+\right)^2\\ -\frac{1}{2}\left(\omega_z/\omega_+\right)^2 & \frac{1}{4} & 1\\ -\left(\omega_z/\omega_+\right)^2 & 1 & 1\end{pmatrix}\begin{pmatrix}E_+\\ E_z\\ E_-\end{pmatrix}. \tag{3.24}$$

As a summary, in order to avoid undesirable frequency shifts of all eigenfrequencies, anharmonic contributions of the electrostatic field have to be minimized in high-precision experiments. For experimental compensation of c_4 and c_6 at PENTATRAP, see Sec. 5.3.2.

3.3.4 Inhomogeneous Magnetic Field

Analog to the electrostatic field discussion, the magnetic field can be expanded in a power series of z and ρ, in order to investigate higher order effects based on the coefficients B_n. Again, the expansion has to satisfy the Maxwell equations and, up to

[6] Within this literature, the trap potential is expanded in spherical coordinates with respect to Legendre polynomials $\phi(r,\vartheta,\varphi) = \frac{1}{2}U_0\sum_{k=0}^{\infty} D_k\left(r/d_0\right)^k P_k(\cos\vartheta)$. However, this description is equivalent to Eq. (3.19) with the condition given in Eq. (3.20) (both expansions are solutions to the Laplace equation). A simple comparison of the coefficients to the expansion in Eq. (3.19) within a given order reveals the relation $c_j = D_j/(2d_0^j)$ to the coefficients defined in Eq. (3.21). Here, the characteristic trap length d_0 is defined by $D_2 = 1$.

second order, it is given by

$$\vec{B}(\rho,z) = B_0 \cdot \hat{z} + B_1\left(-2z\cdot\hat{z} + \rho\cdot\hat{\rho}\right) + B_2\left[\left(z^2 - \frac{\rho^2}{2}\right)\cdot\hat{z} - \rho z\cdot\hat{\rho}\right], \tag{3.25}$$

where, in contrast to the electrostatic field, odd terms are allowed for the fulfillment of the boundary conditions within a superconducting magnet and the material surrounding the trapping region. Typically, in the central region of the magnet the radial contributions in Eq. (3.25) are negligible compared to the strong axial part. In real experiments, the effect of B_2 is much stronger than B_1.
For $B_1 = 0$, the effects on $\omega_+ \approx \omega_c \propto B$ are obvious. An increase of the radial amplitudes ρ changes the magnetic field along the ion's radial orbit and, in turn, ω_+ is shifted. Since the magnetic field probed by the particle in average over one axial oscillation period is given by

$$\langle B\rangle = B_0 + \langle B_2 z_0^2\cos(\omega_z t)\rangle = B_0 + \frac{B_2}{2}z_0^2, \tag{3.26}$$

where $\rho = 0$ is chosen for simplicity, an increase of the axial amplitude has the same effect. The same arguments hold for the magnetron frequency except for the sign of the shift due to $\omega_- \propto 1/B$.
For the axial frequency ω_z, effects from the inhomogeneous magnetic-field contribution are less obvious, since it is independent of B. However, the radial motions are correlated with a magnetic moment due to the circular ion current orbiting perpendicular to the magnetic field. For the cyclotron motion this is given by

$$\vec{\mu}_+ = -q\frac{\omega_+\rho_+^2}{2}\hat{z}. \tag{3.27}$$

In an inhomogeneous magnetic field, this magnetic moment causes a force $F_z^{(2)} = \partial_z(\mu_+ B(z)) = -qB_2\omega_+\rho_+^2 z$ in the axial direction, which adds to the electrostatical force. Consequently, the axial potential is changed and the axial frequency modified[7].
In analogy to the electrostatic anharmonicities, the effect of B_2 on all eigenmotions is calculated in [155] with respect to all mode energies. The matrix form is given by

$$\begin{pmatrix}\Delta\omega_+/\omega_+\\ \Delta\omega_z/\omega_z\\ \Delta\omega_-/\omega_-\end{pmatrix} = \frac{1}{m\omega_z^2}\frac{B_2}{B_0}\begin{pmatrix}-(\omega_z/\omega_+)^2 & 1 & 2\\ 1 & 0 & -1\\ 2 & -1 & -2\end{pmatrix}\begin{pmatrix}E_+\\ E_z\\ E_-\end{pmatrix}. \tag{3.28}$$

The linear axial correction in Eq. (3.26) is given by $\Delta B_z = -2B_1 z$. Hence, in this order the axial magnetic field is constant for all radial amplitudes. Along the axis, the additional magnetic field averages to zero on a axial oscillation period, due to the linear

[7] This effect is used in g-factor measurements. In those experiments, the orientation of an intrinsic magnetic moment is detected by the shift of the axial frequency in a strongly inhomogeneous magnetic field [165].

dependence. However, the magnetic moment of the radial motion causes an axial force $F_z^{(1)} = 2\mu_+ B_1$. Due to the independence of this force with respect to z, the origin of the oscillation in the axial direction is shifted by this force and, in the presence of B_1 (and B_2), the particle experiences a changed magnetic field. The radial eigenfrequencies are shifted. This effect is discussed in [166] and [167], and, for both magnets it is found that the influence is negligible compared to B_2. At PENTATRAP, systematic studies of the magnetic field will be performed, and additional compensation coils might be used to lower the residual influence of B_1, if needed.

3.3.5 Further Effects

Voltage Fluctuations

The requirement on the stability of a voltage source providing the trap voltage U_0 is dictated by the resulting uncertainty in the axial frequency, which might limit the overall uncertainty. Fluctuations which are fast compared to the measurement time lead to a broadening of the line shapes in the detection of the axial frequency (see Sec. 6.1.1). The line center is not affected. However, if drifts are on the same time scale as the measurement time for the axial frequency, a drift ΔU_0 shifts the center of the line shapes at ω_z by

$$\frac{\Delta\omega_z}{\omega_z} = \frac{1}{2}\frac{\Delta U_0}{U_0}. \tag{3.29}$$

Hence, the center of the line shapes smears out, which sets the limit to the precision in the determination of ω_z. Resulting from Eq. (3.16), the determination of the free cyclotron frequency on the 10^{-11} level requires a determination of the axial frequency to $\delta\omega_z/\omega_z \sim 10^{-8}$ (see also Fig. 3.5). According to Eq. (3.29), this requires the relative stability of U_0 to be on the same level within the measurement time.

Relativistic Shifts

The velocity of cooled ions in a Penning trap is typically very small compared to the speed of light. Nevertheless, in order to get an estimate on the relativistic effect and the possible need for corrections in high-precision experiments, the relativistic mass shift $m = m_0/\sqrt{1-(v/c)^2}$ has to be considered. The largest relativistic shift is expected in the fast modified cyclotron motion, which carries almost purely kinetic energy. Here, the shift is given by [155]

$$\omega_+ \approx \omega_\mathrm{c} = \frac{qB}{m_0}\sqrt{1-\left(\frac{v_+}{c}\right)^2} \approx \omega_{c,0}\left(1-\frac{1}{2}\left(\frac{v_+}{c}\right)^2\right) \tag{3.30}$$

$$\leftrightarrow \quad \frac{\Delta\omega_\mathrm{c}}{\omega_\mathrm{c}} = -\frac{1}{2}\frac{v_+^2}{c^2} = -\frac{1}{2}\frac{m_0 v_+^2}{m_0 c^2} \approx -\frac{E_{\mathrm{kin},+}}{m_0 c^2} \approx -\frac{E_+}{m_0 c^2}. \tag{3.31}$$

In cryogenic traps, the energy E_+ can be cooled to typically ~ 10 meV or below. At this energy, the shift is of the order of 10^{-13} for a heavy mass of $A = 150$.

Image-Charge Effects

The charge of an ion within a trap induces image-charges in the trap electrodes, where the resulting field has to be superimposed on the trapping field and, hence, acts back on the ion's motions [168]. In case of highly-charged ions, this effect is not negligible for high-precison experiments. Due to the dependence of the image-charge field on the specific trap-electrode structure, this effect is discussed in the context of cylindrical traps within the PENTATRAP experiment (see Sec. 5.2.2).

Part I

The PENTATRAP Mass Spectrometer

4 Overview of the PENTATRAP facility

The novel cryogenic Penning-trap mass spectrometer PENTATRAP is currently developed at the Max-Planck-Institut für Kernphysik, Heidelberg. A sketch of the main experimental devices is shown Fig. 4.1.
The core piece of the PENTATRAP facility, the five Penning-trap tower, is situated in a 7-T superconducting magnet. The liquid-helium reservoir used for cooling of the magnet's coils is directly connected to the bore of the magnet, in which the chambers housing the traps and the cryogenic detection system are cooled to the 4-K temperature. Around the magnet, a pair of Helmholtz coils connected to a flux-gate magnetometer is designated for the suppression of external magnetic-field noise. Moreover, the level of the liquid helium and the pressure in the bore will be stabilized by an external system (not shown in Fig. 4.1), in order to prevent temperature-dependent changes of the permeability of the material surrounding the trap chamber. For the same reason, the PENTATRAP laboratory is temperature and pressure stabilized. The magnet itself is supported by anti-vibration pneumatic pads, resting on vibration-damped concrete blocks on the floor.
The design foresees the use of different external ion sources, demanding an open trap system. Either a commercial electron beam ion trap (EBIT), the Dresden-EBIT3 [169, 170], or the Heidelberg-EBIT [171] are used for the ionization to high charge states, from which the ions are extracted at high kinetic energy and low beam emittance. The ions are guided from the sources towards the trapping setup by a system of electrostatic lenses and are slowed down by two pulsed drift tubes, where the second one is located directly in front of the Penning traps for the final stopping. Two diagnostic stations, consisting of a Faraday cup and a multi-channel plate (MCP) with phosphor screen, enable the control of efficient injection into the magnet.

Within this thesis, the trap tower and the cryogenic detection system are discussed in Chap. 5 and Chap. 6. For the other main parts, brief summaries are given in the following sections and details are described in several Ph.D. theses, as stated below. Most information given here can also be found in [32].

4.1 Magnet System and Cryogenic Trapping Setup

Superconducting Magnet

At PENTATRAP, a 7-T superconducting magnet is used, where the vertical cold bore has an inner diameter of 160 mm (see Fig. C.1 for a photograph). The liquid helium

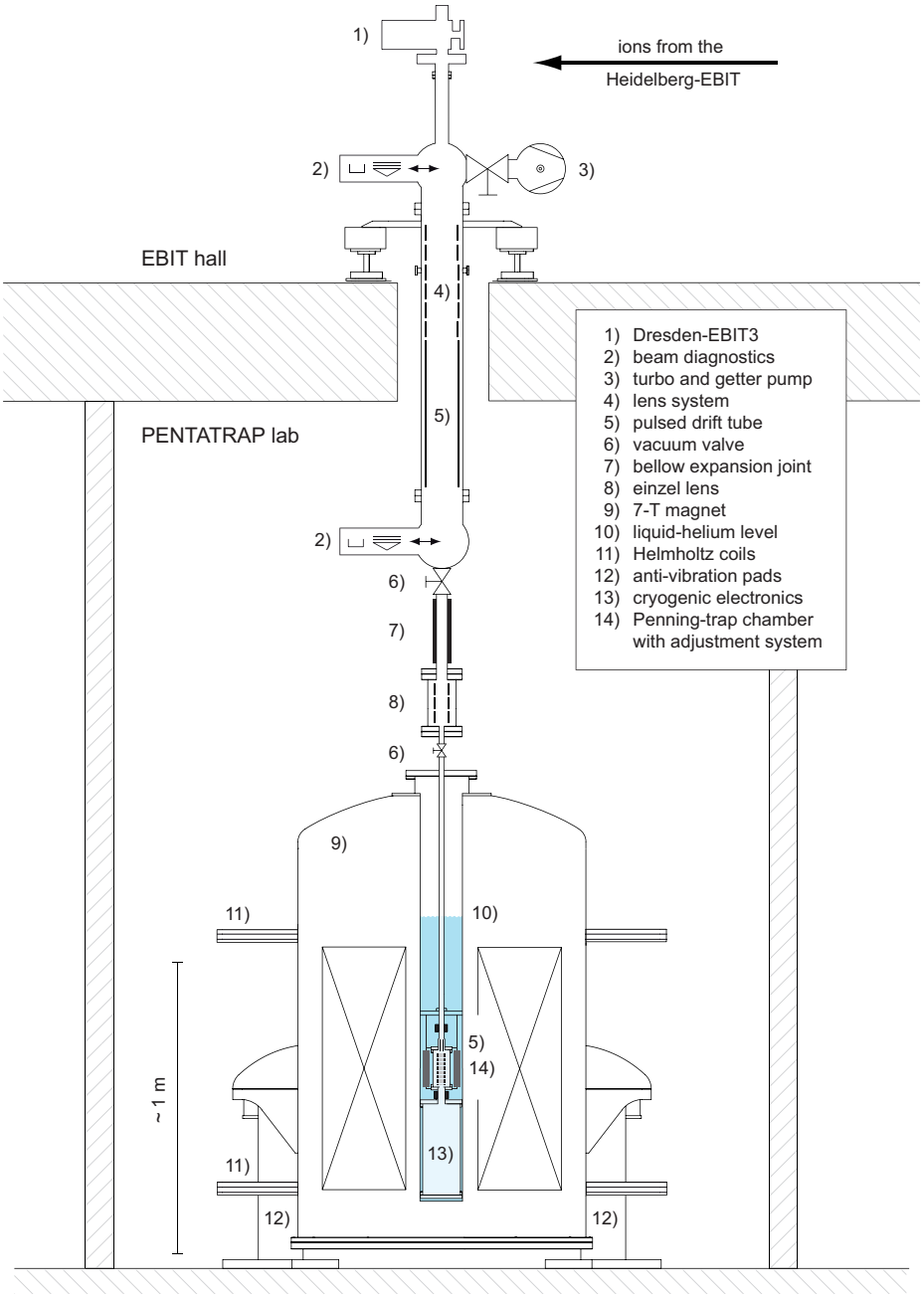

Figure 4.1: Overview of the PENTATRAP facility. The figure is adapted from [32].

reservoir of the magnet's coils is directly connected to the magnet bore, in which the trap chamber as well as the cryogenic detection electronics are placed and immersed into the liquid helium. The self-shielding design of the magnet's coils gives a shielding factor of ~ 100 to external magnetic stray fields. The magnet is supported by anti-vibration pneumatic pads.
In a 1 cm^3 volume in the center of the magnetic field, the spatial homogeneity $\Delta B/B$ is on the order of a few ppm. In a cylinder of 2.5 mm radius and 120 mm length along the magnet's axis, defining the trapping region in the trap tower, the spatial homogeneity is given by about 25 ppm [32]. In order to reduce gradients in the trapping region, future plans imply additional magnetic-field coils directly wound around the trap chamber. A detailed characterization of the magnetic-field properties is given in the Ph.D. thesis of J. Repp [172].

Trap and Electronics Chambers

The trap tower is housed by a copper vacuum chamber, which is connected by flexible titanium bellows to a stainless steel tube for the ion injection on top and to the chamber for the cryogenic detection electronics on the bottom, enabling a direct in-vacuum connection of traps and electronics (see also Fig. 6.5). Both chambers are cooled to 4 K by the surrounding liquid helium in the magnet bore. Although an open system is required for the ion injection, very good vacuum conditions below 10^{-13} mbar are expected due to the cryo-pumping effect of the inner surfaces and several charcoal absorbers glued into both chambers.
In order to align the flexibly mounted trap chamber to the magnetic-field direction and center, a mechanical tilt and shift system enables an on-line adjustment in the range of $\pm 1^\circ$ and ± 2 mm in the horizontal plane. Details of the assembly of the cryogenic chambers and of the functionality of the tilt and shift system will be given in [172].

Level and Pressure Stabilization

In the vicinity of the trap chamber, temperature-dependent changes of the magnetic susceptibility of the surrounding material might influence the magnetic field inside the traps. In order to provide a constant temperature of this material, a stabilization system of the liquid-helium level as well as a pressure regulation of the evaporating helium will be installed at the PENTATRAP magnet. Both systems are based on the principles presented in [24] and are modified for the PENTATRAP magnet.
For the level sensing, a small helical resonator will be partly immersed to the liquid helium, whose resonance frequency changes with the amount of dielectric provided by the liquid. Due to the direct connection, the level in the bore can be adjusted by the pressure above the liquid in the coil reservoir. This pressure will be regulated by a mass-flow controller, to which the level signal from the resonator is fed in.
The pressure in the magnet bore is measured by a commercial transducer relative to an absolute pressure reference (APR) installed next to the magnet. With the difference signal, a valve is controlled to release over-pressure from the magnet bore.

The performance aimed for is a control of the liquid-helium level to better than 0.1 mm and a stabilization of the pressure in the bore on the order of 1 μbar. A detailed discussion of the final performance will be given in the Ph.D. thesis of Ch. Böhm [173].

Shielding of Stray Fields

For passive shielding of stray electric and high-frequency magnetic fields, the PENTATRAP magnet can be enclosed with an aluminum housing (not shown in Fig. 4.1). Low-frequency vertical components of stray magnetic fields will be actively shielded from the magnet by a feedback system, consisting of a flux-gate magnetometer and a pair of Helmholtz coils mounted around the magnet, based on the principle presented in [24]. Combined with the self-shielding of the magnet, the estimated total shielding factor exceeds 1000, where details will be given in [172] and can also be found in the Bachelor thesis of A. Rischka [174].

PENTATRAP laboratory

The total magnet system is assembled in the PENTATRAP laboratory, which is actively pressure and temperature stabilized by a commercial system. Measurements of the remaining temperature fluctuations in the empty room revealed a combined Allan deviation of ~ 0.02 K per day [32]. However, the final performance for the room equipped with the measurement setup still has to be characterized. Details about the temperature measurements will be presented in [172].
For suppression of vibrations, a rubber-damped concrete is embedded in the floor underneath the support of the magnet (not shown in Fig. 4.1), where measured vibration amplitudes from external sources do not exceed 1 μm [32].

4.2 Ion Sources and Beam Line

Ion Sources

Due to the scaling of the cyclotron frequency ω_c with the charge-to-mass ratio q/m, high charge states are needed for heavy masses to increase the frequencies, in order to attain high relative accuracies in the measurement of frequency ratios. At PENTATRAP, two electron beam ion traps (EBIT) [175] are used for the ionization to high charge states, the commercial room-temperature Dresden-EBIT3 [169, 170] and the Heidelberg-EBIT [171], the latter in a second experimental phase.
The Dresden-EBIT3 can produce bare ions up to $Z = 30$. At the heavy masses of, e.g., ^{187}Re and ^{187}Os relevant for the measurement of the β-decay Q-value (see Sec. 2.1.2), charge states around 50+ were demonstrated [32]. Thus, in our 7-T magnetic field the cyclotron frequency amounts to $\nu_c(^{187}\mathrm{Re}^{50+}) \approx 29$ MHz. Moreover, with the current voltage source UM 1-14 (see Sec. 4.3), the axial frequency can be tuned up to $\nu_z \sim 500$ kHz at $U_0 = -12.8$ V (see Fig. 5.7). A detailed characterization of the Dresden-EBIT3 within our setup will be given in [172].

For even higher charge states, as demanded for the measurements of, e.g., atomic binding energies (see Sec. 2.2.2), the ions will be delivered by the Heidelberg-EBIT, where helium-like ions up to Bi ($q = 81+$) and hydrogen-like or even bare ions up to Ba ($q = 56+$) are routinely produced at a beam emittance of $\sim 3\pi$ mm mrad [135, 176]. An upgrade of the maximum electron-beam energy, currently limited to 100 keV, will enable the production of bare uranium in the near future.

Beam Line

A system of electrostatic einzel lenses will guide the ions from the sources to the magnet setup and ensures that the emittance of the ion beam matches the acceptance of the magnet. The high energy beam (up to ~ 7 keV/q) is slowed down by two pulsed drift tubes. The first one reduces the energy down to $\sim 200 - 500$ eV/q, whereas the second one, located directly above the trap tower, reduces the energy down to ~ 5 eV/q such that the ions can be captured in the traps by the ring voltages. The ion-optics setup is simulated with SIMION™ [177] and, for optimal parameters, the injection efficiency exceeds 95 % for a beam energy of 7 keV/q and a beam emittance of 3π mm mrad [32]. In order to control the efficient injection in the experiment, two diagnostic stations consisting of a Faraday cup and a multi-channel plate (MCP) with phosphor screen can be mechanically introduced to the beam axis.

4.3 Precision-Voltage Sources

For the supply of highly stable ring voltages, a commercial voltage source UM 1-14 (*Stahl Electronics*) is available at the PENTATRAP setup. In the 24-bit precision channels, this source offers a voltage range of 0 to -14 V and a resolution of 1 μV. The temporal stability, measured to $\Delta V/V \lesssim 2 \times 10^{-7}$ in interval of 10 min, limiting the achievable resolution in the axial frequency to $\Delta\nu_z/\nu_z \approx 10^{-7}$ even if the average over several measurements is taken, see Eq. (3.29). Moreover, the available voltage range severely limits the range of the charge-to-mass ratio q/m for measurements at $\nu_z \sim 600$ kHz in our trap (see Fig. 5.7).
For this reasons, a new highly stable voltage source called StaReP (Stable Reference source for Penning traps) is currently under development at the Max-Planck-Institut für Kernphysik, Heidelberg, in collaboration with the Physikalisch Technische Bundesanstalt (PTB) in Braunschweig. The new design aims for a voltage range of 0 to -100 V with a resolution < 1.5 μV, a temporal stability of $\Delta V/V < 4\times10^{-8}$ within a measurement interval of 10 min and a temperature stability of $\Delta V/V < 4 \times 10^{-7}$ per K. The source will be equipped with 25 channels with a fast ramping option for ion transport, where every channel can be replaced individually in case of a failure. Details of the design and performance will be given in the Ph.D. thesis of Ch. Böhm [173].

4.4 Control System

At PENTATRAP, a control system (CS) based on the CS-framework (GSI, Darmstadt) will be used. This framework is built in the *Lab View* development system (*National Instruments*) and was originally developed for time-of-flight detection experiments [178]. The CS offers a high stability and a control of all hardware units in use within one frame. At PENTATRAP, the CS is adapted to the specifics of non-destructive image-current detection and allows one for the on-line evaluation of the ion signals. In addition, a logbook data base for the storage of all experimental data and parameters will be implemented. With the definition of new classes, a high flexibility is achieved allowing for the change of settings, inclusion of new measurement schemes and to replace specific hardware components without stopping the experiment. The CS core offers a fast control with time resolution of 12.5 ns for, e.g., the pulsed drift tubes, and standard components, such as signal generators, are addressed in a slow mode without fixed time resolution. Details of the new developments for the PENTATRAP CS will be given in the Ph.D. thesis of M. Goncharov [179].

5 Trap Tower

The core of the PENTATRAP project for performing the mass measurements is the trap tower. It is the first experiment to utilize a stack of five individual Penning traps. The great benefit of this novel mass spectrometer design [32] is described in Sec. 5.1. The analytical basis for the design is discussed in Sec. 5.2.1, followed by a brief description of image-charge effects and ion-ion interaction in adjacent Penning traps in Sec. 5.2.2. The final design of the trap tower is presented in Sec. 5.3.1, together with a discussion of the expected performance in Sec. 5.3.2. A discussion of the design process can also be found in [180].

5.1 Measurement Principle

As introduced in Sec. 3.3.1, if for relative mass measurements two ion species are measured subsequently, temporal fluctuations of the magnetic field might set the dominant limitation on the final accuracy of the mass-ratio determination. Generally, the mean difference ΔB of the magnetic field increases with the time difference between two measurements of the cyclotron frequencies, thereby, a reduction of the time difference is desired. Ultimately, the two species are measured simultaneously. A technique for the simultaneous measurement of two species in one trap is described in [23]. However, a systematic limitation arises from the ion-ion interaction between the two ions, excluding this method for highly-charged ions. Furthermore, the fractional mass difference of the two species is limited to $\Delta m/m \leq 10^{-3}$ for high-accuracy measurements within this method. For details, see [181, 182].
In our novel approach, we utilize a stack of five cylindrical Penning traps, as depicted in Fig. 5.1. This structure offers several advantages over a single trap. The most promising scheme employs the simultaneous measurement in two adjacent traps. In this case, ion-ion interactions imprint much less systematics than they do in a single trap. For the PENTATRAP geometry, the stated effect is estimated to be negligible for the aimed precision (see Sec. 5.2.2).
Following the experimental sequence illustrated in Fig. 5.1: At the first step at time t_1, the simultaneous measurement of the two cyclotron frequencies $\nu_{c,1}$ and $\nu_{c,2}$ of ions with charge q_1 and q_2 and mass m_1 and m_2 is performed in trap 2 and trap 3. The frequency ratio is here given by

$$R(t_1) = \frac{\nu_{c,1}}{\nu_{c,2}} = \frac{q_1}{q_2}\frac{m_2}{m_1} \cdot \frac{B_{(2)}(t_1)}{B_{(3)}(t_1)} \equiv \frac{q_1}{q_2}\frac{m_2}{m_1} \cdot \varrho_B(t_1), \tag{5.1}$$

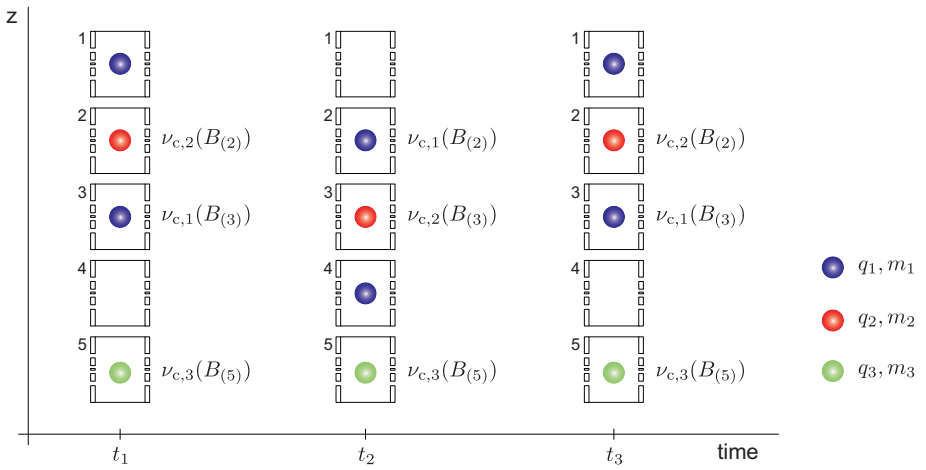

Figure 5.1: Most promising measurement scheme for the PENTATRAP spectrometer. The frequencies $\nu_{c,1}$ and $\nu_{c,2}$ are measured simultaneously at t_1 in trap 2 and 3. Subsequently, the ions of trap 1 to 3 are transported to the next higher trap number in order to exchange the ion species in trap 2 and 3. A repeated measurement eliminates the influence of magnetic-field offsets in the ratio determination. The remaining trap 5 might be used to monitor magnetic-field fluctuations by a measurement of $\nu_{c,3}$, or to serve as a reference for the voltage source.

where $B_{(2)}$ and $B_{(3)}$ are the magnetic-field strengths in trap 2 and trap 3, averaged over the measurement time. In general, the magnetic-field strengths vary slightly in two neighboring traps. But, the ratio $\varrho_B = B_{(2)}/B_{(3)}$ is, to great extent, defined by the geometry of the magnet and expected to be nearly constant over time ($\varrho_B(t) = \varrho_B$). In order to eliminate ϱ_B, the measurement is repeated after swapping the species in trap 2 and trap 3. The ratio at time t_2 is then given by

$$R(t_2) = \frac{\nu_{c,1}}{\nu_{c,2}} = \frac{q_1}{q_2}\frac{m_2}{m_1} \cdot \frac{1}{\varrho_B}. \tag{5.2}$$

Consequently, the square root of the product of the two ratio determinations gets independent of the magnetic field

$$\sqrt{R(t_1) \cdot R(t_2)} = \sqrt{\left(\frac{q_1}{q_2}\frac{m_2}{m_1}\right)^2 \cdot \varrho_B \frac{1}{\varrho_B}} = \frac{q_1}{q_2}\frac{m_2}{m_1}, \tag{5.3}$$

yielding the mass ratio of the two ion species.
Residual temporal fluctuations in ϱ_B of stochastic nature will be averaged out by repeating the experimental cycle, as indicated at time t_3 in Fig. 5.1. However, a slow drift in time would introduce a systematic error in the frequency ratio. Thus, appropriate measures to stabilize the B-field must be implemented. At PENTATRAP, a magnetic-field stabilization system will be installed to minimize fluctuations (see Sec. 4.1). Systematic studies with identical ion species will reveal the temporal fluctuations and yield an estimate for the error budget.

In order to exchange the ions in trap 2 and trap 3, trap 1 is loaded with an ion of species 1 prior to the experimental sequence. The exchange is, thereby, simply achieved by shifting all three ions to the next higher trap number (or vice versa). Trap 1 and 4 are subsequently used to store species 1 during the measurements in trap 2 and 3. In this way, the exchange can be accomplished faster than one second via a simple adiabatic transport between neighboring traps.
In the PENTATRAP design, trap 5 can monitor magnetic-field fluctuations by consecutive measurements of the cyclotron frequency $\nu_{c,3}$ of a monitor ion with charge q_3 and mass m_3. Alternatively, the axial frequency of this ion might serve as a reference for the voltage source providing the trapping voltages in the measurement traps [183].
Other measurement schemes are possible and systematic experimental studies have to decide on the most suitable one. As a further example, the mass-ratio measurement can be performed in an alternating way in trap 3, which has the most symmetric environment and, hence, possibly the best electrostatic performance (see Sec. 5.3). The adjacent trap 2 and trap 4 might, again, serve as ion containers for the ion exchange and the outer trap 1 and trap 5 as monitor or reference traps.

5.2 Cylindrical Penning Traps

In order to generate the ideal trapping potential of Eq. (3.2), a hyperbolical electrode structure (see Fig. 3.1) is used in many high-precision experiments. However, a trap geometry consisting of concentric cylindrical rings is also capable of producing a nearly-perfect quadrupolar potential in the central region of the trap [184].
Major advantages of this trap geometry are an efficient injection of the charged particles and the fabrication to high machining precision. In addition, the resulting trap potential can be calculated analytically, which is crucial for the design process. Consequently, cylindrical traps have become very popular in recent years and are widely used at various Penning-trap experiments such as, e.g., high-precision mass measurements (see [5, 26] and references therein), g-factor experiments of the bound electron and the proton [30, 185] as well as the free electron [111], and for the production of anti-hydrogen [186, 187].
In Sec. 5.2.1, the derivation of an analytical expression for the potential inside a cylindrical trap structure is discussed, giving the basis for the design of our Penning-trap tower in Sec. 5.3. In Sec. 5.2.2, the systematic effects of image charges induced in the trap electrodes and ion-ion interaction in adjacent cylindrical traps are discussed.

5.2.1 Electrostatic Potential

A typical cylindrical trap structure is shown in Fig. 5.2a. Besides the ring electrode (RE) and the endcaps (ECs), additional correction electrodes (CEs) are implemented in order to compensate for higher-order anharmonic terms of the electrostatic potential defined in Sec. 3.3.3. Compensation electrodes were first used in hyperbolical traps [188] and are discussed for cylindrical trap electrodes in [184]. Most commonly, the endcaps

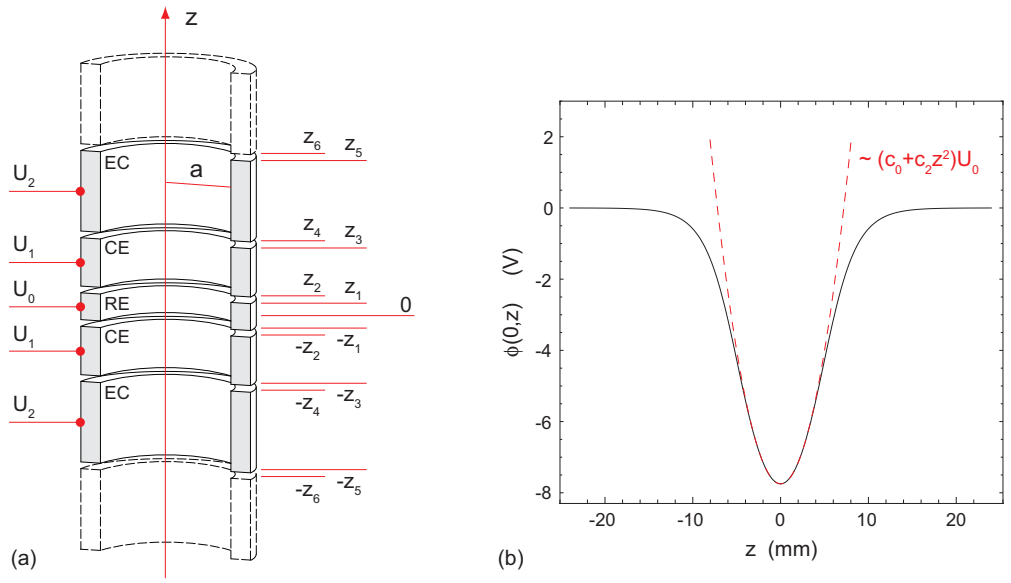

Figure 5.2: (a) Schematic of a cylindrical five-electrode trap inside a trap tower. The inner radius of the electrodes is given by a. The lengths of the trap electrodes are $l_\mathrm{r} = 2z_1$ for the central ring electrode (RE), $l_\mathrm{c} = z_3 - z_2$ for the correction electrodes (CE), and $l_\mathrm{e} = z_5 - z_4$ for the endcaps (EC). All electrodes are separated by the same distance $l_\mathrm{gap} = z_2 - z_1$. The electric potential at the inner surface of the electrodes is defined by the voltages U_i applied to the electrodes. (b) Example of the potential given by the electrode structure shown in (a) along the trap axis z.

are grounded by $U_2 \equiv U_\mathrm{e} = 0$ V and a potential minimum[1] is generated by a negative ring voltage $U_0 \equiv U_\mathrm{r} < 0$. The voltage of the correction electrode is chosen as $0 \leq U_1 \equiv U_\mathrm{c} \leq U_0$, depending on the geometry of the trap.
In order to provide identical conditions in the three inner traps of the PENTATRAP tower, we aim for a stack of five identical traps. The geometry of an individual trap is defined according to Fig. 5.2a. The inner radius of all electrodes is given by a, while the length of the REs is $l_\mathrm{r} = 2z_1$, the length of the CEs is $l_\mathrm{c} = z_3 - z_2$ and the length of the ECs is $l_\mathrm{e} = z_5 - z_4$. All electrodes are separated by an equal distance, given by $l_\mathrm{gap} = z_2 - z_1$.

Solution of the Laplace Equation

The potential in a Penning trap with arbitrary geometry can be obtained by solving the Laplace equation, using a general Green's function approach [161]. For cylindrical traps, an analytical expression is presented for a fixed number of five electrodes in [166]. If the ratio of the length l_r of the grounded endcaps to the inner radius a is sufficiently large, the influence of additional electrodes neighboring the five-electrode trap gets negligible. In this case, the result from [166] can be used to design a trap

[1] For the trapping of positively charged particles, a minimum in the electrostatic potential is needed, while negatively charged particles require a maximum, see Eq. (3.5a).

tower simply by calculating a single trap and repeating its structure. However, in our case there are restrictions to both the inner radius and the length of the endcaps, resulting from experimental constraints and systematic effects in the tower. Hence, the expression has to be expanded to additional electrodes in order to estimate their effect on the potential.
In [162], an expression for an arbitrary number of cylindrical electrodes without a mirror symmetry (with respect to the $z = 0$ plane) is presented, and even asymmetric trap geometries or voltages can be analyzed[2].
In the design of the geometry of our trap tower, a symmetry in z-direction is assumed according to Fig. 5.2. Thus, compared to [162] a simpler expression can be obtained using the reflexion symmetry, where a detailed derivation based on the methods given in [166] and [162] is described below.

To find the potential inside the trap electrodes, one has to solve the Laplace equation in azimuthal symmetry, which reads

$$\nabla^2\phi(\rho, z) = \frac{1}{\rho}\frac{\partial}{\partial\rho}\left(\rho \cdot \frac{\partial\phi}{\partial\rho}\right) + \frac{\partial^2\phi}{\partial z^2} = 0. \tag{5.4}$$

The ansatz $\phi(\rho, z) = R(\rho)Z(z)$ leads to two decoupled ordinary differential equations

$$\frac{1}{\rho}\frac{d}{d\rho}\left(\rho\frac{d}{d\rho}R(\rho)\right) - k^2R(\rho) = 0 = \frac{d^2}{dz^2}Z(z) + k^2Z(z), \tag{5.5}$$

where k is a separation constant. According to Fig. 5.2a, the electrode structure is invariant under $z \mapsto -z$ transformation. Hence, the general solution is given by [189]

$$\phi(\rho, z) = \int_{-\infty}^{\infty} dk A(k) I_0(k\rho)\cos(kz), \tag{5.6}$$

where I_0 is the modified Bessel function of zero order and first kind. The coefficient $A(k)$ is defined by the boundary conditions of Dirichlet type, fixed by the geometry of the trap electrodes and the applied voltages. Equation (5.6) can be expressed as an infinite sum, if the endcaps are grounded and the potential is assumed to vanish at the outer ends of the trap. This results in

$$\begin{aligned}\phi(\rho, z) &= \sum_{\substack{n=-\infty \\ n \text{ odd}}}^{\infty} A(k_n) I_0(k_n\rho)\cos(k_n z) \\ &= \sum_{\substack{n=1 \\ n \text{ odd}}}^{\infty} \underbrace{\{A(k_n) + A(k_{-n})\}}_{\equiv \widetilde{A}_n} I_0(k_n\rho)\cos(k_n z),\end{aligned} \tag{5.7}$$

[2] As discussed in this work, in the experimental realization asymmetries arise due to, e.g., patch potentials leading to voltage differences within a CE pair. The expression derived there is very helpful to analyze such effects on the particle frequencies.

with $k_n = n\pi/\Lambda$ and Λ as the total length of all electrodes. It is shown in [184] by comparison to the limit of infinite endcaps, that the approximated potential in Eq. (5.7) gives results valid to better than 1 % in all electrostatic coefficients, given the length of the grounded endcaps l_e is at least three times the inner radius a of the electrodes. In our case, this ratio is much larger and, hence, even more precise predictions are expected from Eq. (5.7).
The coefficients $\widetilde{A}_n$ are extracted with use of the orthogonality relation of the cosine [190]

$$\int_{-\pi/2}^{\pi/2} dx \cos(mx)\cos(nx) = \frac{\pi}{2}\delta_{nm}, \tag{5.8}$$

provided both n and m are odd integers. Equation (5.7) can be integrated along the z-direction at $\rho = a$:

$$\frac{1}{\Lambda}\int_{-\Lambda/2}^{\Lambda/2} dz \cos(k_n z)\phi(a,z) = \sum_{\substack{m=1\\ m \text{ odd}}}^{\infty} \widetilde{A}_m I_0(k_m a) \underbrace{\frac{1}{\Lambda}\int_{-\Lambda/2}^{\Lambda/2} dz \cos(k_m z)\cos(k_n z)}_{=\delta_{nm}/2}. \tag{5.9}$$

In this way, we obtain

$$\widetilde{A}_n = \frac{2}{\Lambda I_0(k_n a)}\int_{-\Lambda/2}^{\Lambda/2} dz \cos(k_n z)\phi(a,z). \tag{5.10}$$

At the inner surface of the electrodes, $\phi(a,z)$ is defined by the applied voltages. Along the small gaps between the electrodes, the potential at $\rho = a$ can be approximated by a linear interpolation between two adjacent electrodes. This leads to a negligible error if the length l_gap is much shorter than the typical length scales of the electrodes [161]. The integration along a trap with m electrodes, at which the endcaps are grounded[3], leads to the analytical expression

$$\phi(\rho,z) = \frac{4}{\Lambda}\sum_{\substack{n=1\\ n \text{ odd}}}^{\infty}\sum_{i=1}^{\kappa} \frac{U_i - U_{i-1}}{k_n^2 l_\mathrm{gap}} \cdot \frac{\cos(k_n z_{2i}) - \cos(k_n z_{2i-1})}{I_0(k_n a)} I_0(k_n \rho)\cos(k_n z), \tag{5.11}$$

where the voltages U_i and the lengths z_{2i} are defined according to the counting in Fig. 5.2 and $\kappa = (m-1)/2$. This expression relates a given trap geometry to the potential inside a cylindrical trap. Figure 5.2b shows the potential on axis of a typical five-electrode trap with grounded endcaps, calculated from Eq. (5.11). In the region

[3] The outer electrodes have to be grounded in order to justify the use of Eq. (5.7), where it is assumed that the potential vanishes at the outer ends of the trap structure.

close to $z = 0$, the potential of the cylindrical structure nearly coincides with the ideal harmonic potential $\phi_{\text{ideal}} = (c_0 + c_2 z^2)U_0$, defined in Eq. (3.2).

Compensated and Orthogonal Trap

To find an adequate trap geometry and voltage biasing, the potential inside the trap can be analyzed in terms of a Taylor expansion (see Sec. 3.3.3). Inserting Eq. (5.11) into Eq. (3.21) reveals the Taylor coefficients c_j at $z = 0$, for an arbitrary odd number m of electrodes and the corresponding voltages, which writes to[4]

$$c_j = \frac{(-1)^{\frac{j}{2}}}{U_0 j!} \frac{4}{\Lambda l_{\text{gap}}} \sum_{\substack{n=1 \\ n \text{ odd}}}^{\infty} \sum_{i=1}^{\kappa} k_n^{j-2} \left(U_i - U_{i-1}\right) \frac{\cos\left(k_n z_{2i}\right) - \cos\left(k_n z_{2i-1}\right)}{I_0\left(k_n a\right)}, \tag{5.12}$$

with $\kappa = (m-1)/2$. For more than five electrodes in one trap, the numbering in Fig. 5.2 has to be extended to the next electrodes. However, the outermost electrode always has to be grounded, in order to justify the use of Eq. (5.7).
The following discussion is restricted to an m, which corresponds to an odd number of five-electrode traps ($m = 5$ for one trap, $m = 15$ for three traps, and so on). Furthermore, identical voltage biasing of U_0 and U_c is assumed for all traps[5]. As an example, for three traps the voltages are given by $U_r = U_0 = U_5$ for the ring electrodes, $U_c = U_1 = U_4 = U_6$ for the correction electrodes, and $U_2 = U_3 = U_7 = 0$ V for the grounded endcaps. In this situation, the c_j coefficients are only a function of the trap geometry and of the ratio $T = U_c/U_0$, which is called "*tuning ratio*" in the following. Thus, the coefficients can be written as

$$c_j = e_j + \frac{U_c}{U_0} d_j = e_j + T d_j, \tag{5.13}$$

where the coefficients e_j and d_j are given by the geometry. Since $d_j = \partial c_j / \partial T$, the d_j coefficients determine the influence of the correction voltage on the c_j coefficients for a given geometry. In order to use the correction voltage for compensation of higher order terms, the tuning ratio can be chosen to be, e.g., $T|_{c_4=0} = U_c/U_0 = -e_4/d_4$. In this case, the leading anharmonic coefficient c_4 vanishes. If a geometry is found, for which both c_4 and c_6 vanish at the same tuning ratio, the trap is called "*compensated*". However, when the tuning ratio is adjusted by changing the correction voltage U_c, c_2 changes due to the influence of d_2. Consequently, the axial frequency ω_z given by Eq. (3.4a) is shifted in the compensation process. This is an unwanted effect during the course of an experiment. If a geometry is found for which d_2 vanishes, the trap is called "*orthogonal*" [163].

[4] Note that only the even orders are non-zero due to the reflection symmetry along z.
[5] The influence on the trap performance of deviations from the identical biasing is discussed later in Sec. 5.3.2.

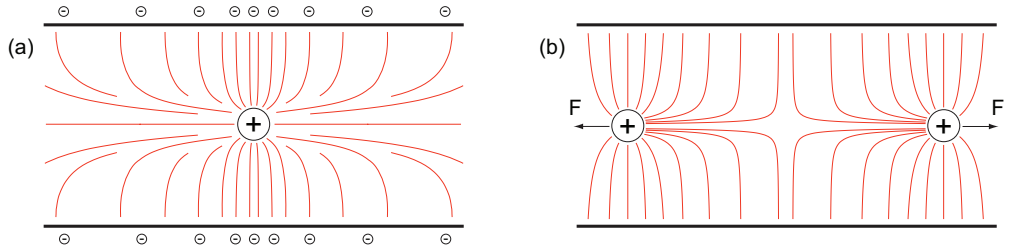

Figure 5.3: (a) Schematic of a single charge inside a conducting cylinder. In red, the electrical field lines are sketched. On the surface of the cylinder, the electrical field induces surface charges in order to fulfill the boundary conditions of the Maxwell equations. (b) Two identical charges inside a conducting cylinder. Due to the Coulomb repulsion, the ions are pushed away from each other.

5.2.2 Systematics in a Stack of Cylindrical Traps

For experiments on highly-charged ions in adjacent cylindrical Penning traps, two systematic effects have to be considered for the design of the trap tower. First, the charges induce image-charge potentials in the conducting surface of the trap electrodes, which act back on the eigenmotions of the ions. Second, two ions simultaneously stored in adjacent traps might influence each other by the Coulomb interaction.

Image-Charge Effects

A charge inside a Penning trap induces surface charges in the trap electrodes, which is sketched in Fig. 5.3a. Thus, the effective image-charge potential arising from the surface charges has to be superimposed to the applied trap potential. This effects the eigenfrequencies of the charged particles, as pointed out in [168]. In this work, a simplified spherical model is developed for hyperbolical traps, which shows that the shift in the calculation of the free cyclotron frequency by Eq. (3.7) scales with $\Delta\omega_c \propto q/a^3$, where q is the charge inside the trap and a the radius of the spherical trap approximation. Consequently, this shift might not be negligible for highly-charged ions and small traps. In [191], a general series solution for the image-charge field is given for arbitrary cylindrically symmetric Penning traps, which is explicitly applied to hyperbolical traps.
In case of cylindrical trap geometries, the electric image-charge field and the resulting effect on the eigenfrequencies of the trapped charged particles is calculated analytically from the Laplace equation in [192]. Here, the axial frequency remains unperturbed since the image-charge field is translationally invariant. The shift in the radial frequencies is given by

$$\Delta\omega_\pm \approx \mp\frac{q^2}{4\pi\epsilon_0 m a^3 \omega_c}. \tag{5.14}$$

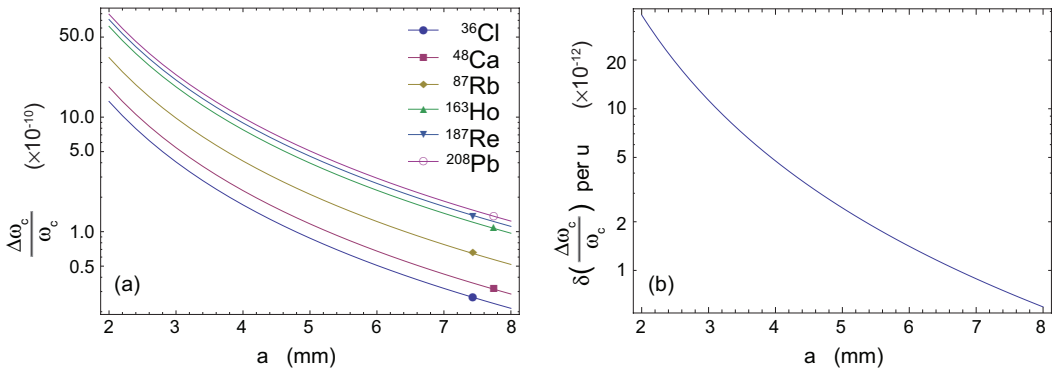

Figure 5.4: (a) Relative shift of the free cyclotron frequency ω_c as a function of the trap radius a. (b) Change of the image-charge shift per mass unit u.

With use of Eq. (3.7), the shift in the free cyclotron frequency is given by

$$\frac{\Delta\omega_c}{\omega_c} = \left(-\frac{\omega_+}{\omega_c} + \frac{\omega_-}{\omega_c}\right) \frac{q^2}{4\pi\epsilon_0 m a^3 \omega_c^2}. \tag{5.15}$$

Note that for typical experimental conditions of $\omega_+ \gg \omega_z \gg \omega_-$, the relative shift in Eq. (5.15) is independent of the charge state q of the ion. In Fig. 5.4a, the relative shift is shown as a function of the trap radius for several measurement candidates at PENTATRAP. From that point of view, a inner radius as large as possible is convenient for the trap design. At, e.g. $a = 5$ mm, the shift is still on the order of a few 10^{-10} for heavy ions like ^{208}Pb.
However, the change $\delta\,(\Delta\omega_c/\omega_c)$ of this image-charge shift per mass unit u is shown in Fig. 5.4b, which is nearly independent of the mass number A and the charge state q. At $a = 5$ mm it is already below 2.5×10^{-12}. For most measurement cases at PENTATRAP, discussed in Sec. 2.1 and Sec. 2.2, the mass difference of the involved ion pairs are well below one atomic mass unit u. Hence, this shift gets negligible in the determination of the cyclotron frequency ratio $\omega_{c,1}/\omega_{c,2}$ of the two involved ion species.

Ion-Ion Interaction

As described in Sec. 5.1, a simultaneous measurement of, at least, two ions in adjacent cylindrical Penning traps is planed in the PENTATRAP spectrometer. Hence, the Coulomb repulsion between ions and a potentially resulting frequency shift (see Fig. 5.3b for a illustration) has to be considered. In order to analyze this systematic effect, the ion-ion potential $\phi_{ii}(\vec{r}, \vec{r}')$ induced by a charge at position $\vec{r}'$ is calculated at the position $\vec{r}$ of the ion of interest.
The distance between the trap centers has to be chosen as large as possible in order to minimize this effect. In our case, the maximum distance is limited by the homogeneous region of the superconducting magnet, given by approximately 120 mm and, hence, a center-to-center distance of 24 mm for five traps (see Sec. 4.1). Comparing this distance to the typical axial amplitudes in a trap (a few μm for cooled ions) allows us to ignore all dynamical aspects for the calculation.

The potential of a point charge at $\vec{r}'$ in a conducting cylinder with length L and radius a can be found in [189]. In cylindrical coordinates $[\rho, \varphi, z]$ it is given by

$$\phi_{\mathrm{ii}}(\vec{r}, \vec{r}') = \frac{q}{\pi\epsilon_0 a} \sum_{m=-\infty}^{\infty} \sum_{n=1}^{\infty} e^{im(\varphi-\varphi')} \frac{J_m\left(x_{mn}\frac{\rho}{a}\right) J_m\left(x_{mn}\frac{\rho'}{a}\right)}{x_{mn} J_{m+1}^2(x_{mn}) \sinh\left(\frac{L}{a}\right)} \times \sinh\left(x_{mn}\frac{z_<}{a}\right) \sinh\left(x_{mn}\frac{L-z_>}{a}\right). \tag{5.16}$$

Here, x_{mn} is the n-th root of the Bessel function J_m of order m and $z_{>/<}$ are the larger or smaller values of z and z'. For the following, the ion of interest is assumed in the center of the cylinder ($z_< = L/2$) and the second one at a distance of Δz in z-direction (hence, $z_> = L/2 + \Delta z$). Furthermore, with $J_m(0) = \delta_{0,m}$ and the assumption that both ions are on the trap axis ($\rho = \rho' = 0$), the expression for the ion-ion potential reduces to

$$\phi_{\mathrm{ii}}(\vec{r}, \vec{r}') = \frac{q}{\pi\epsilon_0 a} \sum_{n=1}^{\infty} \frac{\sinh\left(x_{0n}\frac{L}{2a}\right) \sinh\left(x_{0n}\frac{L}{2a} - x_{0n}\frac{\Delta z}{a}\right)}{x_{0n} J_1^2(x_{0n}) \sinh\left(\frac{L}{a}\right)}. \tag{5.17}$$

In order to analyze the influence of two ions on each other, an expansion to a Taylor series can be used, analog to the case of the trap potential discussed in Sec. 3.3.3. At the position $\vec{r} = (0, 0, L/2)$, the expansion is given by

$$\begin{aligned} \phi_{\mathrm{ii}}(\rho, z, \rho', z') &= \sum_{l=0}^{\infty} \sum_{k=0}^{l} \frac{1}{k!(l-k)!} \cdot \left.\frac{\partial^l \phi_{\mathrm{ii}}(\rho, z, \rho', z)}{\partial\rho^k \partial z^{l-k}}\right|_{(0,0,L/2)} \cdot \rho^k \left(z - \frac{L}{2}\right)^{l-k} \\ &\equiv \sum_{l=0}^{\infty} \sum_{k=0}^{l} g_{k,l-k} \cdot \rho^k \left(z - \frac{L}{2}\right)^{l-k}. \end{aligned} \tag{5.18}$$

In contrast to the trap potential, there is no symmetry with respect to the $z = 0$ plane in this case. From the azimuthal symmetry it can be shown by inserting Eq. (5.18) into the Laplace equation, that the coefficients for odd powers of ρ have to vanish. The potential is, in general, given by

$$\begin{aligned} \phi_{\mathrm{ii}}(\rho, z, \rho', z') &= g_{0,0} + g_{1,0} \cdot \rho + g_{0,1} \cdot z + g_{2,0} \cdot \rho^2 + g_{1,1} \cdot \rho z + g_{0,2} \cdot z^2 + \dots \\ &= g_{0,0} + g_{0,1} \cdot z + g_{0,2} \cdot \left(z^2 - \frac{\rho^2}{2}\right) + \dots . \end{aligned} \tag{5.19}$$

In second order, the ion-ion potential has exactly the same shape as the ideal trap potential defined in Eq. (3.2). In other words, in second order the ion-ion potential acts as a small offset to the trapping voltage and the influence vanishes in the determination of the free cyclotron frequency by Eq. (3.7).
The remaining effect is a small repulsion induced by $g_{0,1}$, which gives a shift of the

axial equilibrium position of the ion of interest. The new potential minimum can be calculated from the superposition of the ideal trap potential and the ion-ion potential. It is given by

$$\widetilde{z}_0 = -\frac{g_{0,1}}{2(U_0 c_2 + g_{0,2})}. \tag{5.20}$$

The product $U_0 c_2$ of the ideal potential can be determined for a given axial frequency from Eq. (3.4a) for every charge-to-mass ratio q/m of the ion of interest. Certainly, the largest shift is expected for a shallow trapping potential, corresponding to a large q/m-ratio of the trapped ion.
The coefficients of the ion-ion potential, defined in Eq. (5.19), can be determined by Eq. (5.17) as a function of the distance of the two ions and of the radius of the trap. Compared to free space, the Coulomb repulsion will be more and more suppressed with a decreasing radius a, due to the shielding by the surrounding electrodes. At a maximum distance of $\Delta z = 24$ mm between the two ions, it turns out that even at a large trap radius of $a = 5$ mm, the shift of the equilibrium position of the ion of interest is negligible for all experimental situations. At the extreme case of a proton as the ion of interest and a charge of $q = 81+$ in the adjacent trap, the shift $\widetilde{z}_0$ is on the order of pm and, thus, ion-ion interactions can be neglected for the design of our trap tower.

5.3 Design of the Trap Tower

In Sec. 5.2.1, an analytical expression of the potential inside a cylindrical Penning trap was presented, providing the main tool for the design of the PENTATRAP tower. In the design process, the boundary conditions for the geometry found from image-charge and Coulomb interaction in Sec. 5.2.2 are taken into account.

5.3.1 Finding the Best Electrode Geometry

In addition to finding an orthogonal trap with $d_2 = 0$, we are seeking for a geometry where the leading anharmonic contributions are as low as possible. The geometry should allow for a simultaneous compensation of c_4 and c_6. In other words, the difference in the tuning ratios $\Delta_T \equiv T|_{c_6=0} - T|_{c_4=0}$ has to vanish. So far, the geometry is limited to the three conditions

$$c_4(a, l_{\mathrm{gap}}, l_{\mathrm{r}}, l_{\mathrm{c}}, l_{\mathrm{e}}, T) = 0, \tag{5.21a}$$
$$c_6(a, l_{\mathrm{gap}}, l_{\mathrm{r}}, l_{\mathrm{c}}, l_{\mathrm{e}}, T) = 0, \tag{5.21b}$$
$$d_2(a, l_{\mathrm{gap}}, l_{\mathrm{r}}, l_{\mathrm{c}}, l_{\mathrm{e}}) = 0, \tag{5.21c}$$

which can be calculated from Eq. (5.12) and Eq. (5.13), and the six parameters are left to choose. Further boundary conditions for the geometry arise from mechanical reasons and the discussion in the previous section. The length of the gaps between the electrodes has to be kept as small as possible and is set to $l_{\mathrm{gap}} = 0.15$ mm for reasons

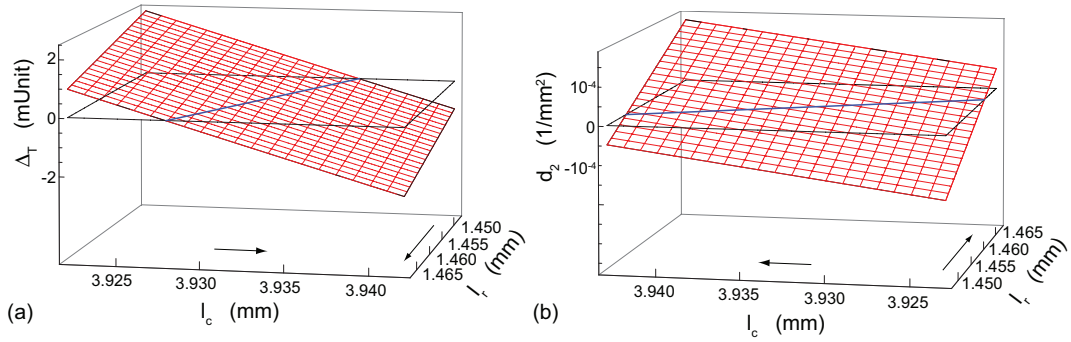

Figure 5.5: (a) Difference in the tuning ratio $\Delta_T = T|_{c_6=0} - T|_{c_4=0}$ as a function of the length of the ring electrode l_r and the correction electrode l_c. (b) d_2 coefficient as a function of l_r and l_c.

of machining precision. As mentioned before, the homogeneous region of our magnet is ~ 120 mm. In order to minimize the influence between two adjacent traps, the length of a single trap is set to a maximum of $l_\mathrm{trap} = l_\mathrm{e} + 2l_\mathrm{c} + 2l_\mathrm{e} + 4l_\mathrm{gap} = 24$ mm. Thus, there are only two free parameters left for the length scales in z-direction. From the discussion of the image-charge shift in Sec. 5.2.2, the radius a has to be chosen as large as possible. However, for the fixed length of the trap, it turns out that the conditions of Eq. (5.21) cannot be fulfilled simultaneously for $a \geq 5.8$ mm. On the other hand, for $a \gtrsim 5$ mm the relative image-charge shift changes much less than for lower radii, due to the scaling with $1/a^3$ (see Fig. 5.4). For those reasons, the radius is set to $a = 5$ mm, and the three parameters l_r, l_c and T are left to be fixed.
For the calculation of the coefficients by Eq. (5.12), only three adjacent traps are used, since the required order n strongly increases with the total length used for the calculation. This is justified, since the result in the central trap is not affected by adding another electrode on the outside and, thus, more electrodes are not needed for the calculation. In the total trap tower, the situation of two neighboring traps is common to the three inner traps, for which the following results are valid. Certainly, the performance in the outer traps will differ slightly from the inner traps due to different surrounding conditions. However, this is of no concern, since no high-precision measurements will be performed in those traps (see Sec. 5.1). Furthermore, identical ring and correction voltages are assumed for all three traps during the course of the design process. In future experiments, the trapping voltages are adjusted to the q/m-ratio of the ion in each trap and deviations can occur between adjacent traps. Such deviations will influence the performance in the neighboring traps. However, since most measurement candidates at PENTATRAP are mass doublets, the voltage biasing will be very similar (see Sec. 5.3.2 for more details).
With the parameters defined above, the results for Δ_T and d_2 as a function of l_r and l_c are shown in Fig. 5.5. The difference in the tuning ratio is given in 1×10^{-3}, denoted by mUnit. The red grid shows a variation of l_r and l_c by 1 μm, to which the geometrical lengths have to be specified for machining[6].

[6] In our case, geometrical lengths can be specified to 1 μm for machining. After coating the electrodes

Table 5.1: Geometric parameters and electrostatic coefficients of the PENTATRAP tower. All length scales are given in mm. For this geometry, the electrostatic parameters c_2 and d_2 as well as the dimensionless tuning ratio $T|_{c_4=0}$ and Δ_T are calculated. In the final trap tower, the geometry of all five traps is chosen identical with the values given here, adding up to the total length of $l_{\text{total}} = 120.6$ mm.

a	l_{gap}	l_{r}	l_{c}	l_{e}	c_2 (1/mm^2)	d_2 (1/mm^2)	$T\|_{c_4=0}$	Δ_T
5	0.15	1.457	3.932	7.040	$-1.496 \cdot 10^{-2}$	$-2.529 \cdot 10^{-6}$	0.881032	$22.9 \cdot 10^{-6}$

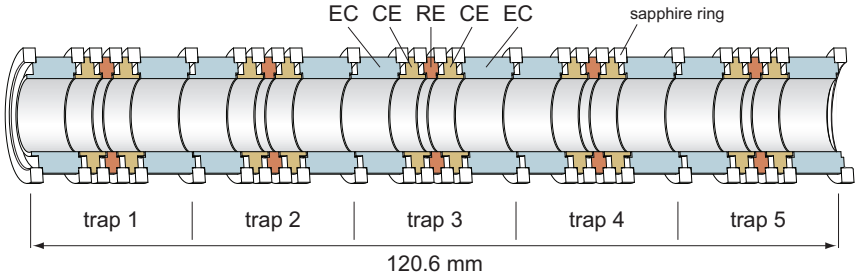

Figure 5.6: Sectional drawing of the PENTATRAP tower. The color-coded electrodes are labeled with RE for the ring electrodes, CE for the correction electrodes and EC for the endcaps. All five traps are identical in geometry. The inner length scales are given in Tab. 5.1.

In order to minimize both Δ_T and d_2 at the precision of 1 μm, the best values of $l_{\text{r}} = 1.457$ mm and $l_{\text{c}} = 3.932$ mm are found, resulting in $d_2 = -2.5 \times 10^{-6}/\text{mm}^2$ and $\Delta_T = 22.9 \times 10^{-6}$. Moreover, the coefficient c_2 can be calculated, which is given by $c_2 = -1.496 \times 10^{-2}/\text{mm}^2$ at $T|_{c_4=0}$. All parameters are summarized in Tab. 5.1 and a sectional drawing of the deduced trap tower is shown in Fig. 5.6, where the length scales refer to the inner surface of the electrodes, which determes the electrostatic performance. The final choice of materials and the mechanical structure is described in detail in the Ph.D. thesis of J. Repp [172]. In Fig. C.2, a photograph of the assembled trap tower is shown.

5.3.2 Performance

In the following section, the resulting electrostatic performance of the trap tower is estimated, where, in addition to the values calculated above, geometrical deviations arising from imperfections in the machining process are taken into account.

Inclusion of Mechanical Tolerances

Due to tolerances in the machining process, the precision of 1 μm in the length scales is not guaranteed [172]. The total deviations are expected to be on the order of ± 5 μm around the ideal values. In order to get accurate estimates for the performance of the

with a gold layer on the surfaces, the final precision is expected to be below ± 5 μm. For details of the mechanical fabrication see [172].

Table 5.2: Leading order electrostatic coefficients of the PENTATRAP tower with errors resulting from the finite machining precision. The c_j coefficients are calculated at the tuning ratio $T = T|_{c_4=0} = 0.881032$ of the ideal geometry. All coefficients are given in $1/\text{mm}^j$.

j	c_j	d_j
2	$-1.496(0.007) \times 10^{-2}$	$-0.025(1.241) \times 10^{-4}$
4	$0.000(4.199) \times 10^{-6}$	$8.406(0.001) \times 10^{-4}$
6	$-0.008(1.892) \times 10^{-7}$	$3.579(0.019) \times 10^{-5}$

spectrometer, the mechanical tolerances are taken into account by error propagation in the calculation of the electrostatic coefficients. The results are listed in Tab. 5.2, where $T = T|_{c_4=0} = 0.881032$ of the ideal geometry is used for the calculation. It is found that the dominant error results from the uncertainty of the gap length l_{gap}. This uncertainty translates to an error contribution ten times larger than from any other length-scale tolerance.

Ring Voltage: c_2

Taking c_2 from Tab. 5.2, the ring voltage U_0 required to provide an axial frequency ν_z can be calculated for every charge-to-mass ratio by Eq. (3.4a). The result is plotted in Fig. 5.7. For reference, a black line at -14 V is shown. It corresponds to the maximum voltage supplied by the currently available source UM 1-14. The limited voltage reduces the available q/m-region, in which a sufficient axial trap frequency can be provided. In order to make lower q/m-ratios available for our measurements, a new source (StaReP) with a voltage range down to -100 V is currently in development (see Sec. 4.3 and the Ph.D. thesis of Ch. Böhm [173] for details).

Orthogonality: d_2

As a measure of the "*orthogonality*" of the trap geometry, the ratio d_2/c_2 can be taken, which is $0.17(8.29) \times 10^{-3}$ according to Tab. 5.2. The dependence of the axial frequency on the tuning ratio can be calculated from Eq. (3.4a) and Eq. (5.13). It is given by

$$\frac{\Delta\nu_z}{\Delta T} = \frac{1}{2}\frac{d_2}{c_2}\nu_z \approx 0.051(2.490)\ \frac{\text{Hz}}{\text{mUnit}}\ , \tag{5.22}$$

at $\nu_z = 600$ kHz. In Fig. 5.8a, the axial frequency shift is shown as a function of the tuning ratio for the ideal geometry (blue line), and for the worst case resulting from the limited machining precision (red line).
The narrow-band detection technique implemented in the PENTATRAP experiment raises some concerns about the orthogonality. The ion signal is only visible in the bandwidth of, typically, 10 to 100 Hz (see Sec. 6.3), and it is very undesirable if the axial frequency is shifted out of this range while tuning out anharmonicities. The accuracy in setting the tuning ratio is determined by the resolution δU of the voltage

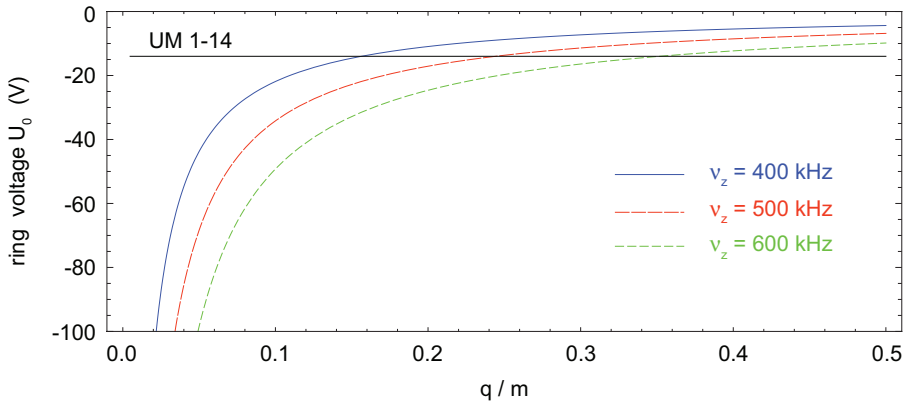

Figure 5.7: Ring voltage required for a given axial frequency ν_z and charge-to-mass ratio q/m. The black line indicates the -14 V provided by the voltage source UM 1-14.

source providing U_0 and U_c. The resolution of the tuning ratio is given by

$$\delta T \approx \frac{\delta U}{U}\sqrt{T^2+1}. \tag{5.23}$$

With $\delta U \sim 10\ \mu$V, the tuning ratio can be set to a precision of 10^{-5} and better. However, in order to quickly find the best tuning ratio, a step size of about one mUnit is typically used first for a course scan around the best T [193]. With the value given in Eq. (5.22), the ion's axial frequency can always be kept visible in the tuning process, even at the large step size of one mUnit.
Another issue concerns the temporal stability of the trapping voltages and the resulting axial resolution (see Sec. 3.3.5). By inserting Eq. (5.13) in Eq. (3.4a), the axial resolution can be written as

$$\frac{\delta\nu_z}{\nu_z} = \frac{1}{2}\sqrt{\left(\frac{e_2}{c_2}\frac{\delta U_0}{U_0}\right)^2 + \left(T\frac{d_2}{c_2}\frac{\delta U_c}{U_c}\right)^2}. \tag{5.24}$$

Consequently, the stability requirements $\delta U_c/U_c$ for the correction voltages are relaxed by, at least, two orders of magnitude compared to the stability needed for the ring voltage.

Compensation: c_4 and c_6

In Fig. 5.8, the leading order anharmonic coefficients c_4 and c_6 in the ideal trap are shown as a function of the tuning ratio. Resulting from the optimized design, both coefficients can be tuned to zero almost simultaneously due to the very low Δ_T. For the ideal geometry, the residual amplitude-dependent[7] anharmonic shift of the axial frequency can be calculated from Eq. (3.23). At $\nu_z = 600$ kHz, it is given by $\partial^2\nu_z/(\partial T\,\partial E_z) \approx 20$ to 1.8 mHz/(mUnit·meV) for masses of 20 to 200 u, respectively.

[7] The amplitude dependence can be translated to an energy dependence by Eq. (3.10).

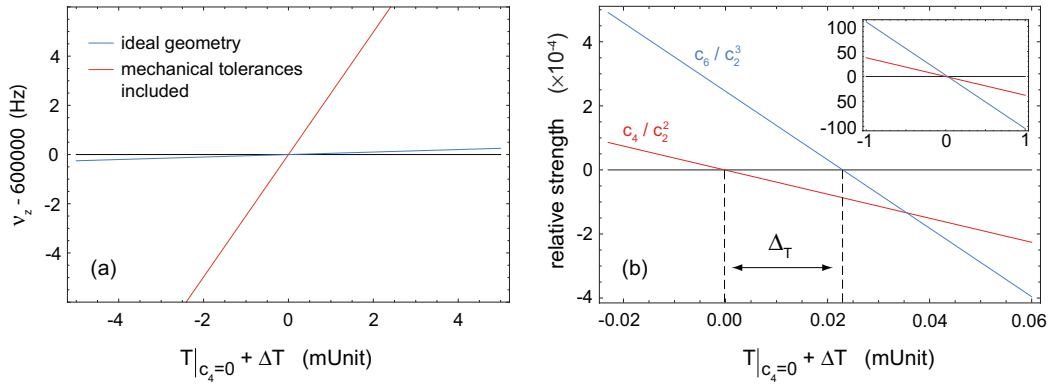

Figure 5.8: (a) Axial frequency as a function of the tuning ratio T due to the influence of d_2. In blue, the shift is shown for the ideal geometry while the red line indicates the worst case resulting from limited machining precision. The center is chosen to $T|_{c_4=0} = 0.881032$. (b) Leading anharmonic coefficients c_4 (red) and c_6 (blue) of the ideal geometry as a function of the tuning ratio, given in the relative strength to c_2.

Here, the inclusion of the machining errors is more subtle than for d_2. In Tab. 5.2, the values for the anharmonic c_j coefficients and their errors are calculated for the tuning ratio $T|_{c_4=0} = 0.881032$, for which the c_4 coefficient vanishes in the ideal trap geometry. However, the tuning ratio itself is a function of the real geometry. It is always possible to find a new value for T, for which the c_4 coefficient vanishes in a geometry deviating from the ideal one. At this new tuning ratio, c_6 will be far below the range given by the error in Tab. 5.2 and close to the value of the ideal trap.
Nevertheless, for the following it is assumed that c_4 is tuned to zero and, as a worst case, the residual anharmonic contribution is given by the range in Tab. 5.2 to $c_6 = \pm 1.892 \times 10^{-7}$ 1/mm^6. At low energies (~ 4 K), the axial frequency shift is on the order of a few μHz/meV for light masses around 20 u and even less for heavy ions. Thus, for the cryogenic dip-detection of the axial frequency at PENTATRAP (see Chap. 6), anharmonic shifts are completely negligible.
However, limits may arise at the measurement of the modified cyclotron frequency ν_+, where the pulse and amplify (PnA) method [194] is planned to be used at PENTATRAP (see also Sec. 6.1.2). There, the cyclotron phase is defined by a dipolar excitation pulse. After a certain waiting time, the cyclotron phase is transferred to the axial mode by a sideband coupling pulse, where it is read out. The phase divided by the waiting time reveals the cyclotron frequency. In order to improve the signal-to-noise ratio for the read out of the phase[8], the axial amplitude is boosted by the coupling pulse. At the high amplitudes, general limits in the phase resolution arise from the anharmonic terms given by c_6.
In [30, 124], ν_+ is measured to a relative accuracy of 3.3×10^{-10} with this method. There, a simulated value of $c_6 \approx 7 \times 10^{-6}$ 1/mm^2 is given. However, the final accuracy was dominated by the finite cyclotron temperature and magnetic-field fluctuations, which limits the available measurement time and, thus, the phase resolution in presence

[8] The relative accuracy of ν_+ scales linearly with the phase resolution.

of noise jitter. The effect of c_6 will only be visible with a significant improvement of the other systematics.
At PENTATRAP, many efforts are spent in order to decrease the limitations mentioned above and, hence, improve the accuracy of the measurement of the modified cyclotron frequency. For example, the cyclotron mode will be directly cooled by a cryogenic resonator (see Sec. 6.6 and Sec. 6.6.1), and the magnetic-field fluctuations are suppressed by the stabilization system of the magnet (see Sec. 4.1). However, the worst case value of c_6 estimated for our traps is smaller by a factor of approximately ~ 36, compared to the value given in [124]. Thus, anharmonic limitations are expected only at a much higher resolution of the cyclotron frequency.

Simultaneous Measurements in Adjacent Traps

In Sec. 5.3.1, the discussion of the trap tower is based on the assumption, that identical voltages are applied to the adjacent traps. However, if the traps are loaded with ions of different charge-to-mass ratio q/m and the measurements are performed at the same axial frequencies, a difference in the ring voltages ($\Delta U = U_{0,2} - U_{0,1}$) is resulting from Eq. (3.4a). Certainly, such differences will affect the electrostatic performance of the traps due to the large openings and the close distance to each other. While d_2 is only a measure of the geometry, the only difference to identical conditions will occur in the anharmonic coefficients and, since c_4 can always be tuned to zero, only in c_6.
The difference ΔU increases for an increasing difference in the q/m-ratios and for a decreasing mean value of q/m. Furthermore, anharmonic effects are most severe at low masses with comparatively high amplitudes. In that sense, the worst case for measurements at PENTATRAP might be light nuclides for direct tests of $E = mc^2$ (see Sec. 2.2.3), where the two nuclides compared to each other differ by one atomic mass unit. An example is the measurement of the mass ratio of $^{37}\mathrm{Cl}/\,^{36}\mathrm{Cl}$. With an extreme charge state of 17+, the q/m-ratio is approximately 0.47 with a difference of $\Delta(q/m) \approx 3$ %. With these numbers, a voltage difference of $\Delta U \approx 0.3$ V results, if the ions are measured at $\nu_z = 600$ kHz. However, at this voltage difference the c_6 coefficient is only changed by ~ 8 % compared to identical conditions. Following from the discussion in the previous paragraph, this will present no limitation for our measurements.

6 Detection System

Besides the trapping setup itself, a high-quality detection system is crucial for mass measurements in a Penning trap, from which all information about the stored ions have to be retrieved. In this chapter, the setup and characterization of the cryogenic detection system of PENTATRAP is described.

6.1 Non-Destructive Ion Detection and Cooling

At PENTATRAP, a non-destructive detection method will be applied, where the ion's eigenfrequencies are measured while the ion is oscillating. In a cryogenic environment, this method offers a single-ion sensitivity and, at the same time, the ion's motions are cooled to low amplitudes, where both issues are crucial prerequisites for highly precise and accurate measurements.

6.1.1 Basic Principle

For an overview, the main components of a cryogenic detection system, a high-quality inductance and a cryogenic amplifier, are introduced schematically in Fig. 6.1, where the basic function is discussed below.

Image Current, Tank Circuit and Peak Detection

The basic model of image-current detection is shown in Fig. 6.2a. The charged particle oscillates between the plates of an infinitely extended capacitor, inducing image currents in an externally attached impedance given by [195, 196]

$$I_{\mathrm{ion}}(t) = \frac{q}{D_i}\dot{\rho}_i(t) = 2\pi\nu_i\frac{q}{D_i}\rho_i(t), \qquad \text{with} \quad i = +, z, -. \tag{6.1}$$

Here, ν_i and ρ_i are the frequency and amplitude of the detected eigenmotion, respectively, and D_i corresponds to the distance of the capacitor plates. It is shown in Sec. 6.1.4 that the model parameter D_i can be transformed into an effective electrode distance for real cylindrical traps.
Typically, the external impedance is realized by a coil with inductance L. Together with the total parallel circuit capacitance C_{total}, consisting of the trap capacitance and parasitic self-capacitance of the coil and the wiring, the inductance forms a parallel

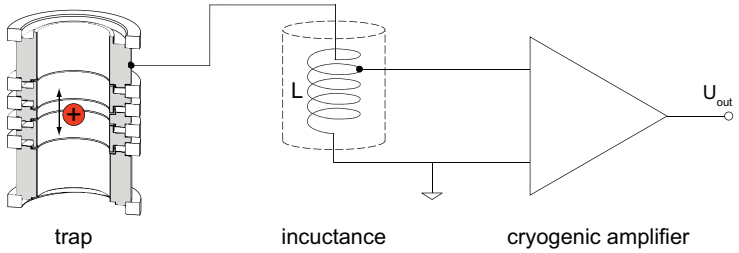

Figure 6.1: Main components of a cryogenic image-current detector, which consists of a high-quality inductance, connected to the trap electrodes and a cryogenic amplifier.

tuned circuit with resonance frequency

$$\nu_{\mathrm{LC}} = \frac{1}{2\pi\sqrt{LC_{\mathrm{total}}}}. \tag{6.2}$$

Resistive contributions in the resonator are taken into account by an effective resistance [197]

$$R_{\mathrm{p}} = 2\pi\nu_{\mathrm{LC}} LQ, \tag{6.3}$$

in parallel to the LC circuit, where Q is the "*quality factor*", which is defined by the ratio of the stored electromagnetic energy to the energy loss per cycle. It is experimentally accessible by measuring

$$Q = \frac{\nu_{\mathrm{LC}}}{\Delta\nu}, \tag{6.4}$$

where $\Delta\nu$ is given by the -3 dB width of the line shape. In total, the impedance of this tuned circuit is given by

$$Z_{\mathrm{LC}}(\nu) = \frac{1}{\frac{1}{R_{\mathrm{p}}} + \mathrm{i}\left(2\pi\nu C_{\mathrm{total}} - \frac{1}{2\pi\nu L}\right)}. \tag{6.5}$$

On resonance at ν_{LC}, the imaginary part cancels and the tuned circuit acts as a real effective resistance R_{p}. Tuned into resonance with the detection system, the ion current produces a voltage drop over the real part of the total impedance Z_{LC}, given by

$$U_{\mathrm{p}}(t) = \mathrm{Re}(Z_{\mathrm{LC}}) I_{\mathrm{ion}}(t) = R_{\mathrm{p}} I_{\mathrm{ion}}(t) = 2\pi\nu_{\mathrm{LC}} LQ I_{\mathrm{ion}}(t). \tag{6.6}$$

This voltage drop is amplified by the cryogenic amplifier and analyzed at room temperature. A simulation of such a noise spectrum is shown in Fig. 6.2b, where the ion signal appears as a peak on top of the root mean square (rms) voltage of the tuned circuit's thermal noise, given by [198, 199]

$$u_{\mathrm{th}} = \sqrt{4k_{\mathrm{B}} T\,\mathrm{Re}(Z_{\mathrm{LC}})}. \tag{6.7}$$

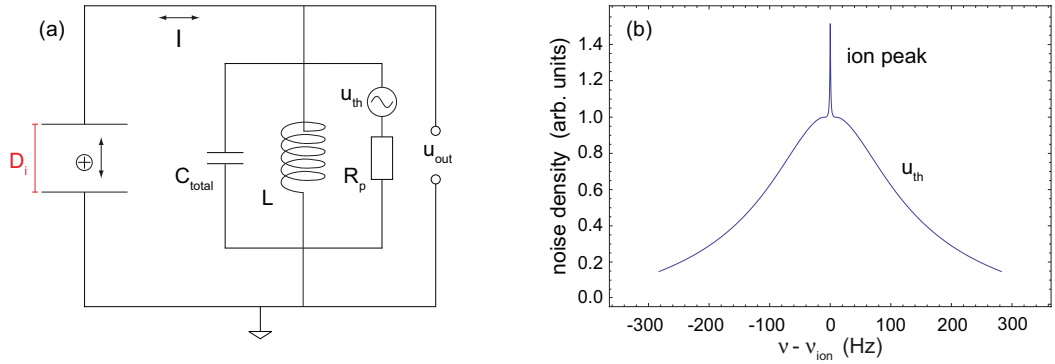

Figure 6.2: (a) Illustration of the basic principle of the image-current detection method. (b) Peak spectrum resulting from the voltage drop over the tuned circuit, caused by the image-current. For the spectrum, $\nu_z = \nu_{\mathrm{LC}}$ was chosen.

Here, k_{B} is the Boltzmann constant and T is the temperature of the tuned circuit. In Eq. (6.7), u_{th} is normalized to a unit detection bandwidth and, thus, also called noise density in the following.

Resistive Cooling

Due to the current flowing through the impedance Z_{LC}, the power

$$P = \mathrm{Re}(Z_{\mathrm{LC}}) \cdot I_{\mathrm{ion}}^2 = \dot{E} \tag{6.8}$$

is dissipated, which results in an energy loss of the ion. This corresponds to a damping force[1] $F_{\mathrm{damp}} = -m\gamma_z \dot{z}$, which arises from a voltage drop over the trap electrodes (due to the induced voltage drop over the impedance). Thus, the force is given by

$$F_{\mathrm{damp}} = \frac{q}{D_z} U_{\mathrm{damp}} = \frac{q}{D_z} \mathrm{Re}(Z_{\mathrm{LC}}) I_{\mathrm{ion}} = -m\gamma_z \dot{z}. \tag{6.9}$$

Using Eq. (6.1), the damping constant can be related to the particle and detector properties, which writes to

$$\gamma_z = \frac{\mathrm{Re}(Z_{\mathrm{LC}})}{m} \frac{q^2}{D_z^2} \quad \leftrightarrow \quad \tau_z = \frac{m}{\mathrm{Re}(Z_{\mathrm{LC}})} \frac{D_z^2}{q^2}. \tag{6.10}$$

Here, τ_z denotes the time constant of the exponential cooling of an initially hot ion to the thermal equilibrium with the detector.

Thermal Equilibrium, Equivalent Ion Model and Dip Spectra

When the ion is in thermal equilibrium with the detector, the line shape of the ion signal fundamentally changes. For an analytic description, models of the ion motion

[1] For simplicity, the following relations are only given for the axial motion. The principle can be directly applied to the other eigenmotions as well.

are given in [196, 200]. The equation of motion of the ion in thermal contact with the detector is given by

$$\ddot{z} + \gamma_z \dot{z} + \omega_z^2 z = \frac{f(t)}{m}, \tag{6.11}$$

where the driving force $f(t) = qU_{\mathrm{ext}}(t)/D_z$ arises from the incoherent thermal noise voltage of the detector, dropping across the trap electrodes[2]. Using Eq. (6.1), Eq. (6.11) can be written as

$$U_{\mathrm{ext}}(t) = m\frac{D_z^2}{q^2}\dot{I}_{\mathrm{ion}} + m(2\pi\nu_z)^2\frac{D_z^2}{q^2}\int I_{\mathrm{ion}}dt + \mathrm{Re}(Z_{\mathrm{LC}})I_{\mathrm{ion}}. \tag{6.12}$$

This equation corresponds to a damped series LC circuit, with an inductance and capacitance given by

$$l_{\mathrm{ion}} = m\frac{D_z^2}{q^2} \quad \text{and} \quad c_{\mathrm{ion}} = \frac{1}{m(2\pi\nu_z)^2}\frac{q^2}{D_z^2}. \tag{6.13}$$

Thus, the ion's motion can be described by an effective series circuit, characterized by a vanishing voltage drop at its resonance frequency $\nu_{\mathrm{ion}} = 1/(2\pi\sqrt{l_{\mathrm{ion}}c_{\mathrm{ion}}}) = \nu_z$. In Fig. 6.3a, the effective ion circuit is shown in parallel to the detector.
The interpretation of the ion's motion as an effective series circuit can be justified as follows. Without the resonator and in an ideal trap, the ion is an intrinsically undamped oscillator. Thus, at the ion's oscillation frequency it acts as a perfect conductor, which shorts the externally applied voltages. The analytical description of the line shape can be derived from the calculation of the total impedance

$$\begin{aligned} Z_{\mathrm{total}}^{-1} &= Z_{\mathrm{ion}}^{-1} + Z_{\mathrm{LC}}^{-1} \\ &= \frac{1}{R} + \mathrm{i}\left(2\pi\nu C_{\mathrm{total}} - \frac{1}{2\pi\nu L} - \frac{1}{2\pi\nu l_{\mathrm{ion}} - (2\pi\nu c_{\mathrm{ion}})^{-1}}\right), \end{aligned} \tag{6.14}$$

from which the total thermal noise density

$$u_{\mathrm{th}} = \sqrt{4k_{\mathrm{B}}T\,\mathrm{Re}(Z_{\mathrm{total}})} \tag{6.15}$$

arises. In Fig. 6.3b noise spectra are shown, where a dip structure occurs at the ion's frequency. If the ion's frequency is detuned from the resonance frequency of the tank circuit, the spectrum shows a dispersive character (red and green line). The full width at half maximum of the dip can be calculated from the damping of the tuned circuit, which results in [196]

$$\Delta\nu_z = \frac{1}{2\pi}\frac{1}{\tau_z} = \frac{1}{2\pi}\frac{R_{\mathrm{p}}}{m}\frac{q^2}{D_z^2}. \tag{6.16}$$

In the following, this quantity is referred to as the *dip width* of a single particle.

[2] For hot ions, this contribution can be neglected.

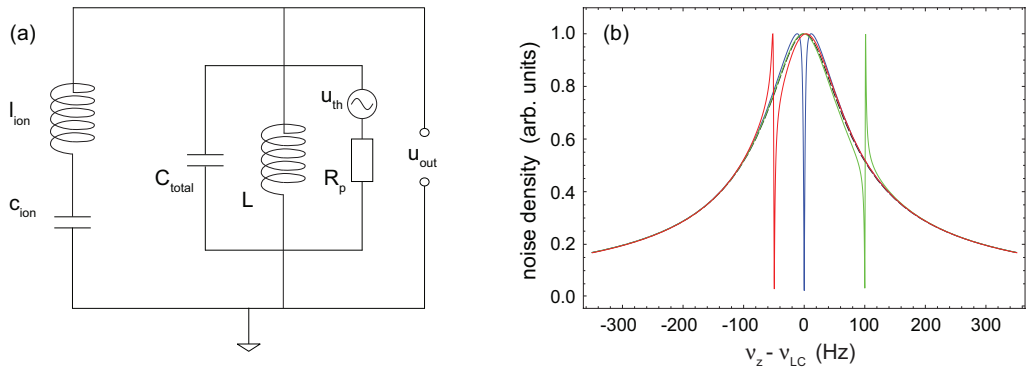

Figure 6.3: (a) Electronic equivalent of the ion's motion. (b) Theoretical dip spectra in the noise resonance of the tuned circuit. For the blue line, the resonance frequency of the tuned circuit coincides with the ion's frequency, while the frequencies are detuned by −50 Hz and 100 Hz for the red and green line, respectively.

6.1.2 Indirect Detection Methods

For the mass-ratio measurements at PENTATRAP, only the axial frequency will be directly detected with a dedicated resonator. The radial modes will be indirectly detected by a coupling to the axial mode, where the basic principles are described in the following.

Multi-Dip Method

In the presence of a quadrupolar radio-frequency drive, the action is transferred between the respectively coupled modes (see Sec. B). Due to the resulting amplitude modulation, the eigenfrequencies of the coupled modes split into two new eigenfrequencies. For the coupling of the axial and the magnetron mode, the new eigenfrequencies are given by [201, 202]

$$\nu_{\mathrm{l,r}} = \nu_z + \epsilon_{\mathrm{l,r}} \quad \text{with} \quad \epsilon_{\mathrm{l,r}} = -\frac{1}{2}\left(\delta \pm \sqrt{\Omega_0^2 + \delta^2}\right), \tag{6.17}$$

where Ω_0 is the Rabi frequency mainly defined by the drive amplitude and $\delta = (\nu_z + \nu_-) - \nu_{\mathrm{rf}}$ is the detuning between the sideband frequency and the excitation frequency ν_{rf}. Consequently, in the noise spectrum of an axial resonator, a *double-dip* structure appears, and the following relation of the frequencies is obtained from Eq. (6.17):

$$\nu_{\mathrm{l}} + \nu_{\mathrm{r}} = \nu_z + \nu_{\mathrm{rf}} - \nu_-. \tag{6.18}$$

Hence, with the measurement of ν_{l} and ν_{r} at a given irradiation frequency ν_{rf} and an independent determination of ν_z, the magnetron frequency can be determined.
With more advanced excitation schemes, a triple-dip [202] or even a quintuple-dip [203] structure can be achieved, offering a simultaneous determination of ν_z and ν_- or even

of all three eigenfrequencies within a single measurement, respectively. At PENTATRAP, the magnetron frequency is planned to be measured with the double or triple-dip method.

Phase Sensitive Methods: PnP and PnA

The pulse and phase (PnP) method was introduced in [20]. There, the cyclotron mode is brought to a defined amplitude and phase by a dipolar excitation at ν_+. After a certain waiting time, a so-called π pulse at the lower sideband $\nu_+ - \nu_z$ transfers the cyclotron action and phase to the axial mode [201], where the cyclotron phase can be read out. The phase divided by the waiting time reveals the cyclotron frequency. However, due to the exchange of action, the cyclotron energy during the waiting time also defines the axial amplitude after the exchange and it has to be chosen large enough to overcome the noise of the axial detector.
At PENTATRAP, the so-called pulse and amplify (PnA) method, recently developed by S. Sturm [194], is planned to be used for the detection of ν_+. The basic idea of this method is very similar to PnP, the frequency is determined dividing the measured phase by the waiting time. Compared to the PnP method, a minor modification of the coupling scheme leads to a tremendous improvement of precision in the PnA method. The cyclotron phase information is transferred to the axial mode by a pulse at the upper sideband $\nu_+ + \nu_z$. Such a drive conserves the phase of the modified cyclotron motion, and boosts at the same time the axial amplitude. Thus, the cyclotron amplitude during the free phase evolution (waiting time) is independent of the axial amplitude which is required for detection. The mode amplitude during the free phase evolution can be chosen "arbitrarily" small, without a loss of phase resolution. Thus, compared to the PnP method, energy dependent systematic shifts of the modified cyclotron frequency are reduced, which improves the experimental precision.

6.1.3 Cryogenic Amplification and Signal-to-Noise Ratio

As discussed in Sec. 6.1.1, the ion signal is a voltage drop over an externally connected tuned circuit (also called resonator in the following). The signal strength mainly depends on the parallel resistance R_p. For further signal processing, the voltage is picked up by a cryogenic amplifier, which is connected to the tuned circuit (see Fig. 6.1).
In order to realize a highly sensitive detection system, the figure of merit is the signal-to-noise ratio (SNR). The higher the SNR, the faster measurements can be performed and effects of temporal fluctuations of the trapping conditions are reduced. Several parameters have to be taken into account, such as the amplifier noise and the reduction of R_p by the amplifier input. For an analysis, a detailed model of the amplifier connected to the tuned circuit is shown in Fig. 6.4, where the basic principle can also be found in [204][3].
According to Eq. (6.1), the oscillating ion is modeled as a current source I_ion in parallel to the trap capacitance C_trap and the resonator, which is characterized by C_p, L

[3] In this work, the input resistance of the amplifier input was approximated as infinite.

and R_p. The amplifier is modeled with an input resistance R_in and capacitance C_in, and its noise is taken into account by an effective voltage source e_n and a current source i_n. The ion signal from the tuned circuit is coupled to the amplifier by a capacitance C_c and a tap at the coil's wire. Effectively, this forms an auto transformer with $N_1 + N_2$ primary and N_2 secondary turns. Thus, a total coupling constant κ can be defined to

$$\kappa = \frac{N_2}{N_1 + N_2} \frac{C_\mathrm{c}}{C_\mathrm{c} + C_\mathrm{in}}. \tag{6.19}$$

For the following discussion, the basic relations of this coupled system have to be identified. From the resonator's point of view, the input resistance of the amplifier appears as

$$\widetilde{R}_\mathrm{in} = \frac{R_\mathrm{in}}{\kappa^2}. \tag{6.20}$$

Thus, the parallel resistance of the coupled system is given by

$$R_\mathrm{sys} = R_\mathrm{p} || \widetilde{R}_\mathrm{in} = R_\mathrm{p} \frac{1}{1 + \kappa^2 \frac{R_\mathrm{p}}{R_\mathrm{in}}}. \tag{6.21}$$

Moreover, voltages dropping across the left hand side (resonator) appear at the right hand side (amplifier's input) as $U_\mathrm{left} = \kappa U_\mathrm{right}$, while currents are transformed by $I_\mathrm{left} = I_\mathrm{right}/\kappa$. Both relations are valid for the opposite direction.

The SNR at the amplifier's input can be calculated as follows: For the dip detection, the signal is given by the noise resonance of the total system resistance $u_\mathrm{th}(R_\mathrm{sys})$. Additionally, the current noise of the amplifier flows to the resonator, giving an additional voltage drop over R_sys. The noise floor is given by the voltage noise of the amplifier. Thus, the SNR can be written as[4]

$$\mathrm{SNR}_\mathrm{dip} = \sqrt{\frac{\kappa^2 4 k_\mathrm{B} T R_\mathrm{sys} + \kappa^4 R_\mathrm{sys}^2 i_\mathrm{n}^2}{e_\mathrm{n}^2}}. \tag{6.22}$$

In case of the dip detection, the SNR increases monotonously with κ. However, the coupling also changes, e.g., the dip width due to the modification of R_sys. The choice of κ at our detection system is given in Sec. 6.3.4.
For the peak detection, the voltage drop of the ion's current over R_sys defines the signal strength, and the noise floor is given by $u_\mathrm{th}(R_\mathrm{sys})$ of the coupled parallel resistance, i_n exciting the resonator, and e_n at the input of the amplifier. Thus, the SNR writes to

$$\mathrm{SNR}_\mathrm{peak} = \sqrt{\frac{\kappa^2 R_\mathrm{sys}^2 I_\mathrm{ion}^2}{\kappa^2 4 k_\mathrm{B} T R_\mathrm{sys} + \kappa^4 R_\mathrm{sys}^2 i_\mathrm{n}^2 + e_\mathrm{n}^2}}. \tag{6.23}$$

[4]Here and for the following expressions, a unit detection bandwidth is assumed.

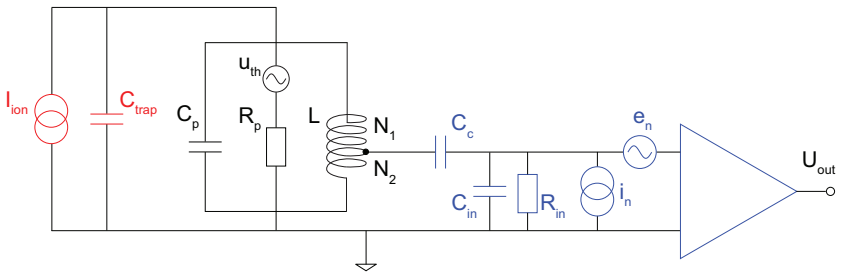

Figure 6.4: Detailed model of the cryogenic detection system. The stored ion is represented by a current source I_{ion} in parallel to the trap capacitance C_{trap} and the resonator (C_{p}, L and R_{p}). The amplifier input is modeled with a resistance R_{in} and capacitance C_{in}. Its noise is represented by an effective voltage source e_{n} and current source i_{n} at the input. The ion signal is coupled to the amplifier by C_{c} and a tap at the coil's wire, forming a transformer with $N_1 + N_2$ primary and N_2 secondary turns.

For the peak detection, an optimum in κ can be found as the tradeoff between the signal strength at the amplifier's input and current noise exciting the resonator. It is given by

$$\kappa_{\mathrm{opt,\ peak}} = \left(\frac{e_{\mathrm{n}}^2}{4k_{\mathrm{B}}T\frac{R_{\mathrm{p}}^2}{R_{\mathrm{in}}} + \frac{R_{\mathrm{p}}^2}{R_{\mathrm{in}}^2}e_{\mathrm{n}}^2 + R_{\mathrm{p}}^2 i_{\mathrm{n}}^2} \right)^{1/4} . \tag{6.24}$$

6.1.4 Effective Electrode Distance

The parameter D_i was introduced in Sec. 6.1.1 as the distance of infinite and plane electrodes used for the ion-signal pickup, defining the signal strength induced in the detection electronics. It was first discussed in [205] that this model distance can be translated into an *effective electrode distance* of the geometry in cylindrical traps, resulting in the same signal strength. In [162], analytical expressions of D_i are derived from the calculation of the surface charge induced in the cylindrical electrode structure by the stored charged particle, where the results are briefly summarized below.
For the detection of the axial oscillation at a signal electrode with length l_{se} and distance d_{se} from the trap center, the effective electrode distance is given by

$$D_z = \frac{\Lambda}{8} \left(\sum_{n=1}^{\infty} \frac{\sin\left(\frac{n\pi}{\Lambda} l_{\mathrm{se}}\right) \sin\left(\frac{n\pi}{\Lambda}(2d_{\mathrm{se}} + l_{\mathrm{se}})\right)}{I_0\left(\frac{2n\pi}{\Lambda} a\right)} \right)^{-1} , \tag{6.25}$$

where I_m is the modified bessel function of m-th order and first kind. Λ is the total length of the trap structure and a the inner radius of the cylindrical electrodes (see also Fig. 5.2). For the pickup at the central ring electrode, the axial electrode distance typically is infinite since the ion amplitudes are much smaller than the ring length.

Table 6.1: Effective electrode distances of the PENTATRAP tower. The electrodes used for the signal tap are labeled by EC for the endcap, CE for the correction electrode and RE for the ring electrode. All lengths are given in mm.

D_z				$D_\pm$ (at halves of the electrodes)			
EC	CE	RE	EC + CE	EC	CE	RE	EC + CE
32.5	11.1	-	8.1	62.5	23.1	31.0	21.1

For the detection of the radial modes, halves of segmented electrodes are used. There, the electrode distance is given by

$$D_{+,-} = \frac{\pi\Lambda}{8}\left(\sum_{n=1}^{\infty}\frac{\cos\left(\frac{2n-1}{2\Lambda}\pi(2d_{\mathrm{se}}+l_{\mathrm{se}})\right)\sin\left(\frac{2n-1}{2\Lambda}\pi l_{\mathrm{se}}\right)}{I_1\left(\frac{2n-1}{\Lambda}\pi a\right)}\right)^{-1}, \tag{6.26}$$

if the electrode is at a distance d_{se} from the trap center. In case of the pick-up at the ring electrode with length l_{r}, the calculation results in

$$D_{+,-}^{\mathrm{ring}} = \frac{\pi\Lambda}{4}\left(\sum_{n=1}^{\infty}\frac{\sin\left(\frac{2n-1}{2\Lambda}\pi l_{\mathrm{r}}\right)}{I_1\left(\frac{2n-1}{\Lambda}\pi a\right)}\right)^{-1}. \tag{6.27}$$

In Tab. 6.1, the effective electrode distances for the trap electrodes of the PENTATRAP tower as defined in Tab. 5.1 are shown. The choice of the electrodes used for the axial and radial signal tap in our experimental setup is discussed in Sec. 6.5.

6.2 Overview of the Cryogenic Arrangement

Prior to the detailed discussion of the detection electronics, a brief overview on the mechanical arrangement in the cryogenic region is given, where a drawing is shown in Fig. 6.5.
The cryogenic detection electronics is housed by a vacuum chamber with direct access to the trap chamber via a titanium bellow. Thus, the signal electrodes can be directly connected to the detectors. Both chambers are cooled by the liquid helium of the magnet's cold bore (see Sec. 4.1). From the electronics chamber, the signal transmission lines are guided to the magnet's bore via cryogenic vacuum feedthroughs. On top of the magnet's bore, the signal lines are connected to room temperature amplifiers.
In the opposite direction, the voltage supply of the trap electrodes is filtered on the top flange at room temperature and on the top of the electronics chamber in the cryogenic region (see Sec. 6.5). From there, the voltage cables enter the vacuum chambers via the feedthroughs, and are connected to the trap electrodes. In the same way, excitation lines are connected to the trap electrodes, which are attenuated at both filter stages.

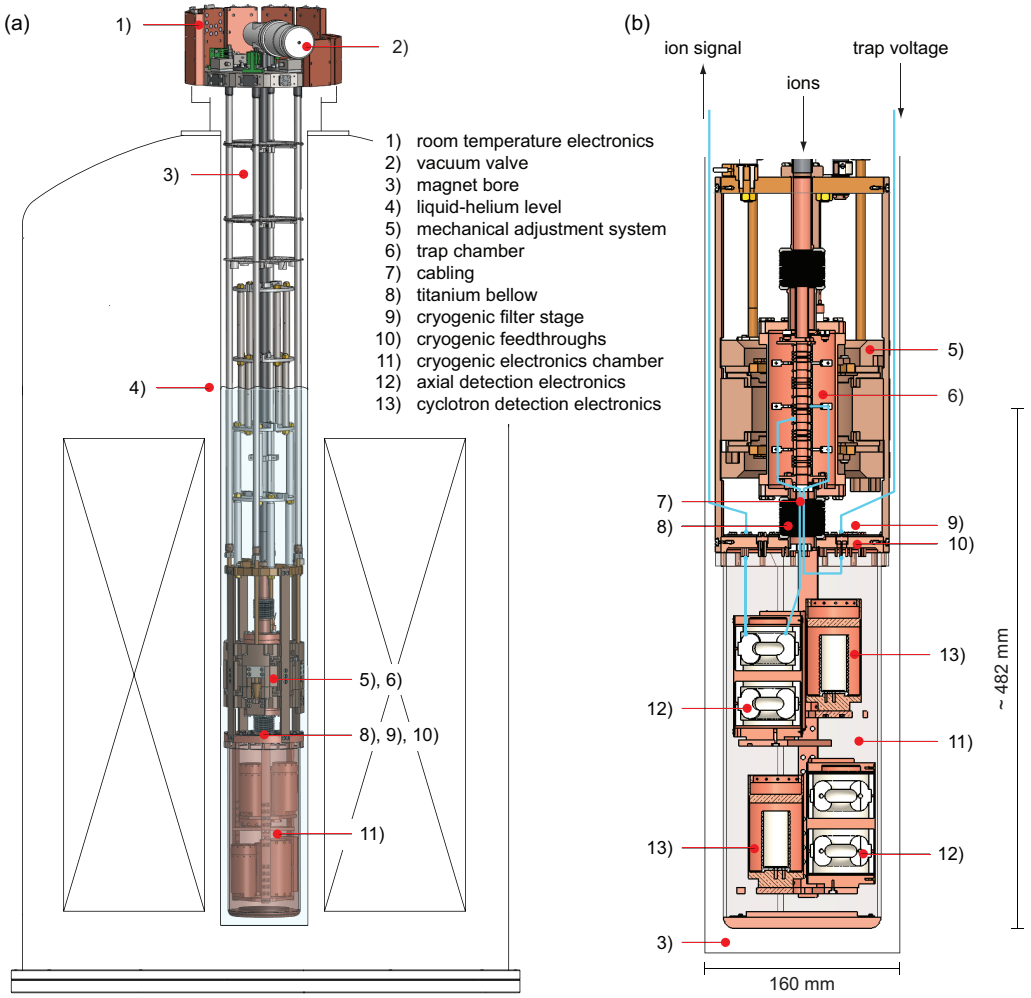

Figure 6.5: Overview of the cryogenic setup in the magnet's bore. The cryogenic detection electronics is housed by a vacuum chamber with direct access to the trap chamber via a titanium bellow. The trap chamber and the cryogenic electronics chamber are cooled by the liquid helium of the magnet's cold bore. From the vacuum area, the cabling of the ion signals and the trap-voltage supply is guided to the magnet's bore through cryogenic feedthroughs, placed on top of the electronics chamber. Close to the feedthroughs a cryogenic filter stage is mounted. An additional filter stage and room temperature amplifiers are mounted on the top flange of the magnet's bore.

6.3 Axial Detection Electronics

As discussed in Sec. 3.2, for a mass-ratio measurement all eigenfrequencies of the ions of interest have to be determined, where the axial detectors are intended to be the main tools at PENTATRAP. The axial frequency will be directly determined by a noise dip, whereas the radial frequencies are planned to be measured by the coupling to the axial eigenmode (see Sec. 6.1).
In the following section, the experimental realization of the axial detection system is discussed. All cryogenic parts of the axial detection system were developed in close collaboration with the *g*-factor Penning-trap experiments in Mainz [30, 165, 185], which is also the case for the cyclotron detectors, discussed in Sec. 6.6.

6.3.1 Introductory Remarks

The axial frequency of a stored particle only depends on its charge-to-mass ratio and on the trapping voltages applied to the trap electrodes, see Eq. (3.4a). Thus, provided a voltage supply with arbitrary voltage range, the choice of frequency is left open in the design of a narrow-band detection system. However, several issues have to be taken into account to find the most suitable axial frequency.

Favoring a low frequency:

- In the determination of the free cyclotron frequency ν_c, the relative contribution of the axial frequency is suppressed by $(\nu_z/\nu_+)^2$, see Eq. (3.16). Thus, the lower the axial frequency, the less accurate it has to be determined for a given accuracy in ν_c.
- A high inductance of the tuned circuit enables a high parallel resistance R_p, see Eq. (6.2) and Eq. (6.3).
- Complications due to high frequency effects in the detection system, such as parasitic feedback, dielectric losses, rf losses in superconductors in a magnetic field or reflections of detection and excitation signals in the transmission lines are reduced.
- Lower demands on the voltage range of a highly stable voltage source, in particular with respect to the construction of a new voltage source for PENTATRAP, see Sec. 4.3.

Favoring a high frequency:

- Reduced or negligible $1/f$ noise of the cryogenic amplifier leading to a higher SNR, compare to Sec. 6.3.3.
- High trapping voltages reduce the relative influence of, e.g., external noise or parasitic patch potentials on the trap electrodes [206].
- The radial modes might be cooled by the axial mode via sideband coupling to $T_\pm = \frac{\omega_\pm}{\omega_z} T_z$ [155], where a higher cooling efficiency is given at a higher axial frequency.

At the *g*-factor experiments in Mainz, the detectors have proven the suitability for high-precision Penning-trap experiments at an axial frequency of approximately ~ 700 kHz.

In our case, we decided to the design the detectors for a slightly lower frequency of about 600 kHz, due to the very first argument given above. However, in the future of our experiment all issues mentioned above will have to be weighted against each other and adjustments might be needed.

6.3.2 Resonator

In our experimental setup, the tuned circuit connected to the pick-up electrodes is realized by a coil placed in a conductive housing, where the combination is called resonator in the following. As discussed in Sec. 6.1.1, the main purpose of such a resonator is to provide a high parallel resistance

$$R_{\mathrm{p}} = 2\pi\nu QL = \frac{(2\pi\nu L)^2}{R_{\mathrm{s}}}, \tag{6.28}$$

where Q is the quality factor and L its inductance. Thus, at a fixed resonance frequency ν_{LC}, R_{p} can be increased by minimizing the self capacity and maximizing L, see Eq. (6.2). Moreover, for a high Q the energy losses have to be minimized, where R_{s} was introduced in Eq. (6.28) as an effective residual series resistance, in which the energy is dissipated. A general guide for the optimization of the quality factor of rf resonators is given in [207], where the main issues are briefly summarized in the following.

Phenomenology of Loss Mechanisms

The main sources of losses in resonators used in our experiments can be split up into the residual resistance of the wire R_{w}, losses induced in the shield R_{sh}, and into losses in dielectric material used for the wire support or the wire insulation.
For the wire material, either normal conducters or superconductors might be used. In both cases, ac currents can only flow in the surface region, where the effective area is characterized by the surface times the skin depth δ in case of normal conductors [189] and the London penetration length λ_{L} for superconductors [208]. For normal conductors, the resistance in this surface area is given by the specific resistance of the material, favoring material with high specific conductivity, such as oxygen free copper. In case of superconductors, an ac resistance at the surface arises from the interaction of the inertial mass of the Cooper pairs with normal conducting electrons. Obviously, for both cases the residual wire resistance can be decreased by the choice of a large wire diameter with high surface area.
In order to characterize the shield resistance, the conductive housing is modeled as a shorted secondary turn of a transformer, which is coupled to the coil (forming the primary turns) by a coupling constant $k^2 = M^2/(LL_{\mathrm{sh}})$. Here, L_{sh} is the inductance of the shield geometry and M the mutual inductance defined by, both, the geometry of the coil and the shield. Thus, the residual resistance is determined by the coupling and the specific ac resistance of the shield material.
Finally, losses in dielectric materials arise from dissipative polarization currents. In an equivalent circuit, the dielectric contributions can be taken into account by an effective

capacitance $C_{\mathrm{p,d}}$ and resistance $R_{\mathrm{p,d}}$ in parallel to the ideal tuned circuit. The dielectric material is characterized by the dielectric loss tangent $\tan(\delta)$ defined as the ratio of reactive to dissipative power. The relation to the resulting parallel resistance is given by

$$R_{\mathrm{p,d}} = \frac{1}{2\pi\nu C_{\mathrm{p,d}} \tan(\delta)}. \tag{6.29}$$

Thus, for wire insulation or wire support, a dielectric material with low loss tangent is favorable and the amount of material should be minimized.

Geometry and Materials

In Fig. 6.6, the geometry of the axial resonator is shown, which was developed in close collaboration with A. Mooser [209]. Due to space constraints in the cryogenic region, the housing is built in a double structure with two separated coil chambers for the detection of the axial frequency in two traps.
The coil wire is wound on a coil body with toroidal shape. There, the magnetic flux is confined within the coil [197], resulting in a low coupling to the shield, which is shown in Fig. 6.6b. On the outside of the coil body, 18 arrays are separated by a spacer structure, in which the wire can be wound. Additionally, the toroid is supported at these spacers by two rings in the housing. For the coil body and the support rings polytetrafluorethylen (PTFE) is used, which has a very low loss tangent of $\tan(\delta) \sim 10^{-4}$. The coil body is divided into two halves, which can be opened for an easy winding of the wire and later fixed to each other with PTFE tape.
For the wire, superconducting material is used. Since the detection electronics is exposed to strong magnetic fields up to 7 T (see Sec. 6.3.5), the type II superconductor Niob-Titanium (NbTi) is chosen, offering a critical temperature of $T_{\mathrm{c}} \approx 9.5$ K and a critical upper magnetic field strength of $B_{\mathrm{c2}} \approx 14.5$ T. However, in an external magnetic field, additional loss mechanisms in type II superconductors arise, which scale with the external field strength and the cube of the frequency. It is shown in [207] that NbTi has still a smaller surface resistance compared to good normal conductors at the low axial frequencies around 600 kHz.
In order to guarantee a good thermalization of the superconductor, the wire with diameter of 75 μm and PTFE insulation is fixed to the coil body by a thin PTFE tape. Both ends are soldered to a copper wire, where one end is grounded at the housing, and the other end is used for the connection to the trap.
Due to the expected low coupling to the shield, the housing of the coils is made of normal conducting oxygen-free high thermal conductivity copper (OFHC), with low residual resistances at low temperatures [210]. An additional reason for the waiving on superconductive bulk material is the disturbance of the homogeneous magnetic field close to the trap.
In Fig. C.3 and Fig. C.5, photographs of the final coil and the total resonator are shown.

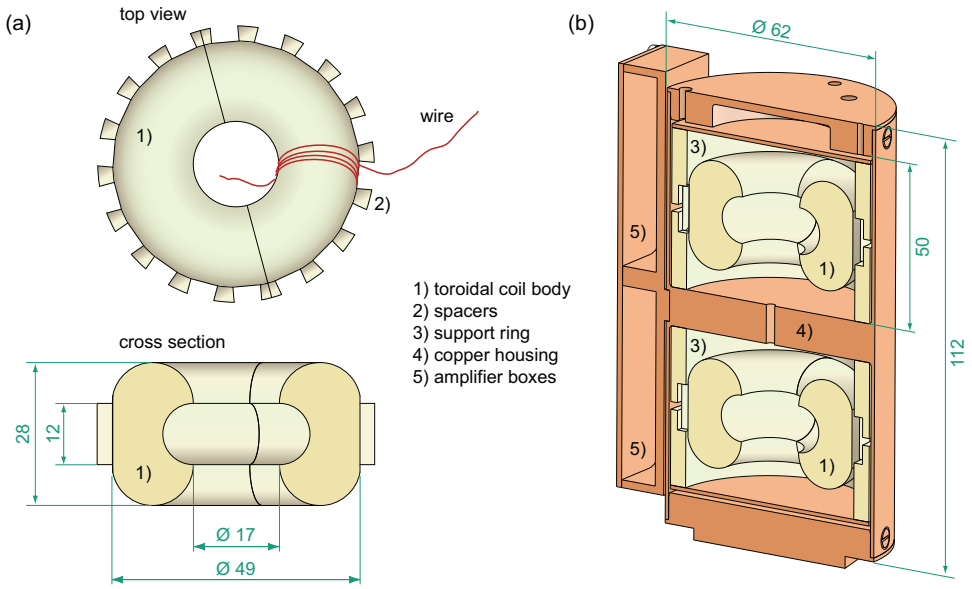

Figure 6.6: Drawing of the axial double resonator. (a) Toroidal coil body made of PTFE, on which the superconducting wire is wound (indicated with the red lines). (b) Double housing for two toroidal coils, made of OFHC. The length scales are given in mm.

Resonator Performance

At room temperature, superconducting material is a bad conductor. Thus, no resonance line shape is visible due to the low Q. All test measurements on the resonator were performed in a cryogenic test setup, where the device under test (DUT) can be cooled to ~ 3 K with a pulse tube cooler (*Sumitomo* SRP-062B-F-50H). The resonance curve was measured with a network analyzer (*HP* 4195A), where the resonance frequency ν_{LC} and the width $\Delta\nu$ can be read out directly. The transmission lines to the network analyzer were coupled by a small air capacitance (a fixed distance of two wires), in order to avoid a coupling to the input resistance of the measurement device.
In order to find the right number[5] of turns N, several test coils were wound for the determination of L and C_{p} as a function of N. Finally, $N \sim 800$ turns were used, resulting in $L = 3.2$ mH and $C_{\mathrm{p}} \approx 7$ pF and a free resonance frequency of $\nu_{\mathrm{LC}} = 841.8$ kHz. With an additional trap capacitance of $C_{\mathrm{trap}} = 13$ pF (see Tab. 6.2) and the input capacitance of the cryogenic amplifier of about 2 pF, this will result in a resonance frequency of about 600 kHz, as aimed for. From the cryogenic measurements, a very high quality factor of $Q = 65000$ was determined, corresponding to a parallel resistance of $R_{\mathrm{p}} \sim 1.1$ GΩ. Expressed in a residual series resistance by Eq. (6.28), this corresponds to $R_{\mathrm{s}} \approx 260$ mΩ. These parameters depict an outstanding performance of the free resonator, where the influence to the total axial detector is discussed below.

[5] For the inductance, $L = N^2\mu_0 A/l$ can be used as a rough estimate, where N is the number of turns, A is the cross section of a turn and l the circumference of the toroidal shape in the middle of the cross section [197]. However, this formula is only valid for an ideal toroidal shape. In our case, the spacing structure and the close winding introduces deviations.

Possible Improvements

Several improvements might lead to an even better performance of the resonator. First of all, the spacer structure might be reduced or avoided, possibly leading to a better confinement of the magnetic flux in the coil. Thus, the residual influence of the housing might be reduced. Furthermore, the amount of PTFE used for the coil body might be reduced, leading to less dielectric losses. As an alternative, dielectric material with lower loss tangents might be used, such as sapphire. Finally, the inner surface of the housing might be polished in order to decrease the effective surface area.

6.3.3 Amplifier

Besides the resonator, the second ingredient for a highly-sensitive detection system is the cryogenic amplifier. This amplifier has to be placed in the vicinity of the resonator in order to reduce the total system capacitance, dielectric losses, and the interference with external noise sources.
As shown in Sec. 6.1.3, a low noise characteristic and a high input resistance are needed for a high SNR. Parasitic feedback paths have to be avoided by a careful amplifier design. Moreover, a low power consumption is mandatory to avoid the heating of the cryogenic area, which is particularly important for the PENTATRAP setup, where several amplifiers will run simultaneously (see Sec. 6.6.1).
For the axial detection system at PENTATRAP, the cryogenic amplifier developed by S. Sturm [124] is directly adopted, offering all the features mentioned above.

Schematic

A schematic of the amplifier layout is shown in Fig. 6.7. The input of the amplifier is formed by two parallel field effect transistors (FET), of the type NE25139 (*NEC*). The common source topology offers a high input resistance and a voltage amplification of the signals connected to their gate electrode. The FETs are based on Gallium-Arsenide (GaAs), which is still working under cryogenic conditions[6].
At low frequencies and low temperatures, the dominant source of noise in such FETs is the scattering of the current at impurities, giving rise to the so-called $1/f$ or flicker noise, which is highly dependent on the production process [211]. The flicker noise density scales with the drain-to-source channel length l_{ds} by

$$u_{1/\mathrm{f}}^2 \propto \frac{1}{l_{\mathrm{ds}}^2 f}. \tag{6.30}$$

This can be qualitatively understood, since with an increase of l_{ds} the number of carriers increases and the drain current decreases. Unfortunately, most commercial devices have short channel lengths. However, the NE25139 is a dual-gate transistor, which internally forms two transistors in series for cascode applications. Thus, by shortening

[6] Most commercial FETs are based on silicon semiconductors, which suffer from carrier freeze-out at low temperatures.

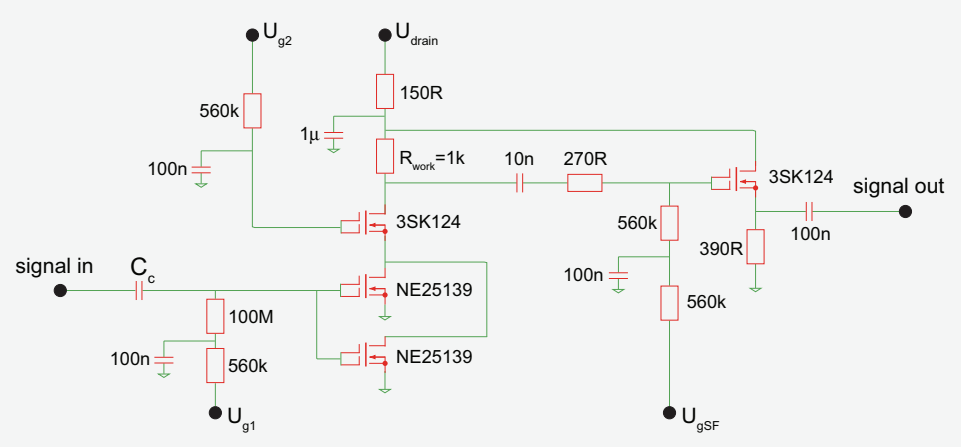

Figure 6.7: Schematic of the ultra low-noise axial amplifier. The amplifier was developed in [124] and adopted for the PENTATRAP setup.

the two gates, the total channel length extends from the source of the first transistor to the drain of the second. Consequently, the noise can be decreased by a factor of four, if both gates are identical in their gate area. At the same time, the capacitance is increased by only a factor of two. Additionally, two dual gate FETs are implemented in parallel, which suppresses incoherent noise sources by a factor of $1/\sqrt{2}$.
In order to suppress feedback on the amplifiers input by means of the parasitic gate-to-drain Miller capacitance of the input FETs [212], a cascode stage is formed by the third transistor 3SK124 (*NEC*). There, the gate is kept on a constant voltage (U_{g2}) and the transistor acts as a low impedance load to the first stage and a high parallel impedance to the resistive load R_{work}. This effectively lowers the voltage between the first stage and the cascode, while the amplified signal appears across R_{work}.
The third stage of this amplifiers is formed by a source follower configuration (3SK124), to match the output impedance of the amplifier to the 50 Ω impedance of the transmission lines. This prevents reflections, which possibly cause amplifier oscillations. The amplifier is biased by external voltages, which are filtered on the board.

Board and Components

The board material contributes to the dielectric losses in the detection system and increases the gate-to-drain capacitance leading to feedback. Thus, a PTFE copper laminate is chosen (*Taconic*), which offers a low dielectric permittivity and a loss tangent of $\delta < 0.002$ at 4 K [162]. The layout is milled by hand. In order to define a proper ground, more than 50 holes were drilled in the board, and thin wires soldered into them to connect the upper and lower clad, which is connected to the ground of the resonator.
In order to avoid parasitic reactances from the components, only surface mountable devices (SMD) are used. High-Q capacitors are used for low values (*Johanson Technologies*), and high values are of ECHU type (*Phillips*). The resistors are of thin-film

type (*Susumu*). Photographs of the final amplifier are shown in Fig. C.4 and Fig. C.5.

Amplifier Performance

For the final amplifier, the voltage gain, the power consumption and the input related voltage-noise density were measured at 4 K. The voltage gain is shown in Fig. 6.8b as a function of the biasing U_{g1}. It reaches approximately 16 dB around $U_{\mathrm{g1}} = -0.65$ V. At maximum amplification, the power consumption is ~ 9 mW at a drain voltage of $U_{\mathrm{d}} = 3$ V. On the cost of voltage gain, this might be reduced to $U_{\mathrm{d}} = 2$ V at a consumption of 5 mW.
The input related voltage-noise density was measured directly with a spectrum analyzer (FSP 3, *Rohde und Schwarz*). In order to make the tiny signal visible in the noise floor e_{a} of the analyzer, the cryogenic signal was amplified at room temperature by a commercial low noise amplifier (ZFL-500LN, *Mini-Circuits*). The noise of the cryogenic amplifier is obtained from

$$e_{\mathrm{n}} = \frac{1}{G_{\mathrm{cryo}}} \sqrt{\frac{1}{G_{\mathrm{rt}}^2}\left(e_{\mathrm{tot}}^2 - e_{\mathrm{a}}^2\right) - e_{\mathrm{rt}}^2}, \tag{6.31}$$

where G_{cryo} is the voltage gain of the cryogenic amplifier, e_{tot} the total noise amplitude measured at the analyzer and e_{rt} and G_{rt} are the voltage-noise density and the gain of the room temperature amplifier, respectively. The measurement result is shown in Fig. 6.8a. Around 600 kHz, the voltage noise is about $e_{\mathrm{n}} \approx 0.62$ nV/$\sqrt{\mathrm{Hz}}$.

The current noise density i_{n} can be measured by the induced voltage drop over a huge resistance coupled to the input of the amplifier. This was done with a test resonator with a parallel resistance of approximately $R_{\mathrm{p}} \sim 20$ MΩ. However, in this measurement the thermal noise of the resonator has to be separated from the voltage drop induced by the current noise. There, errors arise due to the actual temperature of the resonator and due to the exact values of the coupling to the amplifier's input, which are in the same order of magnitude as the quantity to be measured. From a cryogenic measurement, the value of $i_{\mathrm{n}} \approx (3.7 \pm 3)$ fA/$\sqrt{\mathrm{Hz}}$ was extracted.

6.3.4 Coupled Performance

The coupling of the amplifier to the resonator has influence on many parameters. For the dip detection, a higher coupling constant κ introduced in Eq. (6.19) leads to a higher SNR. However, at the same time this changes the effective noise temperature due to the current noise flowing to the resonator. Moreover, the dip width $\Delta\nu$ changes due to the modification of the total parallel resistance R_{sys}, given in Eq. (6.21).
For our test setup, an intermediate coupling with $\kappa = 0.33$ was chosen, defined by a tap to the coil at $N_1 = 2N_2$ and a coupling capacitance at the input of the amplifier of $C_{\mathrm{c}} = 10$ nF. The input capacitance of the amplifier was measured to be $C_{\mathrm{in}} = 2.1$ pF. Additionally, for the following characterization a capacitance $\widetilde{C}_{\mathrm{sim}}$ was connected in

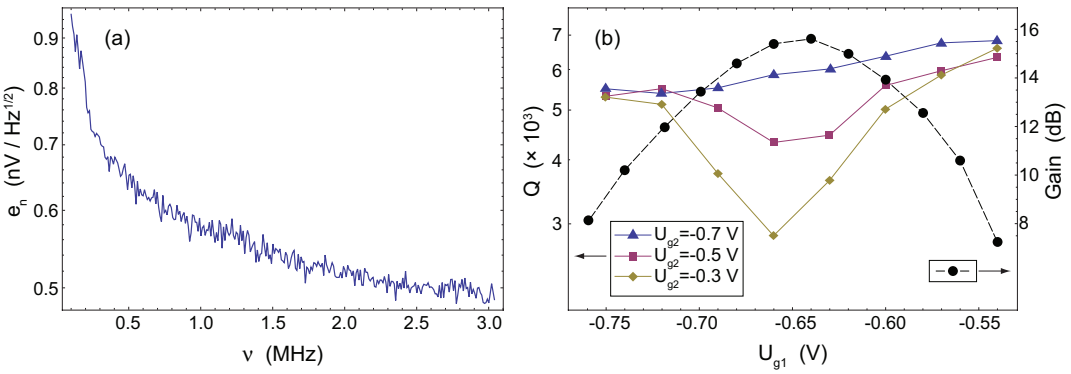

Figure 6.8: (a) Voltage-noise density of the axial amplifier. (b) Quality factor of the coupled system of amplifier and resonator and voltage gain of the amplifier.

parallel in order to simulate the trap capacitance.

Back Action

In high-Q circuits, parasitic feedback of the amplifier to its input might lead to a modification of the total parallel resistance. In presence of a feedback gain G_{FB}, the effective resistance is given by [213]

$$R_{\mathrm{FB}} = R_{\mathrm{p}}(1 + G_{\mathrm{FB}}). \tag{6.32}$$

Thus, for a negative feedback gain (the sign is defined by the phase relation to the input signal), the Q-value might be severely degraded. For a positive value, the uncontrolled increase of Q might cause oscillations in the detector.
For our system, the back action of the amplifier to the resonator is shown in Fig. 6.8b. For a biasing of the cascode transistor at $U_{\mathrm{g2}} = -0.3$ V, a degradation of the Q-value is visible as a function of the gain of the amplifier. According to Eq. (6.32), this corresponds to a strong negative feedback gain, which lowers the total parallel resistance. However, by tuning the cascode biasing to $U_{\mathrm{g2}} = -0.8$ V, the back action gets completely negligible. The remaining slope can be qualitatively explained by a weak parasitic coupling of the load impedance of the first stage to the input of the amplifier. For an analytical model of a simple transistor see [162] and [214].

Noise Resonance and Signal-to-Noise Ratio

In Fig. 6.9, a noise resonance of the coupled system is shown. The signal from the cryogenic amplifier was further amplified with the AF-DC-c room temperature amplifier (*Stahl Electronics*) and down converted to the bandwidth of a fast fourier transform (FFT) analyzer (see Sec. 6.6.2).
At a resonance frequency of $\nu_{\mathrm{LC}} = 661.07$ kHz, the width at -3 dB from the maximum is $\Delta\nu \sim 95$ Hz, which corresponds to a quality factor of $Q \approx 7000$. Expressed in the parallel resistance of the coupled system, R_{sys} is given by 93 MΩ. Thus, compared to

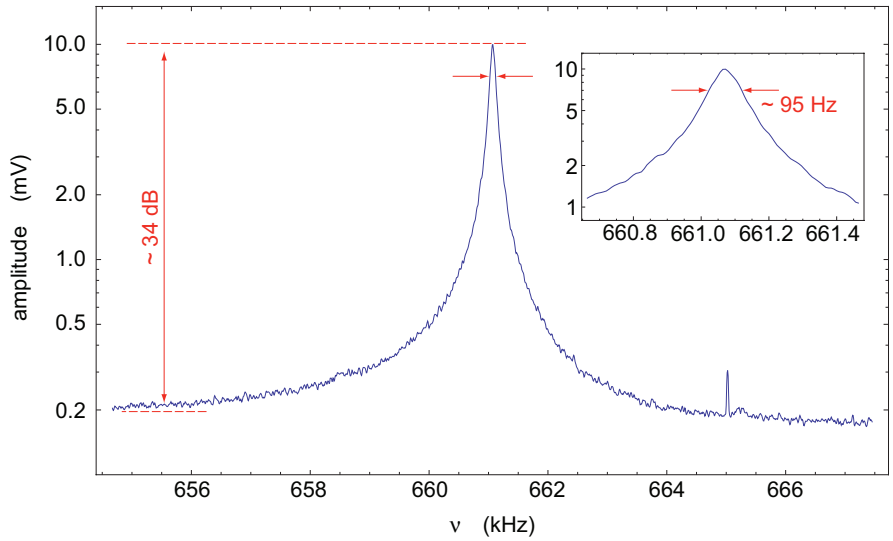

Figure 6.9: Noise resonance of the axial detection system with simulated trap capacitance. At a resonance frequency of 661.07 kHz, the width at −3 dB from the maximum is about 95 Hz, corresponding to a Q-value of ∼ 7000. The distance from the maximum of the noise resonance to the noise floor amounts to approximately 34 dB.

the value of the free resonator of 1.1 GΩ, the coupled system is limited by the input resistance of the amplifier, where the effective value of $R_{\text{in}} = 11.3$ MΩ can be extracted from Eq. (6.21). Within our group and the g-factor experiments in Mainz, the input FET of our amplifier is widely used. It was observed that the input resistance of the FETs vary, presumably depending on the production process. Thus, with a more comprehensive survey individual FETs with a higher input resistance might be found, to lower the limitation of the total parallel resistance.
The signal-to-noise ratio for a dip measurement, defined as the distance of the maximum of the noise resonance to the noise floor, is given by ∼ 34 dB. However, at a temperature of $T = 3$ K and the noise properties given in the last paragraph, a SNR of ∼ 39 dB is expected from Eq. (6.22). On the other hand, the calculated SNR is very sensitive to the parameters plugged in, and the deviation can be explained by slightly different values within the error bars. Furthermore, the measured value might indicate that the current-noise density is much lower than the value given in the last paragraph.

Axial Dip Width

From the parameters of the coupled system, the resulting dip width of the axial noise dip can be calculated from Eq. (6.16) as an estimate for the real experimental situation at PENTATRAP. The dip widths are shown in Fig. 6.10a and Fig. 6.10b for the pick-up at the correction electrode and the endcap, respectively, resulting from $R_{\text{p}} = 93$ MΩ and the effective electrode distances in Tab. 6.1.
According to the discussion in Sec. 3.2, for a measurement to $\Delta\nu_{\text{c}}/\nu_{\text{c}} \sim 10^{-11}$, a precision in the axial frequency of $\Delta\nu_z/\nu_z \sim 10^{-8}$ is needed for, e.g., $^{187}\text{Re}^{45+}$. Thus, the

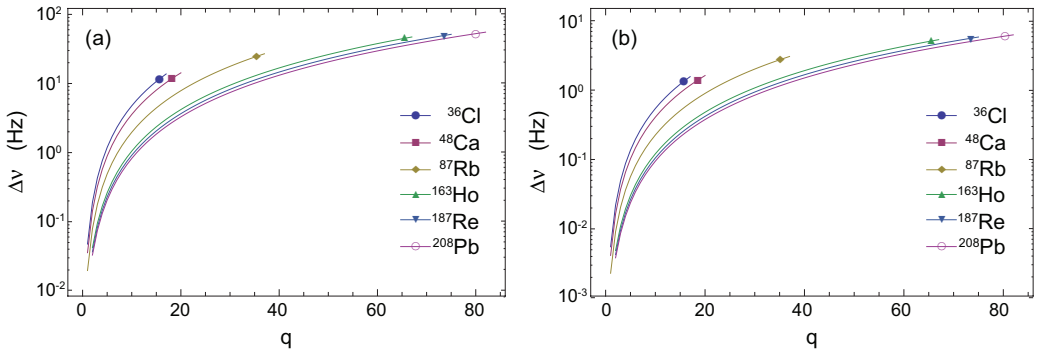

Figure 6.10: Axial dip width for selected ions as a function of their charge state. For the calculation, a parallel resistance $R_p = 93$ MΩ of the detector was used. In (a) the pickup is at the correction electrode and in (b) at the endcap.

axial frequency has to be measured to an absolute value of $\sim$ 10 mHz. As a crude estimate, the center of a noise dip can be determined to approximately 1/10 of the dip width by the fit of the theoretical line shape. Another factor of 10 in resolution might be gained from the accumulation of statistics. Thus, the optimum dip width[7] for the needed resolution is expected to be in the order of $\sim$ 1 Hz.
For $^{187}Re^{45+}$, the dip width is calculated to be $\Delta\nu_z \sim 20.2$ Hz for the pick up at the correction electrode and $\Delta\nu_z \sim 2.5$ Hz at the endcap. Thus, a pick up of the signal at the end cap is clearly favored for the measurements on highly charged Re.
However, the arguments given above will have to be transferred to the experimental reality of a measurement, where probably different masses or charge states will be used. A different coupling of the resonator to the amplifier, detuning of the ion's frequency to the detectors resonance frequency or active electronic feedback will provide several degrees of freedom in order to find the optimum dip width for the individual measurement case.

6.3.5 Effects of the Strong Magnetic Field

As shown in Fig. 6.5, the cryogenic detection electronics is housed by an electronics chamber placed directly underneath the trap chamber. This ensures a close distances for the trap-to-electronics cabling and an efficient cooling of the electronics by the liquid helium in the magnet's bore.
However, the detection electronics is exposed to the strong magnetic field inside the bore due to this placement. In Fig. 6.11a, the dimension of the electronics chamber is marked in the direction of the magnet's axis, where the field inside the chamber ranges up to the full strength of our magnet of 7 T. The effects of such a strong magnetic field on the resonator and the amplifier are discussed in the following.

[7] Note that the dip width is not the only measure for the final resolution. In presence of temporal fluctuations, fast measurements are very important in order to avoid the broadening of the line width. In this context, the noise in the spectrum will set the limit for the accuracy of a fast fit. A detailed discussion of the optimization procedure for the frequency resolution with a noise dip will be given in [209].

Q-Value of the Resonator

For the axial resonator, additional loss mechanisms in strong magnetic fields arise in the superconducting wire material, where details are discussed in [207]. Here, only the phenomenology and measurement results are given, in order to estimate the influence on the measurement performance in the experiment.
In type II superconductors, magnetic flux can penetrate the bulk material above a lower critical magnetic-field strength, which is given by $B_{c,1} \approx 24$ mT in case of our NbTi wire. The rf current in the superconductor interacts with the penetrating magnetic flux by the Lorentz force. As a consequence, the flux lines move perpendicular to the rf current and a motional electric field is created. The interaction of this electric field with the normal conducting phase in the superconductor causes dissipative losses. In a second mechanism, the motion of the flux tubes leads to a breaking of Cooper pairs and heat is dissipated by the recombination of the pairs in a lower magnetic field. In general, the penetrating flux and, thus, the losses scale with the external field strength.
In order to obtain data for our experiment, a test resonator with parameters identical to the one presented in Sec. 6.3.2 was directly inserted into the magnet's bore, where it was cooled by the liquid helium. The measurement results are shown in Fig. 6.11b. As expected, a strong decrease in the Q-value is visible as a function of the magnetic-field strength. At $B = 1$ T, the Q-value is measured to ~ 36000, which drops down to $Q \sim 22000$ at $B = 7$ T. This corresponds to a parallel resistance of 525 MΩ and 372 MΩ, respectively. Expressed in an effective series resistance R_s, the measured values show an increase of ~ 40 mΩ/T in a linear approximation. When these measurements are extrapolated to a vanishing magnetic field, it shows a big difference to the parallel resistance of $R_p = 1.1$ GΩ presented in Sec. 6.3.2. This can be explained by a much stronger coupling of the resonator to the network analyzer, which was chosen due to the turbulences caused by the helium boil-off during insertion.
Taken the value of $Q = 22000$ as the worst case, our detection system is still limited by the input resistance of the amplifier. With the coupling of $\kappa = 0.33$ used in the previous section, a total parallel resistance of $R_p \sim 80$ MΩ results, compared to 93 MΩ of the field-free measurement.

Amplifier Gain

In a second measurement series, the influence of the external magnetic field on the cryogenic amplifier was investigated. The results of gain measurements are shown in Fig. 6.11c. The effect strongly depends on the orientation of the FETs to the magnetic field direction. For the magnetic-field being parallel to the surface, to which the FET is soldered, the gain is independent of the field strength. However, the gain strongly decreases in case the field is perpendicular to this surface.
A similar behavior is reported in [215] for a different GaAs FET. There, an analytical model is developed, based on the Lorentz force acting on the drain-to-source current. The altered electron trajectories affect the transconductance, which lowers the gain of the amplifier. In addition, an increase of the noise temperature of the FET is reported, which is explained by an increase of the effective gate length within the model.

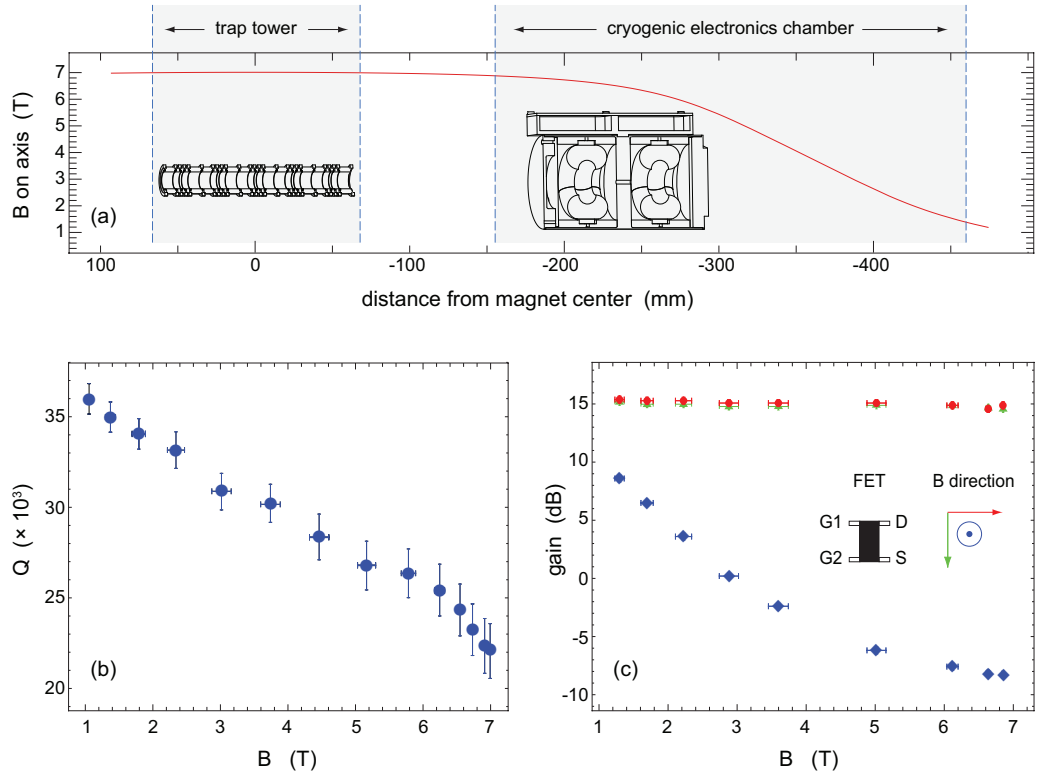

Figure 6.11: Magnetic-field effect on Q of the resonator and on the gain of the amplifier. (a) Position of the cryogenic electronics chamber in the magnetic field. (b) Q-value of a test resonator, measured as a function of the external magnetic-field strength. (c) Amplifier gain as a function of B. The influence strongly depends on the orientation of the FETs to the magnetic field. For the red circles and green triangles, the magnetic field is oriented in the surface to which the FETs are mounted and for the blue squares perpendicular to it.

However, many specific parameters of the FET enter this model, such as the doping of the semiconductor or the width and length of the gate. These parameters are unknown to us for our FET. Therefore, we have to rely on the empirical identification of the orientation, in which the amplification performance is not affected. In these orientations, the input voltage-noise density of the FET was measured, where no difference was found compared to Fig. 6.8a.
As a result of this measurements, the surface to which our FET is mounted has to be in parallel to the magnetic field direction. In the experimental setup, special care has to be taken due to the radial component of the magnetic field in case the amplifier is mounted on a distance ρ to the magnetic field axis. The final orientation of the individual amplifiers will be discussed in the Ph.D. thesis of A. Dörr [216].

6.4 Cyclotron Detection and Refrigeration

Besides the axial detection system presented in the previous section, prototypes of cyclotron detectors were setup and tested within this thesis. In the measurement traps (see Sec. 5.1), the main purpose of the cyclotron detectors is the direct cooling of the cyclotron mode during the detection of ν_+ with the PnA method (see Sec. 6.1.2). In the monitor traps, the cyclotron detectors will be used for a direct determination of ν_+.

6.4.1 Cryogenic Electronics

The basic design rules for a high-Q cyclotron detector are identical to the issues discussed for the axial detection system. However, differences in the realization of the resonator and amplifier arise from the much higher cyclotron frequencies, see Fig. 3.3a. As mentioned earlier, one of the first physics cases planned to be measured at PENTATRAP is the mass ratio of ^{187}Re and ^{187}Os, which is of high interest for the determination of the neutrino mass (see Sec. 2.1.2). Thus, the design of the prototype for the cyclotron detection is focussed on the cyclotron frequency of this isobar pair, where charges states of $q = 35+$ up to $q = 45+$ might be used for the measurement. In the 7-T magnetic field at PENTATRAP, this corresponds to $\nu_+ = 20.1$ MHz up to 25.8 MHz, respectively. The complete design of the cyclotron electronics presented in this section is adopted from the proton g-factor experiment in Mainz [165], in particular from the Ph.D. thesis of S. Ulmer [162]. There, a highly-sensitive detector is set up for a cyclotron frequency of ~ 29 MHz and detailed descriptions can be found. Thus, only the basic principles and the resulting performance are discussed in the following.

Resonator

Compared to the axial resonator, the following issues are of special importance at high frequencies:

- The loss mechanisms of NbTi in external magnetic fields scale with ν^3 [207]. For our experimental conditions of a magnetic field up to 7 T in the electronics chamber and cyclotron frequencies above 20 MHz, the residual resistance of NbTi is expected to be much larger than for OFHC. Thus, only OFHC is used for the wire and the housing.
- Due to the scaling of the dielectric losses with the frequency in Eq. (6.29), care has to be taken to minimize the amount of dielectric material.
- In the normal conducting OFHC, the skin effect scales with $1/\sqrt{\nu}$, which reduces the effective conducting area to a small band along the surface [189]. Thus, the surfaces might be polished in order to decrease the effective surface area and have to be kept clean in order to avoid dielectric losses.

The cyclotron resonator is realized in a helical geometry, where a drawing is shown in Fig. 6.12b. The geometry follows the design rules for an ideal high-Q resonator given

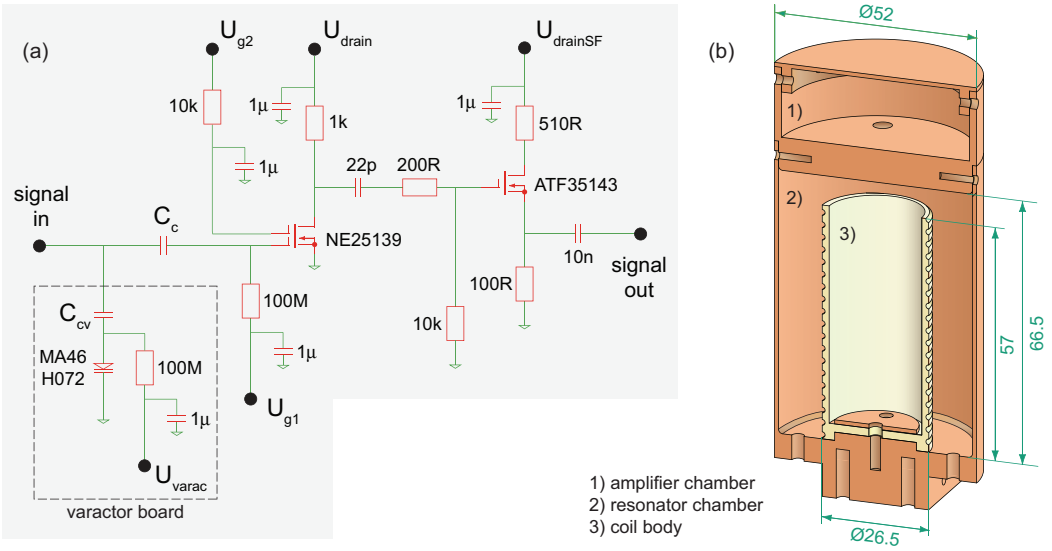

Figure 6.12: (a) Schematic of the cyclotron amplifier. (b) Drawing of the cyclotron resonator. All length scales are given in mm.

in [217], where the optimum ratio of the inner diameter and length of the housing to the diameter and length of the coil are discussed.
A bare wire with 1 mm in diameter is wound to a hollow cylindrical coil body. Both the inner surface of the housing and the surface of the wire are mechanically polished and cleaned in an ultra-sonic acetone bath. For the coil, 15 turns are wound on the coil body, which results in a free resonance frequency of $\nu_0 = 59.26$ MHz due to an inductance of $L = 2.3$ μH and a self-capacitance of $C_\mathrm{p} = 3.2$ pF. From cryogenic measurements, a Q-value of about 4000 was determined, which corresponds to a parallel resistance of $R_\mathrm{p} \sim 3.4$ MΩ or an effective serial resistance of 213 mΩ. A photograph of the resonator is shown in Fig. C.6 and Fig. C.8.

Amplifier

The schematic of the cryogenic cyclotron amplifier is shown in Fig. 6.12a. The input is formed by an NE25139 transistor in common source configuration. As mentioned for the axial amplifier, this FET offers an internal cascode structure, biased by U_g2 at the second gate. The second stage is formed by an ATF35143 (*Avago*) in source follower configuration for impedance matching to the transmission lines. For the board and the passive components, the same material is used as for the axial amplifier. In the final setup, the amplifier is mounted in a separate chamber of the resonator housing to provide a shielding against external noise sources, see Fig. 6.12b. In addition, a voltage controlled capacity diode (varactor) is coupled to the input on a separate board, in order to tune the resonance frequency of the total system to the cyclotron frequency of the ion. More details about the varactor are given below.
In the cryogenic test setup, the gain of the amplifier was measured to be approximately 15.8 dB at $U_\mathrm{g1} = -0.73$ V and $U_\mathrm{drain} = 3$ V (see Fig. 6.13a). There, the power consump-

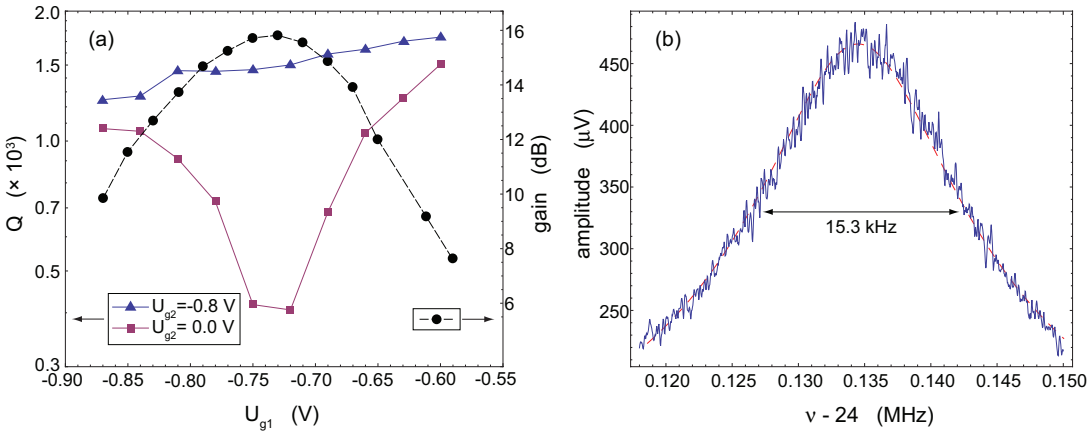

Figure 6.13: (a) Quality factor of the coupled system of cyclotron resonator and amplifier and the gain of the amplifier. (b) Noise resonance of the coupled system without varactor board.

tion amounts to 3 mW. Furthermore, the input voltage-noise density was measured to $e_\mathrm{n} \sim 0.5\ \mathrm{nV}/\sqrt{\mathrm{Hz}}$ for $\nu > 20$ MHz. Photographs of the amplifier are shown in Fig. C.7 and Fig. C.8.

Coupled Performance

For a test setup (without the varactor), the coupling of the amplifier to the resonator was defined by $C_\mathrm{c} = 2.2$ pF in combination with the amplifier's measured input capacitance of $C_\mathrm{in} = 1.1$ pF. In the cyclotron case, the coil is tapped directly on its hot end ($N_1 = 0$), since a lower tap in the resonator introduces a comparatively large parasitic capacitance. The resulting strong coupling of $\kappa = 0.67$ is chosen in order to characterize the back action to the resonator, which might be more severe at the high frequencies than for the axial case. Moreover, a fixed parallel capacitance of $\widetilde{C}_\mathrm{sim} = 15$ pF was added in order to simulate the trap capacitance, the varactor diode and the parasitic capacitance of the cabling in the final setup.
The performance of the coupled system is shown in Fig. 6.13a. For a properly biased second gate of the input transistor at $U_\mathrm{g2} = -0.8$ V, the back action gets negligible. In Fig. 6.13b, a resulting noise resonance is shown at maximum amplification. At the resonance frequency of $\nu_0 = 24.125$ MHz and a -3 dB width of 15.3 kHz, the Q-value results in 1570. Expressed in a parallel resistance, this corresponds to $R_\mathrm{p} = 525\ \mathrm{k}\Omega$. As for the axial case, the coupled performance is limited by the input resistance of the amplifier, where an effective value of $R_\mathrm{in} = 700\ \mathrm{k}\Omega$ can be extracted from the measurement. This limitation can be lowered by the choice of a weaker coupling in the final experimental setup.

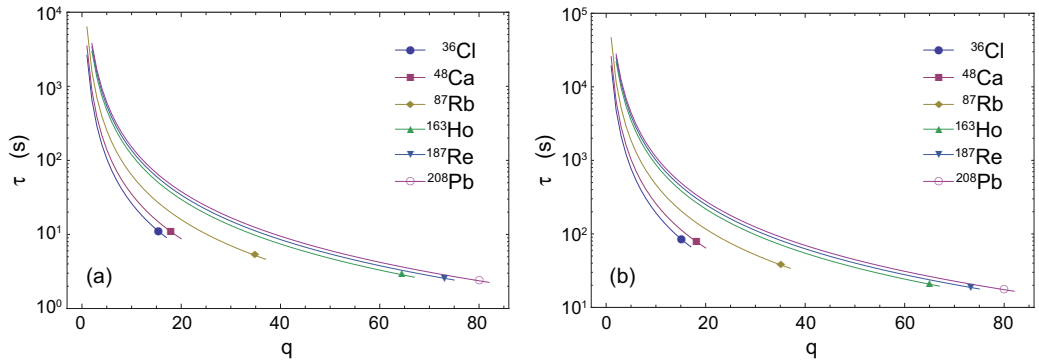

Figure 6.14: Cooling-time constants of the cyclotron mode, for the tap at a half of the segmented correction electrode in (a) and the endcap in (b). For the calculation, the parallel resistance $R_\mathrm{p} = 525$ kΩ of the cyclotron detector without the varactor board is used.

Varactor Diode

As mentioned above, the varactor diode MA46H072 (*MACOM*) can be added at the amplifier's input, in order to tune the resonance frequency of the total system to the ion's frequency by the external voltage U_varac. This diode offers a capacity range of 1 to 8 pF at a supply voltage of −20 to 0 V, respectively. However, in [162] the intrinsic quality factor of this diode was identified as one of the dominant limitations of the total setup. Thus, the varactor is decoupled by means of the capacitance C_cv in order to increase the effective parallel resistance. On the other hand, the decoupling limits the tunable range. With a decoupling of 2.2 pF, the resonance frequency of the total system can be tuned in a range of 2 MHz and in a range of 2.5 MHz for a weaker decoupling with 8.2 pF.

6.4.2 Cooling-Time Constants

As mentioned above, the cyclotron detectors for the measurement traps will predominantly be used for direct cooling of the cyclotron mode during the measurement with the PnA method introduced in Sec. 6.1.2. A schematic of the total assembly is given in Sec. 6.6.1. The cooling time constants arising from our detection system are given in Fig. 6.14 for a tap at the half of the segmented correction electrode in (a) and for the endcap in (b). For the calculation, the parallel resistance of $R_\mathrm{p} = 525$ kΩ without the varactor board is used.
The more efficient cooling is provided by the tap at the correction electrode due to the lower effective electrode distance (see Sec. 6.1.4). For $^{187}\mathrm{Os}^{45+}$, the cooling time is given by $\tau \sim 7$ s. If the value of $R_\mathrm{p} = 380$ kΩ reported in [162] is taken as an estimate for the total system including the varactor board, the cooling time is increased to $\tau \sim 9$ s.

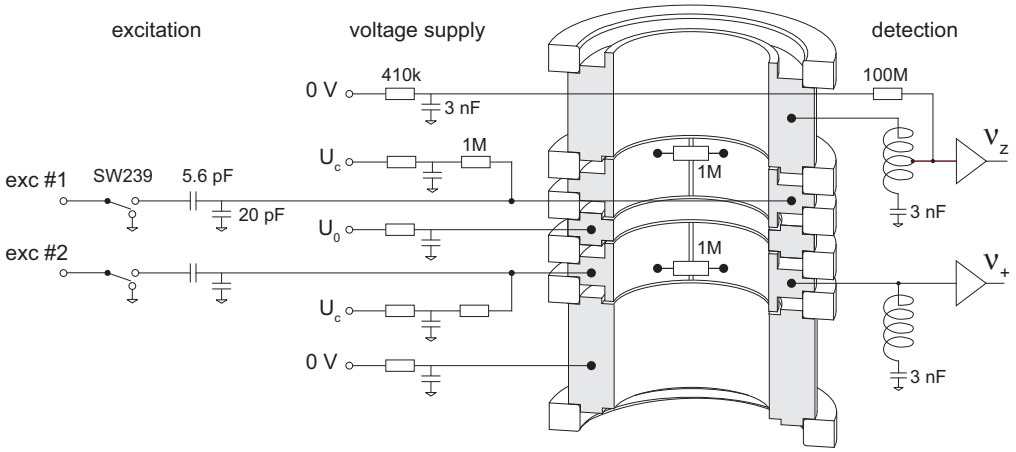

Figure 6.15: Trap wiring of a measurement trap in the cryogenic region. On the right hand side, the axial and cyclotron detectors are shown. On the left hand side, the trap voltage supply and the excitation lines are shown. The trap voltages are filtered by RC filters and the excitation lines are attenuated by capacitive voltage dividers. In addition, the excitation lines can be grounded by a cryogenic switch when they are unused.

6.5 Trap Wiring

As discussed in the previous sections, the choice of the electrode used for the tap of the axial and cyclotron detectors results from the detector performance and the effective electrode distance of the specific electrode. In the following, a brief summary is given with an overview of the cabling shown in Fig. 6.15. In addition, the connection of the trap voltages and the excitations lines in the cryogenic region are indicated, where more details will be given in [172, 216].

Signal Tap in the Measurement Traps

In the traps used for the mass-ratio measurements (see Sec. 5.1), the axial signal will be picked up at the endcap. The endcap is favored to the correction electrode due to the larger effective electrode distance (see Sec. 6.1) and the resulting lower axial dip widths at high charge states (see Fig. 6.10). In addition, a cyclotron detection system is connected to a half of a segmented correction electrode, which provides an efficient cooling during the planned indirect detection of ν_+ by the PnA method (see Fig. 6.14). For the connection of the monitor trap see Sec. 6.6.1.
In the final connection of the experimental setup, the capacitances of the trap electrodes used for the signal tap have to be taken into account when the detectors are tuned to the eigenfrequencies of the ion. The measured values of the electrodes are given in Tab. 6.2.

Table 6.2: Measured capacitances of the trap electrodes. The values are given in pF.

endcap	correction electrode (full)	correction electrode (half)
13	13	8

Trap Voltages and Excitation Lines

In Fig. 6.15, the cabling of the trap voltage supply and the excitation lines is shown for the cryogenic region. The dc lines are filtered by RC filters, where the filter stage is mounted on top of the cryogenic electronics chamber (see Fig. 6.5). An individual filter consists of two 820 kΩ resistances in parallel and two 1.5 nF capacitors in parallel, resulting in a cut-off frequency of $\sim$ 130 Hz. The double structure is chosen in order to guarantee the principal function in case a component brakes during the thermal cycling. The dc line connected to the endcap used for the axial detection is blocked by a 100 MΩ resistance, in order to avoid a limitation of the axial detection system. Moreover, both resonators are separated from the dc ground by 3 nF capacitances, which still allows for a good ac grounding. At the segmented electrodes, a 1 MΩ resistance ensures a dc connection while keeping both halves separated for ac potentials since a low pass is formed in combination with the trap capacitance.
For the supply of dipolar and quadrupolar excitation signals (see Sec. B), the second correction electrode is also segmented into two halves. At both correction electrodes, a excitation line is connected to one half. Thus, both dipolar and quadrupolar excitations can be generated, depending on the phase difference between the two lines. Both excitation lines are guided through capacitive voltage dividers formed by an 5.6 pF capacitance in the line and 20 pF to ground. Thus, high signals can be applied in order to reduce the relative influence of external noise. In order to block the excitation signals from the input of the voltage supply, an 1 MΩ resistance is added at the connection to the dc lines. In addition, the excitation lines can be grounded by the cryogenic switches SW239 (*MACOM*) when they are unused.
A photograph of the cryogenic filter stage including the low pass filters for the dc lines and the voltage dividers for the excitation lines as well as the cryogenic switches is shown in Fig. C.9. In addition to the cryogenic filter stage, a second filter stage is mounted at the top flange of the magnet's bore at room temperature (see Fig. 6.5), where details will be given in [216].

6.6 Total Detection System of PENTATRAP

As discussed in Chap. 5, the trap tower of PENTATRAP consists of five identical traps. In the following section, an overview is given on the planned assembly of the cryogenic detection electronics, in order to realize the measurement scheme discussed in Sec. 5.1. For completeness, the total detection chain including the room temperature electronics is briefly described in Sec. 6.6.2.

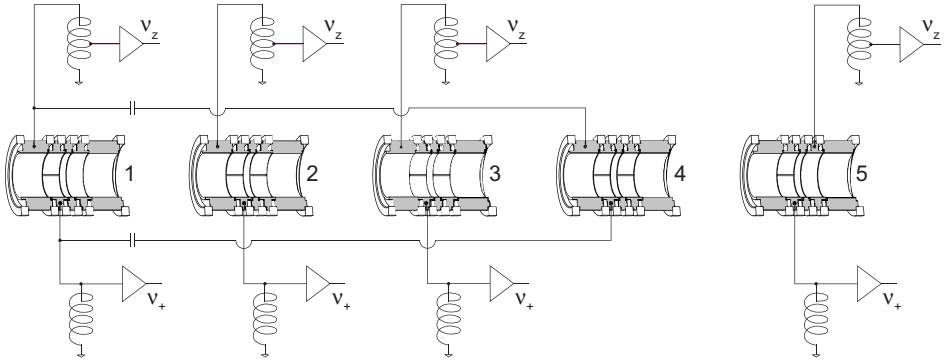

Figure 6.16: Total cryogenic detection system at PENTATRAP. The measurement traps 2 and 3 will be equipped with an individual axial and cyclotron detector for simultaneous high-precision measurements. Trap 1 and 4, serving as ion containers, will share both an axial and a cyclotron detector. Trap 5 will be used for monitoring of magnetic fluctuations or as a reference for the voltage source. Thus, this trap will be equipped with an individual axial and cyclotron detector.

6.6.1 Cryogenic Assembly

In the most favorable measurement scheme at PENTATRAP (see Sec. 5.1), two ion species are measured simultaneously in adjacent inner traps of the trap tower, where trap 2 and 3 are assumed for the following explanation of the wiring scheme[8]. For these measurement traps, both an individual axial detector as well as an individual cyclotron detector are foreseen, as shown in Fig. 6.16. With the axial detector, all eigenfrequencies are planned to be measured, the axial frequency with a noise dip, the magnetron frequency with the double-dip method and the reduced cyclotron frequency with the PnA method (see Sec. 6.1.1 and Sec. 6.1.2). In these traps, the cyclotron detector will ensure an efficient cooling of the cyclotron mode during the whole measurement process and, in particular, during the measurement of ν_+ with the PnA.
Trap 1 and 4 will serve as ion containers to enable a fast exchange of the two species in the measurement traps. In these traps, no high-precision measurements will be performed and the detectors are only needed for the ion identification and pre-cooling of the ions. Thus, both traps will share an axial detector and a cyclotron detector via a capacitive coupling.
The remaining trap 5 will potentially be used to monitor magnetic field fluctuations or serve as a voltage reference for the voltage supply in the measurement traps. In both cases, a continuous monitoring of the axial and the reduced cyclotron frequency is of importance. Thus, this trap will be equipped with an individual axial and cyclotron detector. In trap 5, the axial signal is picked up at the correction electrode for higher signal strengths in case lower charge states are used for the monitor ions.
In order to provide four axial and four cyclotron detectors, the prototypes presented in

[8] Trap 3 and 4 might be used for the simultaneous measurement, in case of a better performance with respect to, e.g. the magnetic field homogeneity. Then, the wiring scheme discussed above will be applied to these traps.

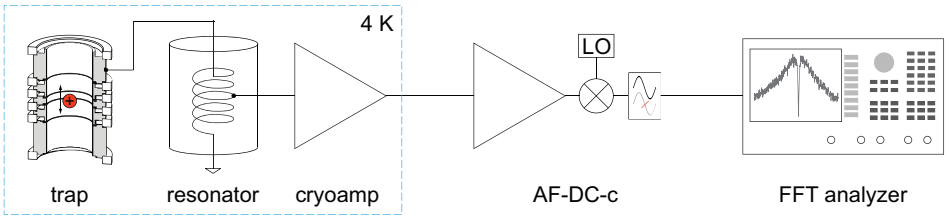

Figure 6.17: Total axial detection chain. The signals from the cryogenic detector are further amplified and downconverted at room temperature by the AF-DC-c amplifier and recorded by an FFT analyzer.

Sec. 6.3 and Sec. 6.6 are copied and the final assembly and performance will be discussed in the Ph.D. thesis of A. Dörr [216].

6.6.2 Room Temperature Electronics

In the total setup of a detection chain, the ion signals provided by the cryogenic detectors are guided to room temperature, where they are analyzed by a fast fourier transform (FFT) analyzer. In order to make the noise floor of the FFT negligible, the signals are further boosted at room temperature by an additional amplifier. Moreover, the spectral range of FFT analyzers is typically limited to a bandwidth up to ~ 100 kHz due to the limited sampling rate of the analog-to-digital converters used in the devices. As an example, the bandwidth of the Agilent 35670A used within this thesis is limited to 102 kHz. Thus, both the axial and the cyclotron signals have to be down-converted in advance.
For the axial detection, both requirements will be provided by a room temperature amplifier with an integrated down converter, the AF-DC-c. For PENTATRAP, the schematic of this commercial amplifier was bought from *Stahl-Electronics* and set up by A. Dörr. The amplifier features a gain of ~ 34 dB and a low input-related noise voltage density of 0.75 nV/$\sqrt{\text{Hz}}$. The downconverter offers a suppression of the lower sideband of more than 55 dB. For the suppression, the input signal is split into two separate signals prior to the downconversion. A proper phase shifting of the corresponding local oscillator signals and the down-converted signals leads to destructive or constructive superposition for signals from the lower or upper sideband after summation. The total axial chain is shown schematically in Fig. 6.17.
For the cyclotron detection, the commercial room temperature amplifier ZFL-500LN and the downconverter ZAD-6+ (both *MiniCircuits*) will be used.

6.7 Properties of the Detection System: Summary Table

For an overview, the main properties of the cryogenic detection systems developed within this thesis are summarized in the following table.

Table 6.3: Summary of the Cryogenic Detection-System Properties.

free resonator	axial	cyclotron
coil geometry	toroidal	helical
wire material	NbTi	Cu
wire insulation	PTFE	bare wire
diameter wire (mm)	0.075	1
turns	~ 800	15
wire length (m)	~ 59.4	1.25
L (mH)	3.2	0.0023
C_p (pF)	7.1	3.2
ν_0 (kHz)	841.79	59261.0
Q	65000	4000
R_p (MΩ)	1105	3.4
R_s (mΩ)	259	213

amplifier	axial	cyclotron
gain (dB)	15.6	15.8
power dissipation (mW)	9 (at $U_\mathrm{d} = 3$ V)	3 (at $U_\mathrm{d} = 3$ V)
e_n (nV/$\sqrt{\mathrm{Hz}}$)	0.61 (at 680 kHz)	0.5 (> 20 MHz)
i_n (fA/$\sqrt{\mathrm{Hz}}$)	3.7 ± 3	not measured
R_in (MΩ)	11.3	0.7
C_in (pF)	2.1	1.1

combined	axial	cyclotron
$\widetilde{C}_\mathrm{sim}$ (pF)	10	15
κ	0.33	0.67
ν (kHz)	661.07	24135
Q	7000	1570
R_p (MΩ)	93	0.525

Part II

Q-Value of Double-Electron Capture in ^{152}Gd and ^{164}Er

7 Search for $0\nu\epsilon\epsilon$ Candidates

As discussed in Sec. 2.1.4, an observation of neutrinoless double-electron capture ($0\nu\epsilon\epsilon$) would reveal the Majorana nature of the neutrino. Moreover, a measurement of the half-life of this process would give access to the effective Majorana mass $m_{\beta\beta}$. However, this process was ignored for a long time by theory and experiments due to the excessively long life-times expected for this second-order weak-interaction transition. On the other hand, a possible resonant enhancement of the transition rate in the case of energetic degeneracy of the mother atom and the excited daughter atom has recently awakened theoretical and experimental interest. For the $0\nu\epsilon\epsilon$-transitions with perfect degeneracy, life-times are expected to be competitive with neutrinoless double-β decay, where experiments are already running in search for the same neutrino aspects.
In order to identify suitable candidates for the observation of neutrinoless double-electron capture, both parts of Eq. (2.23), the lepton-number violating potential $V_{\epsilon\epsilon}$ and the resonance-enhancement factor $r_{\epsilon\epsilon}$, have to be investigated. In [101], a guideline for the theoretical description of the resonant enhancement of $0\nu\epsilon\epsilon$ is given (see Sec. 2.1.4). Moreover, a list of 21 likely resonant transitions is provided, where the degeneracy of the mother nucleus and the excited daughter nucleus lies within three standard deviations of the uncertainty of their ground-state masses. Within this framework and on the assumption of $|m_{\beta\beta}| = 1$ eV, lower bounds of half-lives of $\sim 10^{22}$ years were estimated in the most promising scenario. This is about 100 times below predictions for $0\nu\beta\beta$-rates. Other lists of candidates are proposed in [35, 84, 218, 219].
However, the selection of a candidate is hampered by large uncertainties in experimental data entering the resonance-enhancement factor in Eq. (2.23),

$$r_{\epsilon\epsilon} = \frac{\Gamma}{\Delta^2 + (\Gamma/2)^2} = \frac{\Gamma}{(Q_{\epsilon\epsilon} - B_{2\mathrm{h}} - E_\gamma)^2 + (\Gamma/2)^2}. \tag{7.1}$$

While uncertainties of binding energies and decay widths are on the order of a few eV, uncertainties of ground state mass differences $Q_{\epsilon\epsilon}$ are, in most cases, still on the keV level. Hence, the estimates have large uncertainties spanning over several orders of magnitude. With the progress in Penning-trap mass spectrometry [26], an improvement of those limits is certainly possible and new measurements on $Q_{\epsilon\epsilon}$-values were triggered recently (see Sec. 9.3.1).

Table 7.1: Estimates of the properties of the $\epsilon\epsilon$-transitions in ^{152}Gd and ^{164}Er. The values for the mass excess are taken from [147]. The total decay energy $Q_{\epsilon\epsilon}$ is the difference of the mass excesses of the isobars. As a crude estimate for the hole binding energies, the corresponding electron binding energies B_{2e^-} are taken from [105]. The sum of the two corresponding decay widths can be calculated from [108]. All values are given in keV except otherwise stated.

nuclide	mass excess	$\epsilon\epsilon$-transition	$Q_{\epsilon\epsilon}$	orbital	B_{2e^-}	Γ (eV)
^{152}Gd	−74714.2(2.5)	$^{152}_{64}\mathrm{Gd} \rightarrow {}^{152}_{62}\mathrm{Sm}$	54.6(3.5)	$1s, 2s$	54.6	24.8(2.5)
^{152}Sm	−74768.8(2.5)					
^{164}Er	−65950.0(3.0)	$^{164}_{68}\mathrm{Er} \rightarrow {}^{164}_{66}\mathrm{Dy}$	23.3(3.9)	$2s, 2s$	18.1	8.0(2.0)
^{164}Dy	−65973.3(2.5)					

7.1 Double-Electron Capture in ^{152}Gd and ^{164}Er

The most promising candidates for $0\nu\epsilon\epsilon$ are $0^+ \rightarrow 0^+$ transitions between nuclear ground states, accompanied by the capture of electrons from the K or L shell (see Sec. 2.1.4). In this case, the nuclear matrix elements $M^{0\nu}(J^\pi_\mathrm{f})$ and the electron wave-function factor $\mathcal{A}_{\alpha\beta}$ are expected to be maximal [101]. In total, 12 transitions are known to fulfill those requirements [218].
In order to estimate the resonance-enhancement factor $r_{\epsilon\epsilon}$, the $Q_{\epsilon\epsilon}$-values can be calculated from the difference in mass excesses[1] of the coressponding isobars [147]. Furthermore, the binding energies of the hole states $B_{2\mathrm{h}}$ can be approximated by the sum of the binding energies of the corresponding electron states B_{2e^-}, which can be found in [105]. Furthermore, the decay widths of these states can be found in [108].
An analysis of the 12 transitions shows that only two transitions, ^{152}Gd $\rightarrow$ ^{152}Sm and ^{164}Er $\rightarrow$ ^{164}Dy, might fulfill the resonance condition $\Delta = 0$ within approximately one standard error of the experimental data. The relevant parameters are given in Tab. 7.1. Among the other listed transitions, only for ^{180}W $\rightarrow$ ^{180}Hf the degeneracy is possibly within three standard errors, whereas for the remaining candidates the degeneracy can be excluded by their ground-state masses (see Fig. 9.15).
In Tab. 7.1, the present uncertainties of the $Q_{\epsilon\epsilon}$-values of ^{152}Gd and ^{164}Er, calculated from ground state masses, are greater than 3 keV, which restricts a precise prediction of $r_{\epsilon\epsilon}$ and, thereby, the decay rate $\lambda_{\epsilon\epsilon}$. A significant reduction of those uncertainties by a direct determination of the $Q_{\epsilon\epsilon}$-values is presented in Chap. 9 .

[1] The mass excess is defined as the difference $[M - A]$ between actual mass M and the mass number A of a nuclide, with M given in atomic mass units u = 931494.0090(71) keV (see [67] and references therein).

7.2 Total Decay Energy and Penning-Trap Mass Spectrometry

The Q-value of the double-electron process $Q_{\epsilon\epsilon}$ is defined as the total energy difference between the mother and daughter nuclides. Due to Einstein's energy-to-mass relation $E = mc^2$, the total energy of the nuclear decay can be written as the mass difference

$$Q_{\epsilon\epsilon} = \Delta E = (M_\mathrm{i} - M_\mathrm{f}) \cdot c^2. \tag{7.2}$$

Here, M_i and M_f are the masses of the neutral atoms in the initial and final state, respectively. In the presented experiments, the mass difference is measured by the determination of the free cyclotron frequency $\omega_\mathrm{c} = qB/m$. Here, m denotes the mass of the ions. For the singly charged mother and daughter ions, it is given by

$$m_\mathrm{i,f} = M_\mathrm{i,f} - m_e + B_\mathrm{i,f}/c^2, \tag{7.3}$$

differing from the neutral atom mass by the mass of the free electron m_e and its binding energy $B_\mathrm{i,f}$. Thus, the energy difference can be expressed as[2]

$$\begin{aligned} Q_{\epsilon\epsilon} &= M_\mathrm{i} - M_\mathrm{f} \\ &= (M_\mathrm{f} - m_e)\left(\frac{\omega_\mathrm{c,f}}{\omega_\mathrm{c,i}} - 1\right) + \frac{\omega_\mathrm{c,f}}{\omega_\mathrm{c,i}} B_\mathrm{f} - B_\mathrm{i} \\ &= (M_\mathrm{f} - m_e)\,(R-1) + RB_\mathrm{f} - B_\mathrm{i}, \end{aligned} \tag{7.4}$$

with the ratio of the cyclotron frequencies of the mother and daughter ion

$$R = \frac{\omega_\mathrm{c,f}}{\omega_\mathrm{c,i}}. \tag{7.5}$$

The $Q_{\epsilon\epsilon}$-values for ^{152}Gd and ^{164}Er are in the order of 55 keV and 23 keV (see Tab. 7.1 and Chap. 9). Following from that, $R - 1$ is in the order of few 10^{-7}. Furthermore, the difference in electron binding energies is typically in the order of a few eVs or below [220]. Thus, the last two summands in Eq. (7.4) can be neglected for the aimed precision in our experiments and the expression reduces to

$$Q_{\epsilon\epsilon} = (M_\mathrm{f} - m_e)\,(R-1)\,. \tag{7.6}$$

The final relative uncertainty of $Q_{\epsilon\epsilon}$ is given by

$$\frac{\delta Q_{\epsilon\epsilon}}{Q_{\epsilon\epsilon}} = \sqrt{\left(\frac{\delta M_\mathrm{f}}{M_\mathrm{f} - m_e}\right)^2 + \left(\frac{\delta m_e}{M_\mathrm{f} - m_e}\right)^2 + \left(\frac{\delta R}{R-1}\right)^2}. \tag{7.7}$$

[2] Following the convention in literature, the factor c is set to unity.

The determination of the $Q_{\epsilon\epsilon}$-value to an absolute uncertainty of $\lesssim 100$ eV (see Sec. 7.1) requires $\delta Q_{\epsilon\epsilon}/Q_{\epsilon\epsilon} \sim 2 \cdot 10^{-3}$ and $\sim 4 \cdot 10^{-3}$ for ^{152}Gd and ^{164}Er, respectively. On that scale, the contributions of the atomic mass and the electron mass are negligible and the final uncertainty will be dominated by the error of the frequency ratio R:

$$\frac{\delta Q_{\epsilon\epsilon}}{Q_{\epsilon\epsilon}} \approx \frac{\delta R}{R-1}. \tag{7.8}$$

For $R - 1 \sim 10^{-7}$, as in our case, an uncertainty of $\delta R/R \lesssim 10^{-9}$ is required.

8 The Penning-Trap Mass Spectrometer SHIPTRAP

The SHIPTRAP mass spectrometer at GSI, Darmstadt, is built for direct high-precision mass measurements of heavy and superheavy radionuclides, where the first direct mass measurements of transuranium isotopes, $^{252-254}_{102}$No and $^{255,256}_{103}$Lr, were realized [221–223]. These nuclides are part of α-decay chains, starting at superheavy elements in the $Z \sim 120$ region. Thus, precise mass values of such elements together with the α energy allow for an indirect determination of the masses of superheavy elements, which are not accessible for direct mass measurements. Furthermore, those measurements can give important information to theoretical mass models [224–226] and, thus, help to localize an island of stability in the superheavy mass region. Besides the superheavy elements, mass measurements performed with SHIPTRAP have contributed to many fields of physics, e.g., nuclear astrophysics [227, 228] and mapping of the proton drip-line [229].
Recently, measurements at SHIPTRAP addressed fundamental questions in neutrino physics [230–233]. In Chap. 9, the determination of the Q-values of double-electron capture in ^{152}Gd and ^{164}Er are presented (see also [106, 234]).

8.1 Experimental Overview

For mass measurements on heavy radionuclides, SHIPTRAP is installed downstream of the SHIP (Separator for Heavy Ion reaction Products) velocity filter [235] at GSI, Darmstadt, where the superheavy elements with $Z = 107 - 112$ were discovered [236]. Those kind of nuclides are produced in fusion-evaporation reactions caused by the interaction of heavy nuclides from a target with a primary beam, which originates from a 14-GHz-ECR ion source [237] and is accelerated in the GSI UNILAC (UNIversal Linear ACcelerator). Within the SHIPTRAP facility, those highly-energetic reaction products are stopped in a gas cell [238, 239] and prepared for the mass measurements in dedicated Penning traps by a RFQ cooler and buncher [240, 241]. In addition, the traps can be loaded from off-line ion sources. For the presented measurements, the off-line setup shown in Fig. 8.1 was exclusively used.

Ion Source

The laser ablation ion source was originally used at SHIPTRAP for mass calibrations with carbon clusters [242, 243]. Those clusters are the preferred reference for absolute mass measurements, due to the definition of the atomic mass unit $m_u = m(^{12}C)/12$.

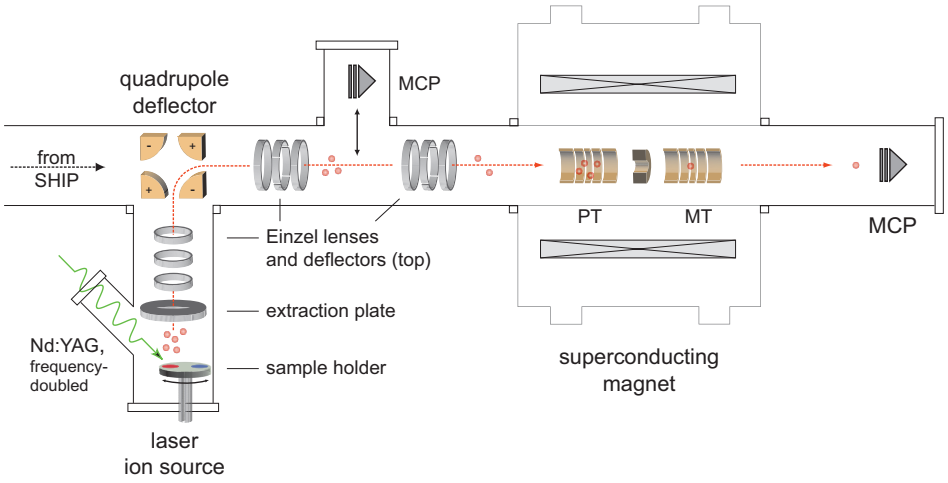

Figure 8.1: Sectional view of the off-line setup at SHIPTRAP. The ions are produced with a laser ablation source, perpendicular to the on-line beam axis. An electrostatic quadrupole deflects the ions by 90°. On axis, ions are guided by an Einzel lenses towards the Penning traps. In the preparation trap (PT), the ions are mass selectively centered and send to the measurement trap (MT), where the cyclotron-frequency measurement takes place.

Additionally, the low molecular binding energy ($\sim$ eV) of the clusters are negligible at the current level of precision, enabling it as a precise absolute reference close to the mass of the ion of interest by reducing mass dependent systematic shifts [244]. The ion source consists of a frequency-doubled Nd:YAG laser, a rotatable sample holder, an extraction electrode and a system of Einzel lenses for ion transport (see Fig. 8.1). The frequency-doubled Nd:YAG laser (532 nm) has a typical pulse duration of $3-5$ ns and a pulse energy of $4-12$ mJ. The laser beam is focussed to a diameter of about 1 mm on the target, where the target material is ionized by laser induced desorption, fragmentation and ionization. The laser is pulsed once per measurement cycle (typical ~ 1 Hz). By biasing the sample holder and the extraction plate, the ion energy can be adjusted for the injection into the trap.

Transfer Section

In the transfer section, the ions are deflected by 90° towards the trap axis by an electrostatic quadrupole deflector [243]. Downstream, the ion beam is focussed and steered by ion-optical elements into the Penning traps. A MCP detector for ion-beam monitoring can be swapped in and out of the beam line.

Penning Traps and Superconducting Magnet

The Penning-trap system of SHIPTRAP, shown in Fig. 8.2, consists of two cylindrical Penning traps, the preparation trap (PT) and the measurement trap (MT) [245]. The design of the preparation trap offers a high capture efficiency, mainly due to the

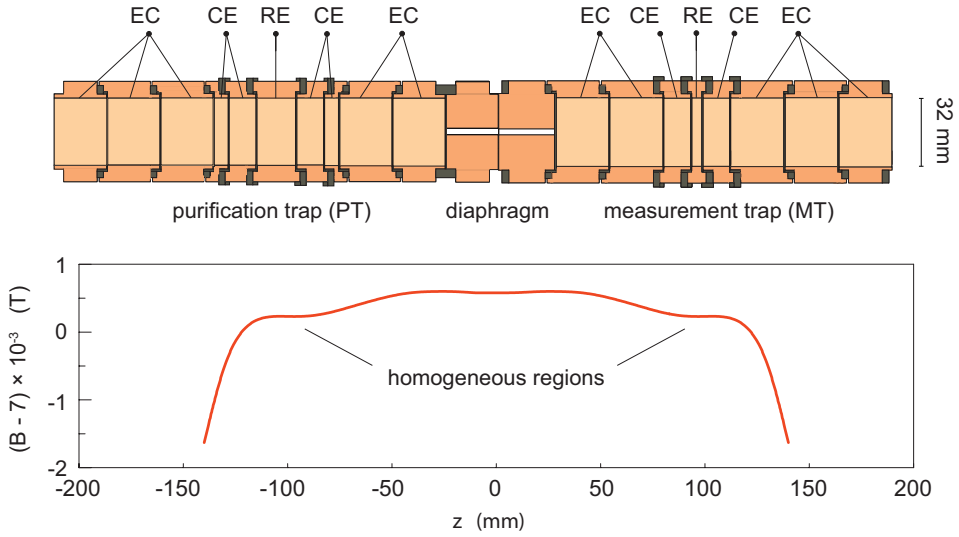

Figure 8.2: Schematic of the trap electrodes at SHIPTRAP (top). On the left, the 7-pole purification trap for mass separation is shown, which consists of segmented endcaps (EC), four correction electrodes (CE) and one ring electrode (RE). On the right, the 5-pole measurement trap is shown, where the actual mass measurements take place. The traps are separated by a diaphragm with a length of 52 mm and an inner diameter of 1.5 mm. The centers of the traps are located at two homogeneous field regions of the 7-T superconducting magnet (bottom).

cylindrical structure with a large inner diameter of 32 mm. In this trap, the mass-selective buffer gas cooling technique [246] with, typically, helium at a pressure of a few 10^{-6} mbar, is applied (see Sec. 8.2.1). Only the selected mass can pass the diaphragm between the two traps, which acts, in addition, as a pumping barrier between the PT and the MT[1].
The measurement trap has a five-pole structure with a pair of correction electrodes for anharmonicity compensation. The trap geometry, with an inner diameter of 32 mm, is chosen to be *orthogonal* (see Sec. 5.2.1). In this trap, the mass of the ions is measured with the time-of-flight technique (see Sec. 8.2.2). More details about the design of the traps can be found in [245].

The traps are located in a 7-T superconducting magnet with two homogeneous field regions at the center of the MT and PT, respectively, as shown in Fig. 8.2 (bottom). The relative spatial homogeneity $\Delta B/B$ in the central volume of 1 cm^3 is 1 ppm for the PT and 0.14 ppm for the MT. The long-term stability, due to a residual finite resistance of the superconducting coils [247, 248], was measured over 440 days to be $\Delta B/B = -4.063(7) \times 10^{-10}$/h [249]. In addition, short-term non-linear B-field changes are dominated by temperature and pressure variations[2] of the environment [249]. The tempera-

[1] The pressure in the measurement trap is below 10^{-7} mbar even if the PT is filled to 10^{-5} mbar.
[2] The influence on the magnetic field mainly results from the temperature dependence of the magnetic susceptibility of the material surrounding the traps.

ture dependence was measured to be $\Delta B/B = 2.9(2) \times 10^{-10}$/mK, while pressure variations in the liquid helium reservoir lead to changes of $\Delta B/B = 1.24(3) \times 10^{-8}$/mbar. A pressure and temperature stabilization system was installed at the magnet setup to limit the relative uncertainty of the magnetic field to $\delta B/B = 7.60(64) \times 10^{-11}$/h during typical daily fluctuations of ambient conditions [249].

8.2 Ion Manipulation and Detection

For high-precision mass measurements, the preparation of a pure ion cloud, cooling of the ion motions, and the determination of the free cyclotron frequency with high resolution is essential. At SHIPTRAP, the main techniques are the mass-selective buffer-gas cooling in the preparation trap as well as the time of flight-ion cyclotron resonance detection in the measurement trap.

8.2.1 Buffer-Gas Cooling

Cooling techniques reduce the ion mode amplitudes and, thereby, minimize systematic effects at high amplitudes in the experiments (see Sec. 3.3). In Penning traps, several cooling techniques are possible, such as the restive cooling used at PENTATRAP (see Sec. 6.1.1). At SHIPTRAP, the buffer-gas cooling technique [246] developed for short-lived radionuclides is applied. In addition to the cooling effect, the ions can be centered due to their q/m-ratio and, in this way, ion clouds can be purified. A detailed description can be found in [250], where the principles are summarized in the following.
In a trap filled with a neutral buffer gas, the energy of the stored ions can be reduced due to collisions with the gas. Usually, a noble gas is used at a pressure of typically $\sim 10^{-6} - 10^{-4}$ mbar at room temperature. The damping effect can be approximated by a velocity-dependent viscous force $\vec{F} = -m\gamma\dot{\vec{r}}$ with damping coefficient

$$\gamma = \frac{q}{K_0}\frac{p_N}{T_N}. \tag{8.1}$$

Here, K_0 is the reduced ion mobility depending on the type of buffer gas, while $p_N = p/p_0$ is the pressure normalized to room temperature condition $p_0 = 1013$ mbar, as well as the temperature $T_N = T/T_0$ normalized to $T_0 = 300$ K. In presence of the electrical field $\vec{E}$ and the magnetic field $\vec{B}$ of the Penning trap, the equation of motion becomes

$$m\ddot{\vec{r}} = q\left(\vec{E} + \dot{\vec{r}} \times \vec{B}\right) - \gamma m\dot{\vec{r}}, \tag{8.2}$$

and it follows that in the presence of buffer gas, the eigenfrequencies are modified[3] by

$$\tilde{\omega}_{\pm} = \omega_{\pm} \pm \left(\frac{\gamma}{2}\right)^2 \frac{8\omega_z^2 + \gamma_2}{(\omega_c^2 - 2\omega_z^2)^{3/2}}, \tag{8.3a}$$

$$\tilde{\omega}_z = \omega_z \cdot \sqrt{1 - \left(\frac{\gamma}{2\omega_z}\right)^2}. \tag{8.3b}$$

The axial amplitude decreases with $z(t) = \rho_z \cdot e^{-\gamma/2 \cdot t}$ and the radial amplitudes become time-dependent by $\rho_{\pm}(t) = \rho_{\pm} e^{-\alpha_{\pm} t}$, with a radial damping coefficient

$$\alpha_{\pm} = \frac{\gamma}{2}\left[1 \pm \left(1 + \frac{1}{8} \cdot \frac{8\omega_z^2 + \gamma^2}{\omega_c^2 - 2\omega_z^2}\right)\right]. \tag{8.4}$$

For this damping coefficients, the relations $\alpha_+ > 0$, $\alpha_- < 0$ and $|\alpha_+| > |\alpha_-|$ follow from Eq. (3.5b). Hence, in the presence of buffer gas, the modified cyclotron amplitude decreases faster than the magnetron amplitude increases. To achieve a reduction of the magnetron amplitude and, thus, to center the ions in the trap, a radial quadrupolar excitation at ω_c can be used (see Sec. B). This couples the two radial modes to each other and action is transferred between them. In the presence of this coupling, the magnetron amplitude is periodically converted into the modified cyclotron amplitude and therefore effectively decreased by the decrease of ρ_+. This process depends on the q/m-ratio of the ions, due to the dependence on the sideband frequency $\omega_c = \omega_+ + \omega_-$. Therefore, it can be used to select a certain species from an impure ion cloud.

8.2.2 Time-Of-Flight Detection

The Time-Of-Flight Ion-Cyclotron-Resonance (TOF-ICR) detection technique is based on the measurement of the flight time of ions ejected from the trap. Due to the interaction of their angular magnetic moment with the magnetic-field gradient outside the trap, the flight time depends on the radial energy of the ions, which can be resonantly excited by application of a quadrupolar rf-field at the free cyclotron frequency. This method was first applied to the measurement of the proton-to-electron mass ratio [17]. A detailed description of the line-shapes can be found in [252].
Due to its destructive nature (the ion is lost after ejection), this method is especially suitable for short-lived ions, where the storage time is limited by their half-life. Currently, this is the only detection technique used at SHIPTRAP.

[3] Usually, frequency shifts in the presence of buffer gas are irrelevant, since buffer gas cooling is only applied in traps used for ion preparation. In traps used for the mass measurements, the rest gas pressure is kept sufficiently low, such that these shifts can safely be neglected [251].

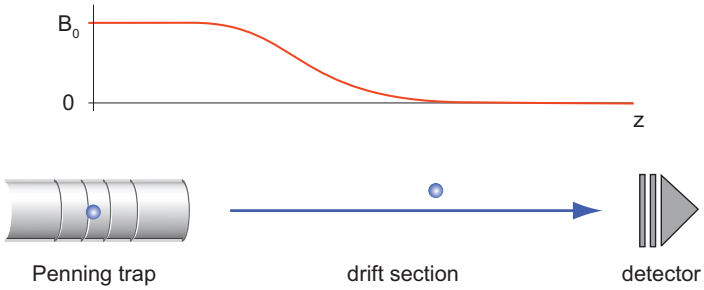

Figure 8.3: Schematic of the experimental setup for the time-of-flight (TOF) technique. The ions are ejected from the trap and sent through a magnetic field gradient (red line) in the drift section. The time-of-flight is typically measured as the difference between the ejection and the arrival at an MCP detector.

TOF Effect

The angular magnetic moment $\vec{\mu}$ of an ion can be calculated from its radial motion in Eq. (A.11). The mean value is given by

$$\vec{\mu} = -\frac{q}{2}\left(\rho_+^2\omega_+ + \rho_-^2\omega_-\right)\hat{z}. \tag{8.5}$$

For a pure cyclotron motion with $\omega_c = qB_0/m \approx \omega_+ \gg \omega_-$ in a magnetic field B_0, the magnetic moment can be written as

$$\vec{\mu} = -\frac{E_r}{B_0}\hat{z}, \tag{8.6}$$

where $E_r = \frac{m}{2}\omega_+^2\rho_+^2$ is the radial kinetic energy of the ion. If the ions are ejected from the trap (see Fig. 8.3), the interaction of the magnetic moment and the magnetic field causes a force $\vec{F} = -\vec{\nabla}(-\vec{\mu}\vec{B})$. For typical experimental conditions, the magnetic moment is constant during the flight, due to an adiabatic motion. Thus, the force is given by

$$\vec{F} = -\frac{E_r}{B_0}\left(\vec{\nabla}\vec{B}\right)\hat{z} = -\frac{E_r}{B_0}\frac{\partial B}{\partial z}\hat{z}. \tag{8.7}$$

The total flight time of the ion in presence of this force can be calculated to

$$T(E_r) = \int_0^{z_{det}} dz \cdot \sqrt{\frac{m}{2\Big(E_0 - qV(z) - \mu(E_r)B(z)\Big)}}, \tag{8.8}$$

where E_0 is the total initial energy of the ion, and $V(z)$ and $B(z)$ are the electric and magnetic fields along the ion path from the trap to the detector, which is located at the position z_{det}.

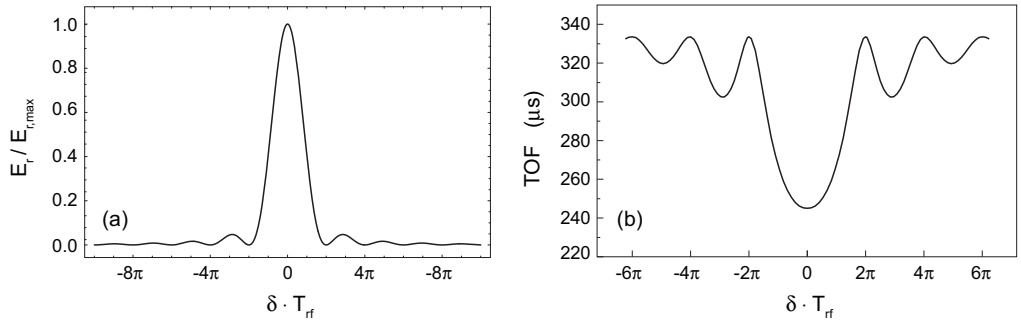

Figure 8.4: (a) Radial energy at the end of the quadrupolar excitation as a function of the detuning δ. The excitation time is chosen as $T_{\mathrm{rf}} = \pi/\Omega_0$. (b) Resulting time-of-flight spectrum $T(E_r)$. The global minimum is located at $\delta = 0$, according to $\omega = \omega_{\mathrm{c}}$. The times given here are arbitrary.

Action Transfer and Line-Shape

The dependence of the magnetic moment $\mu(E_{\mathrm{r}})$ and, therefore, the flight time $T(E_{\mathrm{r}})$ on the radial energy can be used for the measurement of the free cyclotron frequency ω_{c}. For this purpose, ions initially at rest are prepared in a pure magnetron motion by the application of a dipolar excitation at ω_- (see Sec. B). Subsequently, an quadrupolar excitation is applied during a time T_{rf}. Typically, this time is chosen as $T_{\mathrm{rf}} = T_{\mathrm{conv}} = \pi/\Omega_0$, where Ω_0 is given by Eq. (B.7). Hence, for a resonant excitation at $\omega_{\mathrm{rf}} = \omega_+ + \omega_- = \omega_{\mathrm{c}}$, the magnetron radius ρ_- is fully converted into the modified cyclotron radius ρ_+. The resulting radial energy is given by $E_{\mathrm{r}} = \frac{m}{2}\omega_+^2 \cdot \rho_+^2(T_{\mathrm{rf}})$.
For non-resonant excitation with detuning $\delta = \omega_{\mathrm{rf}} - \omega_{\mathrm{c}}$, the conversion of the radii is incomplete. The energy transfer as a function of δ depends strongly on the envelope of the excitation signal. For a rectangular excitation scheme (the coupling drive is simply turned on for the time T_{rf}), the final radial kinetic energy is given by

$$E_{\mathrm{r}} \propto \frac{\sin^2(\omega_b T_{\mathrm{rf}})}{\omega_b^2}, \qquad \text{with} \quad \omega_{\mathrm{b}} = \frac{1}{2}\sqrt{\delta^2 + \left(\frac{\Omega_0}{2}\right)^2}. \tag{8.9}$$

In Fig. 8.4a, the radial energy after the quadrupolar excitation is calculated as a function of the detuning δ. The excitation time is chosen as $T_{\mathrm{rf}} = \pi/\Omega_0$. Only at $\delta = 0$, the action is fully converted from the magnetron to the modified cyclotron mode. Hence, the flight time in Eq. (8.8) has a global minimum at resonance, which is shown in Fig. 8.4b.
The mass resolving power $\mathfrak{R}$, defined by the full width at half maximum $\Delta\omega_{\mathrm{c}}$ of the resulting cyclotron resonance, is mainly determined by the excitation time T_{rf}. It can be written as

$$\mathfrak{R} = \frac{m}{\Delta m} = \frac{\omega_{\mathrm{c}}}{\Delta\omega_{\mathrm{c}}} \approx \omega_{\mathrm{c}} T_{\mathrm{rf}}. \tag{8.10}$$

The approximation reflects the Fourier limitation of this measurement technique [252].

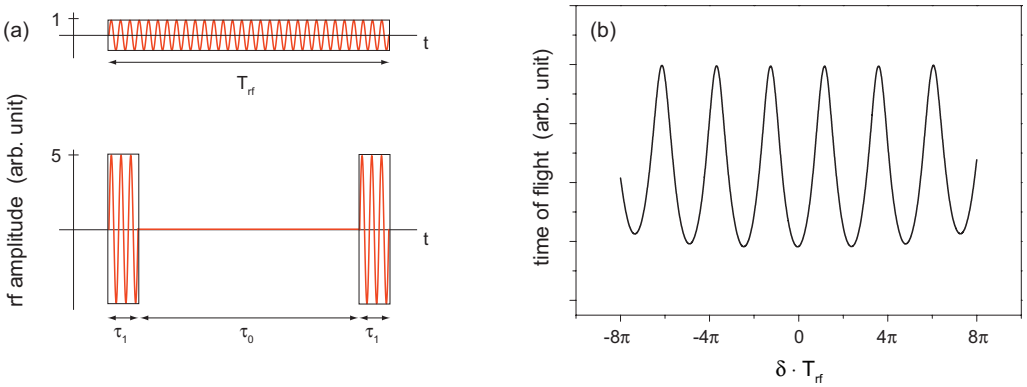

Figure 8.5: (a) Single excitation pulse with length T_{rf} (top). Ramsey excitation pulses with the same product of amplitude and applied excitation time (bottom). For both schemes, a full conversion of magnetron to radial action is obtained for resonant excitation at $\omega_{\mathrm{rf}} = \omega_{\mathrm{c}}$. (b) Theoretical line-shape for the Ramsey scheme.

Ramsey Method

An elegant way to reduce the line width of TOF-ICR measurements was introduced in [253–255]. The idea of this method is illustrated in Fig. 8.5a. The rectangular excitation pulse with length T_{rf} is replaced by time-separated pulses with length τ_1, while the product of the amplitude and the total applied excitation time (T_{rf} or $2\tau_1$) is kept constant. For this case, in both schemes a full conversion of magnetron to cyclotron action is obtained for $\omega_{\mathrm{rf}} = \omega_{\mathrm{c}}$ [254]. In analogy to the Ramsey method of spatially separated oscillatory fields, the latter one is called *Ramsey method* in time-of-flight mass spectrometry.

For non-resonant excitation in the Ramsey scheme, the action conversion depends, besides the strength and total length $\tau_1 + 2\tau_2$, on the ratio $2\tau_1/\tau_0$ of the applied excitation time to the waiting time. A calculated TOF line-shape is shown in Fig. 8.5b. For the same total excitation time $T_{\mathrm{rf}} = \tau_0 + 2\tau_1$ and with the same number of total ions, improvements up to a factor three have been demonstrated in the precision of the determination of ω_{c}, compared to the standard technique with single excitation pulse. This is not only due to the narrower line-width, but also due to the steeper resonance profile with more pronounced sidebands, which improves the uncertainty of fits to measured data.

9 Q-Value Determination

In search for a transition suitable for the observation of neutrinoless double-electron capture ($0\nu\epsilon\epsilon$), precise Q-values are of special importance for the estimate of the magnitude of the resonance enhancement and, ultimately, the decay rate of this process. In Penning-trap mass spectrometry, the Q-value determination is equivalent to a measurement of the frequency ratio of the ions of the mother and daughter nuclide (see Chap. 7). Within this thesis, such measurements on the transitions $^{152}_{64}\mathrm{Gd} \rightarrow {}^{152}_{62}\mathrm{Sm}$ and $^{164}_{68}\mathrm{Er} \rightarrow {}^{164}_{66}\mathrm{Dy}$ were performed with the Penning-trap mass spectrometer SHIPTRAP, using the TOF-ICR technique.

9.1 Introductory Considerations

9.1.1 Alternating Measurement of the Frequency Ratios

For the determination of the Q-values of double-electron capture, the frequency ratios $R = \nu_{\mathrm{c,f}}/\nu_{\mathrm{c,i}}$ have to be determined. The two cyclotron frequencies are measured alternately at times t_i and t_f (see Fig. 9.1). Thus, the frequency ratio can be written as

$$R = \frac{\nu_{\mathrm{c,f}}(t_\mathrm{f})}{\nu_{\mathrm{c,i}}(t_\mathrm{i})} = \frac{q_\mathrm{f}}{q_\mathrm{i}}\frac{m_\mathrm{i}}{m_\mathrm{f}}\frac{B(t_\mathrm{f})}{B(t_\mathrm{i})}, \tag{9.1}$$

where $B(t_\mathrm{i})$ and $B(t_\mathrm{f})$ are the magnetic-field strengths averaged over the individual measurement times. In presence of a temporal drift of the mean magnetic field between two measurements, the magnetic field does not cancel in the ratio determination, leading to a shift of the ratio given by

$$\delta R = \frac{m_\mathrm{i}}{m_\mathrm{f}} \cdot \frac{B(t_\mathrm{f}) - B(t_\mathrm{i})}{B(t_\mathrm{i})}. \tag{9.2}$$

This uncertainty adds to the total uncertainty in the Q-value and might set the dominant limitation.

Interpolation Method

In order to extract the frequency ratio R from alternating measurements, a linear interpolation method is typically used at Penning traps utilizing the TOF detection method (see Fig. 9.1a). The ratio $R(t_\alpha)$ at the time t_α, where $\nu_{\mathrm{c,f}}$ of the final state is

measured, is given as

$$R(t_\alpha) = \frac{\nu_{\mathrm{c,f}}(t_\alpha)}{\widetilde{\nu}_{\mathrm{c,i}}(t_\alpha)}. \tag{9.3}$$

Here, $\widetilde{\nu}_{\mathrm{c,i}}(t_\alpha)$ is the linear interpolation between two measurements of $\nu_{\mathrm{c,i}}$ of the initial state. Hence, the relative uncertainty of R is given by

$$\frac{\delta R}{R} = \sqrt{\left(\frac{\delta\nu_{\mathrm{c,f}}}{\nu_{\mathrm{c,f}}}\right)^2 + \left(\frac{\delta\widetilde{\nu}^{\mathrm{total}}_{\mathrm{c,i}}}{\widetilde{\nu}^{\mathrm{total}}_{\mathrm{c,i}}}\right)^2}, \tag{9.4}$$

with $\delta\nu_{\mathrm{c,f}}$ denoting the measurement uncertainty of the final state and $\delta\widetilde{\nu}^{\mathrm{total}}_{\mathrm{c,i}}$ the total uncertainty of the interpolated frequency of the initial state. As indicated in Fig. 9.1a, the interpolated frequency can be calculated from the measured frequencies by

$$\widetilde{\nu}_{\mathrm{c,i}}(t_\alpha) = \nu_{\mathrm{c,i}}(t_\beta) + \frac{\nu_{\mathrm{c,i}}(t_{\beta+1}) - \nu_{\mathrm{c,i}}(t_\beta)}{t_{\beta+1} - t_\beta}\,(t_\alpha - t_\beta)\,, \tag{9.5}$$

where t_β and $t_{\beta+1}$ are the measurement times of the initial state. The total uncertainty of the interpolated frequency $\delta\widetilde{\nu}^{\mathrm{total}}_{\mathrm{c,i}}$ is a function of the measurement uncertainties $\delta\nu_{\mathrm{c,i}}(t_\beta)$ and $\delta\nu_{\mathrm{c,i}}(t_{\beta+1})$, and of temporal fluctuations. On one hand, the linear fluctuations are covered by error propagation in the linear interpolation in Eq. (9.5). The resulting uncertainty is given as

$$\delta\widetilde{\nu}^{\mathrm{lin}}_{\mathrm{c,i}}(t_\alpha) = \sqrt{\left(\frac{t_{\beta+1} - t_\alpha}{t_{\beta+1} - t_\beta}\right)^2 \left(\delta\nu_{\mathrm{c,i}}(t_\beta)\right)^2 + \left(\frac{t_\alpha - t_\beta}{t_{\beta+1} - t_\beta}\right)^2 \left(\delta\nu_{\mathrm{c,i}}(t_{\beta+1})\right)^2}. \tag{9.6}$$

On the other hand, non-linear fluctuations of the cyclotron frequencies (e.g. by magnetic field drifts) are not covered within the linear interpolation. If such deviations from the linear trend are known as a function of time, they can be taken into account by an additional non-linear uncertainty $\delta\nu^{\mathrm{nonl}}_{\mathrm{c,i}}/\nu_{\mathrm{c,i}}$. This uncertainty has to be added quadratically to the linear uncertainty of the interpolated frequency

$$\left.\frac{\delta\widetilde{\nu}^{\mathrm{total}}_{\mathrm{c,i}}}{\widetilde{\nu}_{\mathrm{c,i}}}\right|_{t_\alpha} = \sqrt{\left.\left(\frac{\delta\widetilde{\nu}^{\mathrm{lin}}_{\mathrm{c,i}}}{\widetilde{\nu}_{\mathrm{c,i}}}\right)^2\right|_{t_\alpha} + \left.\left(\frac{\delta\nu^{\mathrm{nonl}}_{\mathrm{c,i}}}{\nu_{\mathrm{c,i}}}\right)^2\right|_{\Delta t_{\alpha,\beta}}}, \tag{9.7}$$

where $\Delta t_{\alpha,\beta} = t_\alpha - t_\beta$ is the time difference between the first measurement of the interpolation t_β and the time t_α, to which the frequency is interpolated.

Polynomial Method

In the interpolation method, the cyclotron frequency of the species used for interpolation is calculated by $\widetilde{\nu}_{\mathrm{c}}(t) = qB(t)/(2\pi m)$, where the magnetic field is approximated

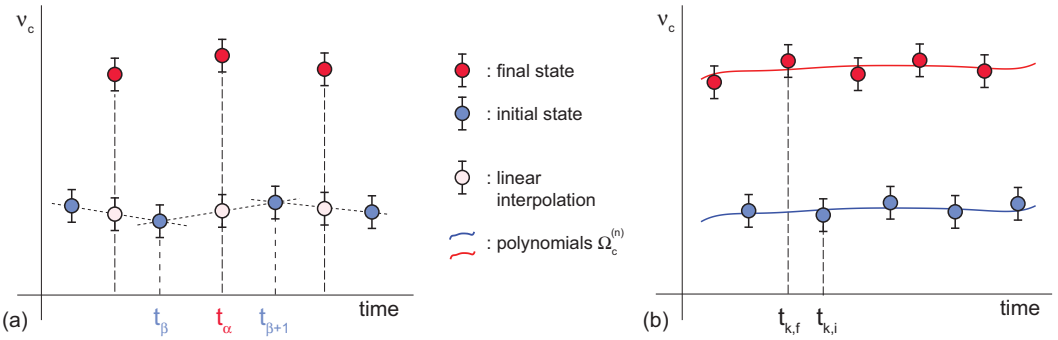

Figure 9.1: (a) Schematic of the interpolation method. The frequency of the initial state measured at times t_β and $t_{\beta+1}$ is linearly interpolated to the measurement time t_α, at which the final state is measured and the ratio R is calculated. (b) Schematic of the polynomial evaluation method. The polynomials given in Eq. (9.10) are simultaneously fitted to the frequency data of the initial and final state. The frequency ratio R can be extracted directly from the best fit.

by a polynomial to first order, and is given by

$$B(t) \approx \tilde{a}_0(t_\beta) + \tilde{a}_1(t_\beta, t_{\beta+1}) \cdot t. \tag{9.8}$$

The coefficients are defined in the short time interval $[t_\beta, t_{\beta+1}]$ and determined from the actual measurements at t_β and $t_{\beta+1}$. Subsequently, the determination is repeated for $\beta = [1, N-1]$, where N is the number of frequency measurements. Such an approximation is necessary, since the time-dependence of the magnetic field is unknown. As an alternative way of determining the frequency ratio R from the alternating measurements, the magnetic field $B(t)$ can be approximated by a polynomial of n-th order

$$B(t) \approx \sum_{k=0}^{n} a_k \cdot t^k, \tag{9.9}$$

which is routinely done for high-precision mass measurements in the group of Pritchard at MIT and later by Myers at FSU (see, e.g. [256]). In general, time-dependent coefficients a_k have to be assumed for the mapping real magnetic-field fluctuations. If we take time-independent coefficients, it greatly simplifies the method. However, it severely constrains the functional behavior of the polynomial to slow drifts within the measurement time. This is in contrast to the interpolation method, where the coefficients are adjusted for every time interval $[t_\beta, t_{\beta+1}]$.
In our case, typical daily variations of ambient conditions lead to very slow and smooth long-term drifts (see Sec. 9.1.2), and a polynomial with constant coefficients is expected to be a good approximation. The advantage of this method is, that it is less sensitive to random and fast fluctuations of the magnetic field and, hence, to outlying data points. However, the choice of the order n of the polynomial is important. If n is chosen too low, not all bumps of the long-term drift will be mapped, while a polynomial with too high order will tend to pin all random noise and short-term fluctuations on top of the drift. In order to extract the coefficients of Eq. (9.9) from the measurements, the time

dependence of the cyclotron frequencies of the initial and final state can be written as

$$\begin{aligned} \Omega^{(n)}_{\mathrm{c,f}}(t) = &\quad R \cdot \tfrac{q_\mathrm{i}}{m_\mathrm{i}} B(t) &\approx &\quad R \cdot \sum_{k=0}^{n} A_k \cdot t^k, \\ \Omega^{(n)}_{\mathrm{c,i}}(t) = &\quad \tfrac{q_\mathrm{i}}{m_\mathrm{i}} B(t) &\approx &\quad \sum_{k=0}^{n} A_k \cdot t^k, \end{aligned} \tag{9.10}$$

with $A_k = a_k \cdot q_\mathrm{i}/m_\mathrm{i}$. Consequently, the ratio R can be determined from a simultaneous fit to both alternating frequency data, which is indicated in Fig. 9.1b.
In order to find the best fit for a polynomial, the χ^2-criteria (see, e.g. [257]) can be used, which reads in our case

$$\chi^2 = \sum_{k=1}^{N} \frac{\left(\nu_k(t_k) - \Omega^{(n)}(t_k)\right)^2}{\delta\nu_k^2}. \tag{9.11}$$

Here, N is the number of frequency measurements ν_k with uncertainty $\delta\nu_k$ and $\Omega^{(n)}$ is the fitted polynomial. With increasing order n the fit will improve, and in the limiting case $n = N - 1$ the polynomial will go through every point with vanishing χ^2. In order to compare the quality of the fit for different orders of the polynomials, the so-called reduced χ^2 can be used, which is simply given by

$$\chi^2_\mathrm{red} = \frac{1}{\mathcal{F}} \cdot \chi^2. \tag{9.12}$$

$\mathcal{F}$ is the number of degrees of freedom, given by $\mathcal{F} = N - p - 1$, and p as the number of parameters used for the fit. A large χ^2_red indicates a poor fit, whereas $\chi^2_\mathrm{red} < 1$ shows that the polynomial is over fitting the data (e.g. due to over-estimated uncertainties $\delta\nu_k$). At $\chi^2_\mathrm{red} = 1$, the fit is in agreement with the error estimates.
For the simultaneous fit of the two polynomials, defined in Eq. (9.10), to the data of the initial- and final-state frequencies, both definitions can be modified to

$$\chi^2 \longmapsto \chi^2_\mathrm{f} + \chi^2_\mathrm{i} \qquad \text{and} \qquad \chi^2_\mathrm{red} \longmapsto \frac{1}{\widetilde{\mathcal{F}}} \left(\chi^2_\mathrm{f} + \chi^2_\mathrm{i}\right). \tag{9.13}$$

Here, χ_i and χ_f denote the individual chi-squared of the fit of the initial and final state, respectively. The normalization is given by $\widetilde{\mathcal{F}} = N_\mathrm{f} + N_\mathrm{i} - p - 1$, with N_f and N_i denoting the number of measurements of the final and initial state. In our case, the number of parameters for the fit is $p = n + 2$, given by the $n + 1$ coefficients of the polynomials and the ratio value R.
The best fit is found by minimizing χ^2 or χ^2_red, from which the frequency ratio R can be extracted to the best value $R = R_0$. Furthermore, the statistical uncertainty δR_stat of the ratio determination is typically defined by the relation

$$\chi^2_\mathrm{red}(R_0 + \delta R_\mathrm{stat}) - \chi^2_\mathrm{red}(R_0) = 1, \tag{9.14}$$

where the coefficients of the polynomials are fixed to the results of the best fit.

9.1.2 Error Estimation

For the $Q_{\epsilon\epsilon}$-values of the double-electron capture in ^{152}Gd and ^{164}Er, a final uncertainty of $\sim 10^{-9}$ for the frequency ratio is needed (see Sec. 7.2). The analysis of the systematic effects follows [258] and [259].

Uncertainty in Measurements of ν_c with TOF Resonances

A semi-empirical estimate for the statistical uncertainty $\delta\nu_c$ in the determination of a cyclotron frequency ν_c by conventional time-of-flight (TOF) techniques is proposed to be [260]

$$\delta\nu_c^{\mathrm{stat}} = \frac{C}{\sqrt{N}T_{\mathrm{rf}}}, \tag{9.15}$$

where N is the total number of ions in the resonance, T_{rf} is the excitation time of the TOF scheme and C is a constant, which is a function of the excitation pattern and the time-of-flight section of the apparatus. This relation is verified experimentally with C on the order of 0.9 for one-pulse excitation patterns [258].
For Ramsey excitation schemes (see Sec. 8.2.2), this uncertainty can be decreased due to an increased steepness of the line shape and more pronounced sidebands compared to conventional TOF resonances, which is advantageous for fitting procedures. Furthermore, the line width of the minimum is reduced. In [255], a reduction of the uncertainty by a factor of 3.4 at $T_{\mathrm{rf}} = 300$ ms and 2.5 at $T_{\mathrm{rf}} = 900$ ms is demonstrated, compared to one-pulse TOF resonances. At given T_{rf}, the reduction clearly scales with the waiting time between the two Ramsey pulses.

In the data set of a TOF resonance, each data point corresponds to the mean time of flight at the given rf frequency (see Fig. 9.3), while a fit of the theoretical line shape [254] provides the center frequency ν_c. For this purpose, an analysis program called EVA developed by S. Schwarz is used at SHIPTRAP and several other TOF Penning-trap mass spectrometers (e.g. ISOLTRAP [261], TRIGA-TRAP [262] and LEBIT [263]). This tool was developed for on-line mass measurements with low production rate and, thus, low statistics. As a consequence, in the internal determination of the errors of the individual data points the total distribution of the time-of-flight is used. The correct way would be to use only the TOF distribution measured at the corresponding rf frequency. As a result, for broad TOF distributions the errors of the individual data points and, consequently, the error of the center frequency $\delta\nu_c$ from the least-square fit is over-estimated. This effect is observed at several groups using EVA and is also visible in the analysis within this thesis (see Sec. 9.2.2) as well as in all recent Q-value measurements at SHIPTRAP.

Magnetic Field Drifts

In the alternating measurement of the cyclotron frequencies $\nu_{c,f}$ and $\nu_{c,i}$, temporal fluctuations of the magnetic field B are expected to dominate the ratio determination, due to the direct influence on $\nu_c = qB/(2\pi m)$ (see Sec. 9.1.1).
After subtracting the linear drift component of $\Delta B/B = -4.063(7)\times10^{-10}$/h, the residual relative uncertainty of the magnetic field was measured to $\delta B^{T+p}/B = 7.60(64) \cdot 10^{-11}$/h during typical daily fluctuations of ambient conditions [249]. With $\delta B^{T+p}/B = \delta\nu_c/\nu_c$, these fluctuations can be taken into account in the ratio determination by Eq. (9.7). In our case, the magnitude of these fluctuations sets the upper limit for the acquisition time of one resonance to less than a few hours.

Ion-Number Dependency

Sideband-frequency measurements are typically done with more than one ion in the trap in order to get as many ions as possible for the resonance determination, see Eq. (9.15). However, the resulting Coulomb interaction will modify the electric potential seen by the ions. The influence can be modeled by an image-charge potential induced in the trap electrodes. Theoretical models and experimental studies can be found in [168, 191] for hyperbolical traps. For cylindrical traps, a theoretical treatment is given in [192]. In both cases, it turns out that the image-charge shift on the sideband frequency $\nu_c = \nu_+ + \nu_-$ is zero (since $\Delta\nu_+ = -\Delta\nu_-$), if the ions are identical in mass. The effect on ions differing in mass, which is the case if contamination ions are present in the measurement trap, is studied extensively in [252, 264]. For a small number of ions, there are multiple resonance lines visible in the spectrum, if the resolving power is sufficiently high to separate them. For an increasing number of ions, the resonance frequencies approach each other while they are all shifted linearly towards lower frequencies [258]. Hence, the sign of the shift $\Delta\nu_c^{cont}$ of the resonance of the ion of interest depends on the mass difference to the contamination ions and their charge. Furthermore, the absolute value depends on the ratio of measurement ions to contaminations. Up to now, no analytical models exists for contamination shifts since perturbation of all eigenmotions due to the Coulomb interaction have to be taken into account.
Contaminations in the trap can be identified by an analysis of the resonance frequency as a function of the number of detected ions. The extrapolation of a linear fit to a single ion in the trap then gives the unperturbed cyclotron frequency.

Anharmonicities, Misalignment and Ellipticities

Cylindrical Penning traps, as used at SHIPTRAP (see Fig. 8.2), can only provide an nearly ideal quadrupolar trapping potential in a limited volume around the trap center. Additionally, misalignments of the trap electrodes or machining imperfections can give rise to additional higher-order contributions of the electrical field. A detailed discussion of the trapping potential can be found in Sec. 3.3.3, where the electrostatic potential is analyzed in terms of expansion coefficients $c_j = C_j/U_0$ of j-th order defined in

Eq. (3.21). Here, U_0 is the trap voltage. The leading anharmonic shift of the sideband frequency $\nu_\mathrm{c} = \nu_+ + \nu_-$ in 4-th and 6-th order is given as [259]

$$\Delta\nu_\mathrm{c}^\mathrm{el} = \Omega_\mathrm{c}^\mathrm{el}\left[\frac{3}{2}\frac{C_4}{d^2}(\rho_-^2 - \rho_+^2) + \frac{15}{4}\frac{C_6}{d^4}\left(\rho_z^2\left(\rho_-^2 - \rho_+^2\right) - \left(\rho_-^4 - \rho_+^4\right)\right)\right], \tag{9.16}$$

with

$$\Omega_\mathrm{c}^\mathrm{el} = \frac{\nu_-}{1 - \nu_-/\nu_+} \approx \nu_-. \tag{9.17}$$

Here, $\rho_{z,+,-}$ are the amplitudes of the ion motion, d is the characteristic trap dimension (~ 10 mm at SHIPTRAP) and ν_- is the magnetron frequency. From Eq. (9.16) it follows that the anharmonic shift can be reduced by cooling of the motional amplitudes as done in the preparation trap at SHIPTRAP. Furthermore, the correction electrodes of the traps allow for a partly compensation of the anharmonic contributions C_4 and C_6. In a first order approximation, the magnetron frequency ν_- depends only on the trap voltage U_0 and the magnetic field strength B. Thus, the anharmonic shift of Eq. (9.16) is mass independent to first order and, therefore, both frequencies of the ratio determination are shifted by the same amount (given identical radii). In contrast, the frequency-ratio shift in presence of such mass-independent frequency shifts gets mass-dependent. For singly-charged ions it is given by

$$\begin{aligned}\frac{\Delta R^m}{R} &= \frac{R(\nu_\mathrm{c,f} + \Delta\nu_\mathrm{c}, \nu_\mathrm{c,i} + \Delta\nu_\mathrm{c}) - R(\nu_\mathrm{c,f}, \nu_\mathrm{c,i})}{R(\nu_\mathrm{c,f}, \nu_\mathrm{c,i})} = \frac{\Delta\nu_\mathrm{c}(\nu_\mathrm{c,i} - \nu_\mathrm{c,f})}{\nu_\mathrm{c,i}(\nu_\mathrm{c,i} + \Delta\nu_\mathrm{c})} \cdot \frac{\nu_\mathrm{c,i}}{\nu_\mathrm{c,f}} \\ &\approx \frac{\Delta\nu_\mathrm{c}(\nu_\mathrm{c,i} - \nu_\mathrm{c,f})}{\nu_\mathrm{c,i}^2} \cdot \frac{\nu_\mathrm{c,i}}{\nu_\mathrm{c,f}} \propto \Delta\nu_\mathrm{c} \cdot (m_\mathrm{f} - m_\mathrm{i}).\end{aligned} \tag{9.18}$$

Another mass-independent frequency shift arises from an unavoidable misalignments between the electric and magnetic field axis or from small ellipticities of the inner surfaces of the electrodes. These effects can be parametrized by two misalignment angles θ and ϕ, and a harmonic distortion parameter ϵ, as done in [265]. It is shown there that the resulting frequency shift for the determination of the sideband frequency $\nu_\mathrm{c} = \nu_+ + \nu_-$ is given by

$$\Delta\nu_\mathrm{c}^\mathrm{mis} \approx \nu_-\left(\frac{9}{4}\theta^2 - \frac{1}{2}\epsilon^2\right), \tag{9.19}$$

deduced from an expansion of the *Brown-Gabrielse* invariance theorem [159]. According to Eq. (9.18), the explicit shift of the frequency ratio reads to

$$\frac{\Delta R^\mathrm{mis}}{R} \approx \left(\frac{9}{4}\theta^2 - \frac{1}{2}\epsilon^2\right) \cdot \frac{\nu_\mathrm{c,i} - \nu_\mathrm{c,f}}{\nu_\mathrm{c,i}} \cdot \frac{\nu_-}{\nu_\mathrm{c,i}} \cdot \frac{\nu_\mathrm{c,i}}{\nu_\mathrm{c,f}}. \tag{9.20}$$

The first factor is typically on the order of 10^{-4} [265], the second one on the order of 10^{-7} (calculated from Tab. 7.1) and the third of 10^{-3}.

In fact, mass-dependent shifts of frequency ratios were studied systematically with carbon-cluster cross-reference measurements at SHIPTRAP [242]. It was found to be in agreement with zero for $|m_1 - m_2| < 100$ u. At comparable experiments, values are reported to $\Delta R^m/R = 1.6 \times 10^{-10} \times (m_1 - m_2)/\mathrm{u}$ for ISOLTRAP [258] or $\Delta R^m/R = 2.2 \times 10^{-9} \times (m_1 - m_2)/\mathrm{u}$ for TRIGA-TRAP [266].
For our Q-value measurements, the mass differences are on the order of a few 10^{-5} atomic mass units (see Tab. 7.1). Hence, mass-dependent systematic shifts and, in particular, anharmonic shifts can be neglected for mass-ratio measurements at an uncertainty of 10^{-9}.

Inhomogeneities of the Magnetic Field

Inhomogeneities of the magnetic field B cause, in analogy to anharmonicities of the electric trapping field, amplitude dependent shifts in the determination of the free cyclotron frequency ν_c (see Sec. 3.3.4). Typically, the inhomogeneity of the magnetic field sensed by the ions is predominantly determined by the lowest-order even expansion coefficient B_2. Hence, the perturbation of the magnetic field in cylindrical coordinates $[\rho, \varphi, z]$ can be written as [155]

$$\Delta B \approx B_2(z^2 - \frac{\rho^2}{2}). \tag{9.21}$$

The free cyclotron frequency ν_c shift is, thus, given by [259]

$$\Delta\nu_\mathrm{c}^\mathrm{inh} \approx \frac{B_2}{B}\nu_\mathrm{c}(\rho_z^2 - \rho_-^2), \tag{9.22}$$

where ρ_z and ρ_- are the amplitudes of the axial and magnetron motion. The proportionality of this shift to the cyclotron frequency ν_c leads to a shift in the ratio determination of

$$\frac{\Delta R^\mathrm{inh}}{R} = \frac{1+\alpha_\mathrm{f}}{1+\alpha_\mathrm{i}} - 1 \quad \text{with} \quad \alpha = \frac{B_2}{B}(\rho_z^2 - \rho_-^2), \tag{9.23}$$

being only a function of B_2 and the motional amplitudes. Provided that the amplitudes of both ions are the same, the shift cancels completely. However, the magnetic field inhomogeneity of the SHIPTRAP magnet is specified to be $\Delta B/B_0 \approx 10^{-7}$ in the central 1 cm^3 volume of the measurement trap. Thus, B_2/B is on the order of $10^{-3}/\mathrm{m}^2$. With motional amplitudes[1] of ~ 1 mm or below, the relative shift of the frequency ratio is on the order of 10^{-10}, even for amplitude differences of 10 %.
In our case, identical trap biasing is used for both isobars measured for the Q-values, where the axial amplitude is cooled to room temperature energy in the preparation trap (see Sec. 8.2.1), and the magnetron radius is excited according to the Ramsey technique

[1] The radius of the excited magnetron motion can be obtained from the fitting routine EVA, and the axial amplitude is determined by thermal equilibrium with the buffer gas at room temperature.

(see Sec. 8.2.2). The axial amplitude is mass independent. Hence, the only amplitude differences can result, at least on average, due to the mass dependency $\rho_- \sim 1/\sqrt{m}$ of the magnetron amplitude (see, e.g. [156]). In our case, the relative differences in mass are on the order of 10^{-7} and, hence, amplitude differences can be expected to be far below 10 %, where remaining systematics can be neglected at the aimed precision.

Fluctuations of the Trap Voltage

In the ideal trap, the sideband frequency determination $\nu_c = \nu_+ + \nu_-$ is independent of the trap voltage, see Eq. (A.9). But, e.g., electrostatic anharmonicities or misalignments of the trapping fields can couple to the sideband frequency. Both effects cause shifts proportional to the magnetron frequency ν_-, which depends linearly on U_0, see Eq. (3.9). Since $\nu_+ \approx \nu_c \propto B$, voltage fluctuations are at least suppressed by ν_+/ν_- compared to magnetic field fluctuations in the sideband cyclotron frequency determination. At SHIPTRAP, voltage fluctuations were never identified as a significant source of uncertainty. As an example, only the shift in Eq. (9.20) due to a tilt of $\theta = 10^{-3}$ degree is taken into account. In this case, the voltage fluctuations on the order of volts would produce a relative shift of the frequency ratio of 10^{-9}. Due to the much more stable voltage source used at SHIPTRAP, this systematic effect can safely be neglected.

9.2 Measurement and Evaluation

In this section, the measurements of the cyclotron-frequency ratio R of the isobaric pairs $^{152}Gd^{1+}$, $^{152}Sm^{1+}$ and $^{164}Er^{1+}$, $^{164}Dy^{1+}$ are described. The relative statistical uncertainty of an individual frequency measurement is typically smaller than 10^{-8}. The dominant source of uncertainty is due to temporal fluctuations of the magnetic field, which is taken into account by alternating frequency measurements. The frequency ratios are extracted from data taken over several days, where the accumulated statistics allows for a final relative uncertainty in R of $\sim 10^{-9}$. The data analysis is performed via two different methods, for a consistency check.

9.2.1 Cyclotron Frequencies

For all $Q_{\epsilon\epsilon}$-value measurements within this thesis, the off-line setup of SHIPTRAP, shown in Fig. 8.1, was used. Crucial points in the determination of the cyclotron frequencies are the provision of identical starting conditions in the measurement trap to avoid systematic effects on the measurement results, and an alternating measurement scheme to map magnetic-field fluctuations. For both issues, the realization within our measurements is discussed below.

Ion Preparation

In the double-electron capture transitions $^{152}Gd \rightarrow {}^{152}Sm$ and $^{164}Er \rightarrow {}^{164}Dy$, all nuclides are part of the same chemical group of lanthanoids, characterized by a similar

valence-shell structure and, hence, similar chemical behavior. Samples of those nuclides in form of an oxide powder (X_2O_3) were deposited on stainless steel plates, serving as targets for the laser ion source. The isotope abundance of the samples were 34.8 % for ^{152}Gd (enriched), 26.75 % for ^{152}Sm (natural), 65.0 % for ^{164}Er (enriched), and 96.8 % for ^{164}Dy (enriched). Chemical impurities were well below 0.5 % for all samples.
The ionization-energy threshold and the velocity distribution is specific for each target material. The physics of the laser ablation is not fully understood and governed by many parameters such as pulse duration, beam energy, wavelength or the beam profile (see, e.g. [267]). For our experiments, the laser energy was chosen such that the count rate of the ions in the measurement trap was about $1 - 5$ ions. In order to avoid isobaric contamination, for every nuclide an individual target plate was prepared. The two targets of an isobar pair were mounted on a rotary feedthrough for alternate laser irradiation, separated by several cm. The laser was pulsed onto the sample once per measurement cycle, which is in total about 2.5 s (see Fig. 9.2).
As mentioned before, the same settings of the laser energy and ion optics were used for both isobars in order to provide identical starting conditions for the ion preparation in the PT. The initial magnetron radius is a particularly crucial parameter, since the other modes are cooled automatically by collisions with the buffer gas in the PT (see Sec. 8.2.1). The initial magnetron radius can, however, be checked by extraction of the ions through the diaphragm (see Fig. 8.2) as a function of the dipole excitation-pulse amplitude at ν_- (see Sec. B). This was done for all nuclides and no differences were found between the isobaric pairs.

After the capture of the ions in the PT, sideband buffer-gas cooling of the magnetron motion was applied for mass-selective centering of the ions (see Sec. 8.2.1). The ion's magnetron radius was first excited by a mass-independent dipole pulse at ν_-, followed by a mass-specific coupling pulse at $\nu_+ + \nu_-$. Hence, only the magnetron radius of the ions at the correct sideband frequency is reduced for transmission through the diaphragm to the measurement trap. The resolution of this centering process was tuned to about 50 Hz, corresponding to a mass resolving power of $\sim 13000 - 14000$. This excludes isotopes of the targets from passing to the MT, since the differences in the cyclotron frequencies are on the order of 10^3 Hz per nucleon in the corresponding mass range. Calculated from the masses in [147], there are several isobars unresolved with this mass selection (at $A = 152$: Nd, Pm, Eu, Tb, Dy and at $A = 164$: Gd, Tb, Ho, Tm, Yb). However, their abundances were negligible in the samples.
The cooling efficiency was controlled by time-of-flight spectra out of the PT. Again, no differences were found between the isobaric pairs. Furthermore, from the TOF spectra of the PT also charge-exchange reactions with rest gas were excluded. In this process, rest gas can be ionized by charge transfer to the ions of interest while neutralizing them. Consequently, additional rest-gas peaks would show up in the TOF spectra. In our case, no rest-gas peaks were visible in the spectra of the experiments.
The cooled bunch from the PT was finally transported to the MT for the frequency measurement. In Fig. 9.2, the typical timing scheme is shown. The total cycle time adds up to about 2.5 s.

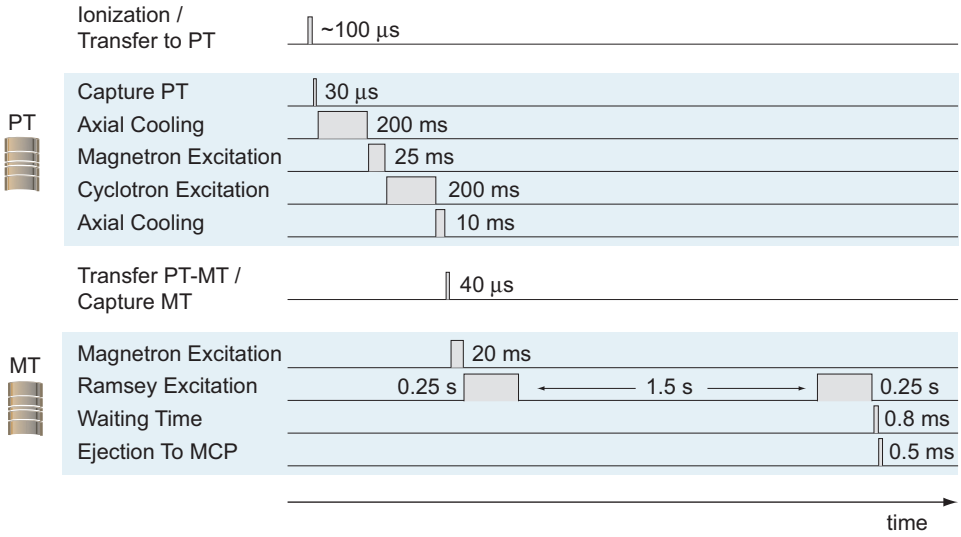

Figure 9.2: Timing scheme of the time-of-flight measurements used for the Q-value measurements. The ions are transported from the laser-ablation ion source to the double Penning-trap setup. In the preparation trap (PT), the buffer gas cooling technique is applied for mass-selective centering and cooling. In the measurement trap (MT), the Ramsey technique is applied. The total time for one measurement cycle adds up to ~ 2.5 s.

Alternating Measurements with the Ramsey Method

The frequency measurements were performed using the Ramsey method, discussed in Sec. 8.2.2. Two general issues had to be taken into account, which influence the final measurement uncertainty. First, in order to map short-term temporal fluctuations of the trapping parameters (e.g. of the magnetic field, see Sec. 9.1.2) by alternating frequency measurements, an individual measurement should be done as fast as possible. Second, according to Eq. (9.15) the uncertainty of a single measurement scales with $1/(\sqrt{N}T_{\mathrm{RF}})$, where N is the total number of ions used for a resonance measurement and T_{RF} the total time for the Ramsey excitation scheme. Additionally, for the least-squares fit of the Ramsey line shape to the measured points of the resonances, scanning of a high number of sidebands as well as points per sideband are advantageous.

As a tradeoff between fast and accurate measurements, the time for a single frequency measurement was restricted to about $20 - 30$ minutes. For the Ramsey excitation scheme, the pulse length of $\tau_1 = 0.25$ s before and after a waiting time of $\tau_0 = 1.5$ s was chosen, leading to ~ 7 fringes in a frequency window of about 4 Hz. In the frequency scan, 62 points were recorded across the frequency window with statistics of $500 - 700$ ions in total, accumulated by one to five ions per shot.
In Fig. 9.3, a typical measurement result of the cyclotron frequencies of $^{152}\mathrm{Gd}^{1+}$ and $^{152}\mathrm{Sm}^{1+}$ is shown. Within the fitting program EVA, a time window of $65 - 105$ μs was used for averaging of the time of flight per frequency point. The fit resulted

in the cyclotron frequencies $\nu_c(^{152}Gd^{1+}) = 708035.664(5)$ Hz and $\nu_c(^{152}Sm^{1+}) = 708035.943(4)$ Hz.
The alternated measurements between mother and daughter nuclide led to about 24 to 37 frequency values per day. In Fig. 9.4 and Fig. 9.5, the total frequency data recorded over 3 and 4 days are shown for the pairs $^{152}Gd \rightarrow {}^{152}Sm$ and $^{164}Er \rightarrow {}^{164}Dy$, respectively. In both cases, the typical statistical uncertainties of the frequency measurements provided by the fit routine EVA are ~ 5 mHz, corresponding to $\delta\nu_c/\nu_c < 8 \cdot 10^{-9}$. Typical daily fluctuations of the frequencies due to changes in the trapping conditions are below 20 mHz, corresponding to $\delta\nu_c/\nu_c \sim 3 \cdot 10^{-8}$.

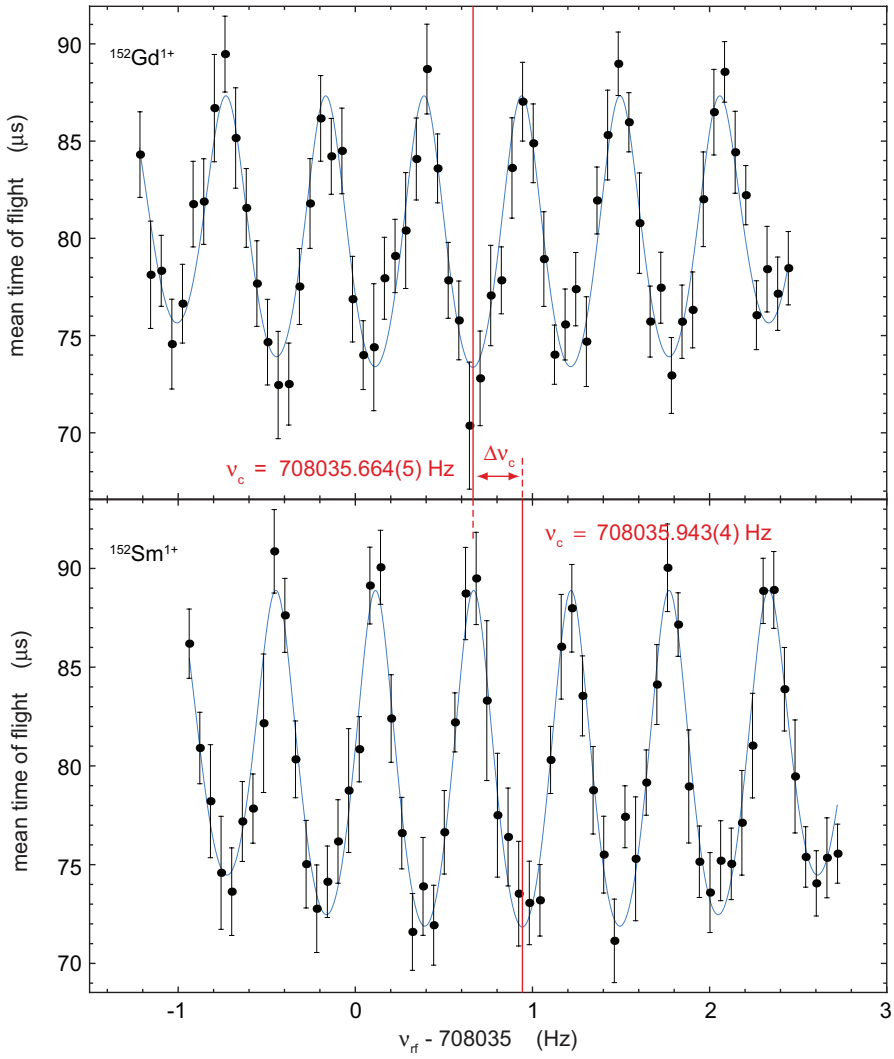

Figure 9.3: Typical time-of-flight resonances for $^{152}Gd^{1+}$ (top) and $^{152}Sm^{1+}$ (bottom). For the Ramsey excitation, a pulse length of $\tau_1 = 0.25$ s before and after a waiting time of $\tau_0 = 1.5$ s was chosen. For statistics, shots with up to 5 ions were used, leading to a total number of ions per resonance of ~ 600. The free cyclotron frequencies were determined by fitting the theoretical line shape to the data points, resulting in $\nu_c = 708035.664(5)$ Hz for $^{152}Gd^{1+}$ and $\nu_c = 708035.943(4)$ Hz for $^{152}Sm^{1+}$.

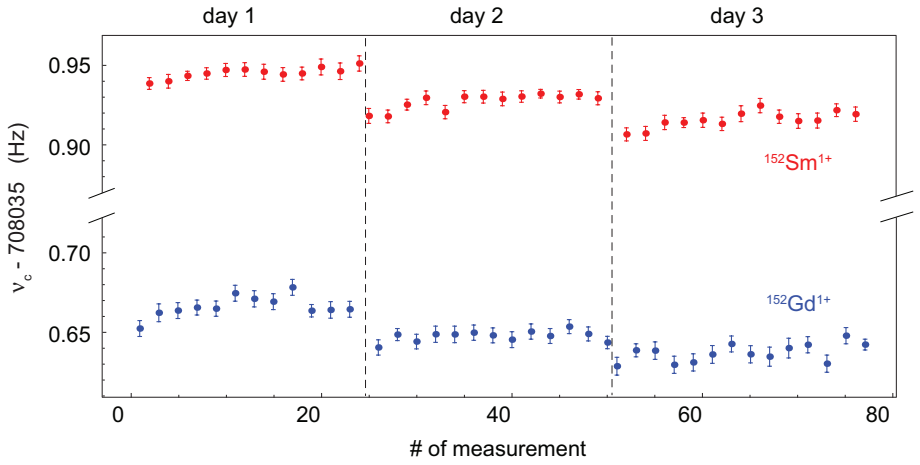

Figure 9.4: Alternating cyclotron-frequency measurements of $^{152}Gd^{1+}$ and $^{152}Sm^{1+}$, measured over 3 days.

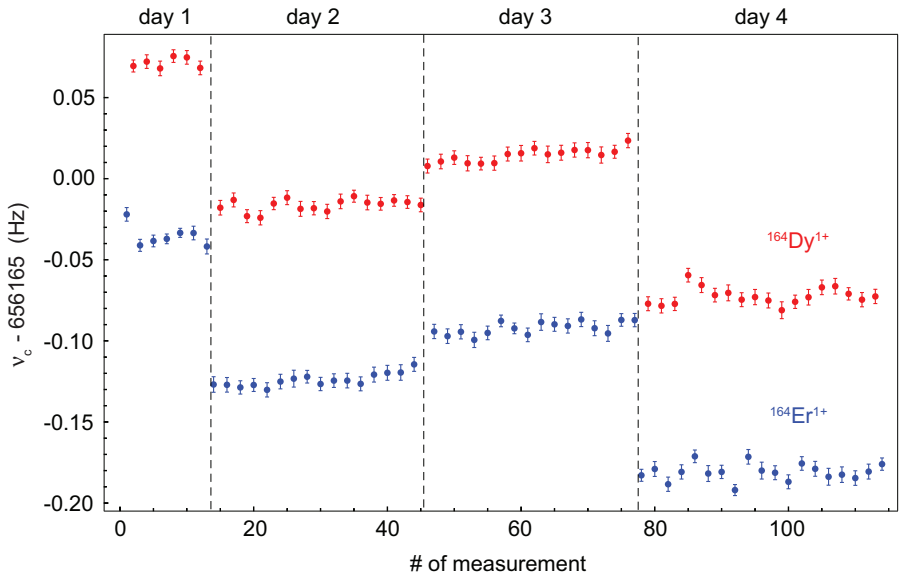

Figure 9.5: Alternating cyclotron-frequency measurements of $^{164}Er^{1+}$ and $^{164}Dy^{1+}$, measured over 4 days.

9.2.2 Determination of the Frequency Ratio by Interpolation

In the following, the data evaluation of the alternating measurements is discussed in the framework of the interpolation method introduced in Sec. 9.1.1. The consecutive application of this method to the data collected over several days leads to a set of ratio data, from which the final value is calculated as the mean.

Uncertainty of an Individual Ratio Measurement

Due to the similarity of the isobars under investigation, most systematical effects cancel in the ratio determination, at the aimed precision (see Sec. 9.1.2). Thus, besides the statistical error of the individual frequency measurement, see Eq. (9.15), the only concerns are magnetic-field fluctuations, and the variations in the simultaneously trapped ion number. The latter systematics can be neglected in our case, as shown below.
The resulting frequency uncertainty caused by magnetic-field fluctuations $\delta\nu_c/\nu_c = \delta B/B$ is well below 10^{-10} within our measurements, where the non-linear part is expected to be even less. Since statistical uncertainties of individual frequency measurements are typically 5 mHz corresponding to $\delta\nu_c/\nu_c \sim 10^{-8}$ (see Fig. 9.4 and Fig. 9.5), uncertainties due to non-linear temporal fluctuations can be neglected. Thus, the final uncertainties of the individual ratios are calculated only on the basis of the uncertainties coming from the frequency determination.

Weighted Mean and its Total Uncertainty

From the repeated ratio determination, the weighted mean value $\overline{R}$ of N individual ratios R_i is given by [268]

$$\overline{R} = \frac{\sum_i^N \frac{1}{\delta R_i^2} \times R_i}{\sum_i^N \frac{1}{\delta R_i^2}}, \tag{9.24}$$

with the weights of the individual ratios given by their uncertainties δR_i. The uncertainty $\delta\overline{R}$ of the mean value $\overline{R}$ can be calculated by the *method of least squares*. It is assumed that the residuals of the measured values to the mean value are only accidental and follow a Gaussian distribution. As discussed in [268], there are two ways to give estimations about the probable error in the calculation of the mean value. The first one is based on internal consistency, where the so-called internal error $\delta\overline{R}_{\text{int}}$ is calculated by application of error propagation of the individual uncertainties δR_i. It is given by

$$\delta\overline{R}_{\text{int}} = \frac{1}{\sqrt{\sum_i^N \frac{1}{\delta R_i^2}}}. \tag{9.25}$$

The second possibility is based on external consistency, where the external error $\delta\overline{R}_{\text{ext}}$ is calculated from the residuals of the measured ratios to the mean value $R_i - \overline{R}$, weighted

by their uncertainties δR_i. It is given by

$$\delta\overline{R}_{\mathrm{ext}} = \sqrt{\frac{\sum_i^N \frac{1}{\delta R_i^2}\left(R_i - \overline{R}\right)^2}{(N-1)\cdot\sum_i^N \frac{1}{\delta R_i^2}}}. \tag{9.26}$$

For identical individual errors $\delta R_i = \delta R$, the external error $\delta\overline{R}_{\mathrm{ext}}$ is equivalent to the standard deviation σ_{st} of the distribution of the individual ratios R_i around the mean value, divided by $\sqrt{N}$:

$$\delta\overline{R}_{\mathrm{ext}} = \sqrt{\frac{\sum_i^N \frac{1}{\delta R^2}\left(R_i - \overline{R}\right)^2}{(N-1)\cdot\sum_i^N \frac{1}{\delta R^2}}} = \sqrt{\frac{\sum_i^N \left(R_i - \overline{R}\right)^2}{(N-1)\cdot N}} = \frac{\sigma_{st}}{\sqrt{N}}. \tag{9.27}$$

Thus, as many measurements as possible should be performed. The internal error $\delta\overline{R}_{\mathrm{int}}$ is a prediction of the probable error, based on the uncertainties assigned to the individual measurements. The external error $\delta\overline{R}_{\mathrm{ext}}$, however, reflects the fluctuations around the mean value, actually measured by the individual ratios. Hence, the external error can be understood as the answer of the measurements to the prediction of the internal error. Consequently, both definitions have to agree in the limit of infinite number of measurements, if only statistical errors are present. In [268], the statistically allowed deviation from unity of the so-called *Birge Ratio* $BR = \delta\overline{R}_{\mathrm{ext}}/\delta\overline{R}_{\mathrm{int}}$ in case of a finite number of measurements is calculated to

$$\frac{\delta\overline{R}_{\mathrm{ext}}}{\delta\overline{R}_{\mathrm{int}}} \approx 1 + \frac{0.477}{\sqrt{N}}. \tag{9.28}$$

Hence, the calculation of the Birge Ratio can give hint to unaccounted systematics. A Birge Ratio higher than the bound of Eq. (9.28) indicates an under-estimation of the uncertainties of the individual measurements δR_i while an $BR < 1$ indicates an over-estimation of the individual uncertainties.

Average of the Measured Ratios

In Fig. 9.6, the individual cyclotron-frequency ratios $R = \nu_{\mathrm{c}}(^{152}\mathrm{Sm}^{1+})/\nu_{\mathrm{c}}(^{152}\mathrm{Gd}^{1+})$ are shown, which are calculated with the linear-interpolation method from the frequency values of 3 days of measurements (see Fig. 9.4). Here, the values for Sm were interpolated to the measurement times of the Gd values. The scattering of the individual ratios R_i is caused by magnetic-field fluctuations between two measurements of the interpolated species (indicated by t_β and $t_{\beta+1}$ in Fig. 9.1) and statistical variations, whereas the uncertainty δR_i is calculated from the frequency determinations (see discussion above).
The averaging of the 35 individual ratios by Eq. (9.24) results in $\overline{R} - 1 = 3.9338 \times 10^{-7}$, which is marked by the red line. The cyclotron-frequency ratios for the other isobar pair $R = \nu_{\mathrm{c}}(^{164}\mathrm{Dy}^{1+})/\nu_{\mathrm{c}}(^{164}\mathrm{Er}^{1+})$ are shown in Fig. 9.7. The frequency data of Fig. 9.5

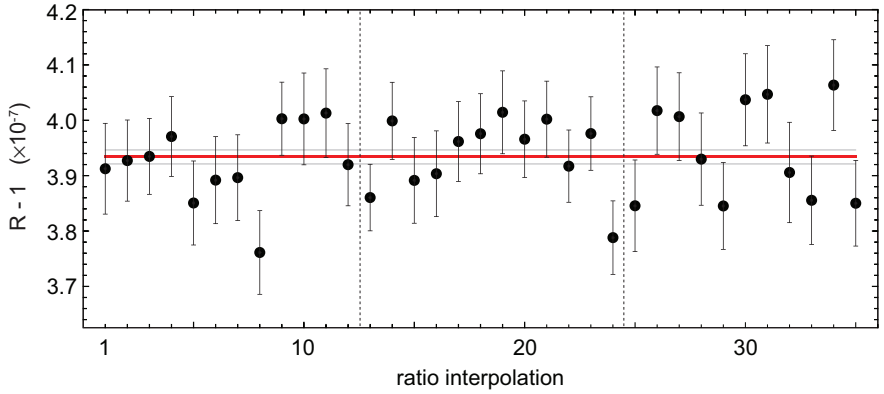

Figure 9.6: Cyclotron frequency ratios of $^{152}Gd^{1+}$ and $^{152}Sm^{1+}$. The red line marks the mean value of $\overline{R}-1 = 3.9338\times10^{-7}$. The gray lines mark the external error of the calculation of the mean value given by $\delta\overline{R}_{\mathrm{ext}} = 1.260\times10^{-9}$. The ratios were calculated with Sm as the interpolated species.

are used for the calculation of 54 ratio values with the frequencies of Er interpolated to the measurement time of Dy. The averaging results in $\overline{R}-1 = 1.6456\times10^{-7}$.
In order to assign the uncertainty of the averaged frequency ratio, typically the higher value of $\delta\overline{R}_{\mathrm{ext}}$ and $\delta\overline{R}_{\mathrm{int}}$ is used in comparable experiments. However, from our experience the fitting routine EVA is over-estimating the uncertainties $\delta\nu$ of individual frequency measurements due to reasons given in Sec. 9.1.2. Consequently, the individual errors δR_i of the frequency ratios are over-estimated, too, according to Eq. (9.4). Following from that, the internal error $\delta\overline{R}_{\mathrm{int}}$ is increased unnecessarily, since it is calculated by error propagation of the individual uncertainties δR_i. As discussed above, this over-estimation can be checked at the present data by calculating the Birge Ratio of the external and internal error $BR = \delta\overline{R}_{\mathrm{ext}}/\delta\overline{R}_{\mathrm{int}}$. The external and internal error as well as the mean ratio are listed in Tab. 9.1 for both data sets, where the interpolation to the alternative species is included. For all cases, the Birge Ratio is clearly below unity, indicating that the individual errors of the ratios are too large compared to the actual measured scattering of the ratio values. This systematic effect is not only visible in the data presented within this thesis, but also in all recent Q-value measurements at SHIPTRAP, presented in [106, 230–234].
For this reason we decided to use only the external error $\delta\overline{R}_{\mathrm{ext}}$ to assign the final uncertainty of the averaged ratio $\overline{R}$. In this error definition, given in Eq. (9.26), the individual uncertainties are only used as weights and a constant systematic over-estimation will cancel out.

The final consideration is concerned with the curvature of the drift of the cyclotron frequencies. If the mean curvature of the overall frequency drift does not vanish, the consecutive interpolation leads to an over- or under-estimation of the calculated mean ratio, depending on which species the interpolation is performed and the absolute scale of the mean curvature. Hence, in a final step the mean values of the frequency ratios

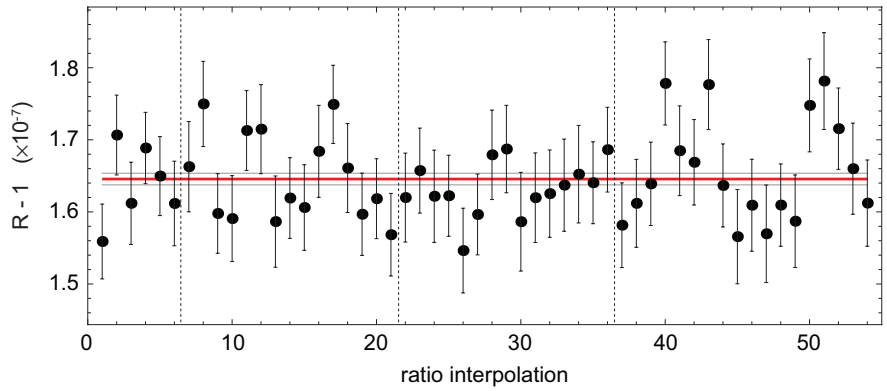

Figure 9.7: Cyclotron frequency ratios of $^{164}Er^{1+}$ and $^{164}Dy^{1+}$. The red line marks the mean value of $\overline{R}-1 = 1.6456\times10^{-7}$. The gray lines mark the external error of the calculation of the mean value given by $\delta\overline{R}_{\text{ext}} = 0.804 \times 10^{-9}$. The ratios were calculated with Er as the interpolated species.

were calculated for both isobars as the interpolated species. The final mean ratio is then calculated as the average of both interpolations, while the larger external error is assigned as the final uncertainty. The summary of the intermediate values, and, the final mean ratios are given in Tab. 9.1.

Dependence on the Number of Ions per Shot

As mentioned in Sec. 9.2.1, in order to obtain the statistics of $500-700$ ions for each resonance scan as quick as possible, $1-5$ ions per shot from the measurement trap were accepted in our Q-value determination. However, multiple ions in the measurement trap can give rise to frequency shifts, if contamination ions are present (see Sec. 9.1.2). In order to avoid such shifts, the preparation trap serves as a barrier to most possible contamination ions. Nevertheless, few isobars with very similar masses to the ions under investigation can possibly pass the PT, although their abundance should be negligible due to careful preparation of the targets in the ion source (see discussion in Sec. 9.2.1). Hence, in order to ultimately identify residual contamination ions, which might have passed the preparation trap, the frequency data are split up by the number of ions, which were simultaneously present in the measurement trap. These count-rate classes (also called *z-classes*) are typically chosen with similar total number of ions and, hence, the same statistical weight. In case of contaminations, the cyclotron frequency will be dependent on the number of ions in the trap. The unperturbed frequency can then be obtained by a linear fit as a function of the ion number and a extrapolation to a single ion [258].
In our case, such an analysis was applied directly to the ratio values in order to justify the data used for the evaluation in the previous paragraph. The total number of ions in a resonance was approximately uniformly distributed over the number of ions per shot. In Fig. 9.8, the mean ratio for the transition $^{152}Gd \rightarrow {}^{152}Sm$ is calculated as a function of ions per shot from the data given in Fig. 9.6. The red line marks a linear fit to these

Table 9.1: Mean cyclotron-frequency ratio $\overline{R}$ of the $\epsilon\epsilon$-transitions ^{152}Gd $\rightarrow$ ^{152}Sm and ^{164}Er $\rightarrow$ ^{164}Dy. The linear-interpolation method is applied to both isobars of the transitions. For all values the external and internal errors, $\delta\overline{R}_{\text{ext}}$ and $\delta\overline{R}_{\text{int}}$, as well as the Birge Ratio are calculated. In a final step, the ratios of both interpolations are averaged and the larger external error is assigned to the resulting value.

$\epsilon\epsilon$-transition	$^{152}_{64}$Gd $\rightarrow$ $^{152}_{62}$Sm		$^{164}_{68}$Er $\rightarrow$ $^{164}_{66}$Dy	
interpolation	^{152}Gd^{1+}	^{152}Sm^{1+}	^{164}Er^{1+}	^{164}Dy^{1+}
$(\overline{R}-1)\times10^{7}$	3.9388	3.9338	1.6456	1.6445
$\delta\overline{R}_{\text{ext}}$ $\times10^{9}$	1.035	1.260	0.804	0.919
$\delta\overline{R}_{\text{int}}$ $\times10^{9}$	1.259	1.368	1.098	1.113
BR	0.82	0.92	0.73	0.83
final average:				
$\overline{R}-1$	$3.9363(126)\times10^{-7}$		$1.6451(92)\times10^{-7}$	

data with a 95 % confidence band indicated in gray. The black line gives the mean value of the ratio, averaged over $1-5$ ions per shot. As shown there, the data scatter around the mean value and the slope of the fit is in agreement with the mean value within 95 % confidence for all days. Hence, there are no indications for contaminations within our measurements. The same analysis for the transition ^{164}Er $\rightarrow$ ^{164}Dy is shown in Fig. 9.9 from the data given in Fig. 9.7. Again, no indication for contaminations was found.

Discarded Data

During the measurement campaign for our Q-value determinations, for both isobaric pairs more data were recorded than presented in Fig. 9.6 and Fig. 9.7, respectively. Several days were spent for optimization of the settings of the whole setup, including the production and transport of the ions, the preparation of the mass-selected and cooled ion cloud in the first trap as well as the settings for the Ramsey technique in the measurement trap. The data during the optimization process were not used for the ratio analysis. Further reasons of bad data can be, e.g., due to fluctuations of the ambient conditions in the experimental hall of SHIPTRAP. In the ideal case, the temperature and pressure stabilization system at SHIPTRAP [249] should compensate for such influence, resulting in negligible drifts of the frequencies of the alternating measurements. In reality, the level of stabilization and, hence, the residual fluctuations of the frequency values depend on the amplitude of the fluctuations of the ambient conditions.

Hence, the recorded data were judged by many criteria and pre-selected for the analysis procedure. In Fig. 9.10, an example of a discarded day of data taking is shown. For the data evaluation, only measurement runs with a total drift of the cyclotron frequencies of 30 mHz at maximum were accepted, which is exceeded almost by a factor of two on the data shown in Fig. 9.10 (left). Furthermore, the drift of the frequency values shows

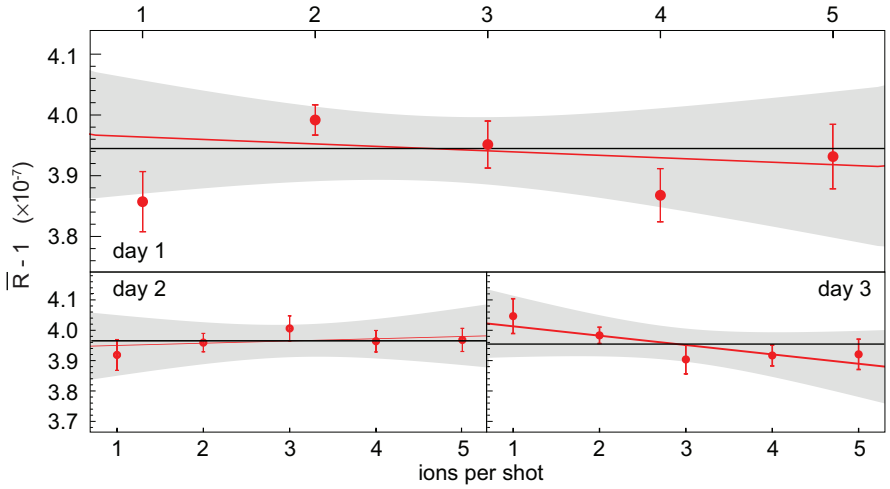

Figure 9.8: Cyclotron-frequency ratio of $^{152}Gd^{1+}$ and $^{152}Sm^{1+}$ as a function of the ion number. The red line marks a linear fit as a function of ions per shot. In gray, the 95 % confidence band of the fit is shown. The black line marks the mean of the ratio, averaged over $1-5$ ions per shot. The slope of the fit is in agreement with the mean value within 95 % confidence for all days.

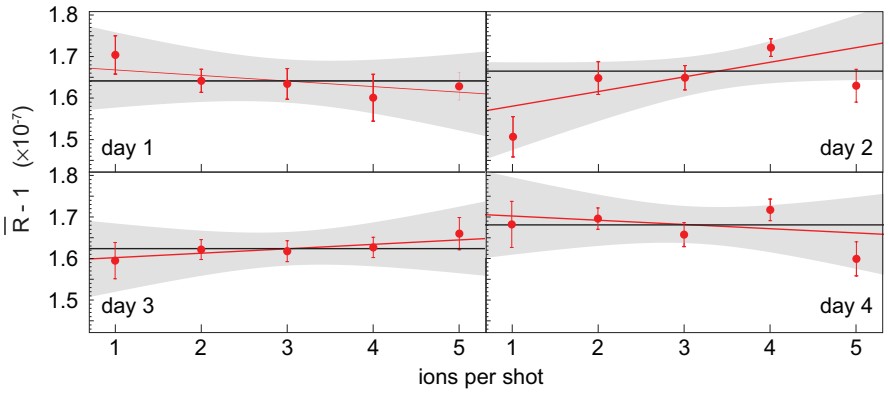

Figure 9.9: Cyclotron-frequency ratio of $^{164}Er^{1+}$ and $^{164}Dy^{1+}$ as a function of the ion number. The red line marks a linear fit as a function of ions per shot. In gray, the 95 % confidence band of the fit is shown. The black line marks the mean of the ratio, averaged over $1-5$ ions per shot. The slope of the fit is in agreement with the mean value within 95 % confidence for all days.

a negative slope, which was only visible on this day of data taking. Both effects might be due to an insufficient stabilization of the magnetic field caused by large ambient fluctuations. Additionally, data were only accepted if the dependence on the ion number is in agreement with zero within two standard errors. As shown on the right hand side of Fig. 9.10, this criteria was exceeded for this day, too, possibly caused by contamination ions due to an insufficient tuning of the preparation trap. Due to the indication of multiple "failures", this day of data taking was discarded for the analysis process of the frequency ratios.

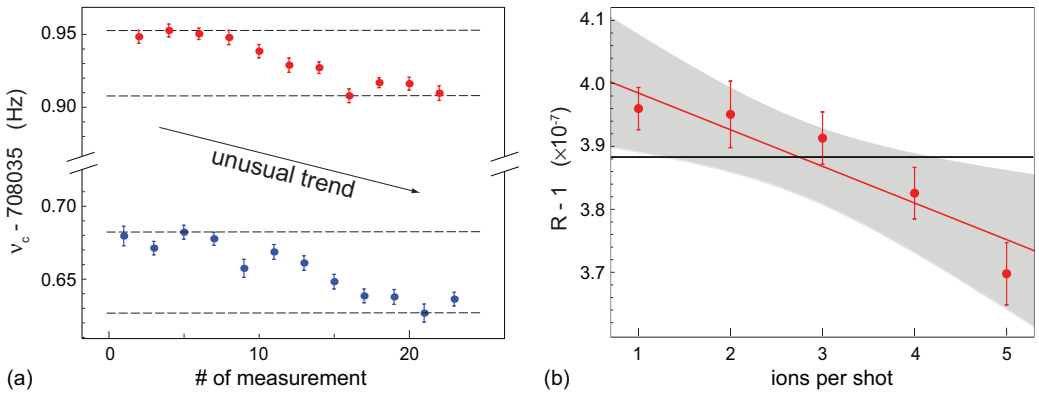

Figure 9.10: Example of a day of data taking, which was discarded for the analysis of the frequency ratios. (a) The alternating frequency measurement is shown where an unusual negative slope is visible. Furthermore, the amplitude of this drift is about 50 mHz, which is about twice as large as for typical other days. Both criteria are possibly an indication that the stabilization system was not working properly. (b) A clear dependency on the number of ions per shot of the resulting frequency ratio is visible. This might be due to contamination ions which passed an insufficiently tuned preparation trap.

9.2.3 Polynomial Method

The crucial aspect of the approximation of the magnetic field by a polynomial is the right choice of the polynomial order. Especially, since, time scales and amplitudes of magnetic-field fluctuations are not fixed and complicate the appropriate choice of the polynomial order.

Choice of the Polynomial Order

In absence of any knowledge about the real magnetic-field behavior besides the measured data points, the quality of a fit has to be judged by statistical methods. The quantity χ^2 defined in Eq. (9.13) is a measure of the residuals of the fit. In general, χ^2 will decrease for every additional order while more and more noise is mapped.
One option for finding a balance is to look at χ^2_{red}. A minima for χ^2_{red} would indicate that the reduction of χ^2 due to additional orders is done at the expense of a disproportionally increasing model complexity. In other words, the data points are fitted better but only due to much higher oscillations of the polynomials, which would be a hint of noise mapping.
Another option is the so-called F-test, defined in [269] and discussed in detail for Penning-trap mass spectrometry in [270]. The figure of merit is the F_χ-number defined by

$$F_\chi(P_n) = \frac{\chi^2(P_{n-1}) - \chi^2(P_n)}{\chi^2_{\mathrm{red}}(P_n)}, \tag{9.29}$$

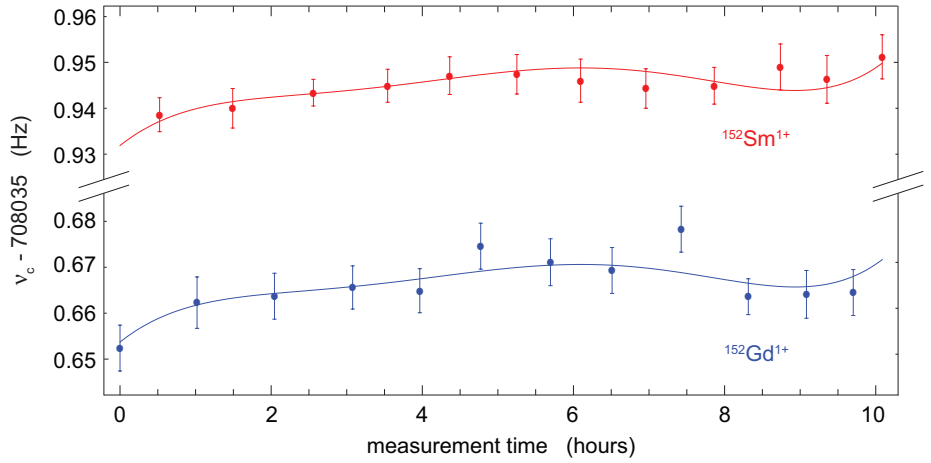

Figure 9.11: Simultaneous fit of the polynomials given in Eq. (9.10) with 5-th order to the cyclotron frequencies of $^{152}Gd^{1+}$ and $^{152}Sm^{1+}$. The data are taken from the first day of Fig. 9.4. From this fit, the ratio of the cyclotron frequencies can be extracted to $R - 1 = 3.9287(167) \times 10^{-7}$.

where P_n refers to the fitted polynomials of order n, defined in Eq. (9.10). The F_χ-number provides a measure of the relative change of χ^2 due to an additional order of the fitted polynomials. Hence, an insignificant change of χ^2 of the fit is marked by $F_\chi \leq 0.5$, which is a definition resulting from the corresponding probability density (for details see [269]). If F_χ is found to be below 0.5, the corresponding order n does not improve the fit significantly and fitting with $n-1$ is sufficient. Long term drifts of the magnetic field, however, can be, e.g., concave during one day of measurement. In this case, the drift is an even function and odd terms of polynomials are, in general, less important for the fit. Hence, F_χ for an odd order can drop below 0.5 although higher even terms are still significant. In such a situation, the check for additional orders should be done for $F_\chi < 0.5$ of two consecutive orders. The same argument is true vice versa for odd magnetic-field drifts.

Frequency Ratio of $^{152}Gd^{1+}$ and $^{152}Sm^{1+}$

In a first step, the alternating cyclotron frequencies for $^{152}Gd^{1+}$ and $^{152}Sm^{1+}$ were fitted with polynomials of order 2 to 10, as shown for the first day with 5-th order in Fig. 9.11. The resulting frequency ratios extracted from the fits are shown in Fig. 9.12a. The statistical error δR_{stat} is given by the condition defined in Eq. (9.14). As expected, the ratio depends on the order of the polynomials. The statistical error δR_{stat} is found to be independent of the order, at least till the order of 10^{-12}.
The minima[2] for χ^2_{red} is found in 5-th order for the first day, as shown in Fig. 9.12b. The F_χ-numbers are given in Fig. 9.12c. For our data even orders contribute much less

[2]The fact that the minimal value of χ^2_{red} is clearly below unity can be explained by the over-estimation of the individual uncertainties of the cyclotron frequencies due to the resonance fit routine EVA (see discussion in Sec. 9.1.2). This issue is also visible in the evaluation by interpolation, see Sec. 9.2.2.

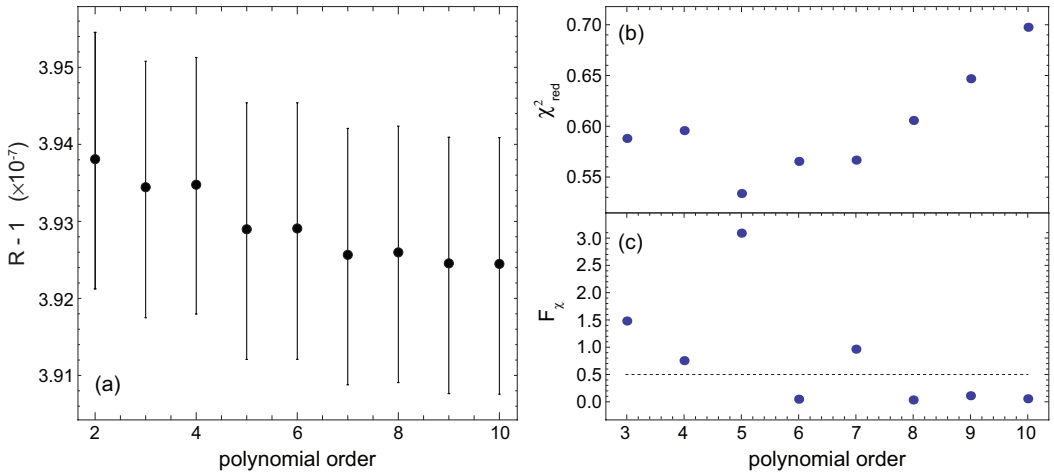

Figure 9.12: (a) Frequency ratio R of $^{152}Sm^{1+}$ and $^{152}Gd^{1+}$ resulting from different orders of the polynomial fit. (b) χ^2_{red} of the fit residuals for the given order n. (c) F-test of the fitted polynomials of order n.

than odd orders. Hence, the value below 0.5 at $n = 6$ is ignored and the insignificant change of fit quality is identified for $n \geq 8$. Consequently, the best order is $n = 7$.
The same procedure is repeated for all three days of data taking. The results are listed in Tab. 9.2, together with the statistical error δR_{stat} of the fit. Only at the third day, both criteria lead to the same optimum order of the polynomial fit. In view of such a discrepancy between the statistical tests, we decided to treat the choice of the polynomial order as a source of a systematic error. As a measure of this error, we chose the standard deviation of the ratios, resulting from different order fits. It is calculated by

$$\sigma_{k,K} = \sqrt{\frac{\sum_{n=k}^{K} \left(R(P_n) - \overline{R(P_n)}\right)^2}{(K-1)}}, \tag{9.30}$$

where $R(P_n)$ refers to the ratio value, resulting from a fit in n-th order. The minimal order is chosen to $k = 2$ and the maximal order to $K = 10$. As shown in Tab. 9.2, the resulting systematic error is below 30 % of the statistical error for the worst case. In the final step, the resulting ratios are averaged over the three days. The comparison of both methods is shown in Fig. 9.13, based on χ_{red} in (a) and on F_χ in (b). The mean ratios are given by

$$\overline{R} - 1 = \begin{cases} 3.9380(100) \times 10^{-7}, & \text{based on the } \chi^2_{\mathrm{red}}\text{-criteria,} \\ 3.9363(098) \times 10^{-7}, & \text{based on the } F_\chi\text{-criteria.} \end{cases} \tag{9.31}$$

Hence, the difference between both methods is below 20 % of the total error. Coincidently, the result based on the F-test exactly matches the value resulting from the interpolation method, given in Tab. 9.1.

Table 9.2: Polynomial order due to the given statistical criteria and resulting frequency ratio R of $^{152}Sm^{1+}$ and $^{152}Gd^{1+}$. The statistical uncertainty δR_{stat} results from the fit procedure while $\sigma_{2,K}$ takes the systematic uncertainty of the choice of the polynomial order into account.

	χ^2_{red}-criteria		F_χ-criteria			
run	order	$(R-1)\times10^7$	order	$(R-1)\times10^7$	$\delta R_{stat}\times10^9$	$\sigma_{2,10}\times10^9$
1	5	3.9287	7	3.9254	1.666	0.477
2	4	3.9558	5	3.9539	1.450	0.282
3	7	3.9240	7	3.9240	1.663	0.163

Frequency Ratio of $^{164}Er^{1+}$ and $^{164}Dy^{1+}$

The same procedure of the polynomial fit was applied to the frequency data of $^{164}Er^{1+}$ and $^{164}Dy^{1+}$ (see Fig. 9.5). Unfortunately, several problems occurred for these data sets, which will be discussed in the following.

On the first day, only 6 frequency values were recorded for $^{164}Dy^{1+}$. Hence, the maximum order is limited to $n = 5$. On this day the F_χ-test failed, most probable due to the limited statistics. The χ^2_{red} has a minimum at $n = 4$. As the only statistical hint for a best order, the ratio was calculated in this order. The resulting value is given in Tab. 9.3. Both the statistical error δR_{stat} as well as the systematic error $\sigma_{k,K}$ are much larger compared to other results, due to the low statistics for that run. The maximum order for the calculation of the systematical error was set to $n = 5$.

For the other days, another problem occurred. For all three days χ^2_{red} is continuously decreasing and no minima was found for polynomial orders up to $n = 12$. In the χ^2_{red}-sense, the fit improves even for high orders. This might be a hint for data, for which it is not really possible to separate random fluctuations from long-term drifts within the considered orders. A fit to 6-th order for the third day is shown in Fig. 9.14a. It might be possible to find a minima for higher orders, but it does not seem to be comprehensible that long-term drifts appear with such high orders. Hence, we restricted ourselves to $n \leq 10$ for all statistical tests. On the other hand, this separation is exactly the primary idea of using polynomial fits. In that sense, at least the χ^2_{red}-criteria failed for all three days and, consequently, the whole method might be doubted for these data sets.

The remaining statistical criteria is the F-test, which is now discussed for the three days separately. On the second day, this criteria results in $n = 2$. Furthermore, a closer look to the data shows that the systematical uncertainty $\sigma_{2,10}$ is very low compared to other days (see Tab. 9.3). In other words, the choice of the polynomial order is less important. The guess from all three aspects might be that it is not possible to separate long-term drifts from fluctuations, due to similar amplitudes of both. For that reason we used $n = 2$ for the ratio extraction.

On the third day, the F-test fails as well. The reason might be the same as discussed for χ^2_{red}. In absence of any criteria the only possibility is to use the mean value of the

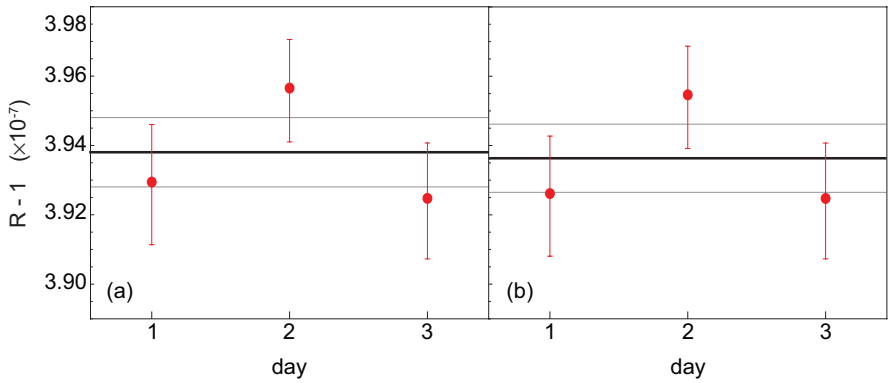

Figure 9.13: Frequency ratios R of $^{152}Sm^{1+}$ and $^{152}Gd^{1+}$ resulting from the χ^2_{red}-criteria shown in (a) and from the F-test shown in (b). The mean value is marked by the thick black line. The total uncertainty is given by the external error of the mean value depicted by thin gray lines.

ratios, averaged over the results from $n = 2$ to $n = 10$. For such a case one has to rely on that the resulting error is taken into account completely by $\sigma_{2,10}$.
On the fourth day, the F-test results in $n = 6$. Nevertheless, this result can be doubted. In Fig. 9.14b, the ratios are shown as a function of the polynomial order. It turns out that, again, two consecutive fits result in almost the same ratio value, where the reason is that the overall trend is even and hence odd orders do not contribute. The F-test now detects that there is no significant change between $n = 6$ and $n = 8$, which is also visible in the plot. In 10-th order, however, the ratio value drops down again. Now there are two possibilities. Either the insignificant change in 8-th order might be accidentally, or the significant change in 10-th order. Nevertheless, for the fourth day we accept the result on the F-test, due to the lack of an alternative criteria. The results for the fits of all four days are summarized in Tab. 9.3. The averaging of the ratios over the four days based on the given criteria results in

$$\overline{R} - 1 = 1.6449(71) \times 10^{-7}. \tag{9.32}$$

In the comparison of the final result to the value from the interpolation method, given in Tab. 9.1, an agreement of better than 3 % of the assigned uncertainty is found. In this case it is even more surprising than for the frequency ratio of the first isobar pair, since data which are problematic for this method are indicated from the beginning by χ^2_{red}.

Conclusion

Within the polynomial evaluation method, the change in magnetic field is approximated by a polynomial of order n and the frequency ratio R can be extracted from a simultaneous fit to alternating frequency measurements of the isobars under investigation. The main idea is that the polynomial reflects slow drifts and ignores random noise on

Table 9.3: Polynomial order due to the given statistical criteria and resulting frequency ratio R of $^{164}Dy^{1+}$ and $^{164}Er^{1+}$. The statistical uncertainty δR_{stat} results from the fit procedure while $\sigma_{2,K}$ takes the systematic uncertainty of the choice of the polynomial order into account.

run	criteria	order	$(R-1)\times10^7$	$\delta R_{\mathrm{stat}}\times10^9$	$\sigma_{2,K}\times10^9$
1	χ^2_{red}	4	1.6470	2.546	2.879
2	F_χ	2	1.6419	1.575	0.093
3	mean	2-10	1.6284	1.689	0.262
4	F_χ	6	1.6629	1.589	0.398

top of the drifts. In absence of knowledge about the real magnetic field behavior, the order of the polynomials as well as the coefficients themselves have to be extracted from the fit by purely statistical methods and are fixed for the total measurement time within our approximation.
Problems arise, e.g., due to the globally fixed coefficients if slow trends change the behavior within the measurement time. Furthermore, sometimes it might be impossible to separate slow drifts and fast noise due to the total interplay of different sources of changes, which presumably happened for our measurements of $^{164}Er^{1+}$ and $^{164}Dy^{1+}$. In such cases, the statistical methods can fail.
Due to these conceptual difficulties, a systematic error $\sigma_{k,K}$ is assigned to the resulting ratio values, which takes the uncertainty of the choice of the order n into account. This error is added even if statistical indications for the best order are available.
However, with the assumptions for the best polynomial orders given above, the results agree very well with the results obtained from the interpolation method. Nevertheless, especially for problematic data there are certainly other decisions possible, which would definitely change the resulting ratio value (see, e.g. Fig. 9.14b). For this reason, the results of the polynomial fit method are ignored for further evaluation of the Q-values.

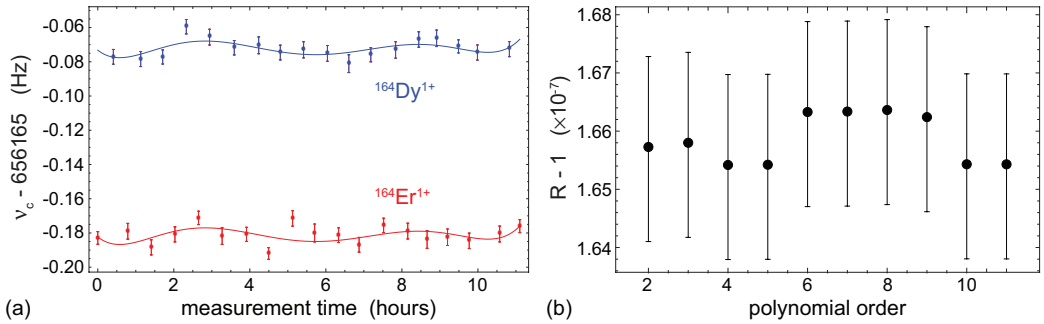

Figure 9.14: (a) Polynomial fit in 6-th order to the fourth day of frequency measurements of ^{164}Er and ^{164}Dy. (b) Ratio as a function of the fitted polynomial order for the same day.

9.3 Results

The total decay energy $Q_{\epsilon\epsilon}$ of the double-electron capture in ^{152}Gd $\rightarrow$ ^{152}Sm and ^{164}Er $\rightarrow$ ^{164}Dy was previously only deduced from differences of absolute values of ground-state masses. However, these data were not precise enough for accurate estimations of the life-time of the mother nuclides. The determination of the cyclotron-frequency ratios discussed in the previous section corresponds to a direct measurement of the mass differences and, hence, to the first direct determination of the $Q_{\epsilon\epsilon}$-value of double-electron capture for these transitions. Together with new calculations of the binding energy of the hole states of the two captured electrons as well as the electron wave functions and the nuclear transition matrix elements, the direct and much more precise determination of $Q_{\epsilon\epsilon}$ allows for a new evaluation of the resonance situation and, ultimately, the life-time of the mother nuclides.

9.3.1 $Q_{\epsilon\epsilon}$-Value and Resonance Condition

With the frequency ratios obtained in Sec. 9.2.2, the total decay energy $Q_{\epsilon\epsilon}$ of the double-electron capture transitions of ^{152}Gd and ^{164}Er can be calculated according to Eq. (7.6). The masses of the daughter atoms as well as the electron mass can be taken from [147] without introducing additional uncertainty (see discussion in Sec. 7.2). For the calculation of the $Q_{\epsilon\epsilon}$-value of ^{164}Er, an additional issue has to be mentioned. The cyclotron-frequency ratio $\nu_c(^{164}\mathrm{Dy}^{1+})/\nu_c(^{164}\mathrm{Er}^{1+})$ was also measured with an octupolar excitation method described in [234], in addition to the value given in Tab. 9.1. This method is beyond the scope of this thesis, although these supplementary ratio data were determined in the same measurement campaign as the value obtained by the Ramsey technique discussed here. The combination of the results of both measurement methods leads to $\nu_c(^{164}\mathrm{Dy}^{1+})/\nu_c(^{164}\mathrm{Er}^{1+}) - 1 = 1.6421(76) \times 10^{-7}$ [234], which shows a decreased uncertainty compared to the value given in Tab. 9.1, due to larger number of individual ratio values.
Hence, in Tab. 9.4 the resulting $Q_{\epsilon\epsilon}$-value of the combined frequency ratio is listed,

Table 9.4: New properties of the $\epsilon\epsilon$-transitions in ^{152}Gd and ^{164}Er. The $Q_{\epsilon\epsilon}$-values were measured within this thesis. Furthermore, precise calculations of the hole binding energies $B_{2\mathrm{h}}$ of the two most likely captured electrons and their total decay width Γ are given and the degeneracy parameter Δ is calculated. The values are taken from [107].

$\epsilon\epsilon$-transition	$Q_{\epsilon\epsilon}$ (keV)	orbital	$B_{2\mathrm{h}}$ (keV)	Δ (keV)	Γ (eV)
$^{152}_{64}\mathrm{Gd} \rightarrow {}^{152}_{62}\mathrm{Sm}$	55.70(18)	$1s, 2s$	54.87	0.83(18)	23
$^{164}_{68}\mathrm{Er} \rightarrow {}^{164}_{66}\mathrm{Dy}$	25.07(12)	$2s, 2s$	18.25	6.82(12)	8.6

whereas the $Q_{\epsilon\epsilon}$-value of ^{152}Gd is directly calculated from the value given in Tab. 9.1. The uncertainties of the resulting $Q_{\epsilon\epsilon}$-values are reduced by a factor of ~ 19 in case of ^{152}Gd and ~ 33 in case of ^{164}Er, compared to the values taken from [147] (see Tab. 7.1).

In order to get insight into the resonance condition for the double-electron capture transitions, the degeneracy parameter $\Delta = Q_{\epsilon\epsilon} - B_{2\mathrm{h}}$ and, ultimately, the resonance-enhancement factor $r_{\epsilon\epsilon} = \Gamma/(\Delta^2 + \Gamma^2/4)$, defined in Eq. (7.1), have to be evaluated. Therefore, besides the determination of the $Q_{\epsilon\epsilon}$-values discussed above, precise calculations of suitable hole binding energies $B_{2\mathrm{h}}$, and the total decay width Γ were performed with the methods discussed in Sec. 2.1.4. The capture of a $1s$ and a $2s$, and two $2s$ electrons are most promising in the case of ^{152}Gd and ^{164}Er, respectively. The values given in [107] are listed in Tab. 9.4, which were calculated with a more advanced method compared to the values given in [106] and [234].
In Fig. 9.15, the degeneracy parameter Δ is shown for all $\epsilon\epsilon$-transition from nuclear ground state to ground state as listed in [218]. In black, crude estimates are shown for which the $Q_{\epsilon\epsilon}$-values are calculated from absolute ground-state mass values given in [147]. The hole binding energies $B_{2\mathrm{h}}$ are approximated by the corresponding electron binding energies B_{2e^-} taken from [105], while the sum of the decay widths Γ of the excited daughter atoms can be found in [108]. The solid lines mark the range of three standard deviations of the experimental error. Solid lines leaving the logarithmic plot at the bottom indicate that the degeneracy is in agreement with complete degeneration $\Delta = 0$ within three σ. In red, the new determination of Δ according to Tab. 9.4 are shown. Besides ^{152}Gd and ^{164}Er, the recent determination of the $Q_{\epsilon\epsilon}$-value of ^{180}W with the calculation of Δ is included [233], too, which is part of the Ph.D. thesis of C. Droese [271]. Furthermore, the $Q_{\epsilon\epsilon}$-value of ^{108}Cd was recently measured at TRIGA-TRAP [272] and the new Δ is calculated with the hole binding energy taken from [101] (see also the Ph.D thesis of C. Smorra [273]). The new degeneracy values are more precise than the previous estimates, mainly due to our first direct determination of the $Q_{\epsilon\epsilon}$-values (without the use of absolute ground state masses), but also due to first calculations of the hole binding energies and their widths.
From the new values, complete degeneracy $\Delta = 0$ can be excluded for all three candidates ^{152}Gd, ^{164}Er and ^{180}W. In Fig. 9.16, the enhancement for all possible $0^+ \rightarrow 0^+$ ground state to ground state transitions is shown, where ^{152}Gd shows the highest $r_{\epsilon\epsilon}$ being at least 6 orders of magnitude larger than the non-resonant case of ^{126}Xe.

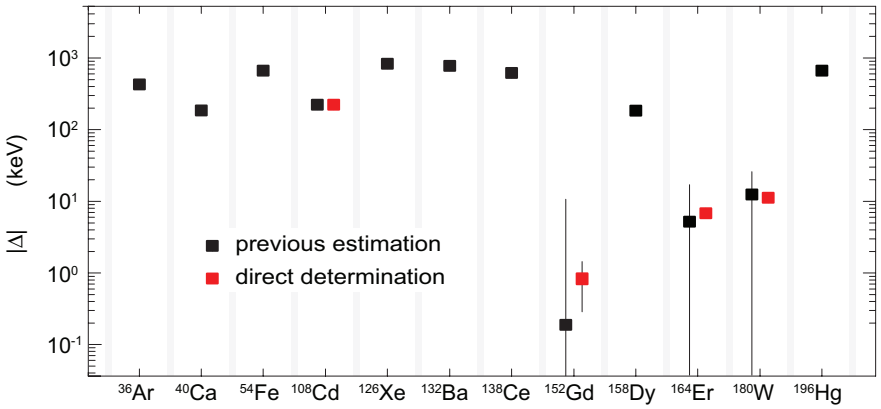

Figure 9.15: Previous estimates and recently determined degeneracy parameters Δ, for all $\epsilon\epsilon$-transition from nuclear ground state to ground state [218]. The previous estimates are based on absolute ground-state mass values, while the new determinations follow from direct $Q_{\epsilon\epsilon}$-value determinations in Penning traps. The values for ^{152}Gd and ^{164}Er are obtained within this thesis. The solid lines mark the range of three standard deviations.

9.3.2 Half-Life of the Double-Electron Capture Process

In order to get estimates on the feasibility of the detection of the double-electron capture process in the candidates under investigation, the decay-rate $\lambda_{\epsilon\epsilon} = |V_{\epsilon\epsilon}|^2 \cdot r_{\epsilon\epsilon}$ given in Eq. (2.23) or, conversely, the half-life $T_{1/2}^{0\nu\epsilon\epsilon}$ has to be calculated. It has the form [101]

$$T_{1/2}^{0\nu\epsilon\epsilon} = \frac{\ln 2}{\lambda_{\epsilon\epsilon}}. \tag{9.33}$$

In the previous section, the resonance-enhancement factor $r_{\epsilon\epsilon}$ was determined for both ^{152}Gd and ^{164}Er, giving the overall scale of the transition half-life. The missing part is the lepton-number violating potential [101]

$$V_{\epsilon\epsilon} \propto \mathcal{A}_{\alpha\beta} M^{0\nu}(J_f^\pi), \tag{9.34}$$

which is proportional to the electron factor $\mathcal{A}_{\alpha\beta}$ and the nuclear matrix element $M^{0\nu}(J_f^\pi)$ (for definition see Eq. (2.24) and Eq. (2.25) and the corresponding discussion). In order to determine the electron factor $\mathcal{A}_{\alpha\beta}$ in a relativistic approach, presented in [101], the well-known wave functions of an electron in the Coulomb field are taken for estimates of the Dirac wave functions, averaged over the volume of the nucleus. In [107], the resulting values are compared with values obtained in the Dirac-Hartree-Fock method with good agreement.
Furthermore, the nuclear matrix elements $M^{0\nu}(J_f^\pi)$ of the transitions ^{152}Gd $\rightarrow$ ^{152}Sm and ^{164}Er $\rightarrow$ ^{164}Dy are calculated in [106] and [234], based on a spherical quasiparticle random phase approximation (QRPA) in analogy to, e.g. [90]. Due to the deformation of all nuclei participating in these transitions, calculations were recently performed

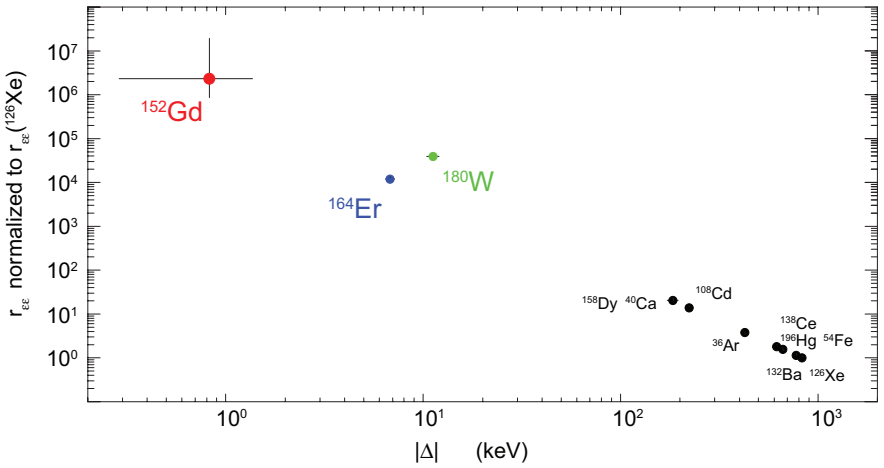

Figure 9.16: Resonance enhancement factor of all $0^+ \rightarrow 0^+$ nuclear ground state to ground state $\epsilon\epsilon$-transitions. The resonance enhancement of ^{152}Gd is at least 6 orders of magnitude larger as the non-resonant case of ^{126}Xe. The solid lines mark the range three standard deviations.

in [107], within a deformed QRPA method with realistic nucleon-nucleon interaction[3]. In this work, the matrix element of $^{180}\mathrm{W} \rightarrow {}^{180}\mathrm{Hf}$ is evaluated, too. The resulting values are $2.67 - 3.23$, $2.27 - 2.64$ and $1.79 - 2.05$ for ^{152}Gd, ^{164}Er and ^{180}W, respectively, depending on the adjustment of the particle-particle strength parameter g_{pp} of the QRPA. This is about a factor of $2 - 3$ smaller than the results obtained by the spherical approximation. For details of the calculation and the used assumptions and approximations see [107].

With the nuclear matrix elements, the electron factors and the resonance-enhancement factors discussed in the previous section, the half-lives of the neutrinoless double-electron capture process can be calculated. In [107], the half-lives are calculated for a Majorana neutrino mass $m_{\beta\beta} = 50$ meV. The upper and lower limits are estimated for mass differences Δ, deviating by three standard errors from the experimental determination (the uncertainty in Δ is by far the largest one of all parameters entering $T^{0\nu\epsilon\epsilon}_{1/2}$). Assuming the capture of the most favored electrons, the limits are given by

$$T^{0\nu\epsilon\epsilon}_{1/2} = \begin{cases} 4.7 \times 10^{28}\ \mathrm{y} \ - \ 4.8 \times 10^{29}\ \mathrm{y} & \text{for } {}^{152}\mathrm{Gd}, \\ 7.5 \times 10^{32}\ \mathrm{y} \ - \ 8.4 \times 10^{32}\ \mathrm{y} & \text{for } {}^{164}\mathrm{Er}, \\ 1.3 \times 10^{31}\ \mathrm{y} \ - \ 1.8 \times 10^{31}\ \mathrm{y} & \text{for } {}^{180}\mathrm{W}. \end{cases} \tag{9.35}$$

From these life-times, the nuclides ^{164}Er and ^{180}W can be excluded as prospective candidates for the detection of the $0\nu\epsilon\epsilon$ process. On the other hand, the capture of electrons from the $1s$ and $2s$ orbitals in ^{152}Gd shows the lowest half-life of all candidates known today, although this transition is still far from full resonance, too. Compared to, e.g. the half-life of the $0\nu\beta\beta$ process in ^{76}Ge, this $0\nu\epsilon\epsilon$ half-life is still $2 - 3$ orders

[3]The details of this method are given in the context of double-β decay in, e.g. [274].

of magnitude longer for the same Majorana neutrino mass. Even in the case of ^{152}Gd, the situation of longer life-time but, presumably, better experimental signatures (see Sec. 2.1.4) might not be advantageous for the detection of the neutrinoless process. Especially in view of the low natural abundance of this isotope (~ 0.2 %), experiments would be faced with immense costs, due to the need of a large enriched sample. Nevertheless, further consideration of all issues of a possible experiment might show a chance of the realization.

9.4 Summary

In Chap. 9, the first direct determination of the $Q_{\epsilon\epsilon}$-values of the double-electron capture process of the transitions ^{152}Gd $\rightarrow$ ^{152}Sm and ^{164}Er $\rightarrow$ ^{164}Dy were presented. The proximity of this total decay energy to the binding energy of the hole-states from captured electrons determines the life-time of this process, where degenerate and non-degenerate cases typically differ by several orders of magnitude. Hence, a precise knowledge is needed in the search for a candidate, which is suitable for the experimental observation of the $0\nu\epsilon\epsilon$.
The new and direct determinations of these mass differences resulted from precise measurements at SHIPTRAP. Most systematical effects canceled in the ratio determination at the presented precision. The residual source of uncertainty were fluctuations of the magnetic field during the frequency measurements, which were, therefore, alternated over several days of data taking.
From two independent ways of data analysis, the frequency ratios were determined to a relative precision of $\sim 10^{-9}$, where the corresponding final uncertainties of the $Q_{\epsilon\epsilon}$-values are given by ~ 180 eV for ^{152}Gd and ~ 120 eV for ^{164}Er. Previous knowledge of the $Q_{\epsilon\epsilon}$-values was based on differences of absolutely measured ground-state masses, where the new directly determined values reduced the uncertainty by a factor of 19 in case of ^{152}Gd and 33 in case of ^{164}Er.
From the new $Q_{\epsilon\epsilon}$-values and first calculations of the binding energy of the hole-states, the degree of degeneracy was re-calculated and, hence, the resonant enhancement of the double-electron capture process determined much more accurate than before. Unfortunately, for both transition it turned out that the full resonance condition is not reached. Together with new calculations of the nuclear matrix elements as well as contributions from the electron wave functions, it was possible to estimate the half-lives of both transitions on a much more profound basis. The lower limits of the half-lives at a hypothetical Majorana neutrino mass of 50 meV are now determined to $\sim 10^{28}$ y and 10^{31} y for ^{152}Gd and ^{164}Er, respectively. From that, ^{164}Er can be excluded as a prospective candidate. In case of ^{152}Gd, this is the lowest life-time of all nuclides known today. Nevertheless, this is still to $2-3$ orders of magnitude longer than typical life-times within $0\nu\beta\beta$ experiments. Hence, the experimental detection of $0\nu\epsilon\epsilon$ with use of this nuclide would be very challenging.

III Conclusion and Outlook

Within this thesis, technical developments and commissioning experiments for the novel high-precision Penning-trap mass spectrometer PENTATRAP as well as Q-value measurements at SHIPTRAP to provide important input parameters in the search for neutrinoless double-electron capture were presented. Following the structure of the thesis, the concluding remarks are separated into the two corresponding parts.

The Penning-Trap Mass Spectrometer PENTATRAP

The novel Penning-trap mass spectrometer PENTATRAP aims for mass-ratio measurement of highly-charged ions with a relative precision of a few parts in 10^{12}. Such a precision is only feasible with an advanced experimental setup. Two key ingredients, the Penning trap tower and the detection system, were presented within this thesis.

- *Trap Tower*

Consisting of five cylindrical Penning traps, the trap tower allows for a simultaneous measurement of two ion species. In the mass-ratio determination, this will greatly reduce the systematic effects of temporal magnetic-field fluctuations compared to an alternating measurement scheme. In order to exclude a shift of the measured mass ratio due to a static magnetic-field gradient, two further traps serve as ion containers, which enables a fast exchange of the two ion species in the measurement traps. The remaining trap is used for a continuous monitoring of the trapping conditions, either the magnetic field or the trapping voltage.
The design of the trap geometry is based on an analytical formula derived from the Laplace equation. In the choice of the geometrical parameters, special care is taken on systemic effects of highly-charged ions stored in the cylindrical traps, in particular on image-charge shifts and the Coulomb repulsion of adjacently stored ions. In the final design, the trap tower offers the possibility of a simultaneous compensation of the leading anharmonic contributions of 4-th and 6-th order and a high degree of orthogonality, both limited by the machining precision of the electrodes.

- *Detection System*

As the second contribution to the PENTATRAP experiment, a cryogenic detection system was developed within this thesis, which will provide all information about the stored ions. In the experimental setup, the axial detector is planned to be the main tool for the measurement of the mass ratios. The axial frequency will be determined directly by a noise dip and the radial frequencies will be measured indirectly by a sideband coupling to the axial mode.

The axial resonator, based on a superconducting wire wound to a toroidal shape, provides an extremely high parallel resistance of ~ 1.1 GΩ. Combined with the cryogenic ultra low-noise amplifier based on GaAs field-effect transistors, the axial detection system shows a remarkable signal-to-noise ratio of ~ 34 dB, limited by the input resistance of the amplifier. Parasitic back action of the amplifier, a crucial source of performance degradation in such highly sensitive detection systems, is negligible in our case.
Moreover, a cryogenic cyclotron detector was setup within this thesis. In the measurement traps, the cyclotron resonator will be used for the direct cooling of the reduced cyclotron mode, while the total detector will be used for the direct detection of ν_+ in the monitor traps. At the high frequencies of 20 to 30 MHz, this detector is characterized by an parallel resistance of ~ 500 kΩ, providing an efficient cooling of highly charged ions.

• *Status of* PENTATRAP *and Outlook*

Besides the developments presented within this thesis, huge effort is invested in order to setup other elements of the PENTATRAP facility, where details of the realization and characterization will be presented in several following Ph.D. theses.
Currently, all mechanical parts, such as the cryogenic chambers, the adjustment system and the beam line to the EBIT, are available and already assembled. The EBIT itself was tested standalone, showing the ability to provide highly-charged ions for our setup. The stabilization system is partly available, where the principle function of the Helmholtz-coils and the stabilization of the pressure in the magnet's bore to 1 μbar are demonstrated. For the newly developed voltage source, all main parts for one channel are available and first tests promise that the needed requirements for high-precision measurements can be fulfilled. A final prototype equipped with 25 channels is expected within the next half year.
In the next step at the facility, planned to be done very soon, the trap setup partly equipped with the detection electronics will be lowered to the magnet's bore. Provided a successful test of, e.g. the vacuum conditions and the thermalization of the setup, the EBIT can be connected to the trap setup for the first time. In subsequent test steps, the full assembly will follow.
For the characterization of the trapping conditions, ^{187}Re ionized to a high charge state will be used. With accumulated experience, this nuclide will, presumably, also be the first measurement case, where the determination of the mass ratio to ^{187}Os reveals the Q-value of the β-decay, an important parameter in the determination of the neutrino mass.

Thus, the future seems to be exciting for this unique experimental setup, which extends the spectrum of high-precision Penning-trap experiments in the division of "stored and cooled ions" at the Max-Planck-Institut für Kernphysik in Heidelberg.

Q-Values of Double-Electron Capture

In the second part of this thesis work, mass-ratio measurements related to neutrino physics, in particular to neutrinoless double-electron capture, were presented. A detection of this process would unambiguously prove the Majorana rather than the Dirac nature of the neutrino, meaning that the neutrino is its own anti-particle. The decision of this long-standing open question in neutrino physics is of basis interest in the construction of theories superior to the Standard Model of elementary particles. In addition, a precise determination of the decay rate of this process would give access to the effective Majorana mass of the neutrino. However, since neutrinoless double-electron capture is a second-order weak-interaction process, expected life-times are excessively long for most nuclides. On the other hand, an energetic degeneracy of the mother nuclide with the excited daughter nuclide leads to a resonant enhancement of the decay rate, which possibly enables a detection in, e.g., micro-calorimetric experiments.
In the search for the most suitable nuclide for the detection, precise information about the total decay energy (Q-value) and the level structure of the excited daughter atom are needed. From the calculation of the Q-values by absolute ground state masses and approximated values of the level structure, the transitions ^{152}Gd $\rightarrow$ ^{152}Sm and ^{164}Er $\rightarrow$ ^{164}Dy were identified as some of the most promising candidates for a resonant enhancement, additionally favored by a comparatively large nuclear matrix element of the nuclear ground-state transition. However, the available data were not accurate enough for a reliable calculation of the decay rate.
In order to provide more precise data, the frequency ratios of ^{152}Sm/^{152}Gd and of ^{164}Dy/^{164}Er were measured with the high-precision Penning-trap mass spectrometer SHIPTRAP at GSI, Darmstadt, where the individual cyclotron frequencies were determined with a destructive time-of-flight detection method. A careful ion preparation and an identical behavior of the isobar pairs due to their almost identical masses and chemical behavior, led to a cancellation of most systematical effects in the traps. The final frequency ratios were obtained to a relative precision of $\sim 10^{-9}$ from an intense data-analysis procedure.
From the frequency ratios, the Q-values were directly extracted to a final uncertainty of $\sim$ 180 eV in case of ^{152}Gd and $\sim$ 120 eV for ^{164}Er. Compared to the previous determination, the values show a reduction of uncertainty by a factor of 19 and 33, respectively.
From the new Q-values and the first calculation of the binding energy of the hole states in the daughter nuclides, the resonant enhancement was determined much more accurate than before. However, in both nuclides the resonance condition is not fully reached. Calculations of the life time with use of recently derived nuclear matrix elements and contributions from the electronic wave functions result in a lower limit of the life times of $\sim 10^{28}$ y and 10^{31} y for ^{152}Gd and ^{164}Er, respectively, if a Majorana neutrino mass of 50 meV is assumed.
Thus, Er can be excluded from the list of prospective candidates for the search of neutrinoless double-electron capture. In case of Gd, this is the lowest life-time of the

neutrinoless double-electron capture transitions known today, where numerous candidates besides this thesis were put under test by Penning-trap mass spectrometry in combination with theoretical input data. However, even for the life-time of Gd a detection seems to be extremely challenging in, e.g., state-of-the-art micro-calorimetric experiments. In addition, due to the low natural abundance of ^{152}Gd of only 0.2 %, the experimenters would be faced with a huge costs for enrichment. In running or planned double-β experiments, which aim for measurements of the same neutrino aspects, life-times are expected to be two to three orders of magnitude lower and, currently, a detection of the neutrinoless mode seems to be more promising.
For the future, more information about the level structure, in particular for the nuclear excitations, is needed for the identification of further candidates and Penning-trap mass-ratio measurements can, again, provide the input parameter of the total decay energy.

Appendix

A Equation of Motion in a Penning Trap

The theoretical description of the motion of particles in a Penning trap can be found in a number of publications, e.g. in [155, 275, 276]. Here, only the basic classical description is reviewed briefly. The electromagnetic field configuration in an ideal Penning trap is given by a homogeneous magnetic field and a quadrupolar electrostatic field defined by

$$\vec{B}(\rho, z) = B_0 \hat{z} \quad \text{and} \quad \vec{E}(\rho, z) = -c_2 U_0 \left(2z\hat{z} + \rho\hat{\rho}\right), \tag{A.1}$$

where U_0 is the voltage applied to a suitable electrode structure and c_2 reflects the strength of the electric field governed by the geometry of the electrodes. The motion of a particle with charge q and mass m inside a Penning trap is determined by the total Lorentz force

$$\vec{F} = q\left(\vec{E} + \dot{\vec{r}} \times \vec{B}\right) = m\ddot{\vec{r}}. \tag{A.2}$$

Hence, the equation of motion can be written by the following system of differential equations:

$$m\begin{pmatrix}\ddot{x}\\ \ddot{y}\end{pmatrix} = qB\begin{pmatrix}0 & 1\\ -1 & 0\end{pmatrix}\begin{pmatrix}\dot{x}\\ \dot{y}\end{pmatrix} + qc_2U_0\begin{pmatrix}x\\ y\end{pmatrix}, \tag{A.3a}$$

$$m\ddot{z} = -2qc_2U_0 z. \tag{A.3b}$$

Axial mode

For the axial mode, Eq. (A.3b) simply describes a harmonic oscillator with the solution

$$z(t) = z_0 \cos\left(\omega_z t + \varphi_z\right), \tag{A.4}$$

where φ_z denotes the phase of the motion. The particle oscillates with the axial frequency given by

$$\omega_z = \sqrt{\frac{q}{m} 2c_2U_0} \qquad \text{for} \qquad qc_2U_0 > 0. \tag{A.5}$$

The amplitude z_0 is given by

$$z_0 = \sqrt{\frac{E_z}{qc_2U_0}}, \tag{A.6}$$

where E_z is the axial energy of the ion.

Radial modes

Due to the coupling of x and y in Eq. (A.3a), more effort is needed for the solution of the radial modes. The transformation

$$u \mapsto x + \mathrm{i}y \tag{A.7}$$

yields in the differential equation

$$m\ddot{u} = \mathrm{i}qB_0\dot{u} + qc_2U_0u. \tag{A.8}$$

This equation corresponds to a damped harmonic oscillator. Nevertheless, due to the purely imaginary damping constant, no energy dissipation is involved. It can be solved by the ansatz $A \cdot \exp(-i\omega t)$, which leads to two characteristic frequencies

$$\omega_\pm = \frac{1}{2}\left(\frac{q}{m}B_0 \pm \sqrt{\left(\frac{q}{m}B_0\right)^2 - 4\frac{q}{m}c_2U_0}\right). \tag{A.9}$$

With the free space cyclotron frequency $\omega_c = qB/m$, this can be written as

$$\omega_\pm = \frac{1}{2}\left(\omega_c \pm \sqrt{\omega_c^2 - 2\omega_z^2}\right). \tag{A.10}$$

A transformation back to cartesian coordinates yields the solution

$$\begin{pmatrix} x(t) \\ y(t) \end{pmatrix} = \rho_+ \begin{pmatrix} \sin(\omega_+ t + \varphi_+) \\ \cos(\omega_+ t + \varphi_+) \end{pmatrix} + \rho_- \begin{pmatrix} \sin(\omega_- t + \varphi_-) \\ \cos(\omega_- t + \varphi_-) \end{pmatrix}. \tag{A.11}$$

The motion in the radial plane is a superposition of two independent oscillations with radii ρ_+ and ρ_-, and the corresponding frequencies ω_+ and ω_-. The lower frequency mode is called *magnetron motion*, while the high frequency mode is called *modified cyclotron motion*.

B Manipulation of the Ion Motion

The trajectories of particles stored in Penning traps can be manipulated by the application of time-dependent electrical fields superimposed to the trapping fields. The response of the particle depends on the amplitude, multipolarity, phase, and frequency of the drive signal. For mass spectrometry, especially dipolar and quadrupolar driving fields are of special importance and will be discussed briefly in the following section. Not discussed here are octupolar excitation schemes, which have recently been used successfully for further improvement of the resolving power in mass spectrometry [234, 277, 278].

Dipolar Excitation

Dipolar excitation can be used to control individual motional modes in a Penning trap [279]. By application of suitable time-varying voltages to the trap electrodes, the dipolar potential close to the center of the Penning trap has the form

$$\phi_i^{(\mathrm{d})}(t) = \phi_{i,0}^{(\mathrm{d})} \cos\left(\omega_{\mathrm{rf}} t + \varphi_{\mathrm{d}}\right) \cdot x_i. \tag{B.1}$$

The resulting electrical field is given by

$$\vec{E}_i^{(\mathrm{d})}(t) = -\nabla \phi_i^{(\mathrm{d})}(t) = -E_{i,0}^{(\mathrm{d})} \cos\left(\omega_{\mathrm{rf}} t + \varphi_{\mathrm{d}}\right) \hat{x}_i. \tag{B.2}$$

This additional field has to be added to the equations of motion (A.3). Taking $\vec{E}^{(\mathrm{d})}$, e.g., pointing in the x-direction, the axial motion is unaffected[4]. The solution for the radial modes has the same form as Eq. (A.11), but with time-dependent radii $\rho_\pm(t)$. In case the external frequency ω_{rf} is resonant with ω_+ or ω_-, the corresponding radial amplitude is given by the relation[5]

$$\rho_\pm(t) = \sqrt{\rho_\pm^2(0) + \frac{k_0^2}{4(\omega_+ - \omega_-)^2} \cdot t^2 \mp \frac{\rho_\pm(0) k_0 \sin\left(\varphi_{\mathrm{d}} - \varphi_\pm(0)\right)}{\omega_+ - \omega_-} \cdot t}, \tag{B.3}$$

with $k_0 = qE_0^{(\mathrm{d})}/m$. As shown in Fig. B.1a, the initial time evolution depends on the phase difference $\Delta\varphi = \varphi_{\mathrm{rf}} - \varphi_\pm$ between the radial motion and the external field. After a certain time, mainly depending on the strength of the excitation, the amplitude increases linearly with time. In case the phase difference $\Delta\varphi$ is equal to $3\pi/2$ for the modified cyclotron motion or $\pi/2$ for the magnetron motion, Eq. (B.3) reduces to

$$\rho_\pm(t) = \rho_\pm(0) + \frac{k_0}{2(\omega_+ - \omega_-)} \cdot t. \tag{B.4}$$

Quadrupolar Excitation

Quadrupolar excitation schemes allow to couple two eigenmotions in the Penning trap to each other. The coupling of the axial mode to both radial modes is treated in [201], while the explicit treatment of the coupling of the two radial modes can be found in [252]. For all cases, the classical equations of motion correspond to a driven quantum mechanical two-level system, which shows a beating between the involved modes.
Near the center of the trap, the quadrupolar coupling field is of the form

$$\vec{E}_{i,j}^{(\mathrm{q})}(t) = \mathcal{E}_0^{(\mathrm{q})} \cos\left(\omega_{\mathrm{rf}} t + \varphi_{\mathrm{q}}\right) \left(x_j \hat{x}_i + x_i \hat{x}_j\right). \tag{B.5}$$

[4] For the axial mode, a result analogical to Eq. (B.3) can be derived by the choice of $\vec{E}^{(\mathrm{d})}$ pointing in the z-direction

[5] The non-resonant radial amplitude remains constant

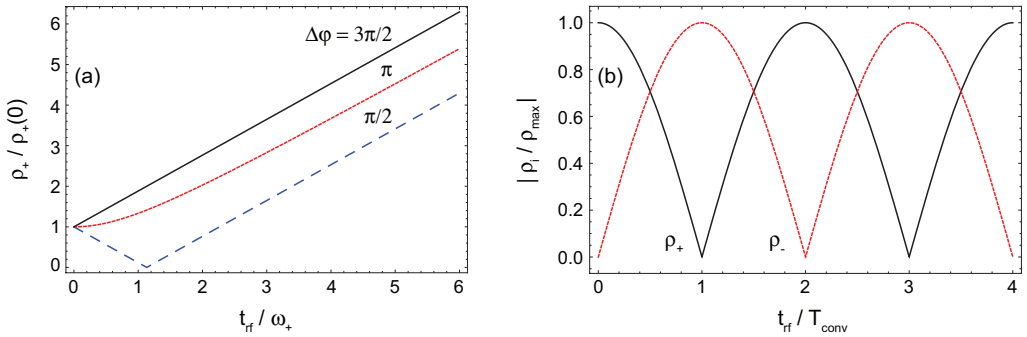

Figure B.1: (a) Time evolution of the modified cyclotron amplitude with dipolar excitation. The initial evolution depends on the phase difference $\Delta\varphi$ between the excitation drive and the ion motion. After some time of excitation mainly depending on the excitation strength, the amplitude increases linearly for all cases. (b) Time evolution of both radial modes with quadrupolar excitation. The amplitudes are continuously converted into each other.

For, e.g., the coupling of the two radial modes, the solution of the equations of motion (A.3), with inclusion of this electrical field, is of the same form as Eq. (A.11), but with time dependent radii of the involved eigenmotions. For a resonant excitation at $\omega_{\mathrm{rf}} = \omega_+ + \omega_-$, the time evolution is given by

$$\rho_\pm(t) = \rho_\pm(0)\cos\left(\frac{\Omega_0}{2}\cdot t\right) \mp \rho_\mp(0)\sin\left(\frac{\Omega_0}{2}\cdot t\right)\cos\left(\varphi_{\mathrm{q}} - \varphi_+ - \varphi_-\right), \tag{B.6}$$

where Ω_0 is the *Rabi frequency*, determined by

$$\Omega_0 = \frac{q}{m}\cdot\frac{\mathcal{E}_0^{(\mathrm{q})}}{2(\omega_+ - \omega_-)}. \tag{B.7}$$

The two radii are harmonically converted into each other with the beating frequency $\Omega_0/2$, which is proportional to the excitation amplitude $\mathcal{E}_0^{(\mathrm{q})}$. The time needed for a complete conversion is given by $T_{\mathrm{conv}} = \pi/\Omega_0$. An excitation with length and strength sufficient for a full exchange of action between two modes is called a π-pulse. In Fig. B.1b, the time evolution of ρ_+ and ρ_- is shown for $\Delta\varphi = \varphi_q - \varphi_+ - \varphi_- = \pi$, with the ion initially prepared in a pure cyclotron state.

As mentioned above, this procedure is suitable for all eigenmodes in the trap. With the right choice of directions in Eq. (B.5), the harmonic conversion occurs at sideband frequencies

$$\omega_{\mathrm{rf}} = \omega_+ + \omega_-, \qquad \text{modified cyclotron - magnetron,} \tag{B.8a}$$
$$= \omega_+ - \omega_z, \qquad \text{modified cyclotron - axial,} \tag{B.8b}$$
$$= \omega_z + \omega_-, \qquad \text{axial - magnetron.} \tag{B.8c}$$

However, for the coupling of the axial to a radial mode, the Rabi frequency is given by [201]

$$\Omega_0^{\mathrm{ax}} = \frac{q}{m}\frac{\mathcal{E}_0^{(q)}}{2\sqrt{\omega_z(\omega_+ - \omega_-)}} \approx \frac{q}{m}\frac{\mathcal{E}_0^{(q)}}{2\sqrt{\omega_z\omega_+}}. \tag{B.9}$$

Finally it has to be mentioned, that the complementary sideband frequencies (meaning that in Eq. (B.8) the sums are changed into differences, and vice versa) do not show a periodic exchange of action between the modes involved. Nevertheless, they have proven to be very useful for high precision experiments, e.g., for the indirect detection of radial modes with the PnA method [194].

C Lab Photographs

Magnet

Figure C.1: 7-T superconducting magnet inside the PENTATRAP laboratory.

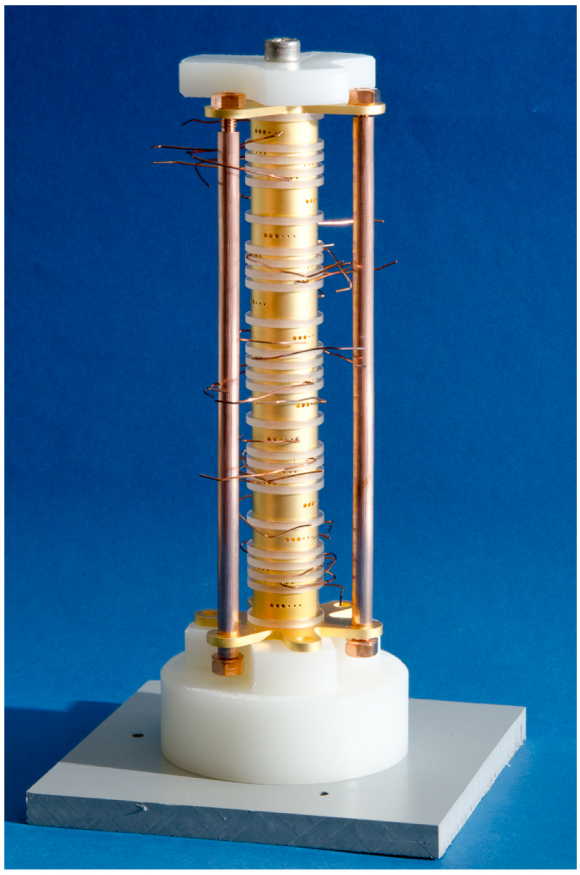

Figure C.2: Trap tower of PENTATRAP.

Cryogenic Axial Detection Electronics

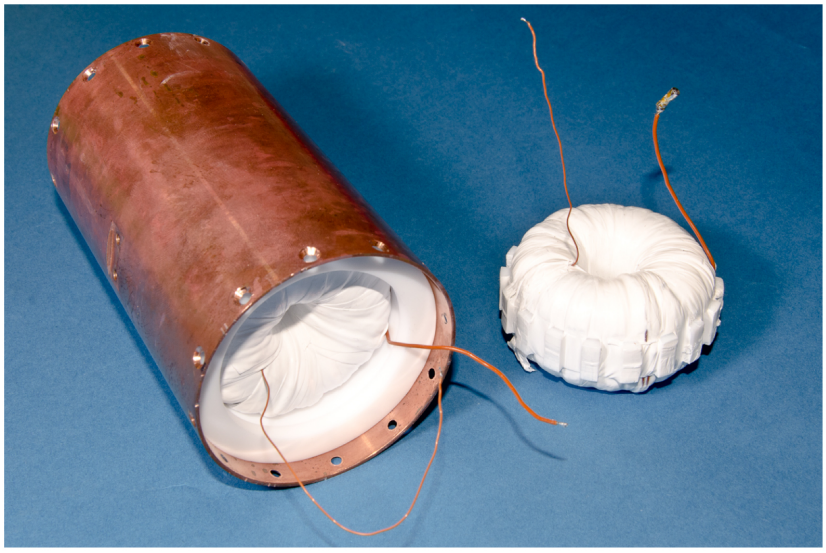

Figure C.3: Axial double resonator with a toroidal coil (left). Second toroidal coil (right).

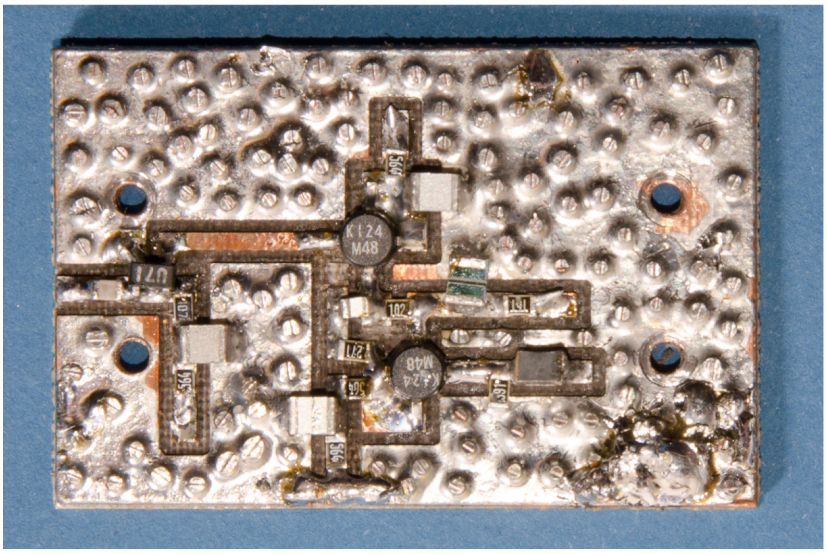

Figure C.4: Cryogenic low-noise amplifier for the axial detection. The input is on the left end of the board.

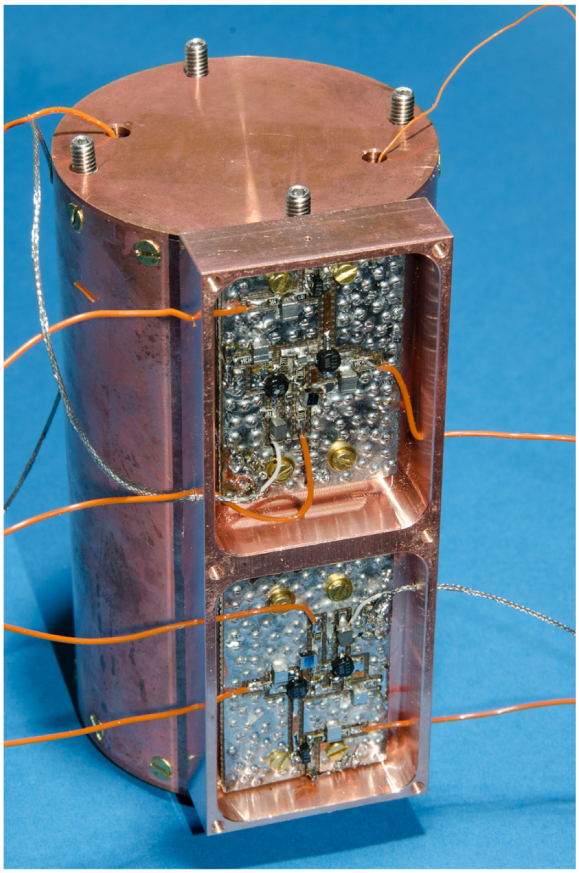

Figure C.5: Axial double resonator equipped with two low-noise amplifiers.

Cryogenic Cyclotron Detection Electronics

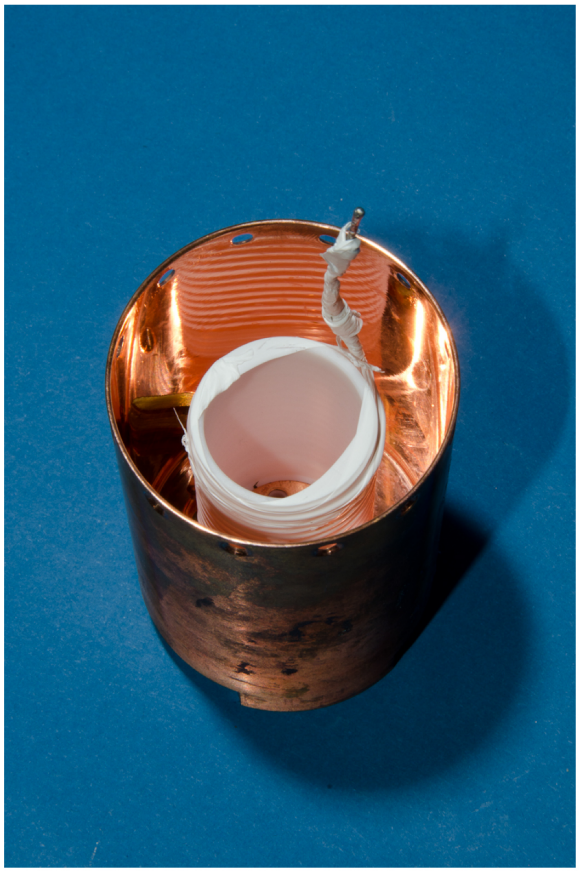

Figure C.6: Cyclotron resonator.

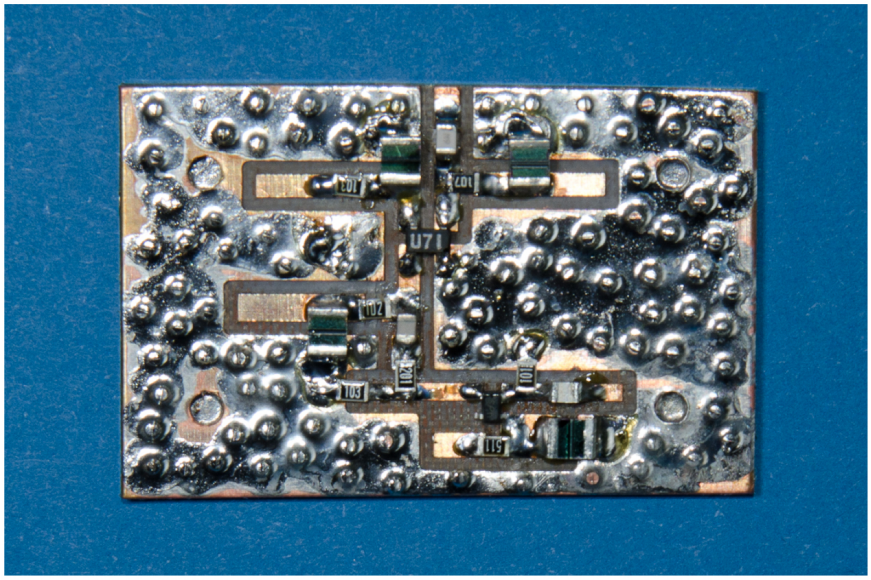

Figure C.7: Cryogenic low-noise amplifier for the cyclotron detection. The input is at the top end of the board.

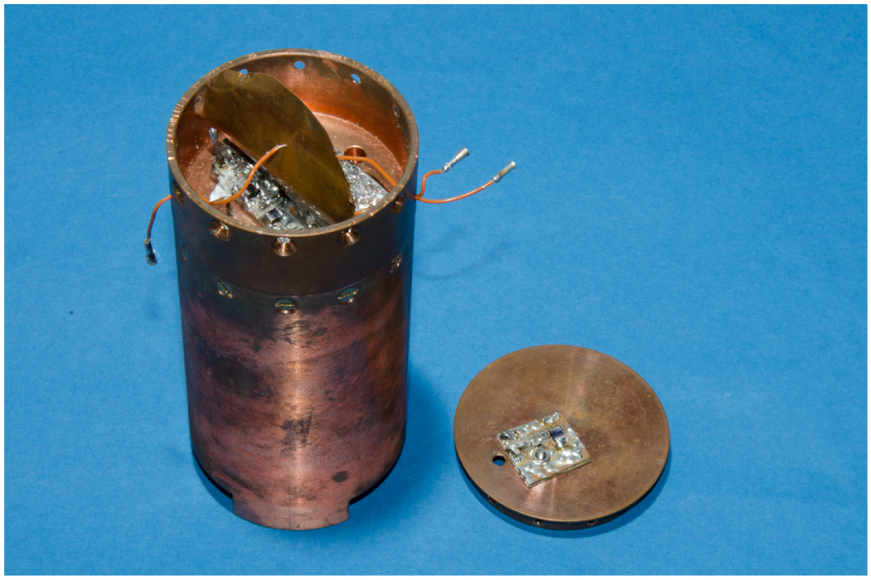

Figure C.8: Cyclotron resonator with amplifier and varactor board. The amplifier is mounted in a separated chamber in the housing (left). The varactor board is mounted on the cap of the amplifier's chamber (right).

Cryogenic Filter Stage

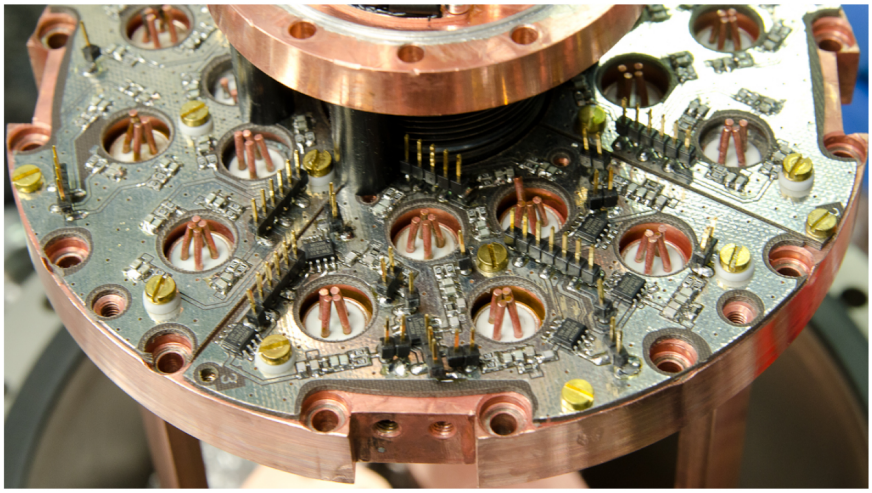

Figure C.9: Cryogenic filter stage on top of the cryogenic electronics chamber. The dc lines for the trap voltages are filtered and the excitation lines are attenuated by capacitive voltage dividers on the board. The excitation lines can be grounded by a cryogenic switch when they are unused.

Bibliography

[1] E. Lichtfouse, *Compound-specific isotope analysis*, Rapid Commun. Mass Spectrom. **14**, 1337 (2000).

[2] B. Domon and R. Aebersold, *Mass Spectrometry and Protein Analysis*, Science **312**, 212 (2006).

[3] R. G. Cooks, Z. Ouyang, Z. Takats and J. M. Wiseman, *Ambient Mass Spectrometry*, Science **311**, 1566 (2006).

[4] A. Einstein, *Ist die Trägheit eines Körpers von seinem Energieinhalt abhängig?*, Ann. Phys. **323**, 639 (1905).

[5] K. Blaum, *High-accuracy mass spectrometry with stored ions*, Phys. Rep. **425**, 1 (2006).

[6] G. Audi, *The history of nuclidic masses and of their evaluation*, Int. J. Mass Spectrom. **251**, 85 (2006).

[7] J. J. Thomson, *Cathode rays*, Phil. Mag. **44**, 293 (1897).

[8] J. J. Thomson, *Further experiments on positive rays*, Phil. Mag. **24**, 209 (1912).

[9] F. W. Aston, *The Mass-Spectra of Chemical Elements*, Phil. Mag. **38**, 707 (1919).

[10] F. W. Aston, *The Atoms of Matter; their Size, Number, and Construction*, Nature (London) **110**, 702 (1922).

[11] W. M. Elsasser, C. R. Acad. Sc. **199**, 46 (1934).

[12] M. Goeppert-Mayer, *On Closed Shells in Nuclei*, Phys. Rev. **74**, 235 (1948).

[13] O. Haxel, J. Jensen and H. Suess, *On the "Magic Numbers" in Nuclear Structure*, Phys. Rev. **75**, 1766 (1949).

[14] W. Paul and H. Steinwedel, *Ein neues Massenspektrometer ohne Magnetfeld*, Z. Naturf. A **8**, 448 (1953).

[15] H. G. Dehmelt, *Experiments with an isolated subatomic particle at rest*, Rev. Mod. Phys. **62**, 525 (1990).

[16] B. Franzke, *The heavy ion storage and cooler ring project ESR at GSI*, Nucl. Instrum. Meth. B **24-25**, 18 (1987).

[17] G. Gräff, H. Kalinowsky and J. Traut, *A Direct Determination of the Proton Electron Mass Ratio*, Z. Phys. A **297**, 35 (1980).

[18] P. B. Schwinberg, R. S. Van Dyck, Jr. and H. G. Dehmelt, *Trapping and thermalization of positrons for geonium spectroscopy*, Phys. Lett. A **81**, 119 (1981).

[19] R. Jertz *et al.*, *Direct determination of the mass of ^{28}Si as a contribution to a new definition of the kilogram*, Phys. Script. **48**, 399 (1993).

[20] E. A. Cornell *et al.*, *Single-ion cyclotron resonance measurement of $M(CO^+)/M(N_2^+)$*, Phys. Rev. Lett. **63**, 1674 (1989).

[21] H. Stolzenberg *et al.*, *Accurate mass determination of short-lived isotopes by a tandem Penning trap mass spectrometer.*, Phys. Rev. Lett. **65**, 3104 (1990).

[22] M. Smith *et al.*, *First Penning-Trap Mass Measurement of the Exotic Halo Nucleus ^{11}Li*, Phys. Rev. Lett. **101**, 202501 (2008).

[23] S. Rainville, J. K. Thompson and D. E. Pritchard, *An ion balance for ultra-high-precision atomic mass measurements*, Science **303**, 334 (2004).

[24] R. S. Van Dyck, D. L. Farnham, S. L. Zafonte and P. B. Schwinberg, *Ultrastable superconducting magnet system for a penning trap mass spectrometer*, Rev. Sci. Instrum. **70**, 1665 (1999).

[25] I. Bergström *et al.*, *SMILETRAP—A Penning trap facility for precision mass measurements using highly charged ions*, Nucl. Instrum. Meth. A **487**, 618 (2002).

[26] K. Blaum, Yu. N. Novikov and G. Werth, *Penning traps as a versatile tool for precise experiments in fundamental physics*, Contemp. Phys. **51**, 149 (2010).

[27] C. Weber, K. Blaum and H. Schatz, *Nuclear Masses in Astrophysics*, arXiv:0812.1675v1 (2008).

[28] G. Gabrielse, *Antiproton mass measurements*, Int. J. Mass Spectrom. **251**, 273 (2006).

[29] M. Vogel, *The anomalous magnetic moment of the electron*, Contemp. Phys. **50**, 437 (2009).

[30] S. Sturm *et al.*, *g Factor of Hydrogenlike $^{28}Si^{13+}$*, Phys. Rev. Lett. **107**, 023002 (2011).

[31] R. S. Van Dyck, D. L. Farnham and P. B. Schwinberg, *Proton-electron mass ratio and the electron's "Atomic Mass"*, IEEE Trans. Instrum. Meas. **44**, 546 (1995).

[32] J. Repp *et al.*, *PENTATRAP: a novel cryogenic multi-Penning-trap experiment for high-precision mass measurements on highly charged ions*, Appl. Phys. B, doi: 10.1007/s00340-011-4823-6 (2012).

[33] H.-J. Kluge *et al.*, *HITRAP: A facility at GSI for highly charged ions*, Adv. Quantum Chem. **53**, 83 (2008).

[34] R. G. Winter, *Double K Capture and Single K Capture with Positron Emission*, Phys. Rev. **100**, 142 (1955).

[35] J. Bernabéu, A. De Rújula and C. Jarlskog, *Neutrinoless double electron capture as a tool to measure the electron neutrino mass*, Nucl. Phys. B **223**, 15 (1983).

[36] M. Block *et al.*, *Towards direct mass measurements of nobelium at SHIPTRAP*, Eur. Phys. J. D **45**, 39 (2007).

[37] K. Zuber, *On the physics of massive neutrinos*, Phys. Rep. **305**, 295 (1998).

[38] S. M. Bilenky, *A Lecture on Neutrinos*, arXiv:hep-ph/0402153v1 (2004).

[39] E. Fermi, *Versuch einer Theorie der β-Strahlen. I*, Z. Phys. **88**, 161 (1934).

[40] C. L. Cowan, F. Reines, F. B. Harrison, H. W. Kruse and A. D. McGuire, *Detection of the free neutrino: A Confirmation*, Science **124**, 103 (1956).

[41] G. T. Danby *et al.*, *Observation of high-energy neutrino reactions and the existence of two kinds of neutrinos*, Phys. Rev. Lett. **9**, 36 (1962).

[42] J. J. Sakurai, *Rest Mass of the Neutrino*, Phys. Rev. Lett. **1**, 40 (1958).

[43] B. Pontecorvo, *Mesonium and anti-mesonium*, Sov. Phys. JETP **6**, 429 (1957).

[44] M. Nakagawa, H. Okonogi, S. Sakata and A. Toyoda, *Possible existence of a neutrino with mass and partial conservation of muon charge*, Prog. Theor. Phys. **30**, 727 (1963).

[45] M. C. Gonzalez-Garcia and M. Maltoni, *Phenomenology with Massive Neutrinos*, Phys. Rep. **460**, 1 (2008).

[46] B. T. Cleveland *et al.*, *Measurement of the solar electron neutrino flux with the Homestake chlorine detector*, Astrophys. J. **496**, 505 (1998).

[47] Y. Fukuda *et al.*, *Solar Neutrino Data Covering Solar Cycle 22*, Phys. Rev. Lett. **77**, 1683 (1996).

[48] R. Becker-Szendy *et al.* (IMB collaboration), *Electron- and muon-neutrino content of the atmospheric flux*, Phys. Rev. D **46**, 3720 (1992).

[49] Y. Fukuda *et al.* (Super-Kamiokande collaboration), *Evidence for Oscillation of Atmospheric Neutrinos*, Phys. Rev. Lett. **81**, 1562 (1998).

[50] Q. R. Ahmad *et al.* (SNO collaboration), *Direct Evidence for Neutrino Flavor Transformation from Neutral-Current Interactions in the Sudbury Neutrino Observatory*, Phys. Rev. Lett. **89**, 011301 (2002).

[51] T. Araki *et al.* (KamLAND collaboration), *Measurement of Neutrino Oscillation with KamLAND: Evidence of Spectral Distortion*, Phys. Rev. Lett. **94**, 081801 (2004).

[52] T. Schwetz, M. Tortola and J. W. F. Valle, *Three-flavour neutrino oscillation update*, New J. Phys. **10**, 113011 (2008).

[53] K. Nakamura *et al.* (Particle Data Group), *Review of Particle Physics*, J. Phys. G Nucl. Partic. **37**, 075021 (2010).

[54] B. A. Reid, L. Verde, R. Jimenez and O. Mena, *Robust neutrino constraints by combining low redshift observations with the CMB*, J. Cosmol. Astropart. P. **2010**, 003 (2010).

[55] E. W. Otten and C. Weinheimer, *Neutrino mass limit from tritium β decay*, Rep. Prog. Phys. **71**, 086201 (2008).

[56] E. Otten, *Searching the absolute neutrino mass in tritium β-decay—interplay between nuclear, atomic and molecular physics*, Hyperfine Interact. **196**, 3 (2010).

[57] J. J. Simpson, *Measurement of the β-energy spectrum of ^3H to determine the antineutrino mass*, Phys. Rev. D **23**, 649 (1981).

[58] Sz. Nagy, T. Fritioff, M. Björkhage, I. Bergström and R. Schuch, *On the Q-value of the tritium β-decay*, Europhys. Lett. **74**, 404 (2006).

[59] V. Lobashev *et al.*, *Direct search for neutrino mass and anomaly in the tritium beta-spectrum: Status of "Troitsk neutrino mass" experiment*, Nucl. Phys. B - Proc. Sup. **91**, 280 (2001).

[60] C. Kraus *et al.*, *Final Results from phase II of the Mainz Neutrino Mass Search in Tritium β Decay*, Eur. Phys. J. C **40**, 447 (2005).

[61] J. Wolf *et al.* (KATRIN collaboration), *The KATRIN neutrino mass experiment*, Nucl. Instrum. Meth. A **623**, 442 (2010).

[62] E. W. Otten, J. Bonn and C. Weinheimer, *The Q-value of tritium β-decay and the neutrino mass*, Int. J. Mass Spectrom. **251**, 173 (2006).

[63] C. Diehl *et al.*, *Progress with the MPIK/UW-PTMS in Heidelberg*, Hyperfine Interact. **199**, 291 (2011).

[64] M. Ubieto-Diaz *et al.*, *A broad-band FT-ICR Penning trap system for KATRIN*, Int. J. Mass Spectrom. **288**, 1 (2009).

[65] B. J. Mount, M. Redshaw and E. G. Myers, *Q Value of $^{115}In \rightarrow ^{115}Sn(3/2^+)$: The Lowest Known Energy β Decay*, Phys. Rev. Lett. **103** (2009).

[66] J. S. E. Wieslander, J. Suhonen and T. Eronen *et al.*, *Smallest Known Q Value of Any Nuclear Decay: The Rare β^- Decay of $^{115}In(9/2^+) \rightarrow {}^{115}Sn(3/2^+)$*, Phys. Rev. Lett. **103**, 122501 (2009).

[67] A. H. Wapstra, G. Audi and C. Thibault, *The AME2003 atomic mass evaluation (I). Evaluation of input data, adjustment procedures*, Nucl. Phys. A **729**, 129 (2003).

[68] C. Arnaboldi *et al.*, *Bolometric Bounds on the Antineutrino Mass*, Phys. Rev. Lett. **91**, 161802 (2003).

[69] M. Galeazzi, F. Fontanelli, F. Gatti and S. Vitale, *End-point energy and half-life of the ^{187}Re β decay*, Phys. Rev. C **63**, 014302 (2000).

[70] A. Nucciotti, *The MARE Project*, J. Low Temp. Phys. **151**, 597 (2008).

[71] A. Nucciotti *et al.* (MARE collaboration), *Neutrino mass calorimetric searches in the MARE experiment*, arXiv:1012.2290v1 **hep-ex** (2010).

[72] L. W. Alvarez, *Nuclear K Electron Capture*, Phys. Rev. **52**, 134 (1937).

[73] C. Bennett *et al.*, *The X-ray spectrum following ^{163}Ho M electron capture*, Phys. Lett. B **107**, 19 (1981).

[74] A. De Rújula, *A new way to measure neutrino masses*, Nucl. Phys. B **188**, 414 (1981).

[75] P. T. Springer, C. L. Bennett and P. A. Baisden, *Measurement of the neutrino mass using the inner bremsstrahlung emitted in the electron-capture decay of ^{163}Ho*, Phys. Rev. A **35**, 679 (1987).

[76] A. De Rújula and M. Lusignoli, *Calorimetric measurements of ^{163}Holmium decay as tools to determine the electron neutrino mass*, Phys. Lett. B **118**, 429 (1982).

[77] L. Fleischmann *et al.*, *Metallic Magnetic Calorimeters for X-Ray Spectroscopy*, IEEE T. Appl. Supercon. **19**, 63 (2009).

[78] C. W. Reich and B. Singh, *Nuclear Data Sheets for A = 163*, Nucl. Data Sheets **111**, 1211 (2010).

[79] S. Eliseev and Ch. Böhm *et al.*, *Direct mass measurements of ^{194}Hg and ^{194}Au: A new route to the neutrino mass determination?*, Phys. Lett. B **693**, 426 (2010).

[80] E. K. Akhmedov, *Neutrino physics*, arXiv:hep-ph/0001264v2 (2000).

[81] J. Schechter and J. W. F. Valle, *Neutrinoless double-β decay in SU(2)$\times$U(1) theories*, Phys. Rev. D **25**, 2951 (1982).

[82] M. Goeppert-Mayer, *Double Beta-Disintegration*, Phys. Rev. **48**, 512 (1935).

[83] K. Zuber, *Double beta decay*, Contemp. Phys. **45**, 491 (2004).

[84] A. S. Barabash, *Double-beta decay: Present status*, Phys. Atom. Nucl. **73**, 162 (2010).

[85] W. H. Furry, *On transition probabilities in double beta-disintegration*, Phys. Rev. **56**, 1184 (1939).

[86] A. S. Barabash, *Double-Beta Decay: Present Status*, Phys. Atom. Nucl. **73**, 162 (2010).

[87] S. M. Bilenky, *Neutrinoless double beta-decay*, Phys. Part. Nuclei **41**, 690 (2010).

[88] H. V. Klapdor-Kleingrothaus, A. Dietz, H. L. Harney and I. V. Krivosheina, *Evidence for neutrinoless double beta decay*, Mod. Phys. Lett. A **16**, 2409 (2001).

[89] H. V. Klapdor-Kleingrothaus and I. V. Krivosheina, *The evidence for the observation of* $0\nu\beta\beta$ *decay: the identification of* $0\nu\beta\beta$ *events from the full spectra*, Mod. Phys. Lett. A **21**, 1547 (2006).

[90] F. Šimkovic, A. Faessler, H. Müther, V. Rodin and M. Stauf, $0\nu\beta\beta$*-decay nuclear matrix elements with self-consistent short-range correlations*, Phys. Rev. C **79**, 055501 (2009).

[91] C. A. Ur *et al.* (GERDA collaboration), *The GERDA experiment: status and perspectives*, Nucl. Phys. B - Proc. Sup. **217**, 38 (2011).

[92] D. G. Phillips *et al.* (MAJORANA collaboration), *The Majorana experiment: an ultra-low background search for neutrinoless double-beta decay*, arXiv:1111.5578v1 **[nucl-ex]** (2011).

[93] F. Šimkovic, A. Faessler, V. Rodin, P. Vogel and J. Engel, *Anatomy of the* $0\nu\beta\beta$ *nuclear matrix elements*, Phys. Rev. C **77**, 045503 (2008).

[94] G. Douysset, T. Fritioff, C. Carlberg, I. Bergström and M. Björkhage, *Determination of the* ^{76}*Ge Double Beta Decay Q Value*, Phys. Rev. Lett. **86**, 4259 (2001).

[95] M. Redshaw, E. Wingfield, J. McDaniel and E. G. Myers, *Mass and Double-Beta-Decay Q Value of* ^{136}*Xe*, Phys. Rev. Lett. **98**, 053003 (2007).

[96] S. Rahaman *et al.*, *Q values of the* ^{76}*Ge and* ^{100}*Mo double-beta decays*, Phys. Lett. B **662**, 111 (2008).

[97] S. Rahaman *et al.*, *Accurate Q Value for the* ^{112}*Sn Double-*β *Decay and its Implication for the Search of the Neutrino Mass*, Phys. Rev. Lett. **103**, 042501 (2009).

[98] M. Redshaw, B. J. Mount, E. G. Myers and F. Avignone, *Masses of ^{130}Te and ^{130}Xe and Double-β-Decay Q Value of ^{130}Te*, Phys. Rev. Lett. **102**, 212502 (2009).

[99] M. B. Voloshin, G. V. Mitsel'makher and R. A. Eramzhyan, *Conversion of an atomic electron into a positron and double β^+ decay*, JETP Lett. **35**, 656 (1982).

[100] Z. Sujkowski and S. Wycech, *Neutrinoless double electron capture: A tool to search for Majorana neutrinos*, Phys. Rev. C **70**, 052501 (2004).

[101] M. I. Krivoruchenko, F. Šimkovic, D. Frekers and A. Faessler, *Resonance enhancement of neutrinoless double electron capture*, Nucl. Phys. A **859**, 140 (2011).

[102] F. Šimkovic and M. I. Krivoruchenko, *Mixing of neutral atoms and lepton number oscillations*, Phys. Part. Nucl. Lett. **6**, 298 (2009).

[103] F. Šimkovic, M. I. Krivoruchenko and A. Faessler, *Neutrinoless double-beta decay and double-electron capture*, Prog. Part. Nucl. Phys. **66**, 446 (2011).

[104] J. Suhonen, *Sub-eV neutrino masses from $0\nu\beta\beta$ decay to an excited 0^+ state*, Phys. Rev. C **62**, 042501 (2000).

[105] F. P. Larkins, *Semiempirical Auger-electron energies for elements $10 \leq Z \leq 100$*, Atom. Data Nucl. Data **20**, 311 (1977).

[106] S. Eliseev and C. Roux *et al.*, *Resonant Enhancement of Neutrinoless Double-Electron Capture in ^{152}Gd*, Phys. Rev. Lett. **106**, 052504 (2011).

[107] D.-L. Fang *et al.*, *Evaluation of the resonance enhancement effect in neutrinoless double-electron capture in ^{152}Gd, ^{164}Er and ^{180}W atoms*, Phys. Rev. C **85**, 035503 (2012).

[108] J. L. Campbell and T. Papp, *Widths of the atomic K-N7 levels*, At. Data Nucl. Data Tables **77**, 1 (2001).

[109] S. Rosen and H. Primakoff, *Double β-Decay*, in: Alpha-, Beta- and Gamma-Ray Spectroscopy, ed. K. Siegbahn, North-Holland Publishing Company, vol. 2.

[110] P. Belli *et al.* (TGV collaboration), *First Results of the Experiment to search for 2β Decay of ^{106}Cd with the help of $^{106}CdWO_4$ Crystal Scintillators*, AIP Conf. Proc. **1304**, 354 (2010).

[111] D. Hanneke, S. Fogwell and G. Gabrielse, *New measurement of the electron magnetic moment and the fine structure constant*, Phys. Rev. Lett. **100**, 120801 (2008).

[112] G. Gabrielse, D. Hanneke, T. Kinoshita, M. Nio and B. Odom, *New Determination of the Fine Structure Constant from the Electron g Value and QED*, Phys. Rev. Lett. **97**, 030802 (2006).

[113] P. J. Mohr and B. N. Taylor, *CODATA recommended values of the fundamental physical constants: 2002*, Rev. Mod. Phys. **77**, 1 (2005).

[114] R. Bouchendira, P. Clade, S. Guellati-Khelifa, F. Nez and F. Biraben, *New determination of the fine structure constant and test of the quantum electrodynamics*, Phys. Rev. Lett. **106**, 080801 (2011).

[115] S. Rainville, M. P. Bradley, J. V. Porto, J. K. Thompson and D. E. Pritchard, *Precise Measurements of the Masses of Cs, Rb and Na–A New Route to the Fine Structure Constant*, Hyperfine Interact. **132**, 177 (2001).

[116] B. de Beauvoir *et al.*, *Metrology of the hydrogen and deuterium atoms: Determination of the Rydberg constant and Lamb shifts*, Eur. Phys. J. D **12**, 61 (2000).

[117] G. Werth *et al.*, *Highly charged ions, quantum-electrodynamics, and the electron mass*, Int. J. Mass Spectrom. **251**, 152 (2006).

[118] B. J. Mount, M. Redshaw and E. G. Myers, *Atomic masses of* $^{6}Li,^{23}Na,^{39,41}K,^{85,87}Rb$, *and* ^{133}Cs, Phys. Rev. A **82**, 042513 (2010).

[119] H. Müller, S.-W. Chiow, Q. Long, S. Herrmann and S. Chu, *Atom Interferometry with up to 24-Photon-Momentum-Transfer Beam Splitters*, Phys. Rev. Lett. **100**, 180405 (2008).

[120] A. O. Jamison, J. N. Kutz and S. Gupta, *Atomic interactions in precision interferometry using Bose-Einstein condensates*, Phys. Rev. A **84**, 043643 (2011).

[121] M. Vogel *et al.*, *The anomalous magnetic moment of the electron in hydrogenlike ions*, Eur. Phys. J. Special Topics **163**, 113 (2008).

[122] H. Häffner *et al.*, *High-Accuracy Measurement of the Magnetic Moment Anomaly of the Electron Bound in Hydrogenlike Carbon*, Phys. Rev. Lett. **85**, 5308 (2000).

[123] J. Verdú *et al.*, *Electronic g Factor of Hydrogenlike Oxygen* $^{16}O^{7+}$, Phys. Rev. Lett. **92**, 093002 (2004).

[124] S. Sturm, *The g-factor of the elctron bound in* $^{28}Si^{13+}$*: The most stringent test of bound-state quantum electrodynamics*, Ph.D. thesis, Universität Mainz (2011).

[125] M. Redshaw, J. McDaniel and E. G. Myers, *Dipole Moment of* PH^{+} *and the Atomic Masses of* ^{28}Si, ^{31}P *by Comparing Cyclotron Frequencies of Two Ions Simultaneously Trapped in a Penning Trap*, Phys. Rev. Lett. **100**, 093002 (2008).

[126] P. J. Mohr, B. N. Taylor and D. B. Newell, *CODATA recommended values of the fundamental physical constants: 2006*, Rev. Mod. Phys. **80**, 633 (2008).

[127] S. Sturm (2012). To be submitted.

[128] I. Bergström *et al.*, *High-precision mass measurements of hydrogen-like $^{24}Mg^{11+}$ and $^{26}Mg^{11+}$ ions in a Penning trap*, Eur. Phys. J. D **22**, 41 (2003).

[129] W. Quint, D. L. Moskovkhin, V. M. Shabaev and M. Vogel, *Laser-microwave double-resonance technique for g-factor measurements in highly charged ions*, Phys. Rev. A **78**, 032517 (2008).

[130] N. P. M. Brantjes, D. von Lindenfels, G. Birkl, W. Quint and M. Vogel, *A Penning trap for g-factor measurements in highly charged ions by laser-microwave double-resonance spectroscopy*, Hyperfine Interact. **199**, 161 (2011).

[131] D. von Lindenfels *et al.*, *Bound electron g-factor measurement by double-resonance spectroscopy on a fine-structure transition*, Can. J. Phys. **89**, 79 (2011).

[132] A. N. Artemyev, V. M. Shabaev, V. A. Yerokhin, G. Plunien and G. Soff, *QED calculation of the n=1 and n=2 energy levels in He-like ions*, Phys. Rev. A **71**, 062104 (2005).

[133] Z. Harman *et al.*, *Benchmarking high-field few-electron correlation and QED contributions in Hg^{75+} to Hg^{78+} ions. II. Theory*, Phys. Rev. A **73**, 052711 (2006).

[134] A. Gumberidze *et al.*, *Quantum Electrodynamics in Strong Electric Fields: The Ground-State Lamb Shift in Hydrogenlike Uranium*, Phys. Rev. Lett. **94**, 223001 (2005).

[135] A. J. González Martínez *et al.*, *Benchmarking high-field few-electron correlation and QED contributions in Hg^{75+} to Hg^{78+} ions. I. Experiment*, Phys. Rev. A **73**, 052710 (2006).

[136] Z. Harman, private communication (2012).

[137] G. C. Rodrigues, P. Indelicato, J. P. Santos, P. Patté and F. Parente, *Systematic calculation of total atomic energies of ground state configurations*, At. Data Nucl. Data Tables **86**, 117 (2004).

[138] S. Rainville *et al.*, *A direct test of $E= mc^2$*, Nature **438**, 1096 (2005).

[139] E. G. Kessler *et al.*, *The GAMS4 flat crystal facility*, Nucl. Instrum. Meth. A **457**, 187 (2001).

[140] A. Brillet and J. L. Hall, *Improved Laser Test of the Isotropy of Space*, Phys. Rev. Lett. **42**, 549 (1979).

[141] C. J. Berglund *et al.*, *New Limits on Local Lorentz Invariance from Hg and Cs Magnetometers*, Phys. Rev. Lett. **75**, 1879 (1995).

[142] S. Coleman and S. L. Glashow, *High-energy tests of Lorentz invariance*, Phys. Rev. D **59**, 116008 (1999).

[143] G. L. Greene, M. S. Dewey, E. G. Kessler and E. Fischbach, *Test of special relativity by a determination of the Lorentz limiting velocity: Does E=mc²?*, Phys. Rev. D **44**, R2216 (1991).

[144] M. Jentschel *et al.*, *Measurement of neutron binding energy of ^{36}Cl for a determination of $N_A h$*, CPEM p. 632 (2008).

[145] J. Krempel *et al.*, *Progress on the GAMS-6 double crystal γ-spectrometer*, CPEM p. 634 (2008).

[146] M. Jentschel, *private communication* (2012).

[147] G. Audi, O. Bersillon, J. Blachot and A. H. Wapstra, *The NUBASE evaluation of nuclear and decay properties*, Nucl. Phys. A **729**, 3 (2003).

[148] S. Earnshaw, *On the nature of the molecular forces which regulate the constitution of the luminiferous ether*, Trans. Camb. Phil. Soc. **7**, 97 (1842).

[149] J. C. Maxwell, *A Dynamical Theory of the Electromagnetic Field*, Philos. T. R. Soc. Lond. **155**, 459 (1865).

[150] J. R. Pierce, *Theory and design of electron beams*, D. Van Nostrand Company (1954).

[151] W. Paul, *Electromagnetic traps for charged and neutral particles*, Rev. Mod. Phys. **62**, 531 (1990).

[152] D. J. Wineland, P. A. Ekstrom and H. G. Dehmelt, *Monoelectron Oscillator*, Phys. Rev. Lett. **31**, 1279 (1973).

[153] R. S. Van Dyck, Jr., P. B. Schwinberg and H. G. Dehmelt, *New High Precision Comparison of electron and Positron G Factors*, Phys. Rev. Lett. **59**, 26 (1987).

[154] F. M. Penning, *The glow discharge at low pressure between coaxial cylinders in an axial magnetic field*, Physica 3 p. 873 (1936).

[155] L. S. Brown and G. Gabrielse, *Geonium theory: Physics of a single electron or ion in a Penning trap*, Rev. Mod. Phys. **58**, 233 (1986).

[156] W. M. Itano and D. J. Wineland, *Laser cooling of ions stored in harmonic and Penning traps*, Phys. Rev. A **25**, 35 (1982).

[157] L. Schweikhard and A. G. Marshall, *Excitation modes for Fourier transform-ion cyclotron resonance mass spectrometry*, J. Am. Soc. Mass Spectr. **4**, 433 (1993).

[158] K. Blaum *et al.*, *Carbon clusters for absolute mass measurements at ISOLTRAP*, Eur. Phys. J. A **15**, 245 (2002).

[159] L. S. Brown and G. Gabrielse, *Precision spectroscopy of a charged particle in an imperfect Penning trap*, Phys. Rev. A **25**, 2423 (1982).

[160] G. Gabrielse, *Relaxation calculation of the electrostatic properties of compensated Penning traps with hyperbolic electrodes*, Phys. Rev. A **27**, 2277 (1983).

[161] J. Verdú *et al.*, *Calculation of electrostatic fields using quasi-Green's functions: application to the hybrid Penning trap*, New J. Phys. **10**, 103009 (2008).

[162] S. Ulmer, *First Observation of Spin Flips with a Single Proton Stored in a Cryogenic Penning Trap*, Ph.D. thesis, Universität Heidelberg (2011).

[163] G. Gabrielse and F. C. MacKintosh, *Cylindrical Penning traps with orthogonalized anharmonicity compensation*, Int. J. Mass Spectrom. **57**, 1 (1984).

[164] M. Kretzschmar, *Single particle motion in a Penning trap: description in the classical canonical formalism*, Phys. Scr. **46**, 544 (1992).

[165] K. Blaum *et al.*, *g-factor experiments on simple systems in Penning traps*, J. Phys. B: At. Mol. Opt. Phys. **42**, 154021 (2009).

[166] J. Verdú, *Ultrapräzise Messung des elektronischen g-Faktors in wasserstoffähnlichem Sauerstoff*, Ph.D. thesis, Universität Mainz (2004).

[167] D. L. Farnham, *A Determination of the Proton/Electron Mass Ratio and the Electron's Atomic Mass via Penning Trap Mass Spectroscopy.*, Ph.D. thesis, University of Washington (1995).

[168] R. S. Van Dyck, Jr., F. L. Moore, D. L. Farnham and P. B. Schwinberg, *Number dependency in the compensated Penning trap*, Phys. Rev. A **40**, 6308 (1989).

[169] V. P. Ovsyannikov and G. Zschornack, *First investigations of a warm electron beam ion trap for the production of highly charged ions*, Rev. Sci. Instrum. **70**, 2646 (1999).

[170] U. Kentsch, G. Zschornack, A. Schwan and F. Ullmann, *Short time ion pulse extraction from the Dresden electron beam ion trap*, Rev. Sci. Instrum. **81**, 02A507 (2010).

[171] J. R. Crespo López-Urrutia *et al.*, *Optimization of the charge state distribution of the ion beam extracted from an EBIT by dielectronic recombination*, Rev. Sci. Instrum. **75**, 1560 (2004).

[172] J. Repp, Ph.D. thesis, *to be submitted*, Universität Heidelberg (2012).

[173] Ch. Böhm, Ph.D. thesis, *to be submitted*, Universität Heidelberg (2013).

[174] A. Rischka, *Aufbau und Charakterisierung eines Systems zur Stabilisierung des Magnetfeldes an PENTATRAP*, Bachelor thesis, Universität Heidelberg (2011).

[175] M. A. Levine *et al.*, *The use of an electron beam ion trap in the study of highly charged ions*, Nucl. Instrum. Meth. B **43**, 431 (1989).

[176] J. R. Crespo López-Urrutia, *private communication* (2011).

[177] D. J. Manura and D. A. Dahl, *SIMION^{TM} 8.0 User Manual*, Scientific Instrument Services, Inc. (2007).

[178] D. Beck, K. Blaum, H. Brand, F. Herfurth and S. Schwarz, *A new control system for ISOLTRAP*, Nucl. Instrum. Meth. A **527**, 567 (2004).

[179] M. Goncharov, Ph.D. thesis, *to be submitted*, Universität Heidelberg (2013).

[180] C. Roux *et al.*, *The trap design of PENTATRAP*, Appl. Phys. B, doi: 10.1007/s00340-011-4825-4 (2011).

[181] S. Rainville, *A Two-Ion Balance for High Precision Mass Spectrometry*, Ph.D. thesis, Massachusetts Institut of Technology (2003).

[182] J. K. Thompson, *Two-Ion Control and Polarization Forces for Precise Mass Comparisons*, Ph.D. thesis, Massachusetts Institut of Technology (2003).

[183] D. B. Pinegar, K. Blaum, T. P. Biesiadzinski, S. L. Zafonte and R. S. Van Dyck, *Stable voltage source for Penning trap experiments*, Rev. Sci. Instrum. **80**, 064701 (2009).

[184] G. Gabrielse, L. Haarsma and S. Rolston, *Open-endcap Penning traps for high precision experiments*, Int. J. Mass Spectrom. **88**, 319 (1989).

[185] S. Ulmer *et al.*, *Observation of Spin Flips with a Single Trapped Proton*, Phys. Rev. Lett. **106**, 253001 (2011).

[186] M. Amoretti *et al.*, *Production and detection of cold antihydrogen atoms*, Nature **419**, 456 (2002).

[187] G. Gabrielse *et al.*, *Background-free observation of cold antihydrogen with field-ionization analysis of its states*, Phys. Rev. Lett. **89**, 213401 (2002).

[188] R. S. Van Dyck, D. J. Wineland, P. A. Ekstrom and H. G. Dehmelt, *High mass resolution with a new variable anharmonicity Penning trap*, Appl. Phys. Lett. **28**, 446 (1976).

[189] J. D. Jackson, *Classical Electrodynamics*, Wiley, New York (1975), third edn.

[190] I. N. Bronstein, K. A. Semendjajew, G. Musiol and H. Mühlig, *Taschenbuch der Mathematik*, Verlag Harri Deutsch (2005), sixth edn.

[191] J. V. Porto, *Series solution for the image charge fields in arbitrary cylindrically symmetric Penning traps*, Phys. Rev. A **64**, 023403 (2001).

[192] H. Häffner, *Präzisionsmessung des magnetischen Moments des Elektrons in wasserstoffähnlichem Kohlenstoff*, Ph.D. thesis, Universität Mainz (2000).

[193] S. Ulmer, *private communication* (2011).

[194] S. Sturm, A. Wagner, B. Schabinger and K. Blaum, *Phase-Sensitive Cyclotron Frequency Measurements at Ultralow Energies*, Phys. Rev. Lett. **107**, 143003 (2011).

[195] W. Shockley, *Currents to conductors induced by a moving point charge*, J. Appl. Phys. **9**, 635 (1938).

[196] D. J. Wineland and H. G. Dehmelt, *Principles of the stored ion calorimeter*, J. Appl. Phys. **46**, 919 (1975).

[197] C. Bowick, *Rf circuit design*, Elsevier (2008), second edn.

[198] J. B. Johnson, *Thermal agitation of electricity in conductors*, Phys. Rev. **32**, 97 (1928).

[199] H. Nyquist, *Thermal agitation of electric charge in conductors*, Phys. Rev. **32**, 110 (1928).

[200] X. Feng, M. Charlton, M. Holzscheiter, R. A. Lewis and Y. Yamazaki, *Tank circuit model applied to particles in a Penning trap*, J. Appl. Phys. **79**, 8 (1996).

[201] E. A. Cornell, R. M. Weisskoff, K. R. Boyce and D. E. Pritchard, *Mode coupling in a Penning trap: π pulses and a classical avoided crossing*, Phys. Rev. A **41**, 312 (1990).

[202] J. Verdú *et al.*, *Determination of the g-Factor of Single Hydrogen-Like Ions by Mode Coupling in a Penning Trap*, Phys. Scr. **T112**, 68 (2004).

[203] S. Ulmer *et al.*, *Direct Measurement of the Free Cyclotron Frequency of a Single Particle in a Penning Trap*, Phys. Rev. Lett. **107**, 103002 (2011).

[204] S. R. Jefferts, T. Heavner, P. Hayes and G. H. Dunn, *Superconducting resonator and a cryogenic GaAs field-effect transistor amplifier as a single-ion detection system*, Rev. Sci. Instrum. **64**, 737 (1993).

[205] S. Stahl, *Aufbau eines Experiments zur Bestimmung elektronischer g-Faktoren einzelner wasserstoffähnlicher Ionen*, Ph.D. thesis, Universität Mainz (1998).

[206] J. B. Camp, T. W. Darling and R. E. Brown, *Macroscopic variations of surface potentials of conductors*, J. Appl. Phys. **69**, 7126 (1991).

[207] S. Ulmer *et al.*, *The quality factor of a superconducting rf resonator in a magnetic field*, Rev. Sci. Instrum. **80**, 123302 (2009).

[208] W. Buckel and R. Kleiner, *Supraleitung*, Wiley-VCH (2004), 6th edn.

[209] A. Mooser, Ph.D. thesis, *to be submitted*, Universität Mainz (2013).

[210] J. W. Ekin, *Experimental techniques for low-temperature measurements*, Oxford University Press (2006).

[211] A. F. Podell, *A functional GaAs FET noise model*, IEEE T. Electron. Dev. **28**, 511 (1981).

[212] U. Tietze and C. Schenk, *Halbleiter-Schaltungstechnik*, Springer (2002), 12th edn.

[213] B. D'Urso, B. Odom and G. Gabrielse, *Feedback cooling of a one-electron oscillator*, Phys. Rev. Lett. **90**, 043001 (2003).

[214] B. R. D'Urso, *Cooling and Self-Excitation of a One-Electron Oscillator*, Ph.D. thesis, Harvard University (2003).

[215] E. Daw and R. F. Bradley, *Effect of high magnetic fields on the noise temperature of a heterostructure field-effect transistor low-noise amplifier*, J. Appl. Phys. **82**, 4 (1997).

[216] A. Dörr, Ph.D. thesis, *to be submitted*, Universität Heidelberg (2014).

[217] W. W. Macalpine and R. O. Schildknecht, *Coaxial resonators with helical inner conductor*, Proc. IRE **47**, 2099 (1959).

[218] V. I. Tretyak and Y. G. Zdesenko, *Tables of double beta decay data—an update*, Atom. Data Nucl. Data **80**, 83 (2002).

[219] D. Frekers, *Nuclear-atomic state degeneracy in neutrinoless double-electron capture: A unique test for a Majorana-neutrino*, arXiv:hep-ex/0506002v2 (2009).

[220] *NIST Chemistry WebBook*, edited by P.J. Linstrom and W.G. Mallard http://webbook.nist.gov.

[221] M. Block *et al.*, *Direct mass measurements above uranium bridge the gap to the island of stability*, Nature **463**, 785 (2010).

[222] M. Dworschak *et al.*, *Penning trap mass measurements on nobelium isotopes*, Phys. Rev. C **81**, 064312 (2010).

[223] M. Block *et al.*, *Mass Measurements of No and Lr isotopes with SHIPTRAP*. GSI Scientific Report (2010).

[224] P. Möller and J. R. Nix, *Stability of heavy and superheavy elements*, J. Phys. G: Nucl. Part. Phys. **20**, 1681 (1994).

[225] M. Bender, K. Rutz, P.-G. Reinhard, J. A. Maruhn and W. Greiner, *Shell structure of superheavy nuclei in self-consistent mean-field models*, Phys. Rev. C **60**, 034304 (1999).

[226] S. Cwiok, P.-H. Heenen and W. Nazarewicz, *Shape coexistence and triaxiality in the superheavy nuclei*, Nature **433**, 705 (2005).

[227] A. Martin *et al.*, *Mass measurements of neutron-deficient radionuclides near the end-point of the rp-process with SHIPTRAP*, Eur. Phys. J. A **34**, 341 (2008).

[228] C. Weber *et al.*, *Mass measurements in the vicinity of the rp-process and the νp-process paths with the Penning trap facilities JYFLTRAP and SHIPTRAP*, Phys. Rev. C **78**, 054310 (2008).

[229] C. Rauth *et al.*, *First Penning Trap Mass Measurements beyond the Proton Drip Line*, Phys. Rev. Lett. **100**, 012501 (2008).

[230] S. Eliseev *et al.*, *Q values for neutrinoless double-electron capture in ^{96}Ru, ^{162}Er, and ^{168}Yb*, Phys. Rev. C **83**, 038501 (2011).

[231] S. Eliseev *et al.*, *Multiple-resonance phenomenon in neutrinoless double-electron capture*, Phys. Rev. C **84**, 012501(R) (2011).

[232] M. Goncharov *et al.*, *Probing the nuclides ^{102}Pd, ^{106}Cd, and ^{144}Sm for resonant neutrinoless double-electron capture*, Phys. Rev. C **84**, 28501 (2011).

[233] C. Droese *et al.*, *Probing the nuclide ^{180}W for neutrinoless double-electron capture exploration*, Nucl. Phys. A **875**, 1 (2012).

[234] S. Eliseev and C. Roux *et al.*, *Octupolar-Excitation Penning-Trap Mass Spectrometry for Q-Value Measurement of Double-Electron Capture in ^{164}Er*, Phys. Rev. Lett. **107**, 152501 (2011).

[235] G. Münzenberg *et al.*, *The velocity filter SHIP, a separator of unslowed heavy ion fusion products*, Nucl. Instrum. Methods **161**, 65 (1979).

[236] S. Hofmann and G. Münzenberg, *The discovery of the heaviest elements*, Rev. Mod. Phys. **72**, 733 (2000).

[237] P. Ludwig, R. Geller and G. Melin, *The 10-GHz NEOMAFIOS upgraded electron cyclotron resonance ion source*, Rev. Sci. Instrum. **63**, 2892 (1992).

[238] J. B. Neumayr *et al.*, *The ion-catcher device for SHIPTRAP*, Nucl. Instrum. Meth. B **244**, 489 (2006).

[239] S. Eliseev *et al.*, *Extraction efficiency and extraction time of the SHIPTRAP gas-filled stopping cell*, Nucl. Instrum. Meth. B **258**, 479 (2007).

[240] D. Rodríguez, *An RFQ buncher for accumulation and cooling of heavy radionuclides at SHIPTRAP and high precision mass measurements on unstable Kr isotopes at ISOLTRAP*, Ph.D. thesis, University of Valencia (2003).

[241] J. Werner, *Flugzeitmassenspektrometrie und Designstudie für einen neuen RF-Quadrupol-Buncher bei SHIPTRAP*, Bachelor thesis, Universität Gießen (2008).

[242] A. Chaudhuri *et al.*, *Carbon-cluster mass calibration at SHIPTRAP*, Eur. Phys. J. D **45**, 47 (2007).

[243] A. Chaudhuri, *Carbon-cluster mass calibration at SHIPTRAP*, Ph.D. thesis, Universität Greifswald (2007).

[244] M. Lindinger *et al.*, *Cluster isobars for high-precision mass spectrometry*, Z. Phys. D Atom. Mol. Cl. **20**, 441 (1991).

[245] G. Sikler, *Massenspektrometrie kurzlebiger Sr- und Sn-Isotope und Aufbau der SHIPTRAP-Penningfallen*, Ph.D. thesis, Universität Heidelberg (2003).

[246] G. Savard *et al.*, *A new cooling technique for heavy ions in a Penning trap*, Phys. Lett. A **158**, 247 (1991).

[247] P. W. Anderson, *Theory of Flux Creep in Hard Superconductors*, Phys. Rev. Lett. **9**, 309 (1962).

[248] P. W. Anderson and Y. B. Kim, *Hard Superconductivity: Theory of the Motion of Abrikosov Flux Lines*, Rev. Mod. Phys. **36**, 39 (1964).

[249] C. Droese *et al.*, *Investigation of the magnetic field fluctuation and implementation of a temperature and pressure stabilization at SHIPTRAP*, Nucl. Instrum. Meth. A **632**, 157 (2011).

[250] M. Kretzschmar, *Calculating damping effects for the ion motion in a Penning trap*, Eur. Phys. J. D **48**, 313 (2008).

[251] S. George *et al.*, *Damping effects in Penning trap mass spectrometry*, Int. J. Mass Spectrom. **299**, 102 (2011).

[252] M. König, G. Bollen, H.-J. Kluge, T. Otto and J. Szerypo, *Quadrupole excitation of stored ion motion at the true cyclotron frequency*, Int. J. Mass Spectrom. **142**, 95 (1995).

[253] S. George *et al.*, *Ramsey Method of Separated Oscillatory Fields for High-Precision Penning Trap Mass Spectrometry*, Phys. Rev. Lett. **98**, 162501 (2007).

[254] M. Kretzschmar, *The Ramsey method in high-precision mass spectrometry with Penning traps: Theoretical foundations*, Int. J. Mass Spectrom. **264**, 122 (2007).

[255] S. George *et al.*, *The Ramsey method in high-precision mass spectrometry with Penning traps: Experimental results*, Int. J. Mass Spectrom. **264**, 110 (2007).

[256] M. P. Bradley, J. V. Porto, S. Rainville, J. K. Thompson and D. E. Pritchard, *Penning Trap Measurements of the Masses of ^{133}Cs, $^{85,87}Rb$, and ^{23}Na with Uncertainties ≤ 0.2 ppb*, Phys. Rev. Lett. **83**, 4510 (1999).

[257] R. J. Barlow, *Statistics*, John Wiley & Sons (1989).

[258] A. Kellerbauer *et al.*, *From direct to absolute mass measurements: A study of the accuracy of ISOLTRAP*, Eur. Phys. J. D **22**, 53 (2002).

[259] G. Bollen *et al.*, *ISOLTRAP: a tandem Penning trap system for accurate on-line mass determination of short-lived isotopes*, Nucl. Instrum. Meth. A **368**, 675 (1996).

[260] G. Bollen, *Mass measurements of short-lived nuclides with ion traps*, Nucl. Phys. A **693**, 3 (2001).

[261] M. Mukherjee *et al.*, *ISOLTRAP: An on-line Penning trap for mass spectrometry on short-lived nuclides*, Eur. Phys. J. A **35**, 1 (2008).

[262] J. Ketelaer *et al.*, *Recent developments in ion detection techniques for Penning trap mass spectrometry at TRIGA-TRAP*, Eur. Phys. J. A **42**, 311 (2009).

[263] S. Schwarz *et al.*, *The LEBIT facility at MSU*, Hyperfine Interact. **173**, 113 (2006).

[264] G. Bollen *et al.*, *Resolution of nuclear ground and isomeric states by a Penning trap mass spectrometer*, Phys. Rev. C **46**, R2140 (1992).

[265] G. Gabrielse, *Why Is Sideband Mass Spectrometry Possible with Ions in a Penning Trap?*, Phys. Rev. Lett. **102**, 172501 (2009).

[266] J. Ketelaer, *The construction of TRIGA-TRAP and direct high-precision Penning trap mass measurements on rare-earth elements and americium*, Ph.D. thesis, Universität Mainz (2010).

[267] R. E. Russo, X. L. Mao, C. Liu and J. Gonzalez, *Laser assisted plasma spectrochemistry: laser ablation*, J. Anal. At. Spectrom. **19**, 1084 (2004).

[268] R. Birge, *The calculation of errors by the method of least squares*, Phys. Rev. **40**, 207 (1932).

[269] P. R. Bevington and D. K. Robinson, *Data Reduction and Error Analysis for the Physical Sciences, 2nd ed.*, McGraw-Hill (1992).

[270] F. DiFilippo, *Precise Atomic Masses for Determining Fundamental Constants*, Ph.D. thesis, Massachusetts Institut of Technology (1994).

[271] C. Droese, Ph.D. thesis, *to be submitted*, Universität Greifswald (2012).

[272] C. Smorra *et al.*, *Direct mass measurements of cadmium and palladium isotopes and their double-β transition Q values*, Phys. Rev. C **85**, 027601 (2012).

[273] C. Smorra, *High-precision Q-value and mass measurements for neutrino physics with TRIGA-TRAP and commissioning of an on-line ion source for TRIGA-SPEC*, Ph.D. thesis, Universität Heidelberg (2012).

[274] D.-L. Fang, A. Faessler, V. Rodin and F. Šimkovic, *Neutrinoless double-β decay of deformed nuclei within quasiparticle random-phase approximation with a realistic interaction*, Phys. Rev. C **83**, 034320 (2011).

[275] G. Bollen, R. B. Moore, G. Savard and H. Stolzenberg, *The accuracy of heavy-ion mass measurements using time of flight-ion cyclotron resonance in a Penning trap*, J. Appl. Phys. **68**, 4355 (1990).

[276] M. Kretzschmar, *Particle motion in a Penning trap*, Eur. J. Phys. **12**, 240 (1991).

[277] R. Ringle, G. Bollen, P. Schury, S. Schwarz and T. Sun, *Octupolar excitation of ion motion in a Penning trap–A study performed at LEBIT*, Int. J. Mass Spectrom. **262**, 33 (2007).

[278] S. Eliseev *et al.*, *Octupolar excitation of ions stored in a Penning trap mass spectrometer—A study performed at SHIPTRAP*, Int. J. Mass Spectrom. **262**, 45 (2007).

[279] K. Blaum *et al.*, *Recent developments at ISOLTRAP: towards a relative mass accuracy of exotic nuclei below* 10^8, J. Phys. B: At. Mol. Opt. Phys. **36**, 921 (2003).

Danksagung

Als erstes geht mein Dank an *Klaus Blaum*. Volle Unterstützung, permanente Ratschläge, des öfteren Aufmunterung, beste Stimmung, alles rund um die Uhr und für so viele Leute. Als Familienvater und Max-Planck-Direktor. Ich hab keine Ahnung wie das zusammen geht, es ist weit weit mehr als man sich erhoffen kann von einem Chef. Also wer es noch nicht wusste, das ist ein Guter. VIELEN DANK.

Vielen Dank für die Unterstützung an das gesamte PENTATRAP-Team: *Sergey Eliseev, Christine Böhm, Andreas Dörr, Mikhail Goncharov, Christian Hökel-Schmöger und Julia Repp*, insbesondere an den Andreas für die reibungslose Übernahme vieler Aufgaben; der Christine fürs angenehme Büroteilen über die Jahre; thanks to Mikhail for understanding; und ein ganz spezielles Dankeschön an den Sergey, immer eine offene Tür, immer gute Ratschläge und sehr sehr fruchtbare Diskussionen, hab viel gelernt, vielen Dank. Danke an *Sebastian George* für Beiträge der ersten Stunde, and thanks to *Yuri Novikov* for insightful explanations.

Vielen Dank an *Ralph Zilly*, für den Spaß über die Jahre und die wertvolle Unterstützung bei vielen Aufgaben v.a. im technischen Bereich. Vielen Dank.

Vielen Dank an die anderen Heidelberger Fallenexperimente THE-TRAP und KATRIN-FT-ICR für die Kollegialität, insbesondere an *Christoph Diehl, Sebastian Streubel, Martin Höcker und Tommi Eronen*. Ihr bringt Spaß. Vielen Dank.

Besten Dank an alle Mainzer Fallenleute, für die angenehme Atmosphäre und den Know-How-Transfer nach Heidelberg an vielen Stellen, insbesondere an *Holger Kracke, Andreas Mooser* und *Anke Wagner*; und ganz ganz besonders an den *Sven Sturm*, wow, vielen Dank für Deine zahlreichen Beiträge für meine Arbeit und die gesamte Arbeitsgruppe. Vielen Dank.

Vielen Dank an die *Frau Dücker* für die warmen Worte bei vielen Gelegenheiten.

Vielen Dank auch an *Wolfgang Quint* für die selbstverständliche Bereitschaft ein zweites Gutachten für die Arbeit zu erstellen.

Special thanks to *Bennaceur Najjari* for theoretical support and practical Kicker-Matches.

Vielen Dank an das gesamte MPI-Umfeld, für die sehr angenehme Arbeitsatmosphäre da oben, insbesondere an die Werkstätten und die Konstruktion für die professionellen Beiträge zu unseren Experimenten.

Ganz ganz besonderen Dank für die Freundschaft und unfassbare Unterstützung an *Ulrich Warring, Jochen Ketter* und *Stefan Ulmer*. Man kann sich auf Euch verlassen, bei so vielem, das weiß ich zu schätzen! VIELEN DANK.